

NUREG/CR-4465

SAND85-2563

R4

Printed February 1986

TRAC-PF1/MOD1 Independent Assessment: Semiscale MOD-2A Intermediate Break Test S-IB-3

L. N. Kmetyk

Prepared by

Sandia National Laboratories

Albuquerque, New Mexico 87185 and Livermore, California 94550

for the United States Department of Energy

under Contract DE-AC04-76DP00789

Prepared for

U. S. NUCLEAR REGULATORY COMMISSION

SF2900Q(8-81)

B604010182
PDR NUREG
CR-4465 R

B6022

PDR

NOTICE

This report was prepared as an account of work sponsored by an agency of the United States Government. Neither the United States Government nor any agency thereof, or any of their employees, makes any warranty, expressed or implied, or assumes any legal liability or responsibility for any third party's use, or the results of such use, of any information, apparatus product or process disclosed in this report, or represents that its use by such third party would not infringe privately owned rights.

Available from
Superintendent of Documents
U.S. Government Printing Office
Post Office Box 37082
Washington, D.C. 20013-7982
and
National Technical Information Service
Springfield, VA 22161

NUREG/CR-4465
SAND85-2563
R4

TRAC-PF1/MOD1 INDEPENDENT ASSESSMENT:
SEMISCALE MOD-2A INTERMEDIATE BREAK TEST S-1B-3

L. N. Kmetyk

Date Published: February 1986

Sandia National Laboratories
Albuquerque, NM 87185
Operated by
Sandia Corporation
for the
U. S. Department of Energy

Prepared for
Reactor Systems Research Branch
Division of Accident Evaluation
Office of Nuclear Regulatory Research
U. S. Nuclear Regulatory Commission
Washington, DC 20555
Under Memorandum of Understanding DOE 40-550-75
NRC FIN No. A-1374

ABSTRACT

The TRAC-PF1/MOD1 independent assessment project at Sandia National Laboratories is part of an overall effort funded by the NRC to determine the ability of various system codes to predict the detailed thermal/hydraulic response of light water reactors during accident and off-normal conditions. The TRAC code is being assessed at SNLA against test data from various integral and separate effects test facilities. As part of this assessment matrix, an intermediate break test (S-IB-3), performed at the Semiscale Mod-2A facility, has been analyzed. Using an input model with a 3-D VESSEL component, the vessel and downcomer inventories during S-IB-3 were generally well predicted, but the core heatup was underpredicted compared to data. An equivalent calculation with an all 1-D input model ran about twice as fast as our basecase analysis using a 3-D VESSEL in the input model, but the results of the two calculations diverged significantly for many parameters of interest, with the 3-D VESSEL model results in better agreement with data.

CONTENTS

	<u>Page</u>
EXECUTIVE SUMMARY	1
1.0 INTRODUCTION	3
2.0 NODALIZATION	5
2.1 Semiscale S-IB-3 Model with 3-D VESSEL Component	5
2.2 Semiscale S-IB-3 Model with all 1-D Components	7
3.0 BASECASE RESULTS	17
3.1 Transient Initialization	17
3.2 Primary Side Thermal/Hydraulics	19
3.3 Loop Inventory Distribution	20
3.4 Vessel Inventory	22
3.5 Core Response	24
4.0 NODING STUDY	67
4.1 Basecase 3-D vs Original 1-D Model Results	67
4.2 Density Gradient Inversion at Component Boundary	68
4.3 Inverted Annular Flow Modelling Option	70
4.4 Basecase 3-D vs Final 1-D Model Results	71
5.0 DISCUSSION	111
5.1 User Experience	111
5.2 Pump Degradation/Flow Stagnation Sensitivity Studies	113
5.3 Vessel Heat Slab Sensitivity Studies	114
5.4 "Multiple PLENUMs" Code Error	115
5.5 Computational Run Times	116
6.0 SUMMARY AND CONCLUSIONS	127
7.0 REFERENCES	131
APPENDIX I Semiscale Mod-2A Facility	133
APPENDIX II Input Listing	153

ILLUSTRATIONS

	<u>Page</u>
2.1.1 Semiscale Mod-2A Test Facility	9
2.1.2 Facility Nodalization Schematic for Model with 3-D VESSEL Component	10
2.1.3 3-D Vessel Nodalization	11
2.2.1 Facility Nodalization Schematic for Model with All 1-D Components	12
2.2.2 1-D Vessel Nodalization	13
3.2.1 Intact and Broken Loop Cold Leg Pressures	28
3.2.2 Break Flow Rate	29
3.2.3 Broken Loop Cold Leg Liquid and Vapor Temperatures	30
3.2.4 Broken Loop Hot Leg Liquid and Vapor Temperatures	31
3.2.5 Intact Loop Hot Leg Liquid and Vapor Temperatures	32
3.2.6 Intact Loop Cold Leg Liquid and Vapor Temperatures	33
3.2.7 Accumulator Injection Flow Rate	34
3.3.1 Intact Loop Cold Leg Densities at and Downstream of Accumulator Injection	35
3.3.2 Intact Loop Pump Suction Leg Liquid Levels	36
3.3.3 Intact Loop Pump Suction Leg Densities	37
3.3.4 Intact Loop Steam Generator Tube Liquid Levels	38
3.3.5 Intact Loop Hot Leg Densities	39
3.3.6 Intact Loop Hot Leg Mass Flow Rates	40
3.3.7 Broken Loop Hot Leg Mass Flow Rates	41
3.3.8 Broken Loop Hot Leg Densities	42
3.3.9 Broken Loop Steam Generator Tube Liquid Levels	43
3.3.10 Broken Loop Pump Suction Leg Densities	44
3.3.11 Broken Loop Pump Suction Leg Liquid Levels	45

	<u>Page</u>
3.3.12 Broken Loop Pump-Side Cold Leg Densities	46
3.3.13 Broken Loop Vessel-Side Cold Leg Densities	47
3.4.1 Downcomer Mass Flow Rates	48
3.4.2 Vessel and Downcomer Liquid Levels	49
3.4.3 Mid-Downcomer Densities	50
3.4.4 Lower Plenum, Heated Length and Upper Plenum Liquid Levels	51
3.4.5 Lower Plenum Densities	52
3.4.6 Lower Core Densities (1.13 m Core Elevation)	53
3.4.7 Middle Core Densities (1.83 m Core Elevation)	54
3.4.8 Upper Core Densities (3.42 m Core Elevation)	55
3.4.9 Upper Head Liquid Level	56
3.5.1 Core Power and Total Rod Heat Transfer	57
3.5.2 Maximum Rod Clad Temperature	58
3.5.3 Lower Core Heater Rod Temperatures (0.15 m Core Elevation)	59
3.5.4 Lower Core Heater Rod Temperatures (1.12 m Core Elevation)	60
3.5.5 Lower Core Heater Rod Temperatures (1.36 m Core Elevation)	61
3.5.6 Middle Core Heater Rod Temperatures (1.83 m Core Elevation)	62
3.5.7 Upper Core Heater Rod Temperatures (2.30 m Core Elevation)	63
3.5.8 Upper Core Heater Rod Temperatures (2.91 m Core Elevation)	64
3.5.9 Upper Core Heater Rod Temperatures (3.53 m Core Elevation)	65
4.1.1 Intact and Broken Loop Cold Leg Pressures with 3-D and 1-D Models	74
4.1.2 Break Flow Rates with 3-D and 1-D Models	75
4.1.3 Accumulator Injection Flow Rate with 3-D and 1-D Models	76
4.1.4 Vessel and Downcomer Liquid Levels with 3-D and 1-D Models	77
4.1.5 Lower Plenum, Heated Length and Upper Plenum Liquid Levels with 3-D and 1-D Models	78

	<u>Page</u>
4.1.6 Maximum Rod Clad Temperatures with 3-D and 1-D Models	79
4.1.7 Middle Core Heater Rod Temperatures (1.83 m Core Elevation) with 3-D and 1-D Models	80
4.2.1 Mid-Downcomer Densities with 3-D and 1-D Models	81
4.2.2 Lower Plenum Densities with 3-D and 1-D Models	82
4.2.3 Lower Core Densities (1.13 m Core Elevation) with 3-D and 1-D Models	83
4.2.4 Middle Core Densities (1.83 m Core Elevation) with 3-D and 1-D Models	84
4.2.5 Upper Core Densities (3.42 m Core Elevation) with 3-D and 1-D Models	85
4.2.6 Vessel Void Fraction Profiles with 3-D and 1-D Models	86
4.2.7 Lower Plenum/Core Nodalizations in (Basecase) 1-D and Modified 1-D Models	87
4.2.8 Vessel Void Fraction Profiles with 3-D, (Basecase) 1-D and Modified 1-D Models	88
4.2.9 Vessel Void Fraction Profiles with our 3-D Model, and both our and LANL's (Basecase) 1-D and Modified 1-D Model Calculations	89
4.3.1 Vessel Void Fraction Profiles with (Basecase) 1-D Model using Different Inverted Annular Flow Logic	90
4.3.2 Lower Plenum Densities with (Basecase) 1-D Model using Different Inverted Annular Flow Logic	91
4.3.3 Lower Core Densities (1.13 m Core Elevation) with (Basecase) 1-D Model using Different Inverted Annular Flow Logic	92
4.3.4 Middle Core Densities (1.83 m Core Elevation) with (Basecase) 1-D Model using Different Inverted Annular Flow Logic	93
4.3.5 Upper Core Densities (3.42 m Core Elevation) with (Basecase) 1-D Model using Different Inverted Annular Flow Logic	94
4.3.6 Lower Plenum, Heated Length and Upper Plenum Liquid Levels with (Basecase) 1-D Model using Different Inverted Annular Flow Logic	95
4.3.7 Vessel and Downcomer Liquid Levels with (Basecase) 1-D Model using Different Inverted Annular Flow Logic	96

	<u>Page</u>
4.3.8 Maximum Rod Clad Temperatures with (Basecase) 1-D Model using Different Inverted Annular Flow Logic	97
4.3.9 Middle Core Heater Rod Temperatures (1.83 m Core Elevation) with (Basecase) 1-D Model using Different Inverted Annular Flow Logic	98
4.4.1 Intact and Broken Loop Cold Leg Pressures with 3-D and Final 1-D Models	99
4.4.2 Accumulator Injection Flow Rate with 3-D and Final 1-D Models	100
4.4.3 Vessel and Downcomer Liquid Levels with 3-D and Final 1-D Models	101
4.4.4 Lower Plenum, Heated Length and Upper Plenum Liquid Levels with 3-D and Final 1-D Models	102
4.4.5 Maximum Rod Clad Temperatures with 3-D and Final 1-D Models	103
4.4.6 Middle Core Heater Rod Temperatures (1.83 m Core Elevation) with 3-D and Final 1-D Models	104
4.4.7 Mid-Downcomer Densities with 3-D and Final 1-D Models	105
4.4.8 Lower Plenum Densities with 3-D and Final 1-D Models	106
4.4.9 Lower Core Densities (1.13 m Core Elevation) with 3-D and Final 1-D Models	107
4.4.10 Middle Core Densities (1.83 m Core Elevation) with 3-D and Final 1-D Models	108
4.4.11 Upper Core Densities (3.42 m Core Elevation) with 3-D and Final 1-D Models	109
4.4.12 Vessel Void Fraction Profiles with 3-D and Final 1-D Models	110
5.3.1 Vessel and Downcomer Liquid Levels with (a) no Vessel Internal Insulation and (b) Perfect Vessel Internal Insulation	118
5.3.2 Lower Plenum, Heated Length and Upper Plenum Liquid Levels with (a) no Vessel Internal Insulation and (b) Perfect Vessel Internal Insulation	119
5.3.3 Lower Plenum Densities with (a) no Vessel Internal Insulation and (b) Perfect Vessel Internal Insulation	120
5.3.4 Middle Core Densities (1.83 m Core Elevation) with (a) no Vessel Internal Insulation and (b) Perfect Vessel Internal Insulation	121

	<u>Page</u>
5.3.5 Maximum Rod Clad Temperatures with (a) no Vessel Internal Insulation and (b) Perfect Vessel Internal Insulation	122
5.4.1 Different Interpretations of "Liquid Level"	123
5.5.1 Total CRAY-XMP CPU Time with 3-D and 1-D Models	124
5.5.2 Time Step History with 3-D and 1-D Models	125
AI.1 Isometric View of the Semiscale Mod-2A System	137
AI.2 Semiscale Mod-2A Intact Loop Spool Pieces	138
AI.3 Semiscale Mod-2A Broken Loop Spool Pieces	139
AI.4 Break Simulator for Semiscale Test S-IB-3	140
AI.5 Semiscale Mod-2A Steam Generator Assembly	141
AI.6 Semiscale Mod-2A Pressurizer Vessel	142
AI.7 Semiscale Mod-2A Vessel Assembly	143
AI.8 Semiscale Mod-2A Vessel Upper Head Region	144
AI.9 Semiscale Mod-2A Vessel Downcomer Inlet and Upper Plenum Region	145
AI.10 Semiscale Mod-2A Vessel Core Region	146
AI.11 Semiscale Mod-2A Core Axial Power Profile	147
AI.12 Semiscale Mod-2A Vessel Lower Plenum and Lower Downcomer Region	148

TABLES

	<u>Page</u>
2.1.1 Nodalization with 3-D Vessel	14
2.2.1 Nodalization with all 1-D Components	15
3.1.1 Steady State Initial Conditions	26
3.1.2 Experimental Boundary Conditions	27
5.5.1 Run Time Statistics	126
AI.1 Semiscale Primary Coolant System Elevations	149
AI.2 Semiscale Intact Loop Spool Pieces	150
AI.3 Semiscale Broken Loop Spool Pieces	151
AI.4 Semiscale Type II Steam Generator Data	152

ACKNOWLEDGEMENTS

I would like to express my appreciation for the efforts of other Sandia staff in support of this analysis: Millie Elrick for maintaining TRAC on the Sandia computer system and for general graphics support; Jan Frey for construction of this final report; and Larry Buxton, Dean Dobranich and Don King for useful feedback during their review of this report.

EXECUTIVE SUMMARY

The TRAC-PFI/MOD1 independent assessment project at Sandia National Laboratories is part of an overall effort funded by the NRC to determine the ability of various system codes to predict the detailed thermal/hydraulic response of light water reactors during accident and off-normal conditions. The TRAC code is being assessed at SNLA against test data from various integral and separate effects test facilities. As part of this assessment matrix, an intermediate break test (S-IB-3), performed at the Semiscale Mod-2A facility, has been analyzed.

The S-IB-3 transient was first run using an input model which included a 3-D VESSEL component. The vessel and downcomer inventories were generally well-predicted, but the core heatup was underpredicted compared to data. The major discrepancies between measurement and calculation were:

- a later stagnation of the loop flow after pump degradation in the calculation (possibly due to known inapplicability of the published pump curves for the pumps currently installed) causing a ~20 s delay in core uncover and heatup relative to data;
- a calculated partial clearing of the intact loop pump seal compared to an observed total loop seal clearing, causing a smaller level recovery to be predicted than observed; and
- less predicted steam generation and superheat (due to underprediction of core heatup) causing a more rapid calculated depressurization after loop seal clearing, which in turn resulted in an earlier onset of accumulator injection and a higher injection rate in the calculation, quenching the core earlier than was measured.

An input model using all 1-D components was developed to allow us to assess the new PLENUM component by comparing results for that model to those obtained with our basecase model, which included a 3-D VESSEL component. The purely 1-D model calculation ran about twice as fast as the equivalent 3-D vessel model, but the results of the two models diverged significantly for a number of major variables, with the basecase 3-D vessel model results generally in better agreement with data. Further analysis showed the 1-D model calculation predicting an unphysical void fraction profile, with a "discontinuity" (i.e., a density gradient inversion) at the component boundary between the lower plenum TEE and the CORE components.

This result was given to the code developers at Los Alamos. After some examination, they determined that the key lay in the code assumption of inverted annular flow in the 1-D CORE component. This inverted annular flow regime is not documented in the TRAC manual, is limited to 1-D components with generalized heat slabs, and is explicitly disallowed at the component boundaries (explaining the dependence of our results on the location of the component boundary). The use of this inverted annular flow regime also can be affected by changing an undocumented NAMELIST variable, INVAN. The default value of zero causes the inverted annular flow regime to be considered whenever the wall temperature is greater than saturation; setting this flag to 1 causes this flow regime to be allowed only when the temperature is greater than the critical heat flux temperature, T-CHF, (which seems more reasonable).

Before evaluating the impact of changing the inverted annular flow option, we had to obtain additional error corrections from LANL, correcting the T-CHF calculation so that the INVAN flag would have the proper effect. After this was done, we reran our basecase 1-D model calculation for the transient period being analyzed, setting INVAN=1. The new void fraction profiles from this final 1-D calculation were more like step functions than the more smoothly varying 3-D profile, but the unphysical density inversion had been eliminated. However, the results from the 3-D model calculation were still generally in better overall agreement with data than the final 1-D model calculation results.

1.0 INTRODUCTION

The TRAC-PFI/MOD1 independent assessment project at Sandia National Laboratories in Albuquerque (SNLA) is part of an overall effort funded by the U. S. Nuclear Regulatory Commission (NRC) to determine the ability of various system codes to predict the detailed thermal/hydraulic response of light water reactors during accident and off-normal conditions. This TRAC-PFI/MOD1 assessment project is a successor to the RELAP5/MOD1 independent assessment program previously performed at Sandia.

TRAC-PFI/MOD1 [1] is the latest version of a systems code developed at Los Alamos National Laboratory (LANL) to provide advanced best-estimate predictions of postulated accidents and transients in pressurized water reactors (PWRs). TRAC-PFI features a two-fluid nonequilibrium hydrodynamics model with a flow-regime-dependent constitutive equation treatment; additional models have been incorporated in TRAC-PFI/MOD1 to allow simulation of a broad range of accidents relevant to current licensing issues.

Most of the early work in our assessment program was done using Version 11.0, received from LANL in October 1983 when our program started. Some calculations have been done with intermediate versions such as 11.6, 11.9 or 12.0, but any such runs are considered and are clearly identified here as being preliminary calculations. The final S-IB-3 transient runs discussed herein were done with Version 12.1+EC2 for the basecase calculation which used a 3-D VESSEL component in the input model, and with both Version 12.1+EC2 and Version 12.1+EC12.3 for the purely 1-D component input model sensitivity studies (using LANL's changing nomenclature).

TRAC-PFI/MOD1 is being assessed at SNLA against test data from various integral and separate effects experimental test facilities. The TRAC assessment test matrix includes counterpart intermediate break LOCA transient tests performed at the Loop Blowdown Investigations (LOBI) test facility in Italy [2,3,4,5] and in the Semiscale Mod-2A facility at the Idaho National Engineering Laboratory (INEL) [6,7,8]. Semiscale Mod-2A test S-IB-3 [9,10,11] was designed to duplicate as closely as possible the LOBI B-RIM test [12,13,14], a 25% break in the LOBI facility which, when area-to-volume scaled to the Semiscale facility, resulted in a 21.7% break test. The Semiscale S-IB-3 calculations were generally run in parallel with our B-RIM assessment study, with user experience feeding back and forth between the two analyses. The results of our B-RIM assessment calculations, and a discussion of the code's ability to predict the similarities and differences between these two counterpart tests, have been documented elsewhere. [15]

This report summarizes our TRAC analyses of the Semiscale S-IB-3 intermediate break transients. The TRAC nodalizations used are described in Section 2. Calculational results are presented in Section 3 for the basecase transient analyses, as well as for the steady state initialization. Section 4 discusses the results of a noding study using 3-D and 1-D vessel models for S-IB-3, while user experiences, sensitivity study results, code errors and run time statistics are given in Section 5. Overall conclusions and their possible relevance to future TRAC code development and/or modification are discussed in Section 6. The appendices provide a brief description of the test facility, and input listings for the transient, for reference.

2.0 NODALIZATION

Although 3-D effects were not expected to be important in Semiscale (a "tall thin" facility), a 3-D VESSEL component was originally used in the basecase model rather than a 1-D CORE component to allow easier and more accurate modelling of vessel connections and geometry than could be achieved using numerous TEE components. The PLENUM component, which permits an arbitrary number of multiple connections to a single cell, did not become available until some months after the S-IB-3 analysis had started; an input model using all 1-D components was then developed for a nodalization sensitivity study as part of the S-IB-3 analysis. In the rest of the report, the basecase input model (described in Section 2.1) containing a 3-D VESSEL component is referred to as "the 3-D model", while the input model developed with all 1-D components (described in Section 2.2) is referred to as "the 1-D model" henceforth.

2.1 Semiscale S-IB-3 Model with 3-D VESSEL Component

The Semiscale Mod-2A test facility [6,7,8], shown in Figure 2.1.1, is located at the Idaho National Engineering Laboratory and supported by the NRC. This scaled integral facility is used to investigate the thermal and hydraulic phenomena accompanying various hypothesized loss-of-coolant accidents and operational transients in a PWR system. It is a 2/3411-scale model of a four-loop PWR, consisting of two primary coolant loops and external downcomer connected to an electrically-heated reactor pressure vessel, in which 25 rods provide a peak power of 2.0 MW. While both loops contain a fully active circulation pump and steam generator, the intact loop has three times the water volume and mass flow of the broken loop. A more complete description of the test facility is given in Appendix I.

The TRAC-PFI/MOD1 nodalization developed for the S-IB-3 transient calculation is shown in Figure 2.1.2. Both loops are modelled, with the intact loop shown on the left, the broken loop on the right and the vessel in the middle. This model contains 35 components, with 186 1-D cells and 48 3-D cells in the vessel, for a total of 234 cells overall. The detailed distribution of these cells is summarized in Table 2.1.1. A complete listing of the input for this S-IB-3 basecase transient analysis model is given in Appendix II.

There is a total of 233 heat slabs (with 183 in various 1-D components and 50 in the 3-D VESSEL, of which 2 represent the heater rods) in this S-IB-3 nodalization. Most of the heat slabs in the 1-D components contain three nodes, although the 17 or 16 slabs, respectively, modelling the U-tubes in the intact or broken loop steam generator and the 45 or 41 slabs representing various secondary side walls and fillers have five nodes each. The majority of the 3-D vessel slabs use the lumped-parameter model and thus have only one node, while the heater rods have 14 nodes. The minimum tube-to-tube spacing is used as the heated equivalent diameter for the outside of the steam generator U-tubes, according to our own internal user guidelines. [16]

The 3-D vessel used has 1 radial ring, 2 unequal azimuthal sectors (split 2:1 between the intact and broken loop sides) and 24 axial levels (4 in the lower plenum, 12 in the core heated length, and 4 each in the upper plenum and in the upper head). The vessel nodalization is shown in more detail in Figure 2.1.3. The relative

elevations of the level boundaries are given (for comparison with Figures AI.8 through AI.12). The core region axial levels were chosen based on the axial rod geometry and power profile information given in Figure AI.11. The azimuthal sectors were chosen primarily so that 2/3 of the VESSEL flow area and volume would be associated with the sector containing the two (lumped) support columns, while 1/3 would be associated with the single guide tube. Both the lumped support columns and the guide tube were modelled with 1-D components attached to appropriate cells in different levels of the 3-D VESSEL. The support columns are represented by a PIPE component connecting the lowest upper plenum level with the lowest upper head level. The guide tube is modelled as a TEE component whose primary side connects the second upper plenum level with the top upper head level; the secondary side of the guide tube TEE represents vent holes drilled in the guide tube near the top of the upper plenum and therefore connects to the fourth (uppermost) upper plenum level. (The hot legs come in at the third upper plenum level.)

Besides the core rods, heat slabs have been included for some of the internal vessel structure. Heat slabs for the pressure vessel, core barrel, fillers, flanges, etc., were not included in the final model because we assumed the interior insulation to be perfect, i.e., no energy transfer from these structures to the fluid. (Calculations were also done with the effects of the internal insulation neglected and all the metal mass available for stored energy transfer; the results will be given as part of the discussion section.) The simplistic heat slabs available in the 3-D VESSEL component precluded a more accurate representation of the actual situation. For example, the limitation of one heat slab per vessel cell precludes modelling both thin heat slabs corresponding to uninsulated heater rod extensions and thick heat slabs representing partially-insulated vessel walls.

The external downcomer and the bypass line are also modelled with 1-D volumes, usually connected to cells in the 3-D VESSEL component. The downcomer inlet annulus was modelled with a PLENUM component, allowing the intact and broken loop cold legs, downcomer pipe and bypass line to all connect into a single cell. As with the pressure vessel itself, the downcomer pipe and annuli in the Semiscale facility are internally insulated and the downcomer PIPE in our model therefore was modelled without heat slabs representing wall structural heat transfer. (No provision for heat slabs is currently available in the PLENUM component.)

The single-phase homologous head and torque curves for the intact and broken loop pumps were based on data supplied by the Semiscale program [7]. The single-phase data for the broken loop pump were obtained before the broken loop pump was modified, and hence are not strictly applicable (but are the only data available). The intact loop two-phase head and torque multiplier and difference curves were also supplied by Semiscale [7]. Since there were no two-phase data for the broken loop pump, the intact loop two-phase data is used for the broken loop pump, as usually recommended by INEL.

Piping elbows and area changes in the loop piping are carefully modelled, using guidelines developed at Sandia during the course of this assessment project. The resulting pressure drops calculated are in reasonably good agreement with the differential pressure measurements for steady state conditions. Our Semiscale

Mod-2A TRAC nodalization was derived largely from RELAP5/MOD1 input models developed during an earlier code assessment project at Sandia [16,17]. Our results from various calculations (e.g., the PKL natural circulation tests [18] and the B&W OTSG separate effects tests [19]) indicate that previously-developed RELAP5 input loss coefficients cannot be used without some modifications. When converting RELAP5 loss coefficients for TRAC use, user-input loss coefficients representing pipe bends are unchanged but user-input loss coefficients for pipe tees are removed, because the TRAC TEE component apparently calculates some of the losses due to momentum effects (unlike RELAP5 BRANCH components). Hydraulic diameters (a cell-edged input in TRAC) must be adjusted to produce the correct overall wall friction whenever two pipes of different areas (and hence different cell-centered diameters) are adjacent. The vena contracta area is input for orifices rather than the geometric area, and the friction factor option NFF is usually set to -2 at area changes and to +2 in smooth pipes and at both VESSEL connections and TEE primary-to-side connections.

The ECC injection line geometry is not well-documented for the Semiscale Mod-2A facility. We took line lengths from an old Semiscale Mod-1 blueprint. An accumulator surge line resistance $R' = 2.0 * 10^{10} \text{ m}^{-4}$ is given in the S-IB-3 test documentation [10]. Using the flow area for a 1-in Sch 80 pipe (0.00046 m^2), this corresponds to a total loss coefficient $K = 4300$. Assuming the high wall friction generally typical of accumulator injection ($f=0.03$) and using a surge line length of 16.5 m and diameter of 0.0243 m, the wall friction fL/D gives a loss factor ($K\text{-fric}$) of 20, leaving the remaining resistance $4300-20$ to be user-input to represent piping bends, orifices, valves, loop-entrance effects, etc. A user-input K of 475 is thus set at each of the 9 junctions in the surge line. These values depend on the flow area assumed; using a smaller flow area would result in a smaller user-input K , if so desired.

A similar procedure was used to convert the pressurizer surge line resistance given as $R' = 3.2 * 10^9 \text{ m}^{-4}$ [10] to user-input loss coefficients.

2.2 Semiscale S-IB-3 Model with all 1-D Components

The 1-D TRAC-PF1/MOD1 model developed for the S-IB-3 nodalization sensitivity study is shown in Figure 2.2.1. Both loops are modelled, with the intact loop shown on the left, the broken loop on the right and the vessel in the middle. This model contains 42 components, with 213 1-D cells. The detailed distribution of these cells is given in Table 2.2.1. A complete listing of the input used for the Semiscale S-IB-3 1-D transient analysis is given in Appendix II.

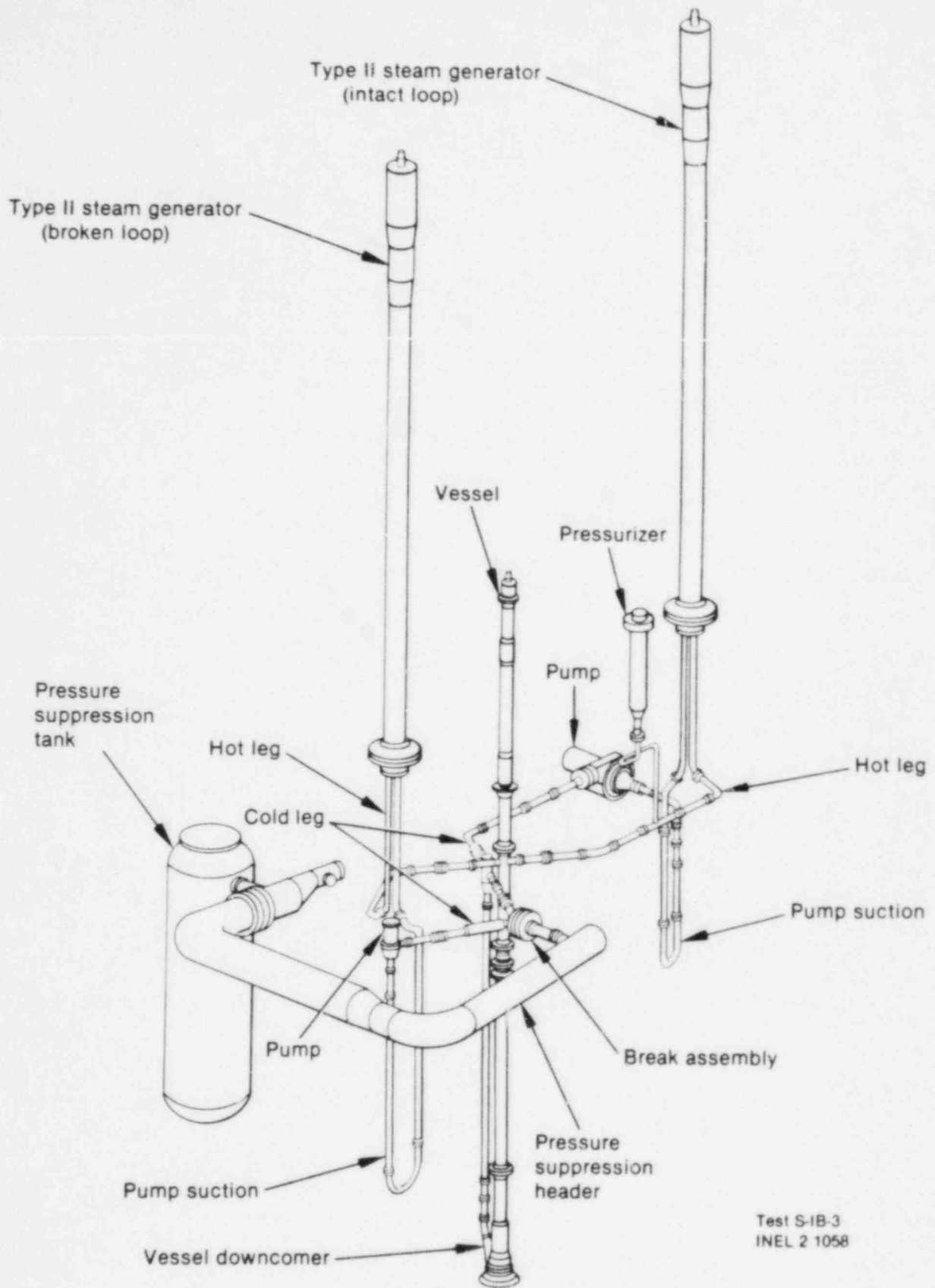
There is a total of 184 heat slabs (with 1 representing the heater rods in the CORE component) in this S-IB-3 nodalization. The heat slabs in the 1-D components are the same as in the base S-IB-3 model described in the previous section; the single core rod has 14 nodes, with the same radial and axial geometry and power shape as the rods in the 3-D VESSEL.

Because 1-D components (except for STGEN components) only allow wall heat slabs, no heat slabs were included in any of the new 1-D components representing the vessel, except for the core rods. As in the 3-D VESSEL model, the pressure vessel, core barrel, fillers, flanges, etc., were not included in the model because we assumed the interior insulation to be perfectly effective. As before, the internally-insulated downcomer pipe and annuli were also modelled with no heat slabs representing the wall metal.

The 1-D vessel nodalization is shown in more detail in Figure 2.2.2. The relative elevations of the level boundaries are given (for comparison with Figure 2.1.3). The downcomer nodalization is essentially unchanged. The four levels in the lower plenum and the twelve levels in the heated length are also axially equivalent to their counterparts in the 3-D VESSEL, with the two parallel azimuthal sector flow paths combined. The upper head noding (as well as the plenum support column and guide tube connections), now assembled from PIPEs and TEEs, is not exactly equivalent axially to its 3-D counterpart because connections to axial faces in 3-D cells occur at boundaries while TEE connections are cell-centered.

Both the lumped support columns and the guide tube are still modelled with 1-D components, but the various TEEs used do not correspond exactly to those in the basecase 3-D model due to the noding compromises required. The lumped support columns are represented by the joined side tubes of two TEE components whose primaries are the lowest upper plenum level and the lowest upper head level, respectively. The guide tube is modelled as three TEE components with one primary and two joined side tubes; the primary sides of two of these guide tube TEEs are the second upper plenum level and the top upper head level. The side tube of the third (middle) guide tube TEE corresponds to the vent holes drilled in the guide tube near the top of the upper plenum and therefore connects to the top of the fourth (uppermost) upper plenum PIPE.

The external downcomer and the bypass line are also modelled with 1-D components, similar to the basecase model; the downcomer inlet annulus was modelled with a PLENUM component, allowing the intact and broken loop cold legs, downcomer pipe and bypass line to all connect into a single cell. The rest of the loop nodalization was the same as the base model described in the previous section, although some components and junctions were renumbered for user convenience.



Test S-1B-3
INEL 2 1058

Figure 2.1.1 Semiscale Mod-2A Test Facility

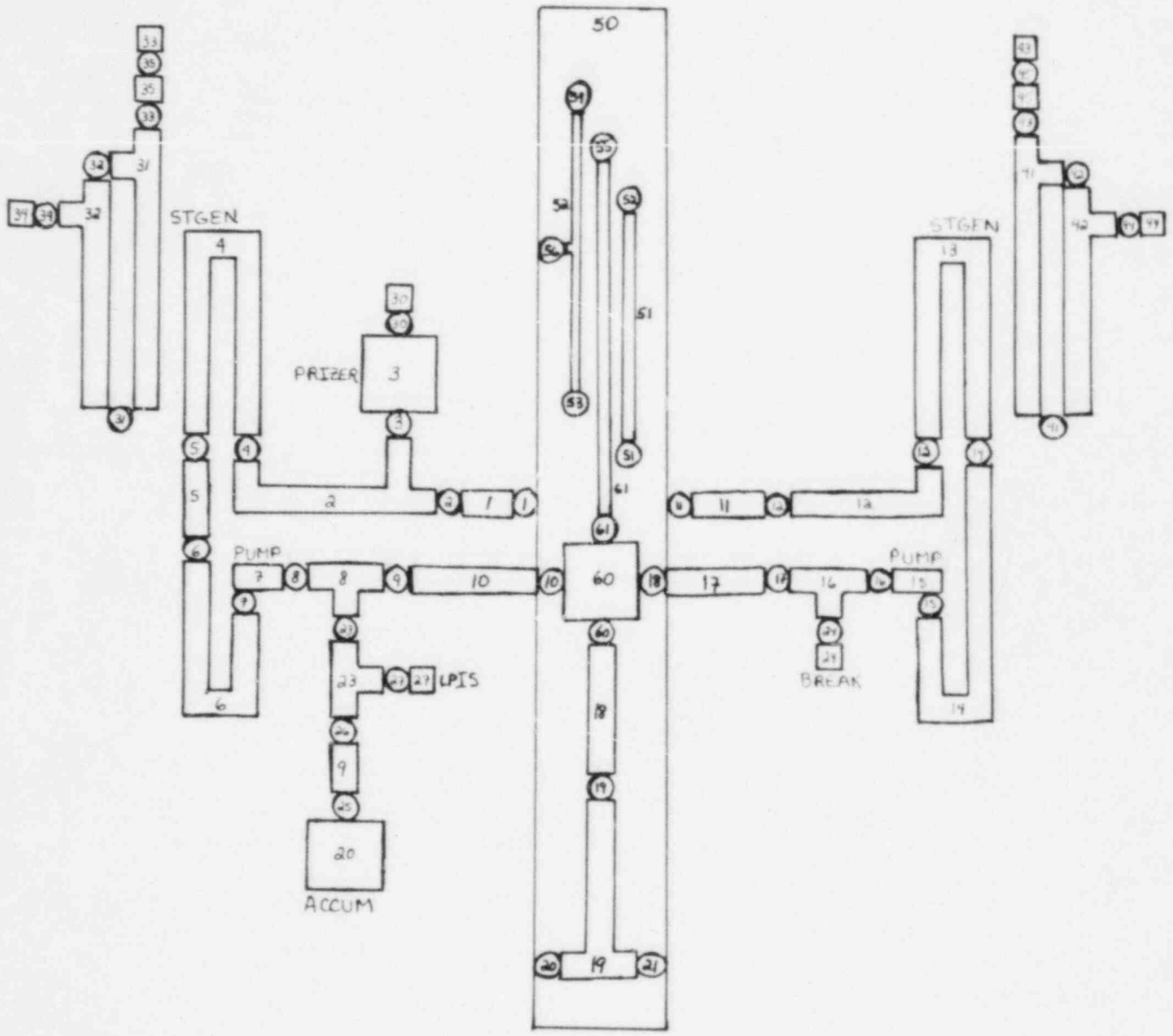


Figure 2.1.2 Facility Nodalization Schematic for Model with 3-D Vessel Component

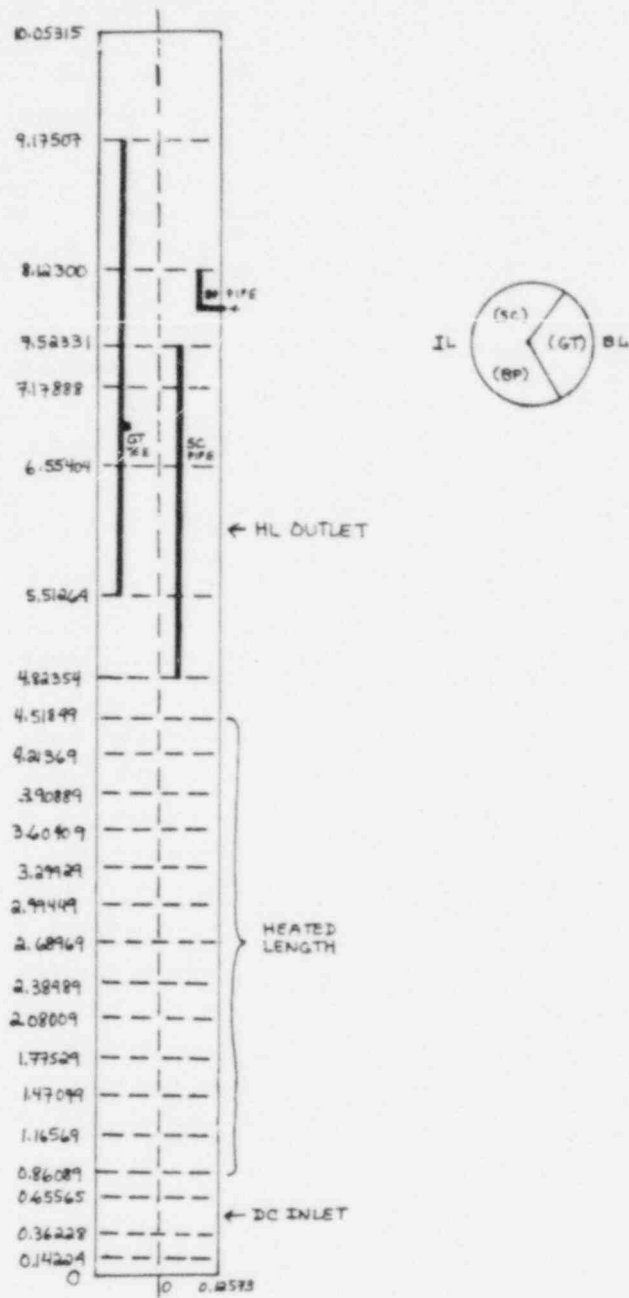


Figure 2.1.3 3-D Vessel Nodalization

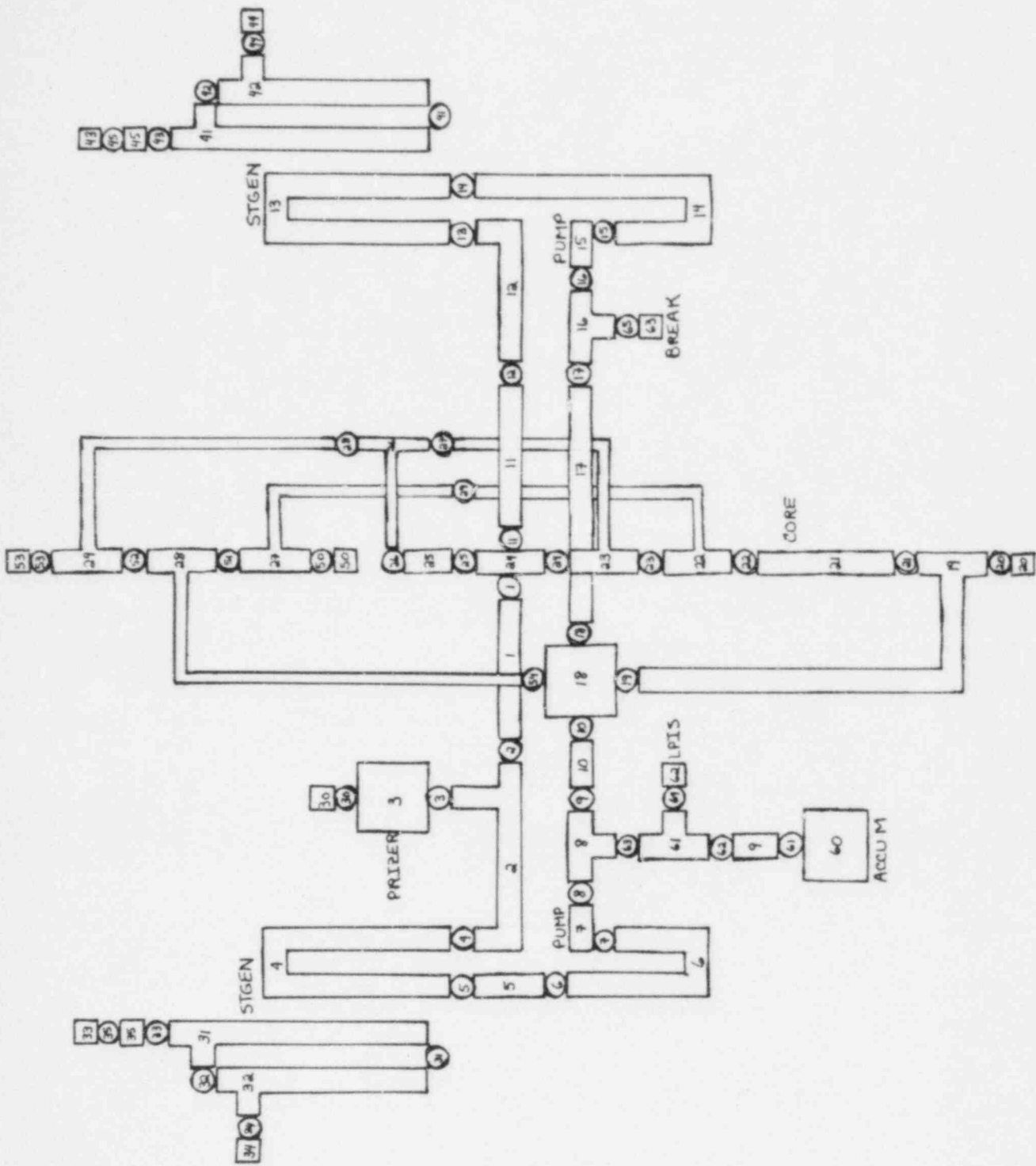


Figure 2.2.1 Facility Nodalization Schematic for Model with All I-D Components

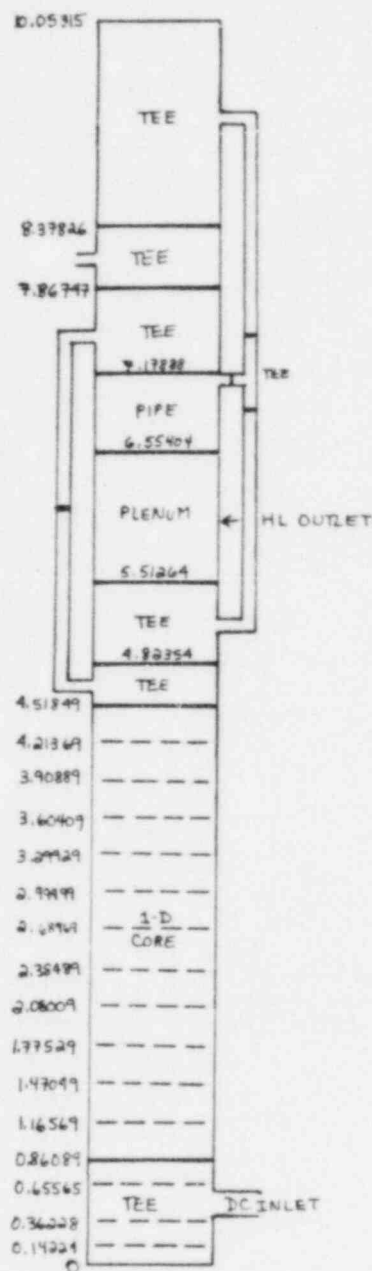


Figure 2.2.2 1-D Vessel Nodalization

Table 2.1.1 Nodalization with 3-D VESSEL

	<u>Hydro Cells</u>	<u>Heat Slabs</u>	<u>BREAK/FILLs</u>
Intact Loop			
Hot Leg	10	10	
SG Primary	19		
U-Tubes		17	
SG Secondary	28	45	2
Pump Suction	8	8	
Pump	2	2	
Cold Leg	5	5	
Pressurizer			
Vessel	4	4	1
Surge Line	5	5	
Accumulator			
Vessel	4		
Valve/Surge Line/LPIS	9	7	1
Broken Loop			
Hot Leg	8	8	
SG Primary	18		
U-Tubes		16	
SG Secondary	26	41	2
Pump Suction	8	8	
Pump	2	2	
Cold Leg and Break	5	5	1
Vessel			
Downcomer	12		
Lower Plenum	8	8	
Core	24	24 (+2 rods)	
Upper Plenum	8	8	
Upper Head	8	8	
Support Columns	1		
Guide Tube	4		
Bypass Line	1		

Table 2.2.1 Nodalization with all 1-D Components

	<u>Hydro Cells</u>	<u>Heat Slabs</u>	<u>BREAK/FILLs</u>
Intact Loop			
Hot Leg	10	10	
SG Primary	19		
U-Tubes		17	
SG Secondary	28	45	2
Pump Suction	8	8	
Pump	2	2	
Cold Leg	5	5	
Pressurizer			
Vessel	4	4	1
Surge Line	5	5	
Accumulator			
Vessel	4		
Valve/Surge Line/LPIS	9	7	1
Broken Loop			
Hot Leg	8	8	
SG Primary	18		
U-Tubes		16	
SG Secondary	26	41	2
Pump Suction	8	8	
Pump	2	2	
Cold Leg and Break	5	5	1
Vessel			
Downcomer	12		
Lower Plenum	4		1
Core	12	(+1 rod)	
Upper Plenum	4		
Upper Head	3	2	
Support Columns	2		
Guide Tube	4		
Bypass Line	1		

3.0 BASECASE RESULTS

This section presents the results of our final basecase calculation (using a 3-D VESSEL component) for the Semiscale S-IB-3 test [9,10,11]; the results from our purely 1-D model will be given in Section 4. Our user experience and sensitivity studies for this S-IB-3 analysis will be discussed in Section 5, together with run time statistics.

3.1 Transient Initialization

Table 3.1.1 shows the measured and calculated steady state initial conditions, with good agreement eventually achieved for all major parameters. The TRAC steady state calculation for S-IB-3 was begun from cold no-flow conditions, because no good estimate of the steady state was previously available. As in our earlier calculations, we found that using the minimum tube-to-tube spacing as the heated equivalent diameter on the outside of the U-tubes (rather than the usual hydraulic diameter) was required to allow simultaneous matching of the primary side cold leg temperature and the secondary side pressure. The resulting primary side conditions are generally in good agreement with data, except for the broken loop pump speed (which was expected [17]), and the intact and broken loop cold leg temperatures (which are too high for given secondary side conditions even with the minimum tube-to-tube spacing used as the heated equivalent diameter). The predicted loop ΔT 's are significantly less than reported but, given that we matched the core power and the loop flows exactly and hence should match the energy balance well, this suggests that either the reported temperatures or the reported loop flows were significantly affected by measurement uncertainties.

Based primarily upon the results of our LOBI B-RIM analyses [15], we also have taken care to ensure a good secondary side steady state before beginning any transient analyses. When we first began calculating the B-RIM steady state, we did not include any representation of the steam generator steam separators in the nodalization used. Such steam separators can be modelled in TRAC-PF1/MOD1 by specifying a user-input loss coefficient of 10^{**24} or greater at the junction corresponding to the separator location, which should allow only steam flow. (Pure liquid flow is obtained by specifying the loss coefficient to be less than or equal to -10^{**24} .) The separator model in TRAC thus results in perfect separation, with no allowance for any carryover or carryunder effects, and is known often to create difficulties during calculations. With no separators in the steam generators and resulting substantial liquid entrainment in the secondary side outflows, the steady state feedwater required was higher than measured and the secondary inventories were quite low for B-RIM.

We then extracted each steam generator and recalculated its steady state initial conditions with the separator modelled; these small "stand-alone" decks allowed a large number of calculations changing the input and controller setpoints to be made much more economically than using the full facility model. The final secondary system steady states had pure steam outflows, much lower feedwater injection rates and substantially higher secondary side inventories. The individual steam generator secondary side steady state conditions were then recombined with the primary side steady state conditions, and a final B-RIM steady state calculation made to fully integrate the results.

In contrast, the first S-IB-3 steady state results (also run without separators modelled, as was done in the first B-RIM steady state analyses) had too much secondary side liquid inventory in both steam generators, and the feedwater flows were much higher than needed to remove the core power (with most of the feedwater being entrained and swept out the steam outlet without participating in the heat transfer processes). We reran the steady state with feedwater flow controllers referencing the secondary side liquid level (developed for the S-SF-3 steady state [20]) and with a "separator K" to ensure pure steam outflow.

For these reruns, the steam generators were first run as "stand-alone" problems to test various control strategies and boundary conditions. In these stand-alone problems, the feedwater was first reduced and the secondary inventory allowed to boil off until it was substantially below the desired experimental value. A steam-separator K of 1.0E30 was then put in at the model junction corresponding to the actual location of the steam separator, and the feedwater was controlled to achieve a specified downcomer collapsed liquid level without overshooting the desired conditions. This technique was eventually successful for both steam generators, but with two problems encountered; one was an interpretation error we could correct, but the other was a code failure we could only hope to avoid.

The interpretation error lay in assuming the collapsed liquid level control function was a cell-centered variable so that the ordering of the component cells to be included did not matter. In fact, this variable is referenced to particular cell edges and the ordering is important (and was originally wrong). With the wrong liquid level driving the feedwater controller, a number of odd results were calculated.

This interpretation error in liquid level definition resulted in a signal variable value lower than the actual liquid level being calculated. As the feedwater controller then tried to increase this liquid level, the actual level approached the downcomer-separator junction and the calculation would usually predict rising pressures until a code steam table failure occurred; the "perfect" separator in TRAC has great difficulty in relieving steam generator overpressurization due to excess liquid inventory because it can only pass vapor.

With careful adjustments in the controller constants (based on the experience gained in the S-SF-3 steam generator steady state calculations [20]), the correct secondary side steady state conditions were eventually calculated. These conditions were then put in the overall S-IB-3 deck, and the system steady state was successfully run.

Table 3.1.2 gives the boundary conditions for the transient. A simulated communicative intermediate cold leg break was accomplished using a rupture disc and blowdown nozzle (shown in Figure A1.4) having a total break area of 1.24 cm². Effluent was ejected from the primary system to the pressure suppression system, which was vented to maintain a constant pressure of 0.241 MPa. Power to the electrically-heated core was automatically controlled to simulate the thermal decay response of nuclear fuel rods. At blowdown initiation, power to the intact and broken loop primary circulation pumps was reduced and the pumps were allowed to coast down to approximately 40% of initial speed. The intact loop pump maintained this speed for the duration of the test, but the broken loop pump power was tripped off when the pressurizer pressure reached 1 MPa. The intact and broken loop steam

generator steam discharge valves closed fully at the same primary system pressure setpoint of 1 MPa. The coolant injection systems were arranged to discharge into the cold leg of the intact loop. The accumulator operated automatically in response to system pressure during the test. The low-pressure coolant injection pump was used and its operation started when system pressure reached 1 MPa; the injection rate then varied with system pressure at a predetermined computer-controlled flow rate [10].

3.2 Primary Side Thermal/Hydraulics

Figure 3.2.1 shows the intact and broken loop cold leg pressures. (In all plots, solid lines give calculated results, while the measured data is shown in dashed lines.) There is very good agreement between calculation and experiment for the first and last thirds of the transient. This is somewhat unexpected, as the behavior early in the transient is controlled by the initial temperatures (and associated saturation pressures), which were high in our steady state compared to the data; the late-time agreement may also be fortuitous as there is a substantial discrepancy during the middle of the transient. The calculated pressure falls significantly below the measured value around ~100-200 s; the intact loop seal also clears at around 100 s in both test and calculation, which would be expected to increase the depressurization rate. (The broken loop seal clears at around 25-30 s in both experiment and calculation.) This effect is seen in the calculation, but not in the measured data; as will be shown later, the calculation underpredicts the core heatup throughout the transient and the associated steam production and superheat (beginning at ~100 s), which apparently maintained the higher pressures observed in the test in mid-transient.

The calculated break flow rate is given in Figure 3.2.2. There is no break flow data on the experimental data tape for S-1B-3; the measured data shown is digitized from a published plot [21] which only gave the break flow for the first 50 s of the transient. That break flow was not directly measured, but reportedly was obtained by differencing the broken loop cold leg mass flows on each side of the break. These cited broken loop cold leg mass flow rates are also not given in the experimental data report [11] or on the experimental data tape, but are probably combinations of densitometer and turbine flowmeter and/or drag screen measurements. Given the existence of both top and middle densitometer traces for the indicated locations and no documentation on the exact data processing used, we did not attempt to derive measured break flow for the entire period analyzed.

The partial data indicates good prediction of the subcooled break flow early in the transient (using a subcooled discharge coefficient of 1.0) and suggests the subsequent saturated break flow (for a saturated discharge coefficient of 0.9) may be high, particularly after the broken loop seal clears at ~25 s. (These subcooled and saturated discharge coefficient values were chosen to give good agreement for the peak break flow and the time that the 1 MPa primary pressure setpoint was reached, respectively.) A high saturated break flow would help explain why the pressure in the first 100 s is in such excellent agreement with data despite the fact that the calculated initial temperatures (and associated saturation pressures) are greater than measured; overpredicted saturated break flow would also be consistent with the greater depressurization calculated starting at ~100 s. However, the data is not adequate for true quantitative judgement.

As mentioned above, though, the more rapid depressurization calculated during the middle of the transient could as easily be due to general underprediction of vapor generation and superheat (due to underprediction of core heatup). Comparison of measured and calculated fluid temperatures throughout the loops show this discrepancy (with vapor superheat and/or liquid subcooling visually inferred from the deviations of either the measured or calculated temperatures from a smooth saturation curve corresponding to the measured or calculated system pressure). The best agreement with data is seen in the cold legs, as shown for the broken loop cold leg liquid and vapor temperatures in Figure 3.2.3; the large vapor superheat throughout most of the transient due to steam generator reverse heat transfer is well-predicted, and the small vapor superheat near the break after about 100 s is alternatively under- and overpredicted.

The general underprediction of vapor superheat is much more visible in the hot legs. Figures 3.2.4 and 3.2.5 give the liquid and vapor temperatures in the broken and intact loop hot legs, respectively. Although some superheat is calculated at about the right times, it is much less than measured. The intact loop cold leg liquid and vapor temperatures in Figure 3.2.6 show that the superheat due to reverse heat transfer in the intact loop is also underpredicted. These intact loop cold leg temperatures also show a small degree of liquid subcooling after the onset of accumulator injection.

Accumulator injection begins when the primary system pressure falls below the accumulator pressure of 2.6 MPa, at 163 s in the test. Due to the lower pressures predicted during the ~100-200 s period, this setpoint is reached at 138 s in the calculation and accumulator injection is thus predicted to begin early. Figure 3.2.7 shows the measured and calculated accumulator injection flow rates. In addition to beginning early, the calculated injection is both qualitatively different and not as smooth and well behaved as the data, although the integrated flow rate of injected liquid is nearly that observed by the end of the period analyzed. The discrepancies in the calculated accumulator injection rate are a direct consequence of the discrepancies between the calculated and measured primary system pressures (Figure 3.2.1). The accumulator injection rate is controlled by the pressure difference between the accumulator gas and the primary system. The initially higher predicted accumulator injection is due to the lower primary system pressures being calculated at those times; the lower predicted accumulator injection later in the transient, when the measured and calculated primary system pressures come back to agreement, is due to a depleted accumulator driving pressure due to the earlier overpredicted injection. The higher calculated injection after about 300 s is again due to lower primary system pressures being calculated than were measured.

3.3 Loop Inventory Distribution

The early onset of accumulator injection in the calculation and the subsequent alternating over- and underpredictions of the injection rate are mirrored in the calculated intact loop cold leg densities in the latter part of the transient. Figure 3.3.1 shows the densities at and downstream of the accumulator injection port. This figure also shows that the effect of the intact loop seal clearing at ~100 s on the cold leg densities is correctly calculated.

The intact loop seal clearing is shown in more detail in Figures 3.3.2 and 3.3.3, which give the intact loop pump suction leg collapsed liquid levels and selected localized densities, respectively. (All collapsed liquid level data shown in plots in this section are digitized from experimental data report figures [10,21] rather than plotted from experimental data tapes.) The data shows the loop seal completely clearing from 100 to 150 s, while the calculation shows only a partial clearing at 100 s with some liquid remaining in the upflow side throughout the transient. With the lower calculated primary pressures after ~100 s, this may also be due to underpredicting the core heatup and subsequent steam generation and superheat.

Figure 3.3.4 gives calculated and measured intact loop steam generator primary side U-tube collapsed liquid levels. In the upflow (hot-leg) side where data is available, the agreement is generally very good, although the oscillations are somewhat out-of-phase in the test and calculation.

Although the intact loop steam generator U-tubes appear to drain correctly in the calculation, there are some discrepancies in the predicted hot leg draining, as shown in Figure 3.3.5. This figure gives measured and calculated intact loop hot leg densities near the vessel (on the left) and near the steam generator (on the right). Besides a delayed draining of the entire horizontal portion after 25 s, the vertical portions of the hot leg do not empty in the calculation until after ~200 s, while the data suggests much earlier complete draining.

The delay in the early-time hot leg draining (as well as the delay in core uncover and heatup, discussed in the next section) is due to higher calculated intact loop (and vessel) flows after ~25 s than measured. Intact loop hot leg mass flow rates are shown in Figure 3.3.6. As mentioned in the previous section, mass flow rates were not given on the experimental data tape. The mass flow rate data in this and subsequent sections were generated by multiplying center or middle densitometer traces with turbine flowmeter and/or drag screen data, and multiplying by a constant chosen to give the initial flow rate shown in the corresponding experimental data report plots. This procedure is not to be considered highly reliable. However, there is very clearly significantly more flow calculated from 25 to 70 s than measured.

The measured intact loop mass flows stagnate suddenly and completely to near-zero velocities at about 15-25 s, when the intact loop pump head is fully degraded due to cold leg liquid flashing. The calculation instead shows a flow decrease at that time due to the density decrease as the fluid flashes followed by a more gradual flow stagnation. A number of sensitivity studies were done concentrating on this discrepancy, as discussed below in Section 5.2. Our conclusion was that this discrepant behavior was more likely due to errors in the Semiscale pump curves used (in their applicability rather than in their implementation) than to code errors, and that the inadequacy and uncertainty in the pump modification descriptions precluded any significant improvement in calculated results.

The problem appears to be associated with the intact loop pump head degradation and flow stagnation only, as evident from the broken loop hot leg mass flow rates shown in Figure 3.3.7 where there is good agreement between calculation and data. This good agreement in broken loop flow stagnation results in good agreement in broken loop hot leg draining, with Figure 3.3.8 giving measured and

calculated broken loop hot leg densities. The horizontal portions of the broken loop hot leg correctly drain before ~ 75 s, although again the draining of the vertical portions of the hot leg are somewhat delayed.

Figure 3.3.9 shows the broken loop steam generator U-tube collapsed liquid levels in the calculation. Figures 3.3.10 and 3.3.11 give the broken loop pump suction leg densities and collapsed liquid levels, respectively, showing the broken loop seal clearing at 25–75 s. The broken loop seal clearing during this period is also visible in the broken loop cold leg densities, shown in Figures 3.3.12 and 3.3.13 for the pump-side and vessel-side of the break, respectively. These density plots also suggest that the calculated break flow may be high in the 25–75 s period due to more liquid in the broken loop cold leg fluid mixture than observed in the experiment. (The calculated increase in the vessel-side broken loop cold leg density late in the transient is due to ECC liquid flowing around the downcomer inlet annulus from the intact to the broken loop cold leg.)

3.4 Vessel Inventory

The problems in matching the intact loop flow stagnation early in the transient are also visible as discrepancies in predicting the vessel and downcomer responses correctly. Figure 3.4.1 shows measured and calculated downcomer mass flow rates. As with the intact loop flows in Figure 3.3.6, the predicted decrease in flow to near-stagnation is more gradual than that observed in the test; the data shows zero flow by 25 s while the calculation does not reach zero flow until after 50 s. The calculation also exhibits more flow oscillations later in the transient than measured.

The delayed intact loop and downcomer flow stagnation after ~ 25 s shows up as a delayed vessel level depression at the same time, as seen from the vessel and downcomer collapsed liquid levels in Figure 3.4.2. (The experimental levels are based on Δp measurements and are not reliable during steady state and the very early transient, when flow effects are dominant.) The predicted vessel level is higher than occurred from ~ 25 to ~ 75 s while the downcomer level is lower than measured, with the small recovery in downcomer level after ~ 25 s not predicted. The calculated vessel level is then correctly depressed to the observed minimum level after the 75 s period. The subsequent vessel level recovery predicted at ~ 100 s is only half that observed, probably due to the partial intact loop seal clearing calculated contrasted to the total intact loop seal clearing in the test (shown in Figures 3.3.2 and 3.3.3).

After intact loop seal clearing, the calculation has more water in the downcomer and less in the vessel than measured. This discrepancy is then exacerbated by the differences in observed and predicted accumulator injection flows, given in Figure 3.2.7. Earlier and higher accumulator injection causes both levels to begin rising earlier than in the test, and is responsible for the higher calculated downcomer liquid levels after ~ 150 s; subsequent underprediction of accumulator injection around 200 s causes the levels to then rise more slowly so that, by the end of the transient analyzed, the agreement between measured and predicted levels is generally good.

Despite the quantitative discrepancies just noted, all the correct qualitative behavior is being calculated. Figure 3.4.3 shows the densities at the downcomer

midplane, for example. The agreement for the first 150 s closely mirrors the measured vs calculated downcomer collapsed liquid level behavior. The voiding during the 150-250 s period is predicted, although the calculation has somewhat more water in the downcomer than measured, again paralleling the collapsed level behavior. However, although both measured and calculated responses change at ~250 s, the calculation does not show a steadily increasing density afterwards but instead a sudden jump in density at 350 s occurs after a long period of relatively low and steady two-phase mixture density. (A number of our calculated downcomer and vessel densities show such quasi-steady mixture densities bracketed by sudden shifts to and from nearly pure liquid or vapor; the reason for this behavior has not yet been determined.)

Figure 3.4.4 shows the vessel response in more detail; it gives the lower plenum, core heated length and upper plenum collapsed liquid levels. (As with the vessel and downcomer collapsed liquid levels, the data are derived from Δp measurements and are not accurate at the start of the transient. Also, the instrumentation zero does not always correspond exactly to the physical boundaries between lower plenum, core and upper plenum.) These calculated component liquid levels show delayed level drops after ~25 s, in the core heated length and upper plenum. However, the data shows the lower plenum staying essentially full throughout the transient; the calculation shows substantial void in the lower plenum starting after about 20 s, with significant liquid in the core heated length above the lower plenum. Late in the transient, at ~250 s, the calculation shows liquid appearing in the upper plenum, above a substantially voided core heated length. These results suggest that, in the calculation, more phase separation is needed in the vessel to help ensure the liquid inventory being distributed correctly, and suggests that the interfacial shear correlations used may be overpredicting liquid entrainment substantially.

Measured and calculated lower plenum densities are given in Figure 3.4.5, for an elevation 6 cm below the bottom of the core heated length. The level depression at ~75 s reaches this point in both the calculation and the test. Afterwards, the calculation does not show either a slow boiloff from 125 to 175 s or a gradual vessel refill after 175 s, but maintains a nearly-constant two-phase mixture density. Although there is no density data for lower vessel elevations, the calculated densities throughout the four lower plenum levels all show similar two-phase mixtures during most of the transient, while the lower plenum Δp measurement shows the lower plenum mostly full of liquid (somewhat inconsistent with the lower plenum density trace shown here in Figure 3.4.5, although that measurement is near the very top of the lower plenum).

Figures 3.4.6 through 3.4.8 show representative measured and calculated densities at various elevations within the core, 1.13 m above the bottom of the heated length, at the core midplane and 0.24 m from the top of the heated length. These density comparisons show the same phenomena already described in the discussion of the collapsed liquid level comparisons earlier in this section. The delayed vessel voiding after ~25 s is seen in all the heated length densities (and in the upper plenum, also). The partial recovery after intact loop seal clearing is also visible in the densities in the lower half of the core heated length, with the calculated recovery being too early (Figure 3.4.6) and too little (Figure 3.4.7). No slow boiloff and later gradual refill are seen in the density predictions after this level recovery; instead, the calculation shows various levels in the core progressively filling to and stabilizing at a two-phase mixture density corresponding to $\alpha \sim 0.7$ (actually ranging from 0.68 to 0.73 in the various axial levels).

The two-phase fluid mixture in a number of vessel levels was predicted to remain very near a void fraction of 0.7, simultaneously, for prolonged periods of time. This suggests that this value of void fraction is a "magic number" in the vessel flow regime map and/or one of the vessel constitutive packages, or that a discontinuity in some correlation exists at this value, causing the "hang-up". The only place we found a void fraction of 0.7 in the TRAC manual [1] was inside the nucleate boiling heat transfer correlation suppression factor (although, given the size of the manual, we may not have found all occurrences); we did not check the coding itself. The rods adjacent to these vessel levels were in the nucleate boiling regime during the relevant times, but how this could have the effect observed is not known. Alternatively, because the TRAC flow regime assumes annular flow starting from a void fraction of 0.75 with interpolation to slug or bubbly flow at somewhat lower void fractions, the code may be having difficulties switching to pure annular flow and thus "hanging up" at void fractions just below 0.75.

Uncertainties in the upper head flow paths (in particular for the support columns, supposedly plugged but with a flow area of undocumented size accidentally provided by removed instrumentation [10,22]) made modelling the upper head geometry a matter of trial and error. Figure 3.4.9 shows the measured and calculated upper head collapsed liquid levels. The upper head in the calculation initially drains too quickly, but at later times has more water remaining than was measured. A few studies with different support column, guide tube and bypass flow areas and resistances were done in attempts to determine why discrepant upper head draining was being predicted in the calculation, but the discrepancies were not judged important enough to justify the resources required for resolution. The discrepancies are believed to be due primarily to inadequate modelling of the upper head drainage paths, due in turn to inadequate facility geometry and modifications descriptions [10,21].

3.5 Core Response

The calculated core thermal response reflects the discrepant vessel hydraulic response discussed in the previous section, and feeds back to the overall primary system hydraulic response described in Section 3.2. The delayed flow stagnation and associated retarded vessel level depression and core uncover results in a delayed core rod heatup. This later predicted dryout and heatup, combined with intact loop seal clearing and vessel level recovery at the correct time, produces lower core temperatures. The underprediction of core heatup results in less steam generation and superheat helping to maintain primary system pressure in mid-transient. The lower pressures predicted cause earlier and more accumulator injection than occurred, resulting in more water in the vessel and an earlier total quench by the end of the transient period analyzed.

Figure 3.5.1 shows the input core power and the total rod heat transfer to the core fluid. The core power exceeds the rod heat transfer rate only during the period from ~65 to ~100 s. The maximum core rod temperature in Figure 3.5.2 confirms that it is during this period that core heatup occurs. The delay in core dryout and heatup is clearly seen, as is the overall underprediction of the core heatup and the premature core quench in the calculation.

Measured and calculated rod temperatures at various core elevations are shown in Figures 3.5.3 through 3.5.9. The vessel level depression reaching the bottom of the heated length in both calculation and experiment can be seen in Figure 3.5.3. At all the core levels, the calculated heatup starts later than observed. With the heatup rate determined by the power input and with the slightly early level recovery due to intact loop seal clearing, the core heatup predicted in the 50-100 s period is everywhere less than measured.

Figure 3.5.6 shows that the rod rewet due to the intact loop seal clearing and associated vessel level recovery reached above the core midplane (i.e., 1.83 m core elevation) in the test, but barely touched this elevation for one of the two rods in the calculation. Figure 3.5.5 shows that, at a lower core elevation of 1.36 m, both calculated and measured rod temperatures showed a total rewet as the intact loop seal cleared; Figure 3.5.7 shows that, at a higher core elevation of 2.30 m, neither the calculated nor the measured rod temperatures showed a rewet as the intact loop seal cleared.

The calculated rod temperatures are progressively more discrepant compared to data both in transient time and in core elevation. The temperature deviations seen in the lowest core levels, after the initial heatup and rewet, are primarily due to differences in saturation temperature due to mispredicting the primary system pressure in the 100-200 s time period (e.g., Figure 3.5.3). At slightly higher core elevations, there is also a discrepancy at later times due to underestimating the amount of liquid boiloff after loop seal clearing (clearly visible in Figures 3.5.4 and 3.5.5); the duration of this late-time inventory boiloff before accumulator-driven refill is also underpredicted (e.g., Figures 3.5.6 and 3.5.7). The lower rod temperatures throughout the core in the calculation result in less steam generation and allow more of a two-phase mixture to exist in the core so that, at the higher core elevations, the calculated rod temperatures are lower (as seen in Figures 3.5.8 and 3.5.9) due to less depleted heat removal capacity of the fluid flowing past the rods.

Table 3.1.1 Steady State Initial Conditions

<u>Variable</u>	<u>Data</u>	<u>TRAC</u>
Core Power (MW)	1.451	1.451
System Pressure (MPa)	15.53	15.53
IL Cold Leg Temperature (K)	560	565
IL ΔT (K)	36	30
IL Cold Leg Flow (kg/s)	6.18 (8.02 ℓ/s)	6.18
IL Pump Speed (rad/s)	177	178
BL Cold Leg Temperature (K)	566	571
BL ΔT (K)	31	25
BL Cold Leg Flow (kg/s)	2.13 (2.74 ℓ/s)	2.13
BL Pump Speed (rad/s)	872	1281
SG Feedwater Temperature (K)	494	494
IL SG Pressure (MPa)	6.48	6.30
IL SG Liquid Level (m)	7.327	$\sim 7.3^*$
BL SG Pressure (MPa)	7.53	7.40
BL SG Liquid Level (m)	7.138	$\sim 7.1^*$

* Slow oscillations of ~ 0.1 m present in calculation

Table 3.1.2 Experimental Boundary Conditions

Break Opens	0- s	
Core Power	0- 1.2 s	100%
	1.2- 3.2 s	71%
	3.2- 5.2 s	51%
	5.2- 10.1 s	33%
	10.1- 15.1 s	16%
	15.1- 20.1 s	11%
	20.1- 100.1 s	7%
	100.1-	2%
Intact Loop Pump Speed	0 s	100%
	0-30 s ramp to	37%
	30-	37%
Broken Loop Pump Speed	0 s	100%
	0-30 s ramp to	52%
	30-240 s	52%
	240- s ramp to	0%
IL SG Feedwater Flow	ramp to 0 in 30 s	
BL SG Feedwater Flow	full flow for 1 s ramp to 0 in 1.5 s	
IL SG Steam Valve	close at 1 MPa	
BL SG Steam Valve	close at 1 MPa	

TRAC-PF1/MOD1 SEMISCALE S-1B-3

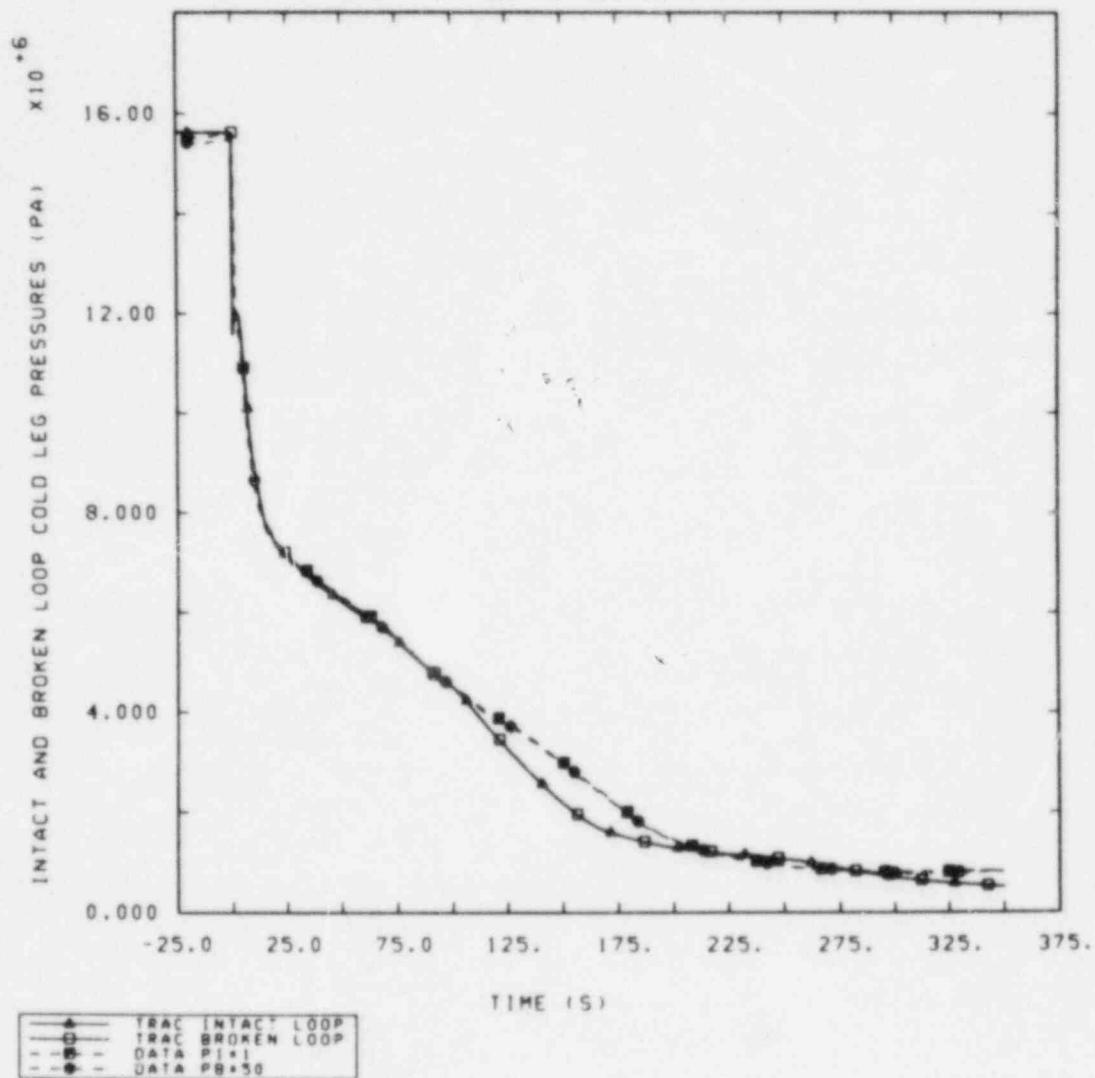


Figure 3.2.1 Intact and Broken Loop Cold Leg Pressures

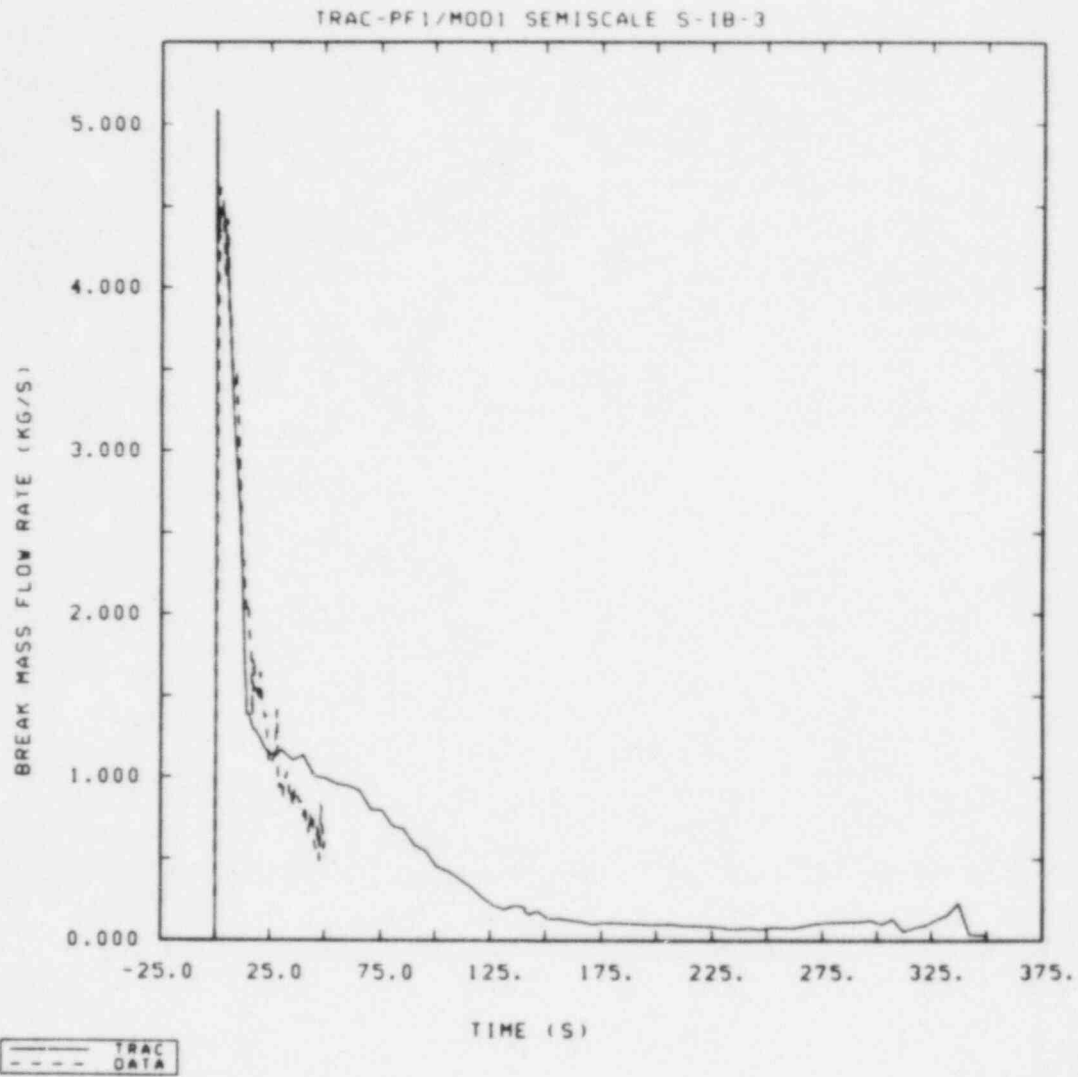


Figure 3.2.2 Break Flow Rate

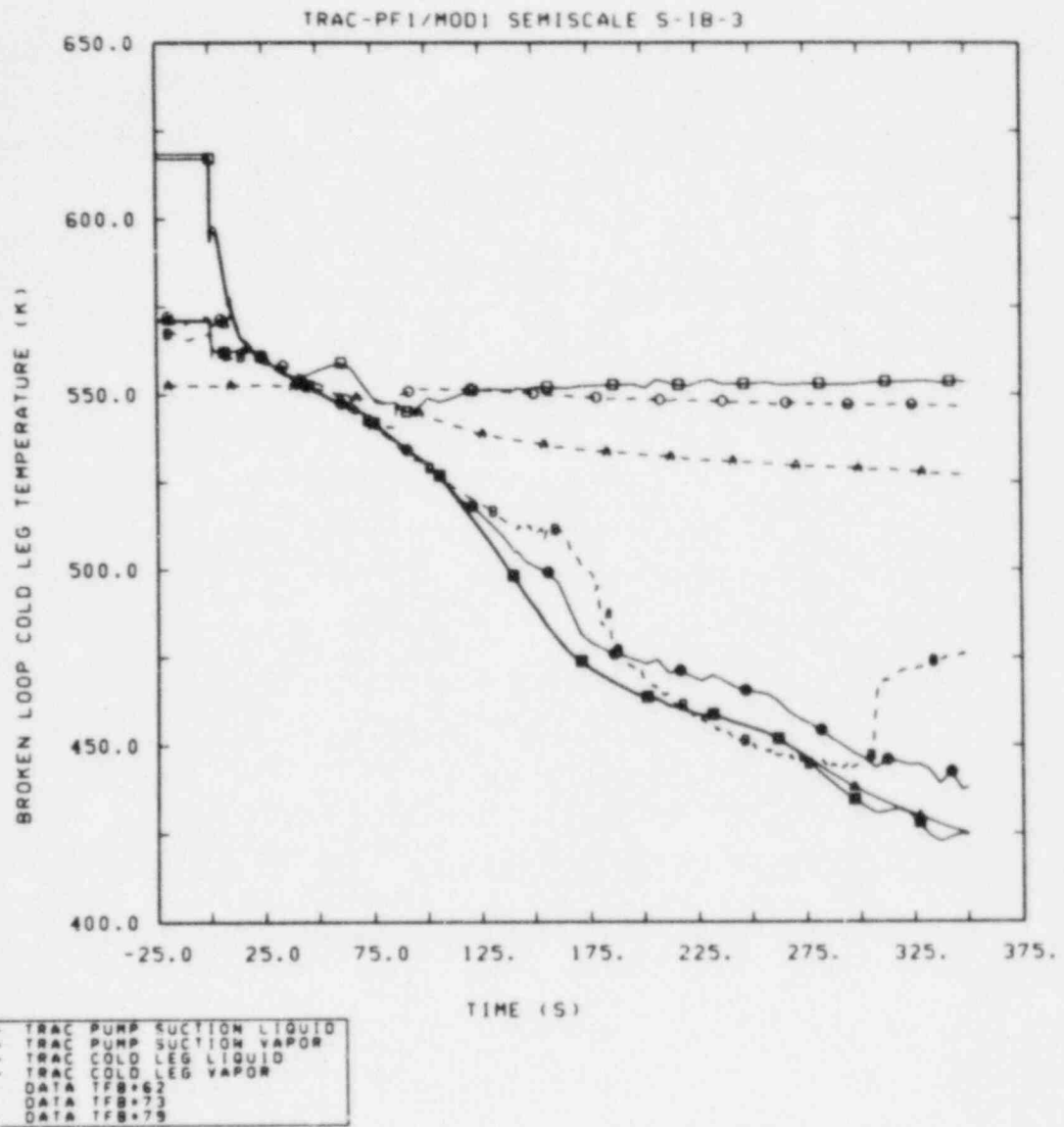
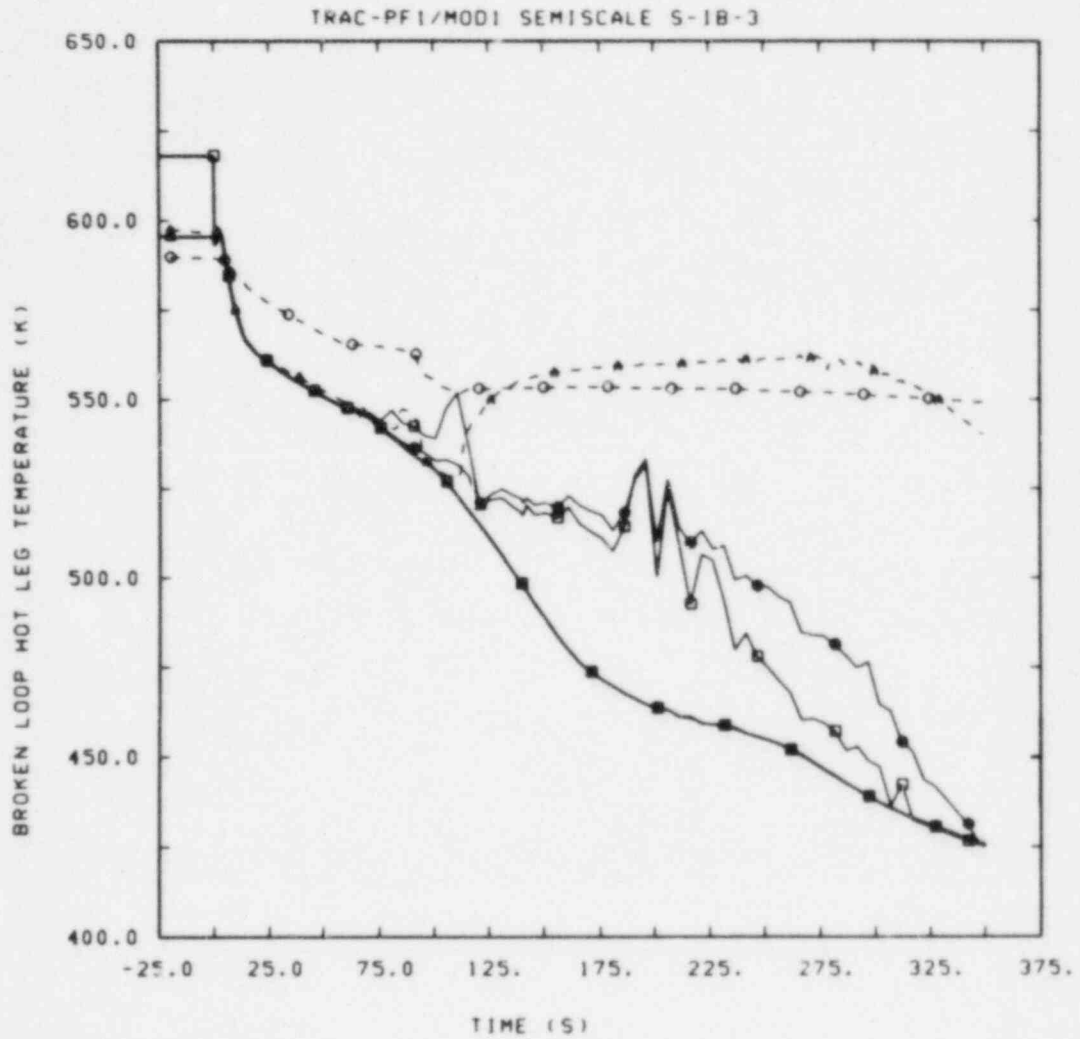


Figure 3.2.3 Broken Loop Cold Leg Liquid and Vapor Temperatures



—▲—	TRAC	VESSEL	OUTLET	LIQUID
—○—	TRAC	VESSEL	OUTLET	VAPOR
—■—	TRAC	MID	HOT	LEG
—◇—	TRAC	MID	HOT	LEG
—	DATA	TFB#30		
—	DATA	TFB#37		

Figure 3.2.4 Broken Loop Hot Leg Liquid and Vapor Temperatures

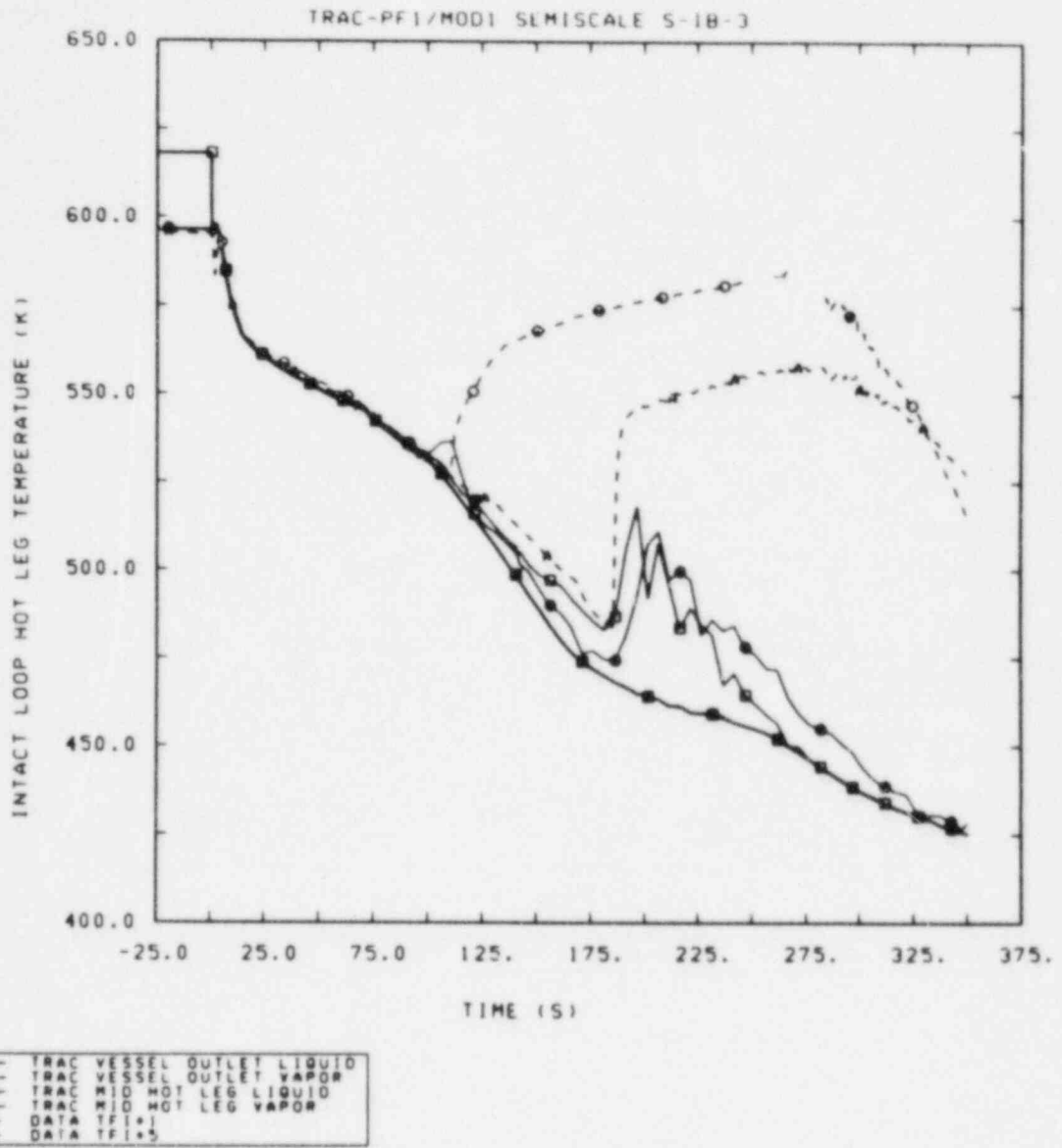


Figure 3.2.5 Intact Loop Hot Leg Liquid and Vapor Temperatures

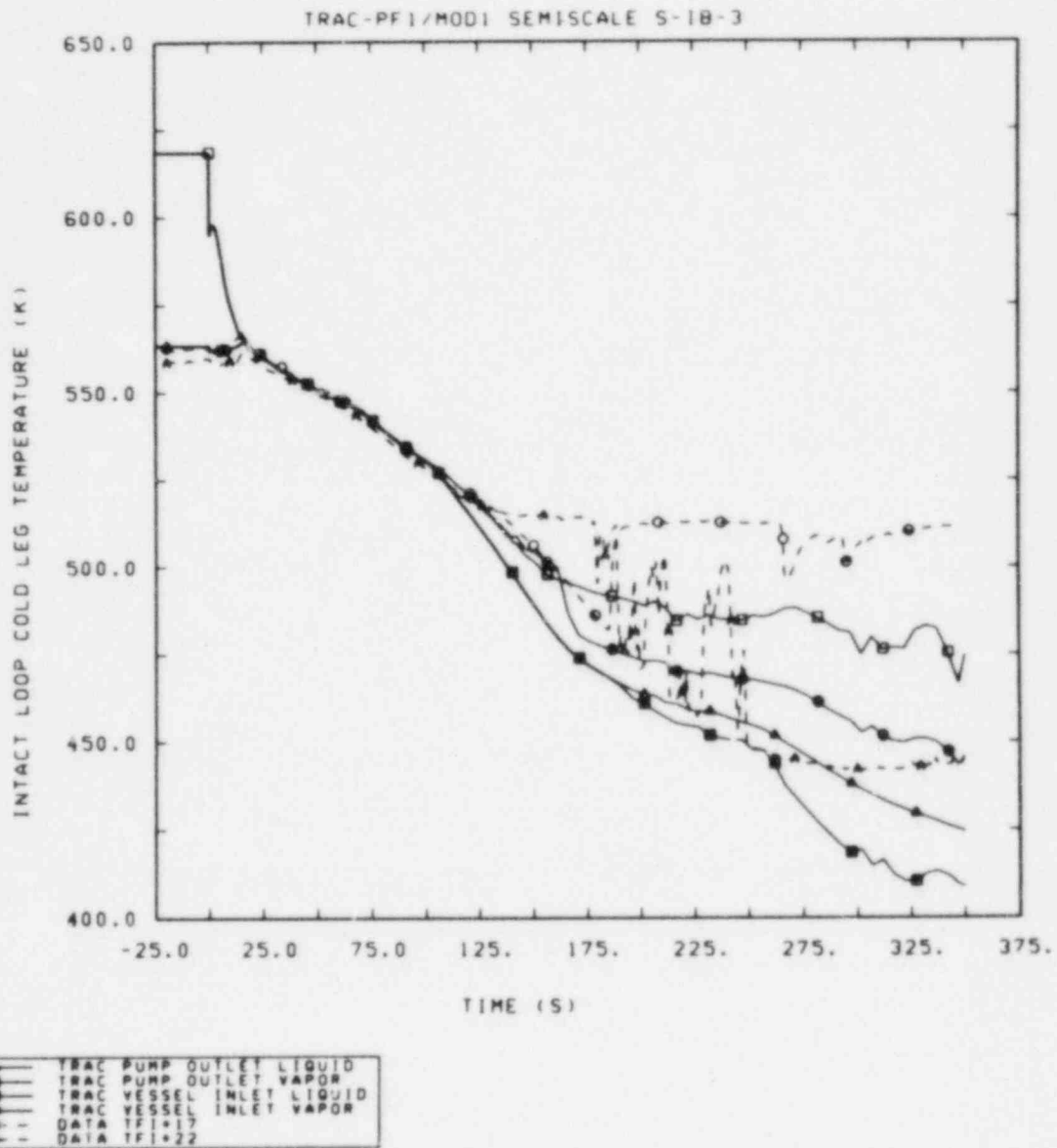


Figure 3.2.6 Intact Loop Cold Leg Liquid and Vapor Temperatures

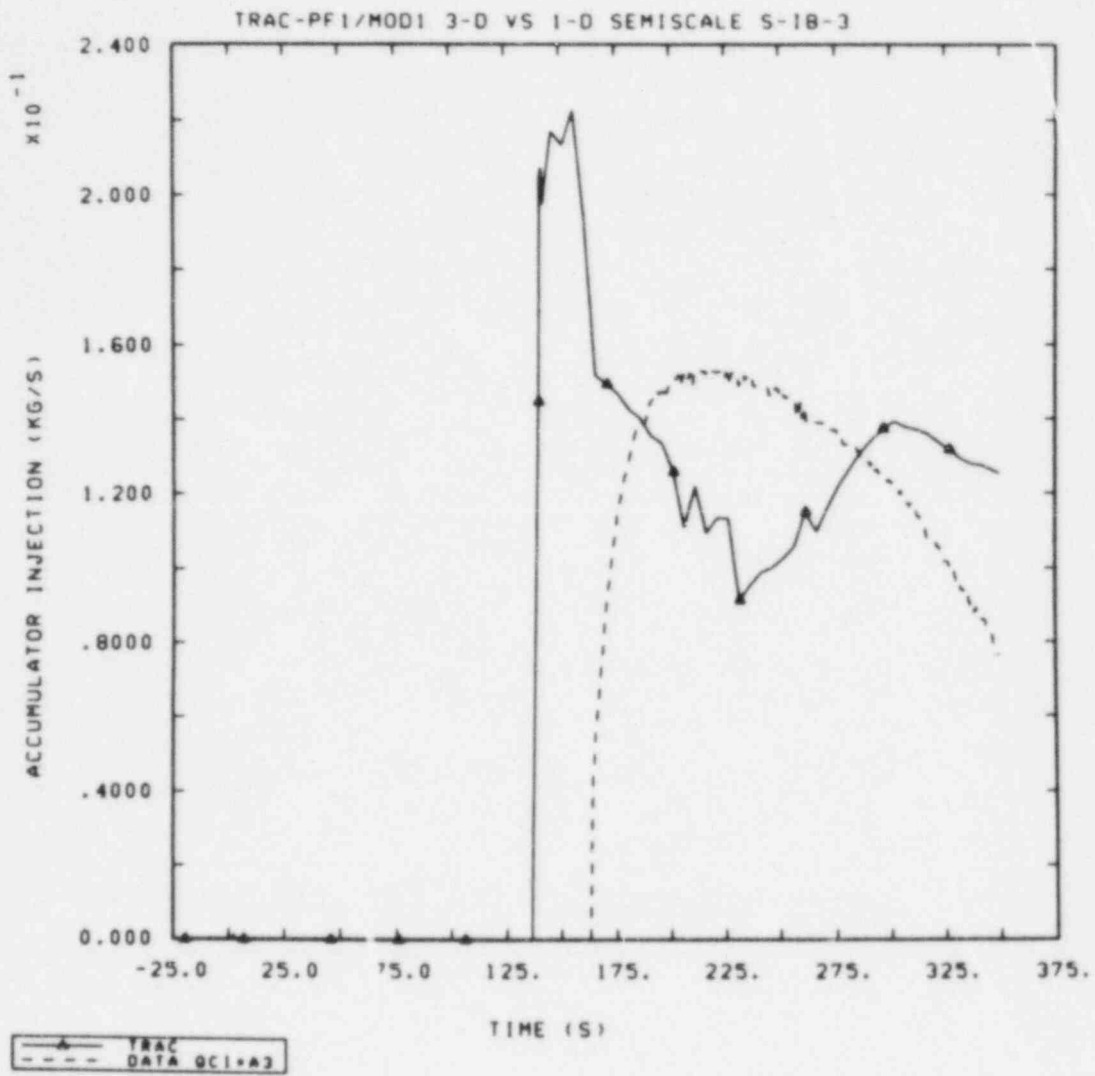


Figure 3.2.7 Accumulator Injection Flow Rate

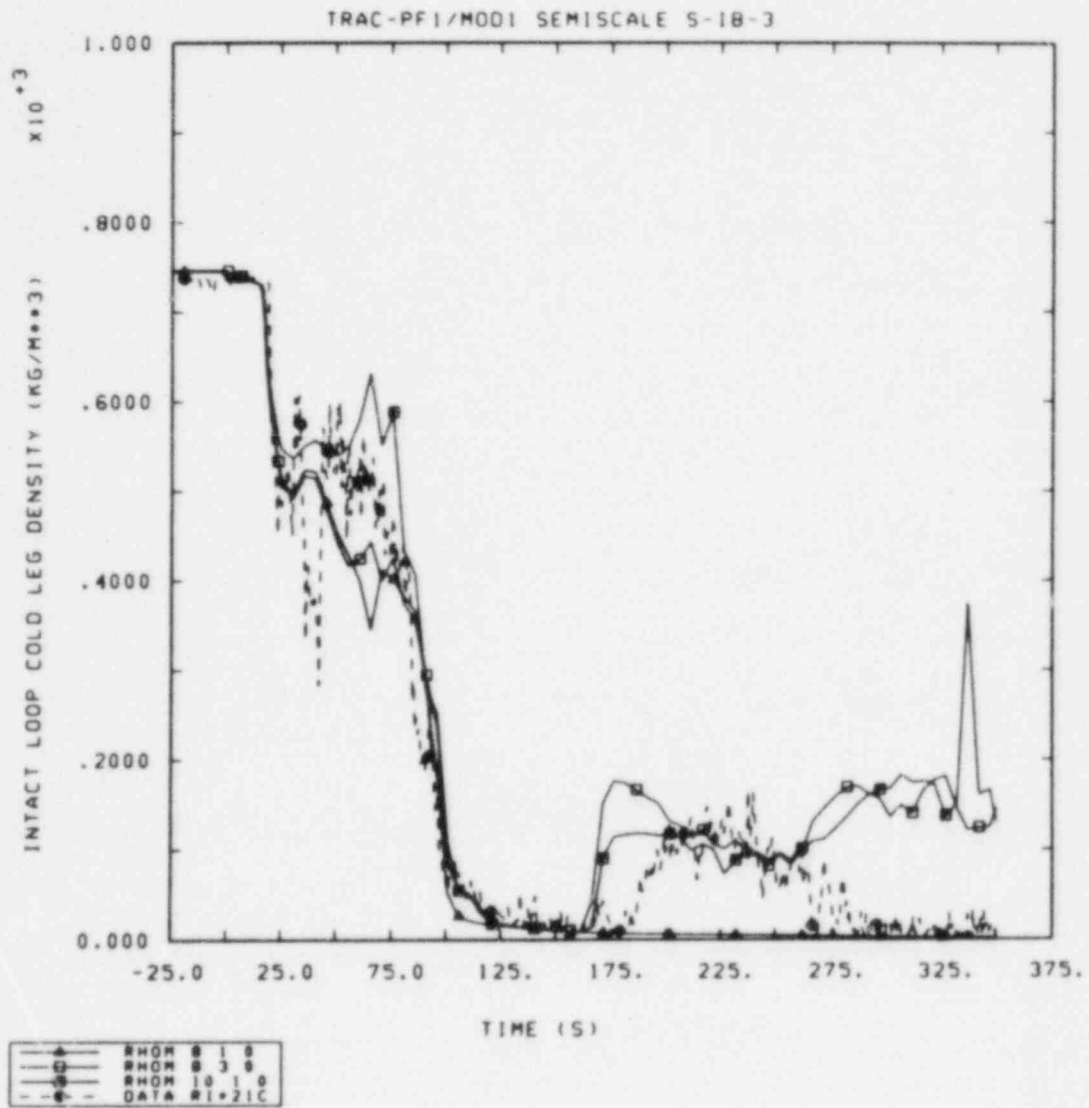


Figure 3.3.1 Intact Loop Cold Leg Densities at and Downstream of Accumulator Injection

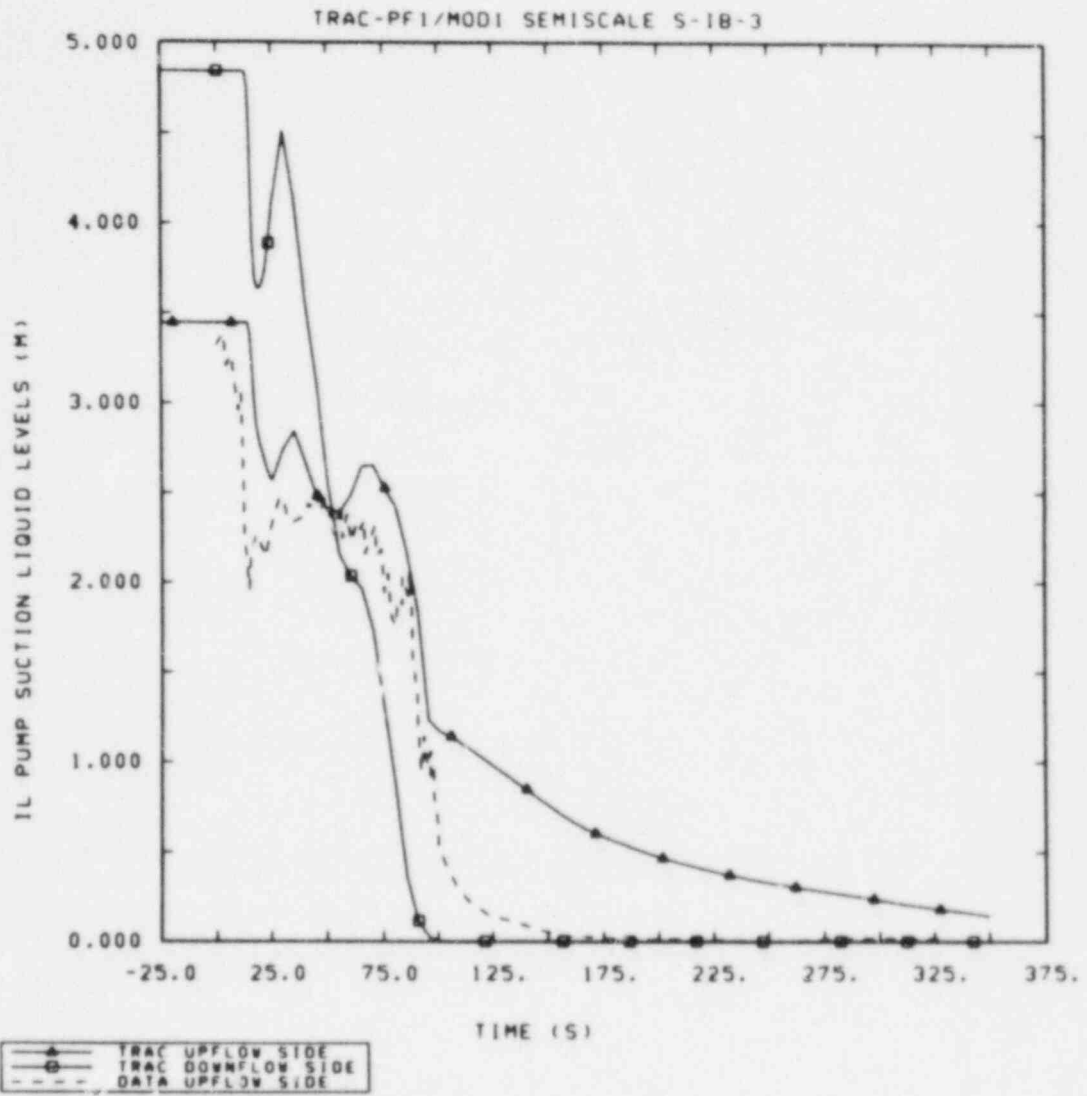


Figure 3.3.2 Intact Loop Pump Suction Leg Liquid Levels

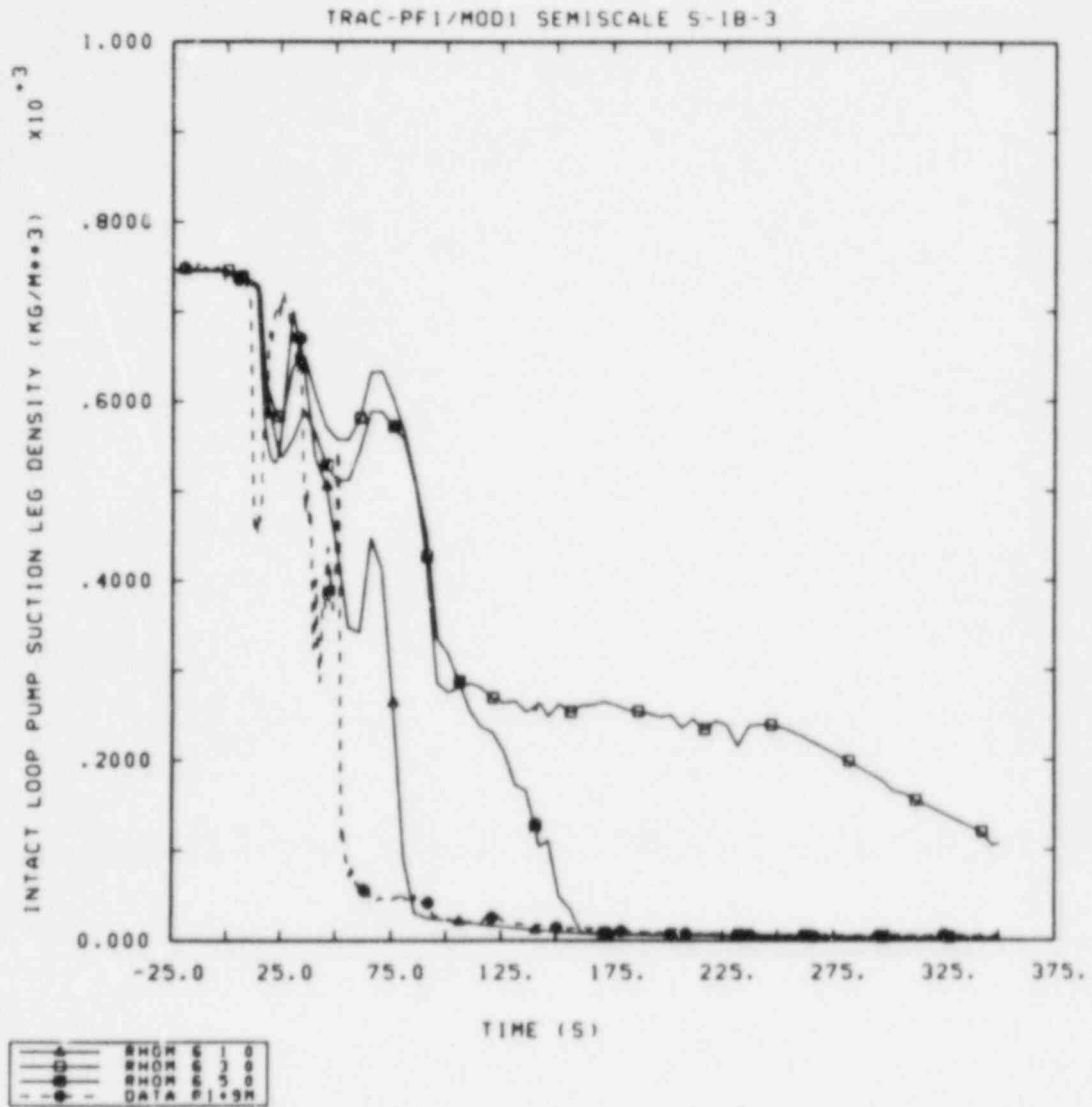


Figure 3.3.3 Intact Loop Pump Suction Leg Densities

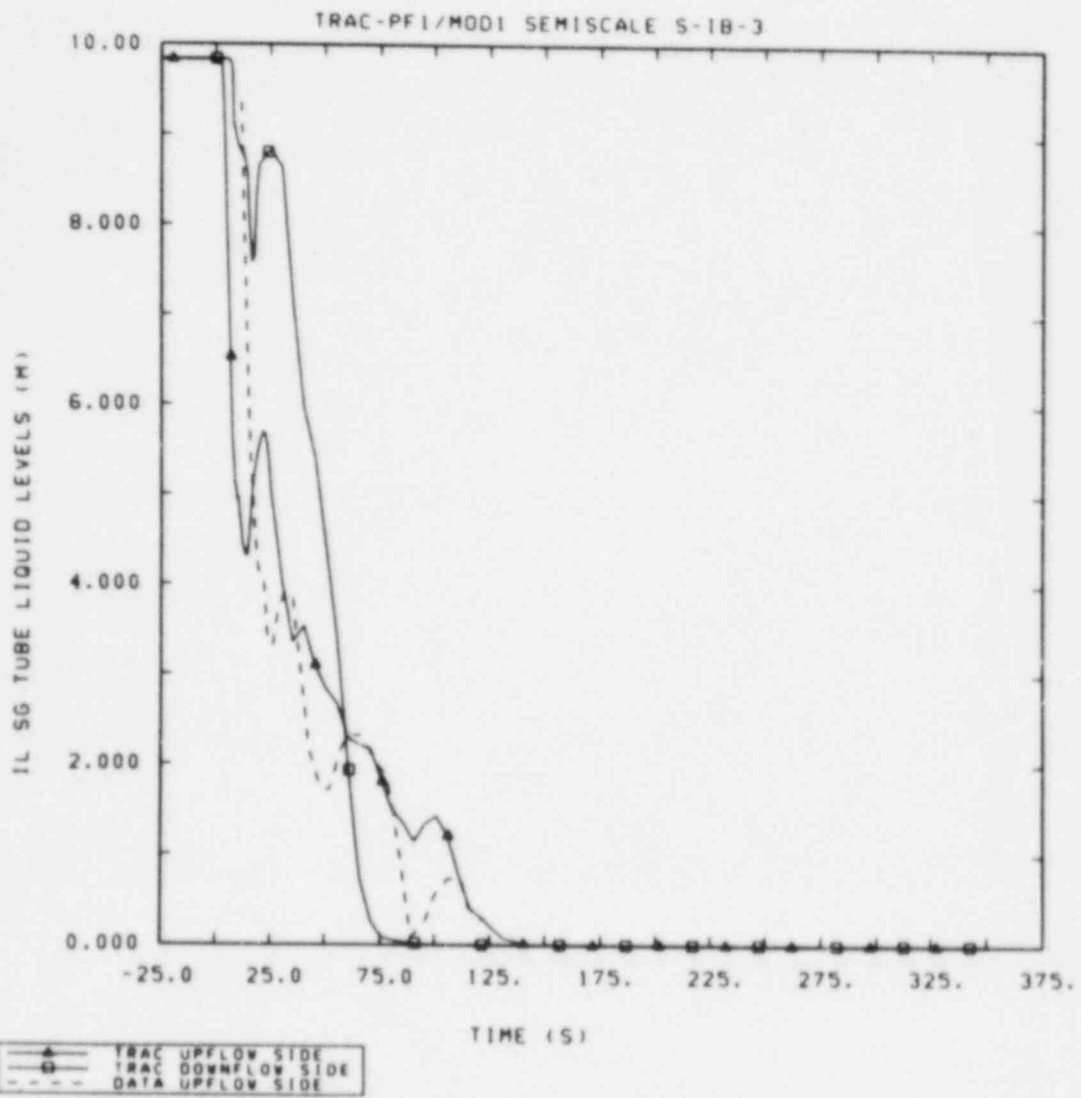
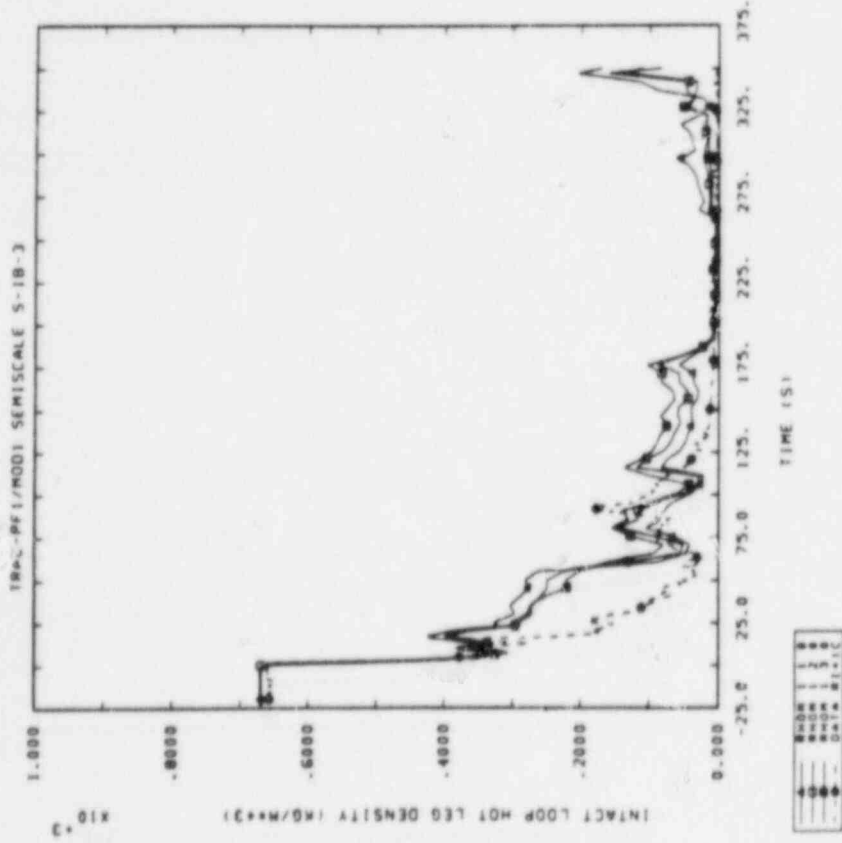


Figure 3.3.4 Intact Loop Steam Generator Tube Liquid Levels

(a)



(b)

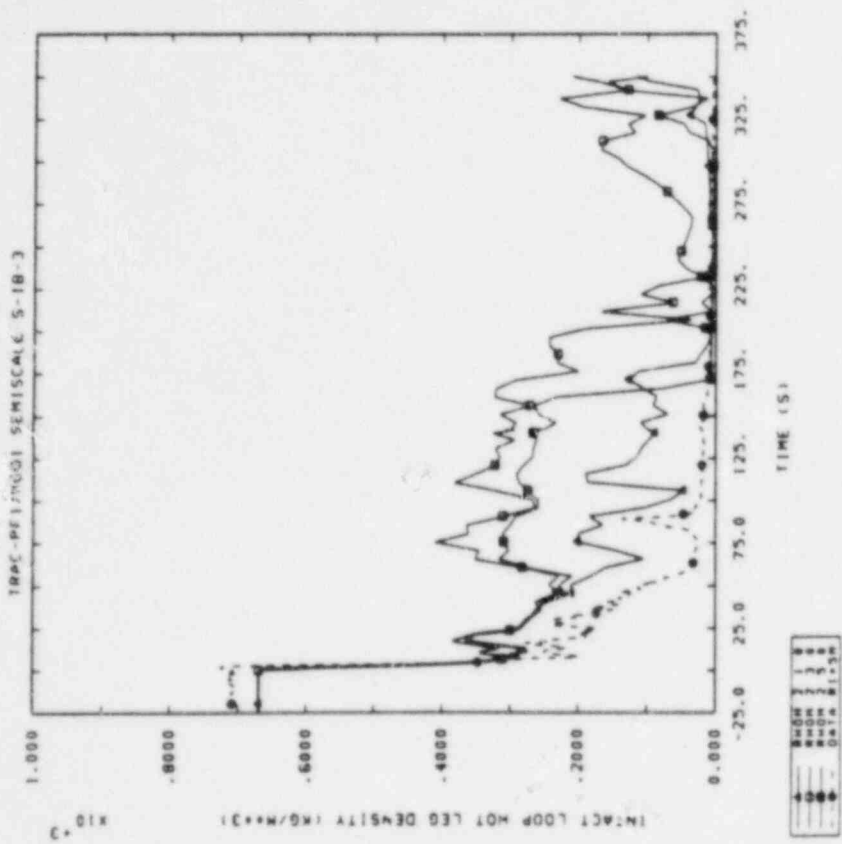


Figure 3.3.5 Intact Loop Hot Leg Densities

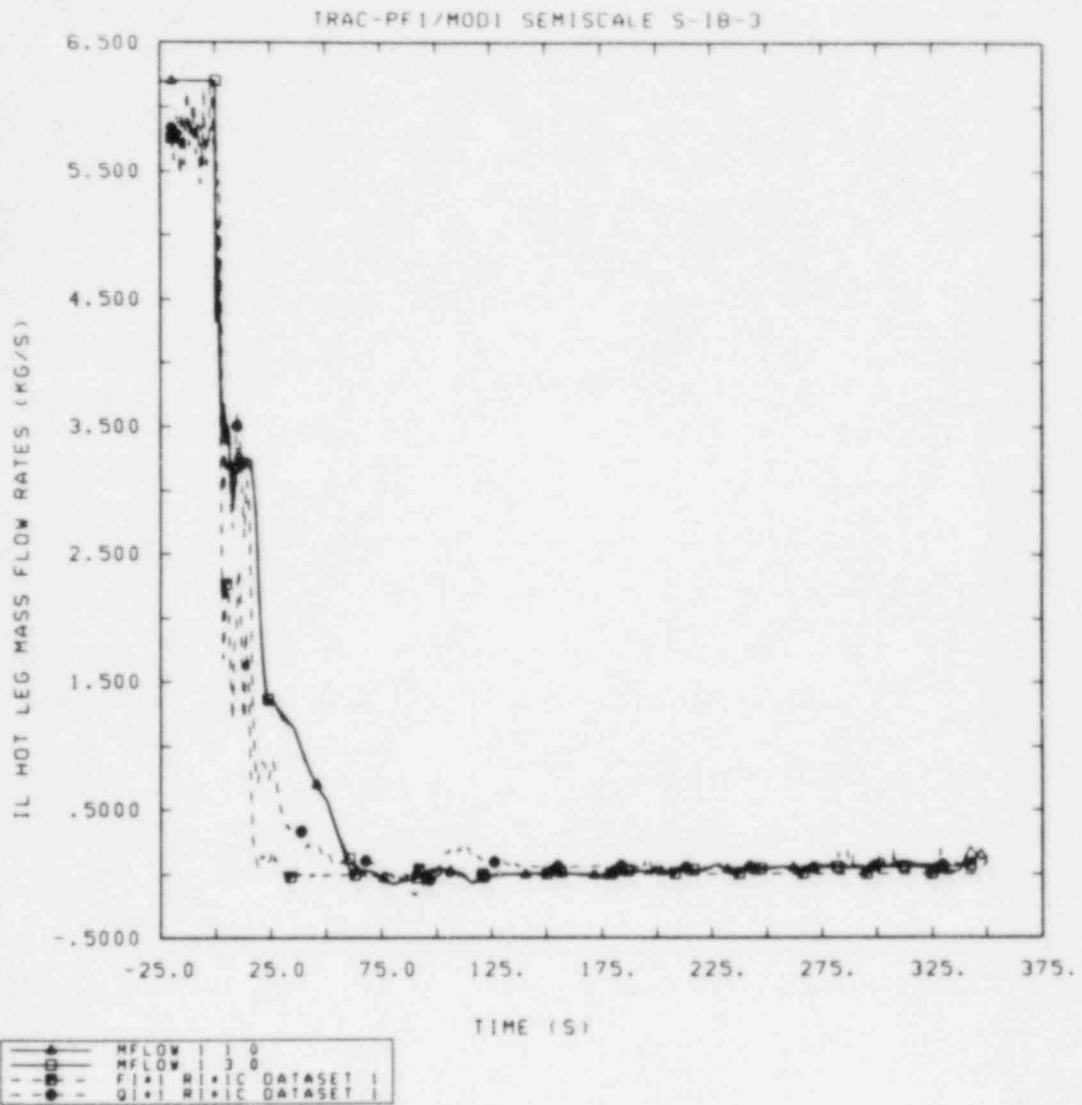
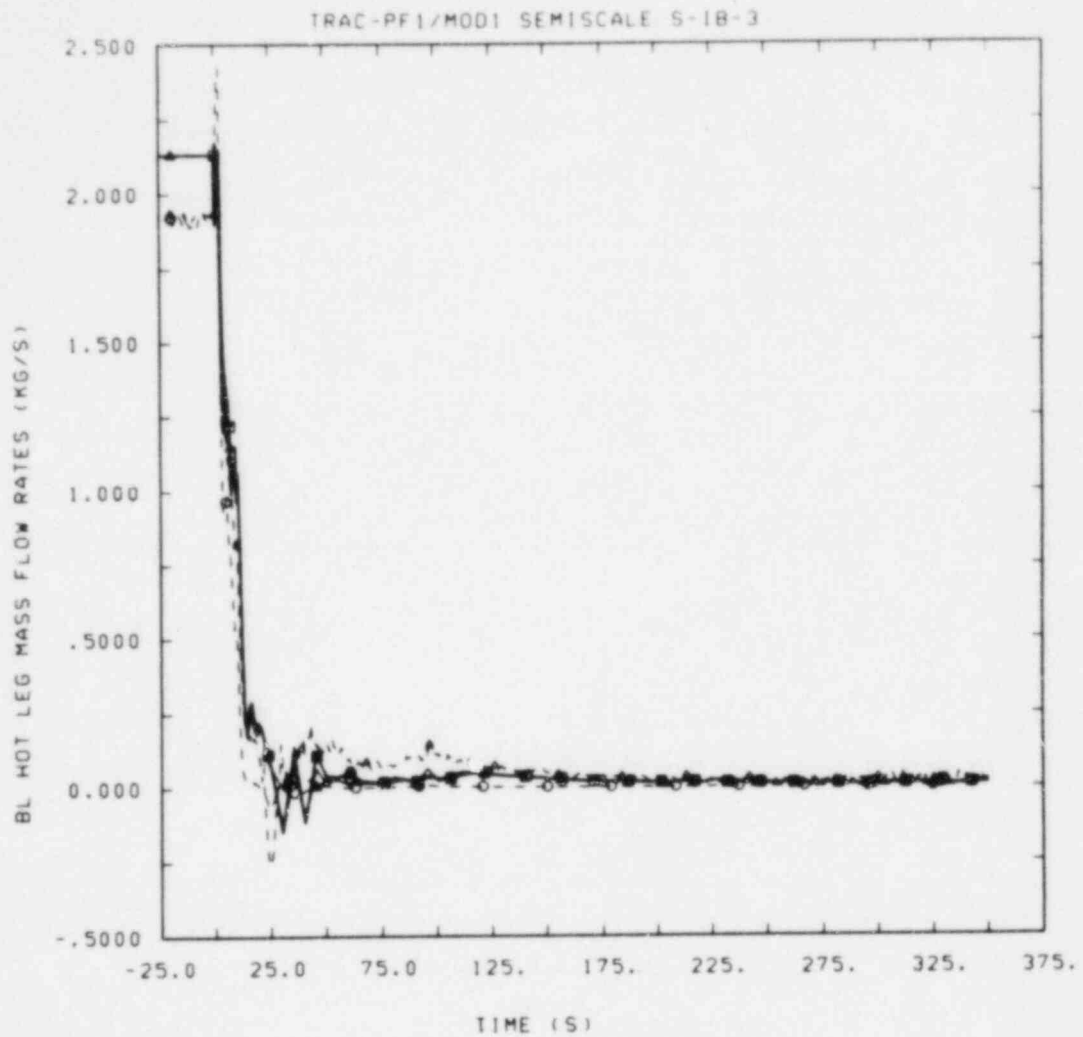


Figure 3.3.6 Intact Loop Hot Leg Mass Flow Rates



—▲—	MFLOW 12 1 0
—●—	MFLOW 12 3 0
—○—	MFLOW 12 5 0
—●—	MFLOW 12 7 0
—○—	FB*57RB*57 DATASET 1
—▲—	GB*57RB*57 DATASET 1

Figure 3.3.7 Broken Loop Hot Leg Mass Flow Rates

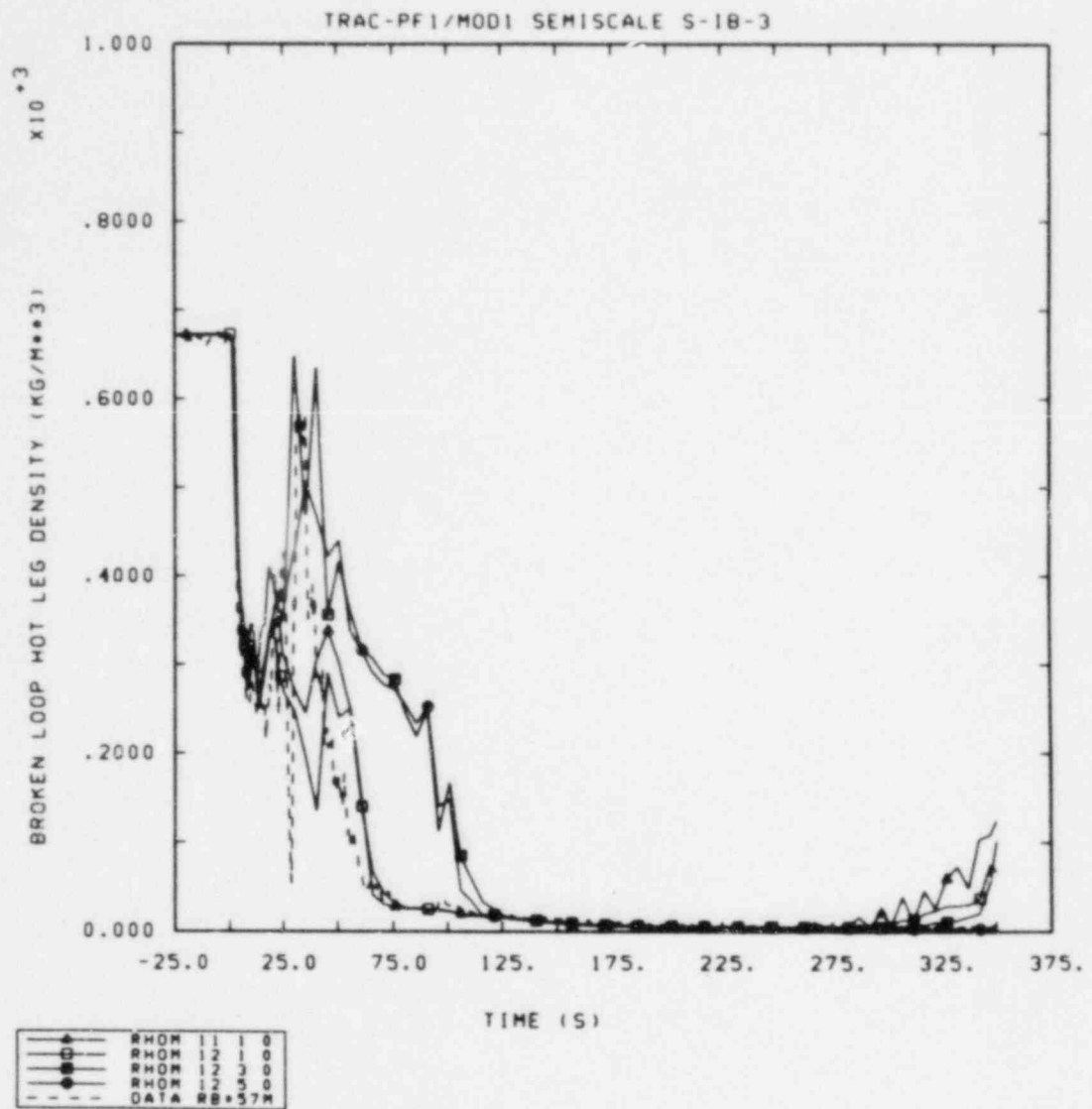


Figure 3.3.8 Broken Loop Hot Leg Densities

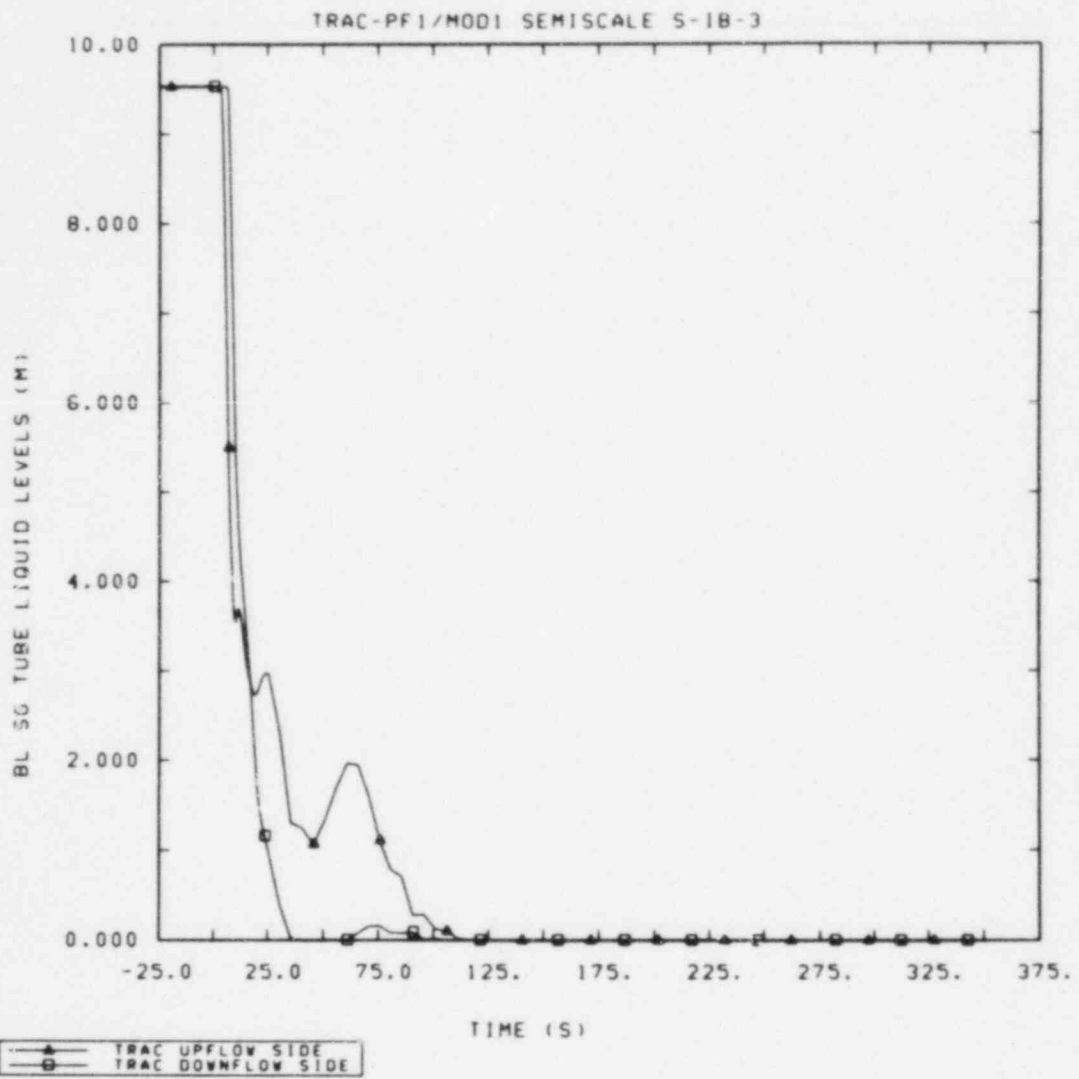


Figure 3.3.9 Broken Loop Steam Generator Tube Liquid Levels

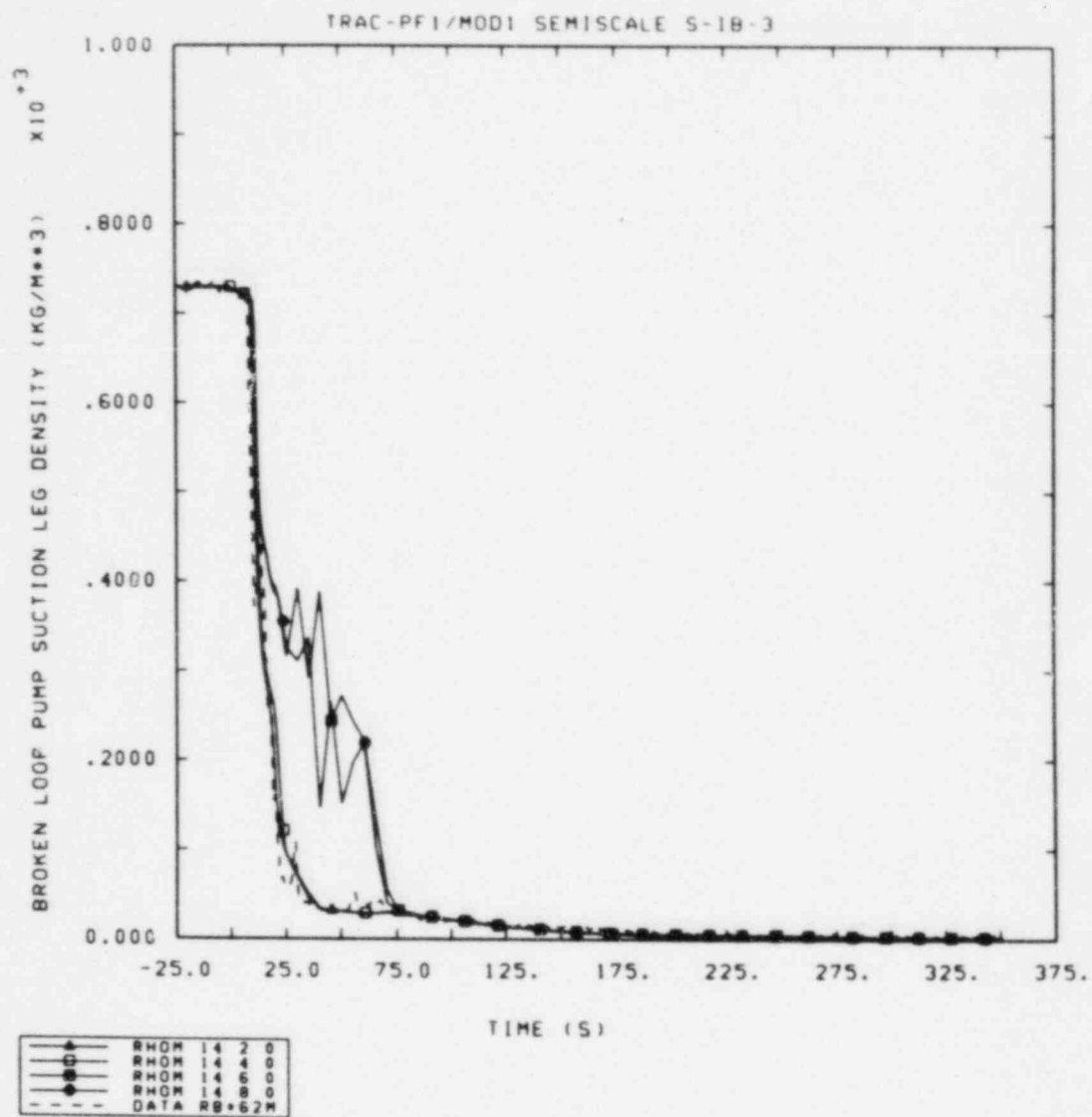


Figure 3.3.10 Broken Loop Pump Suction Leg Densities

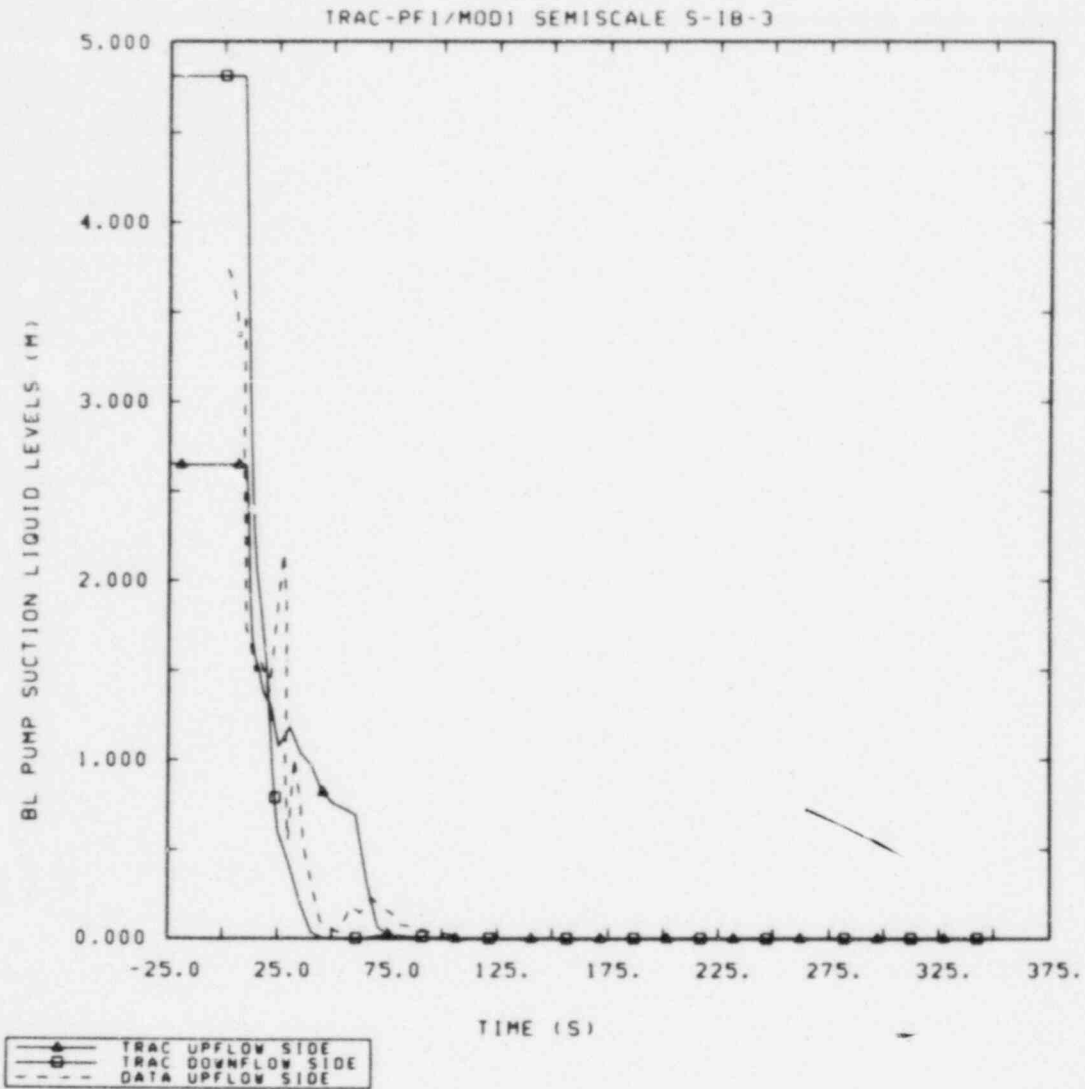


Figure 3.3.11 Broken Loop Pump Suction Leg Liquid Levels

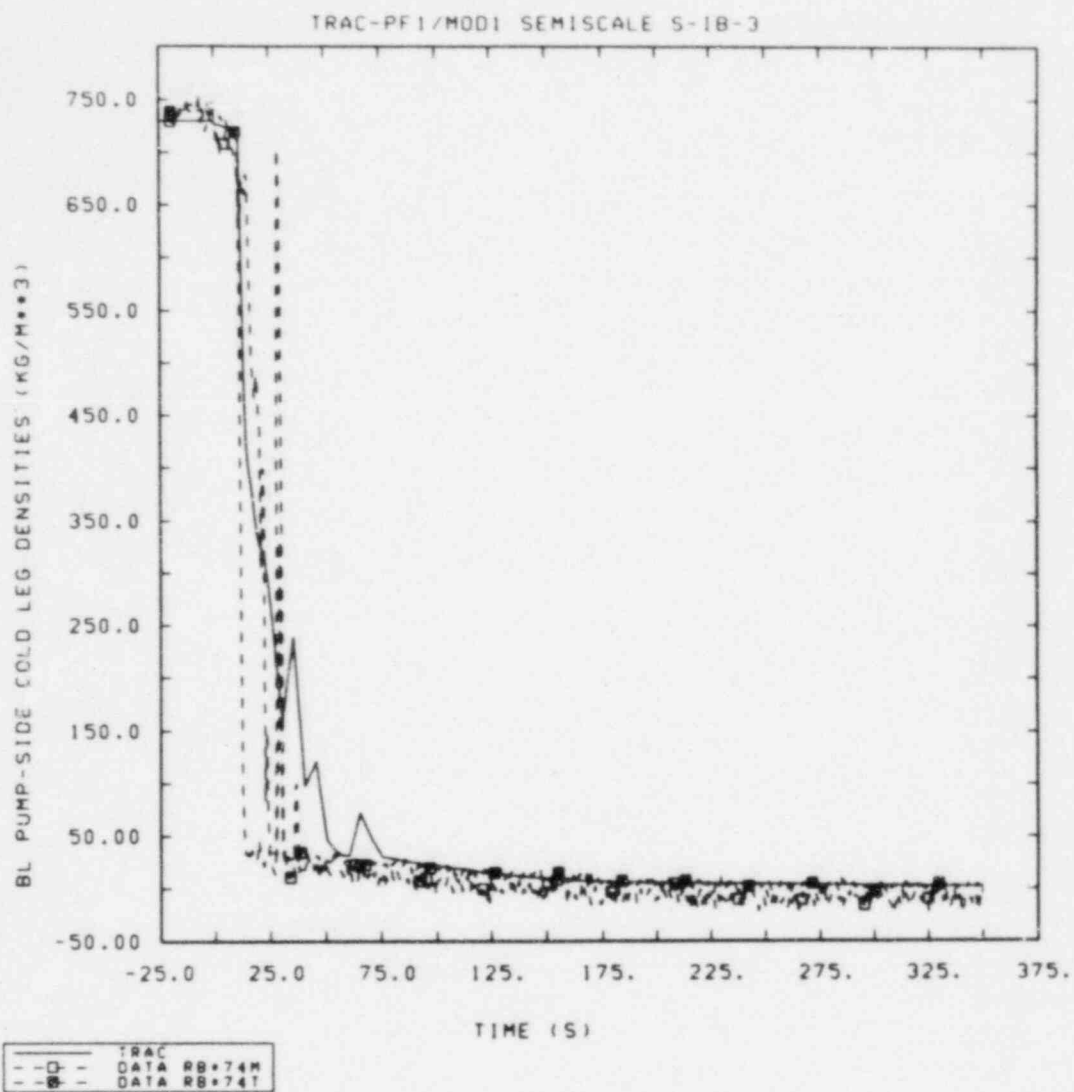


Figure 3.3.12 Broken Loop Pump-Side Cold Leg Densities

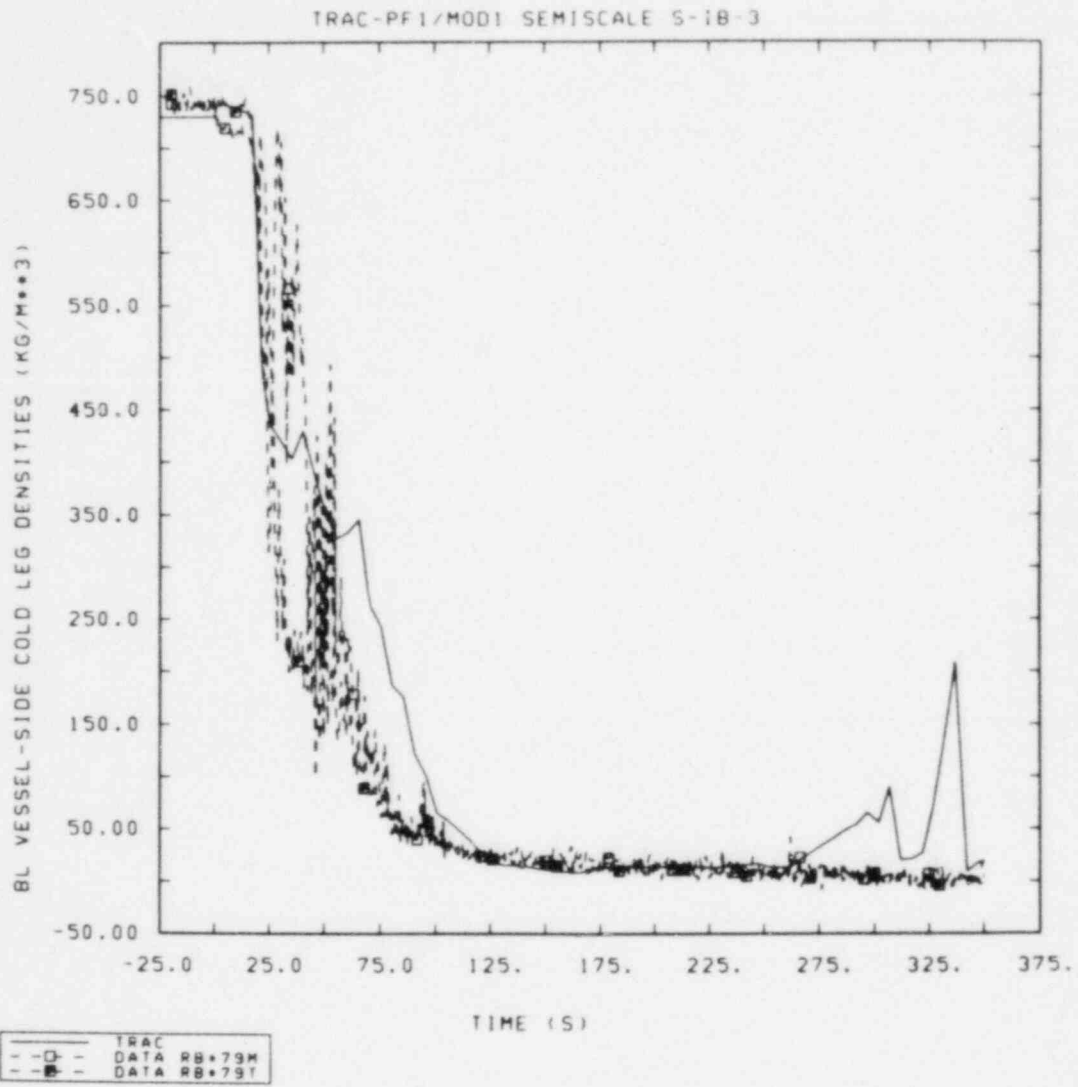


Figure 3.3.13 Broken Loop Vessel-Side Cold Leg Densities

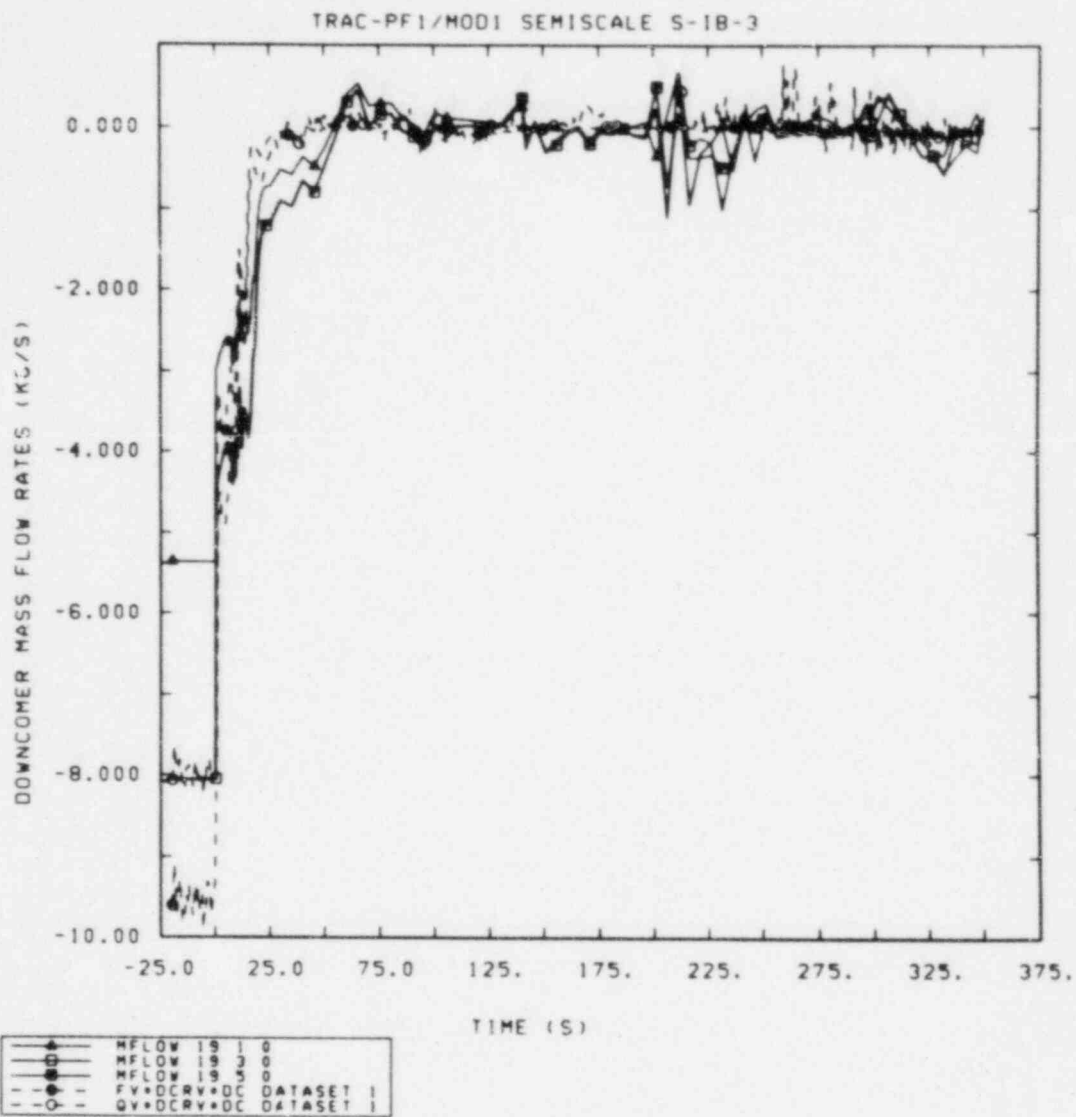


Figure 3.4.1 Downcomer Mass Flow Rates

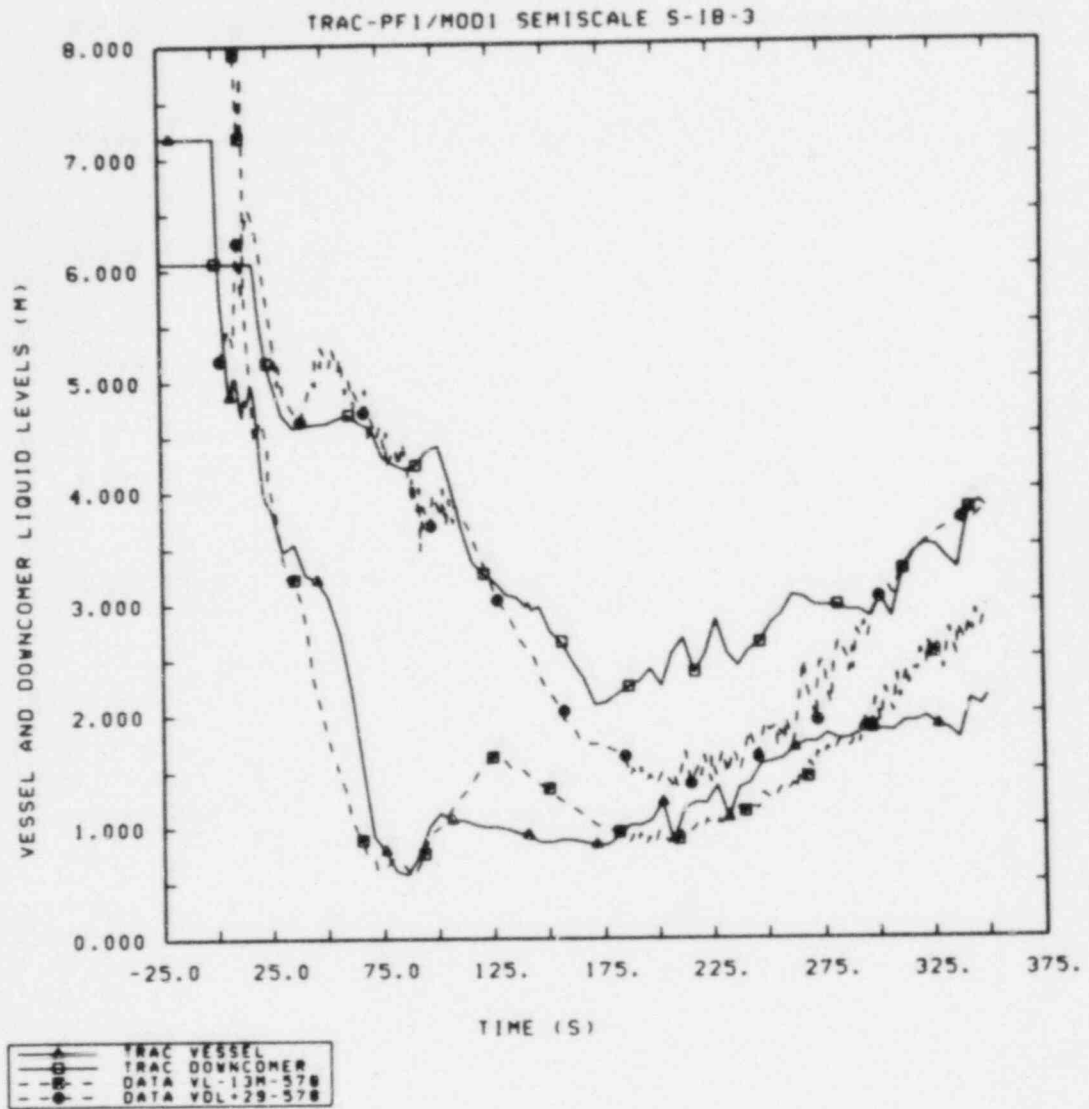


Figure 3.4.2 Vessel and Downcomer Liquid Levels

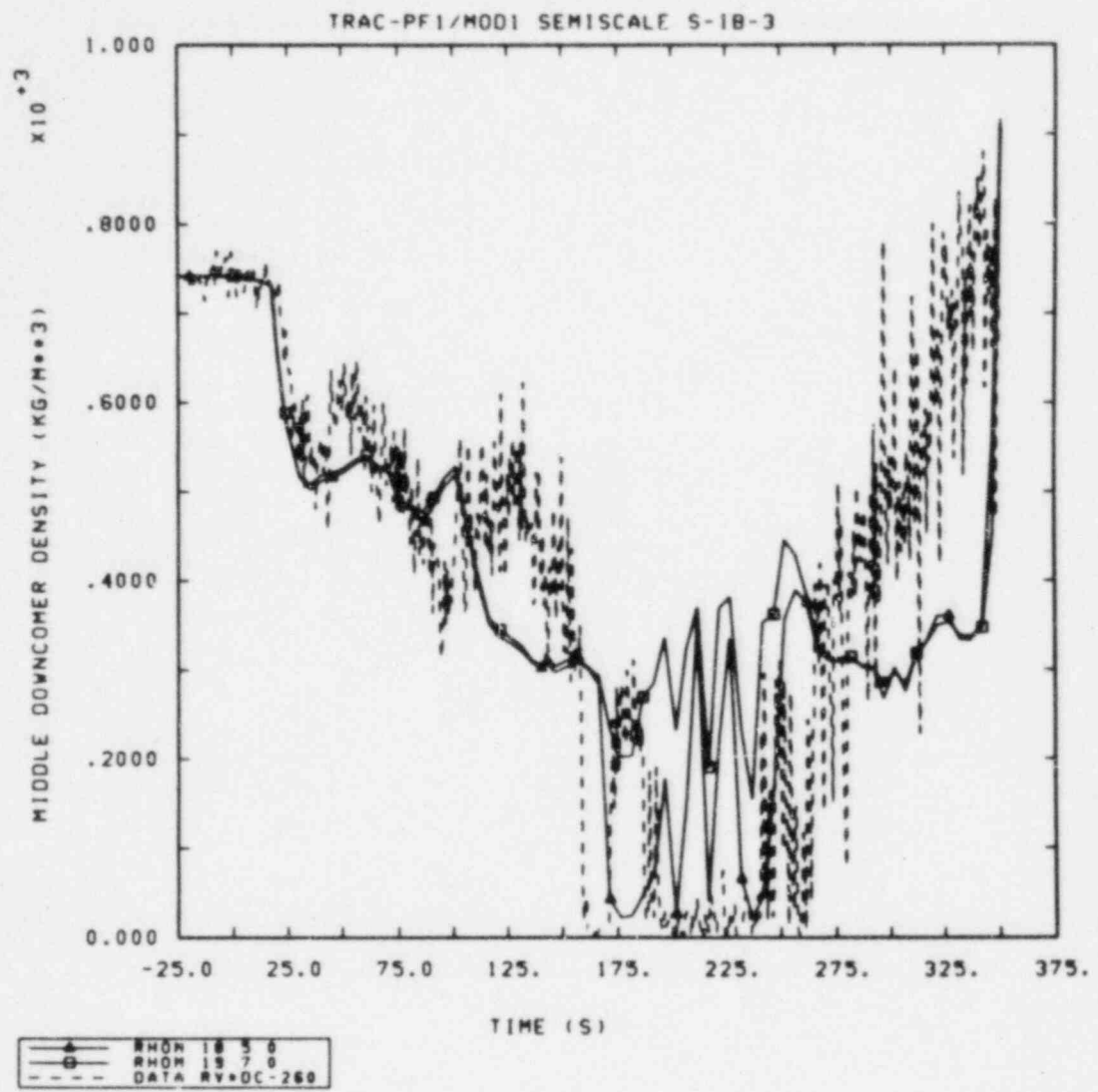


Figure 3.4.3 Mid-Downcomer Densities

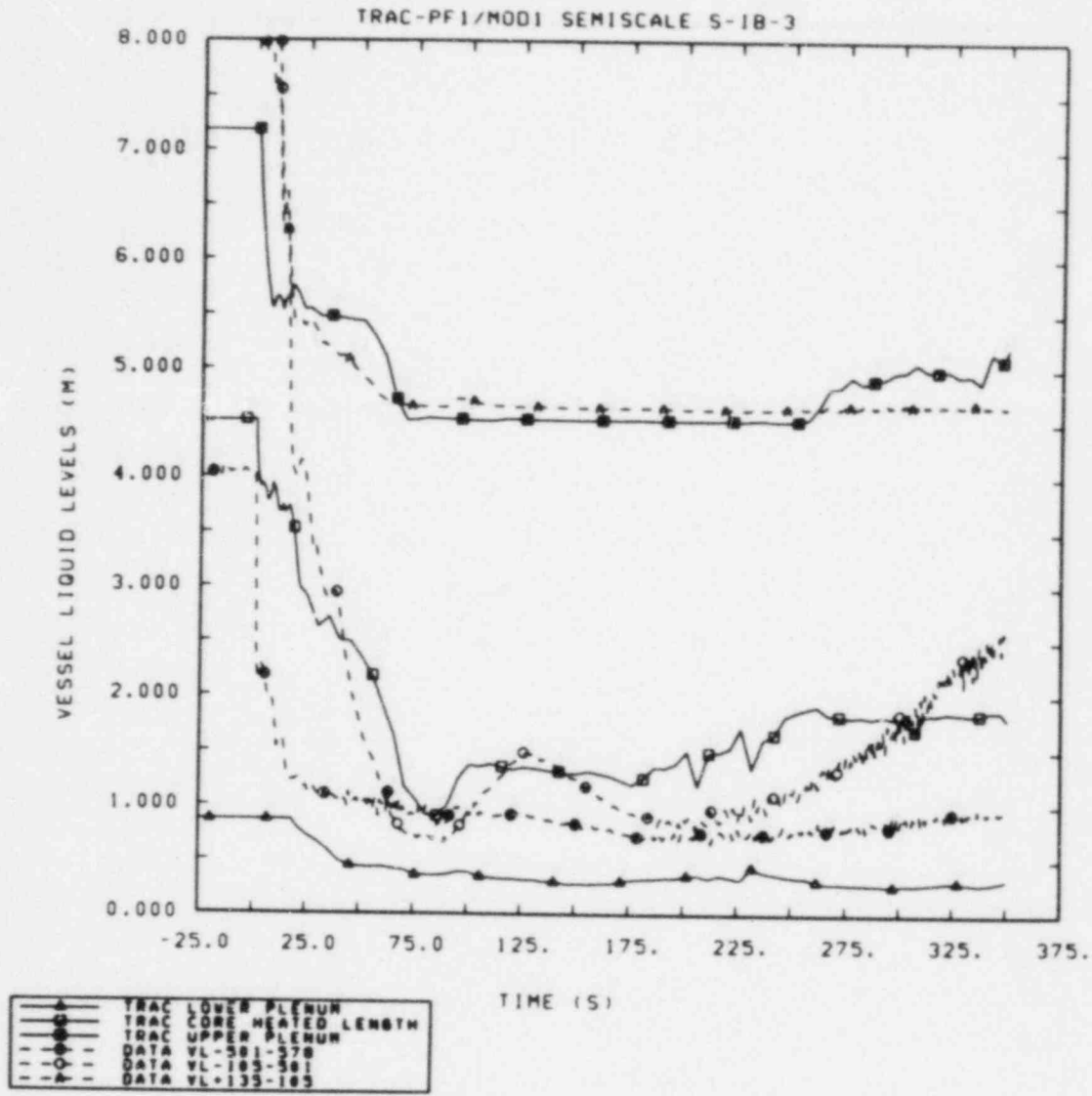


Figure 3.4.4 Lower Plenum, Heated Length and Upper Plenum Liquid Levels

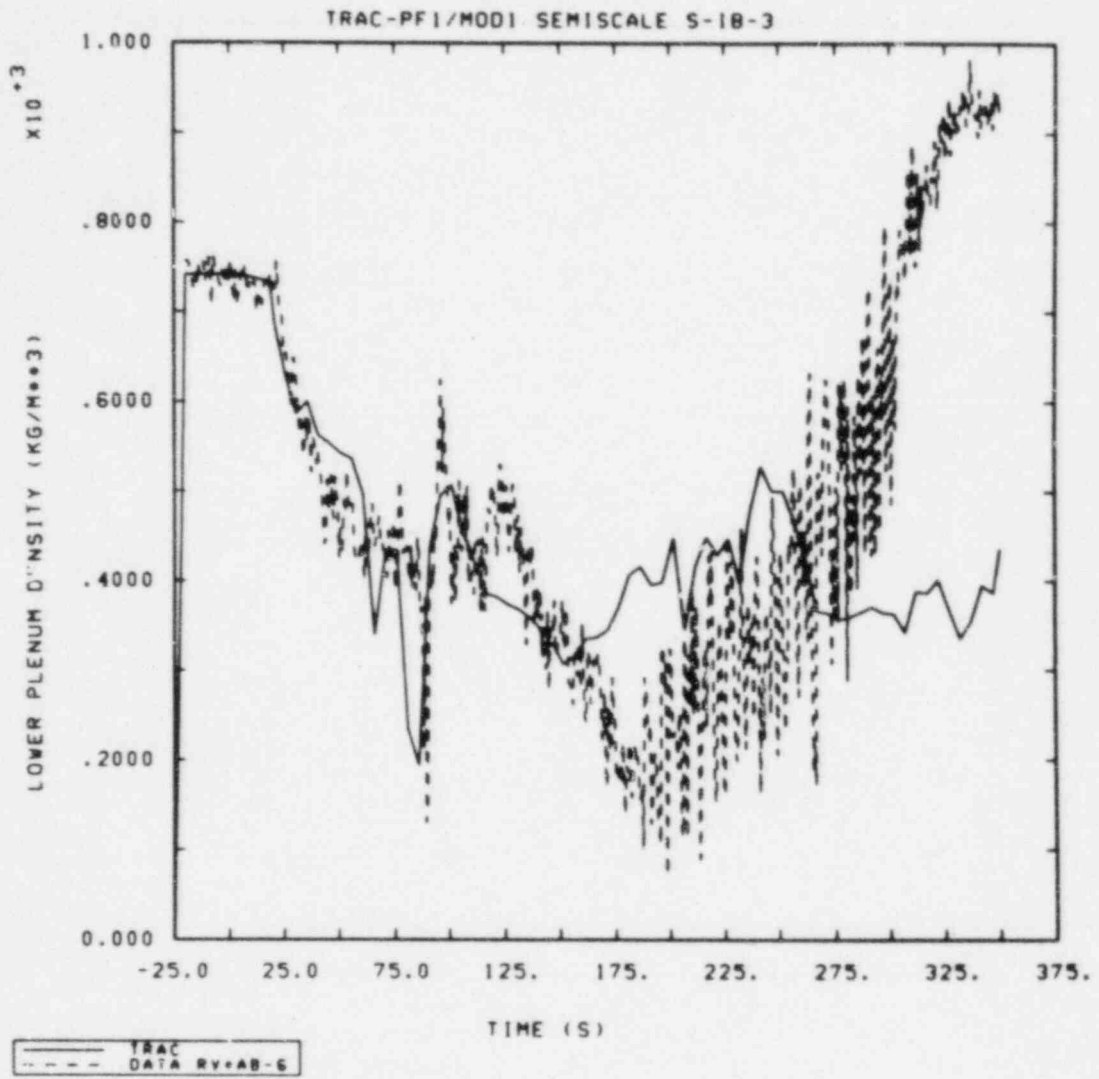


Figure 3.4.5 Lower Plenum Densities

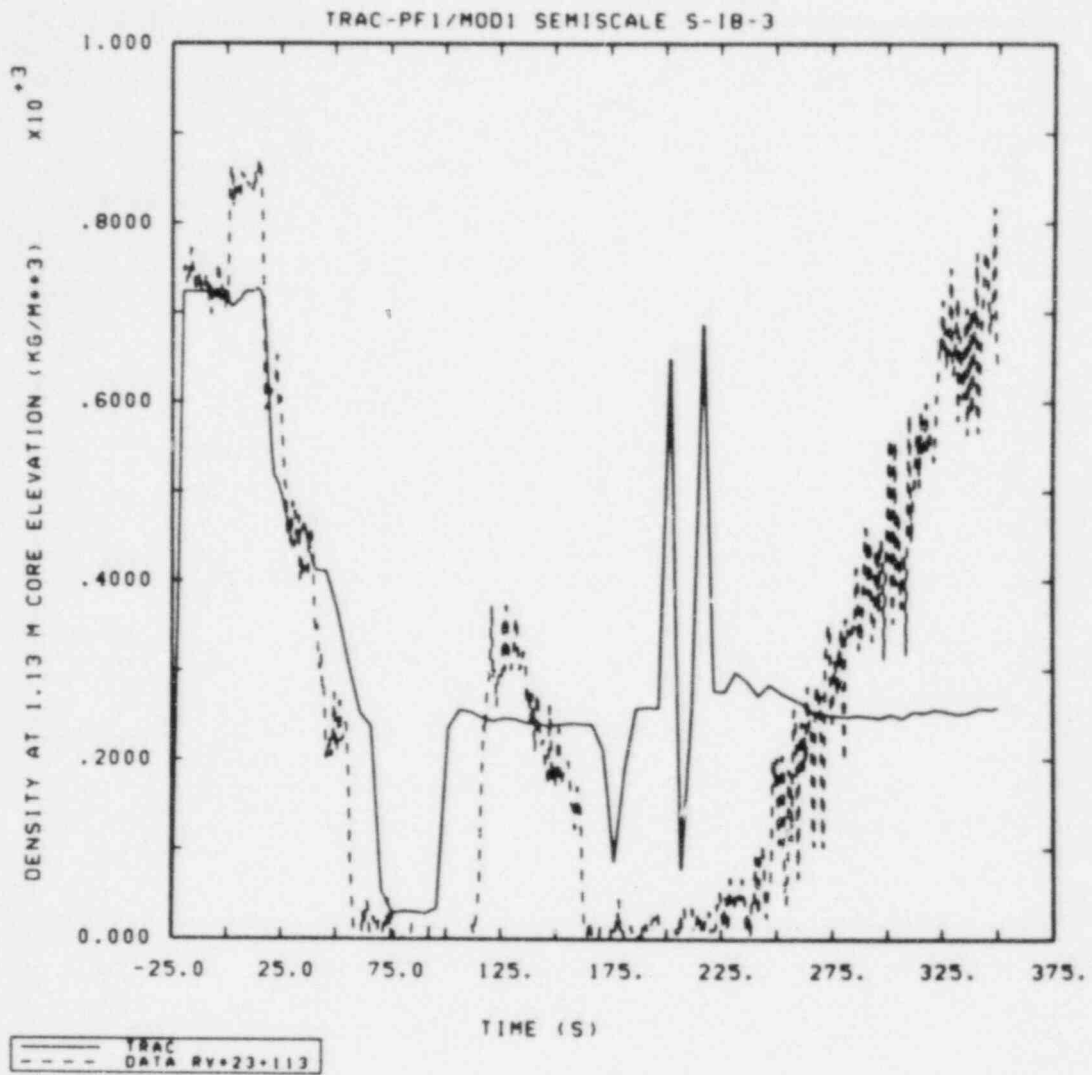


Figure 3.4.6 Lower Core Densities (1.13 m Core Elevation)

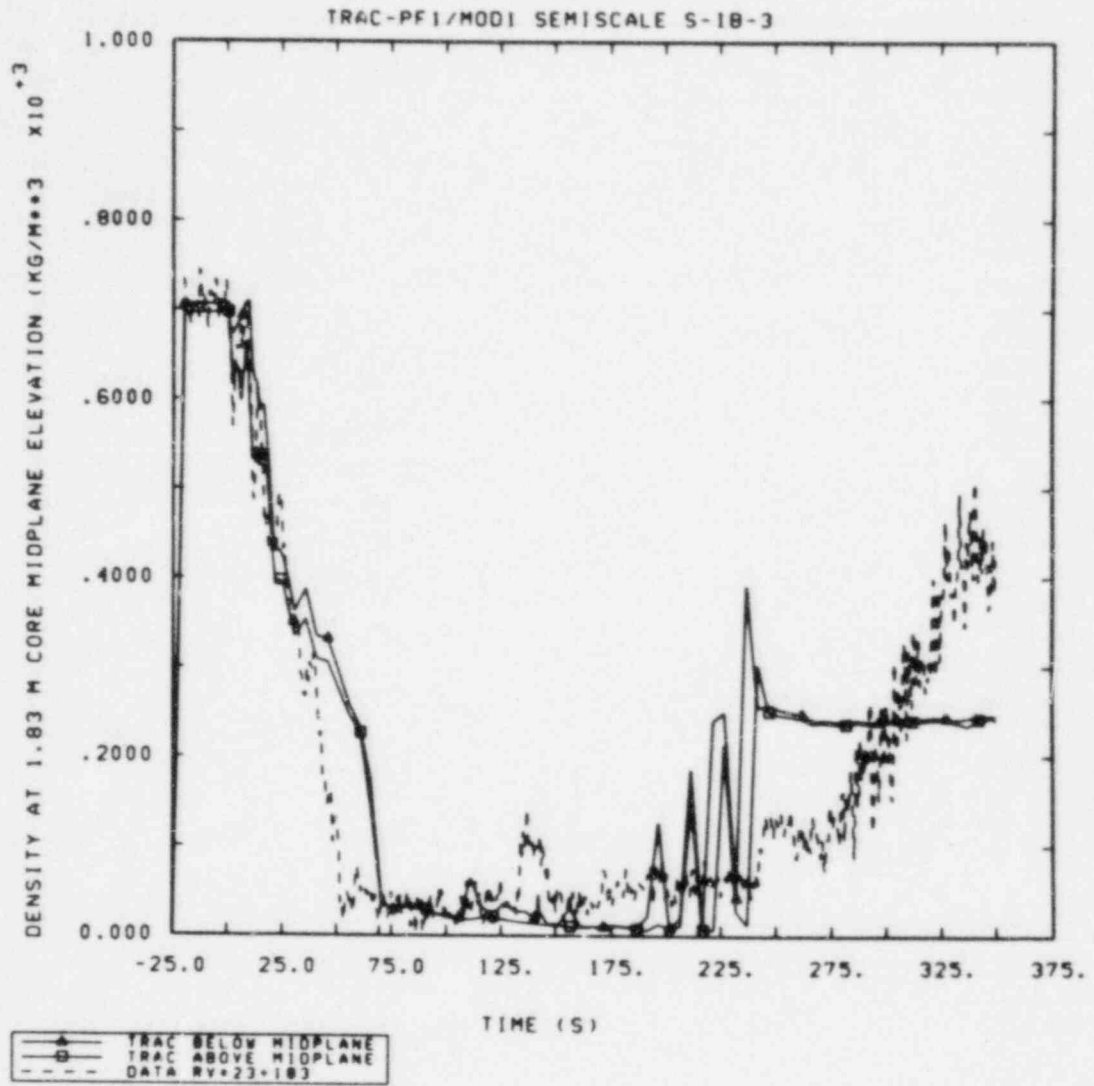


Figure 3.4.7 Middle Core Densities (1.83 m Core Elevation)

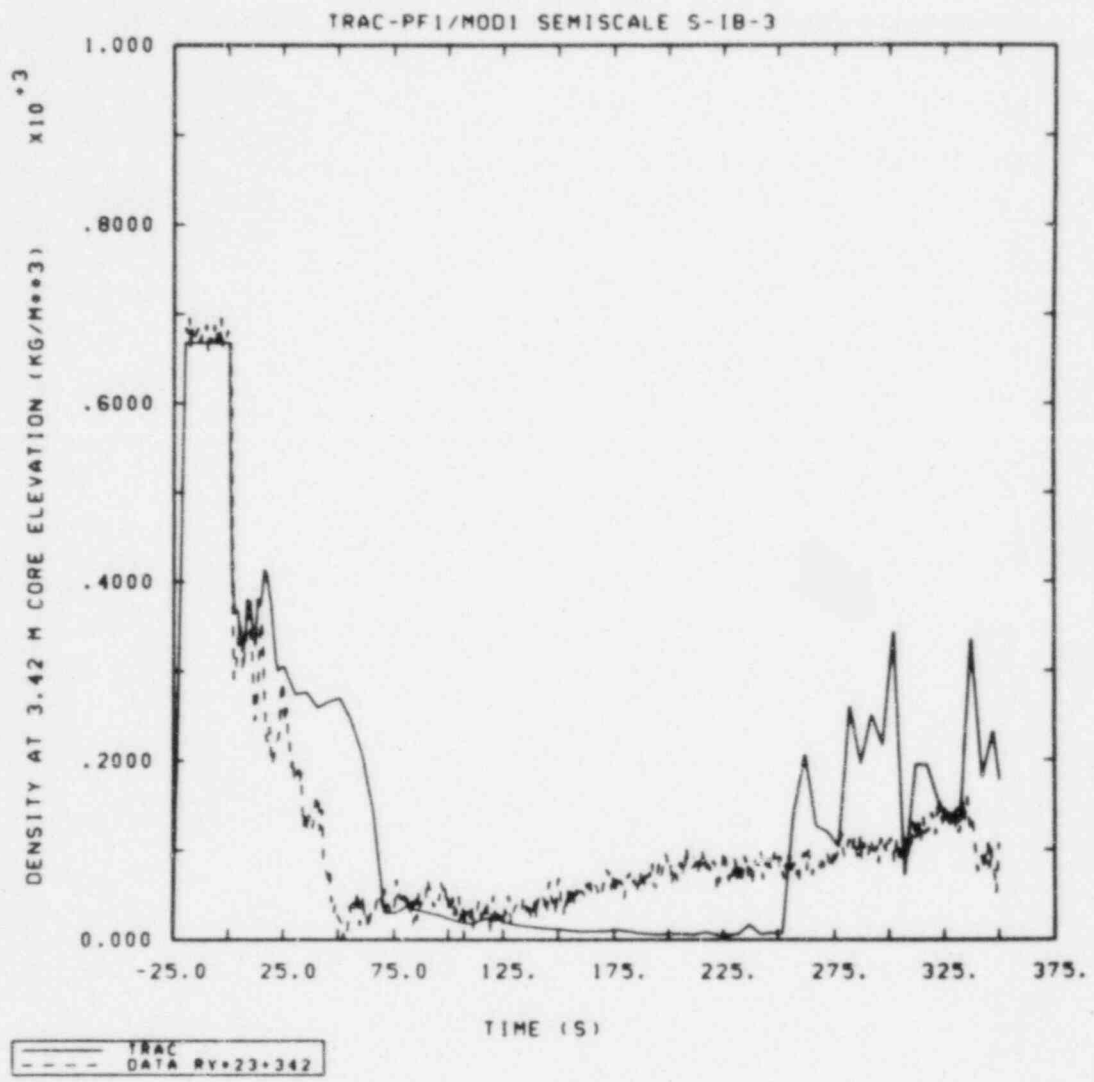


Figure 3.4.8 Upper Core Densities (3.42 m Core Elevation)

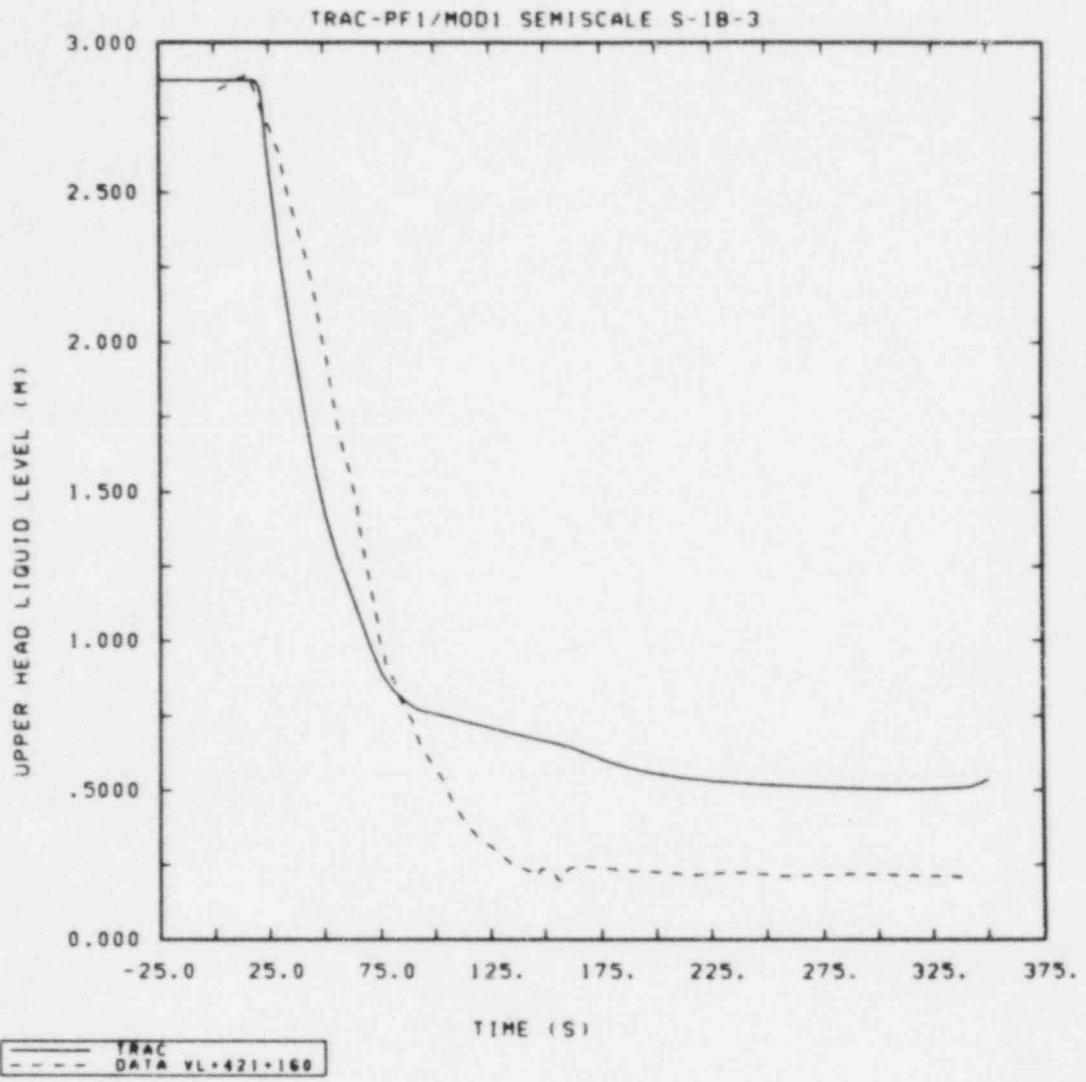


Figure 3.4.9 Upper Head Liquid Level

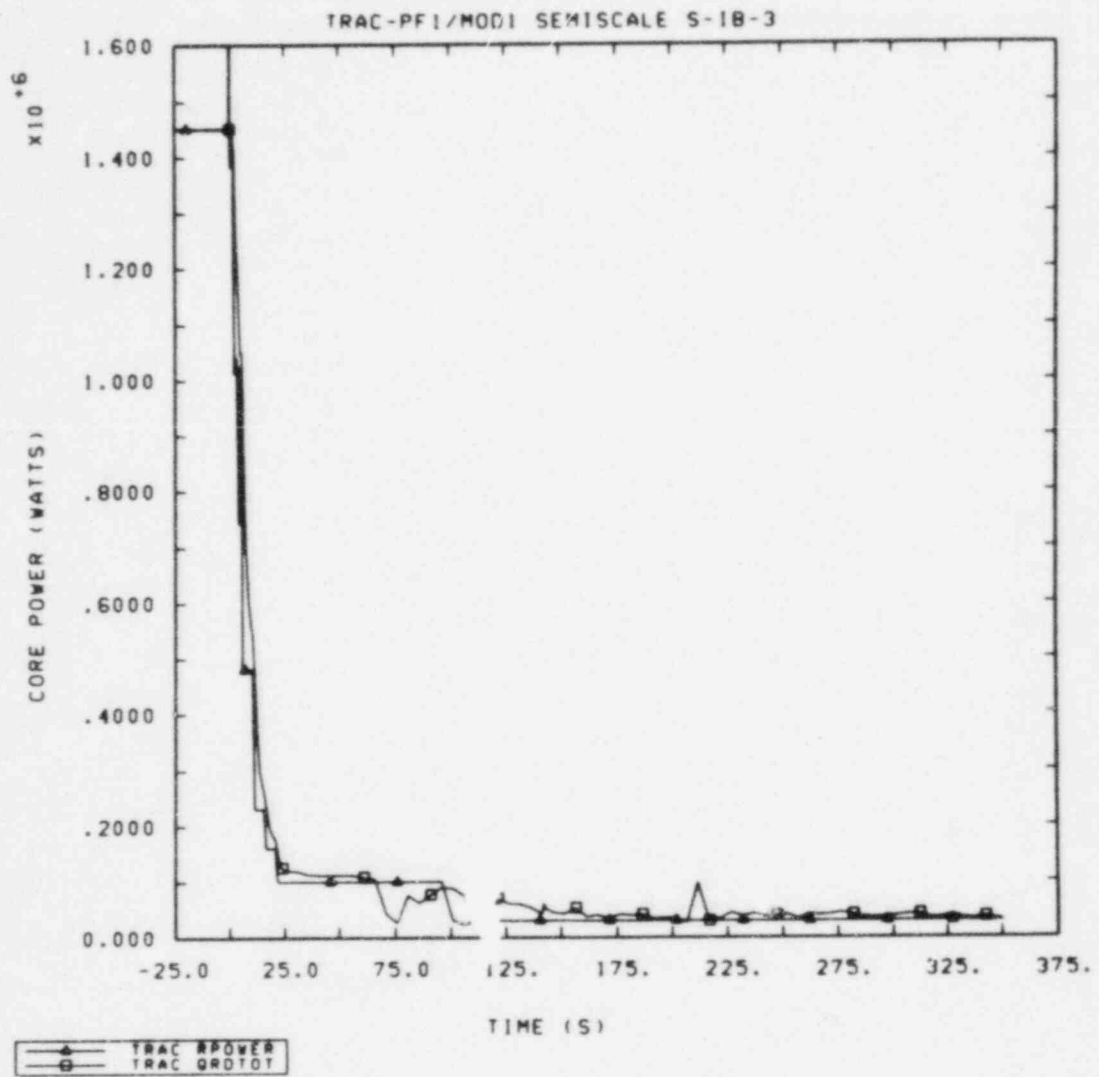


Figure 3.5.1 Core Power and Total Rod Heat Transfer

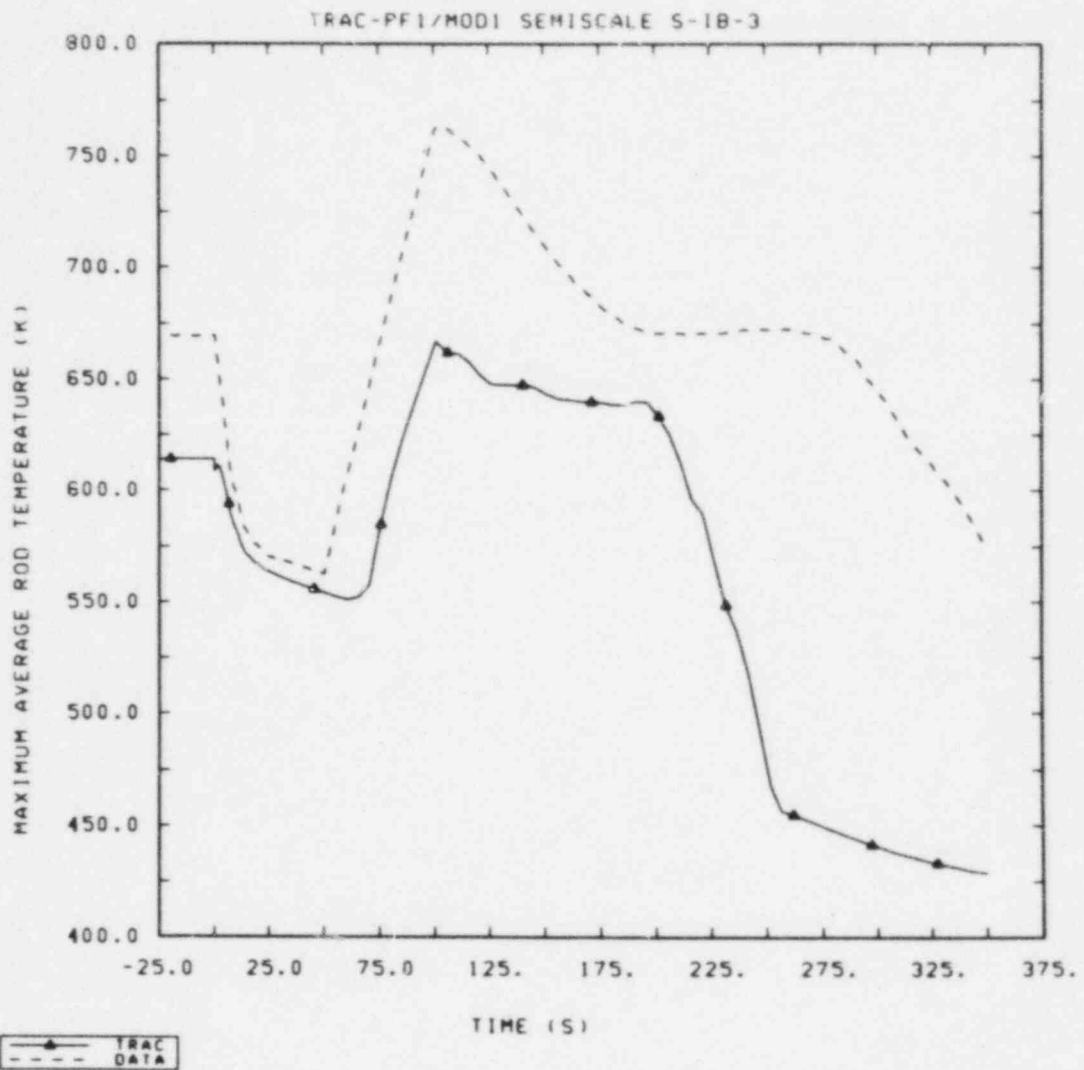


Figure 3.5.2 Maximum Rod Clad Temperature

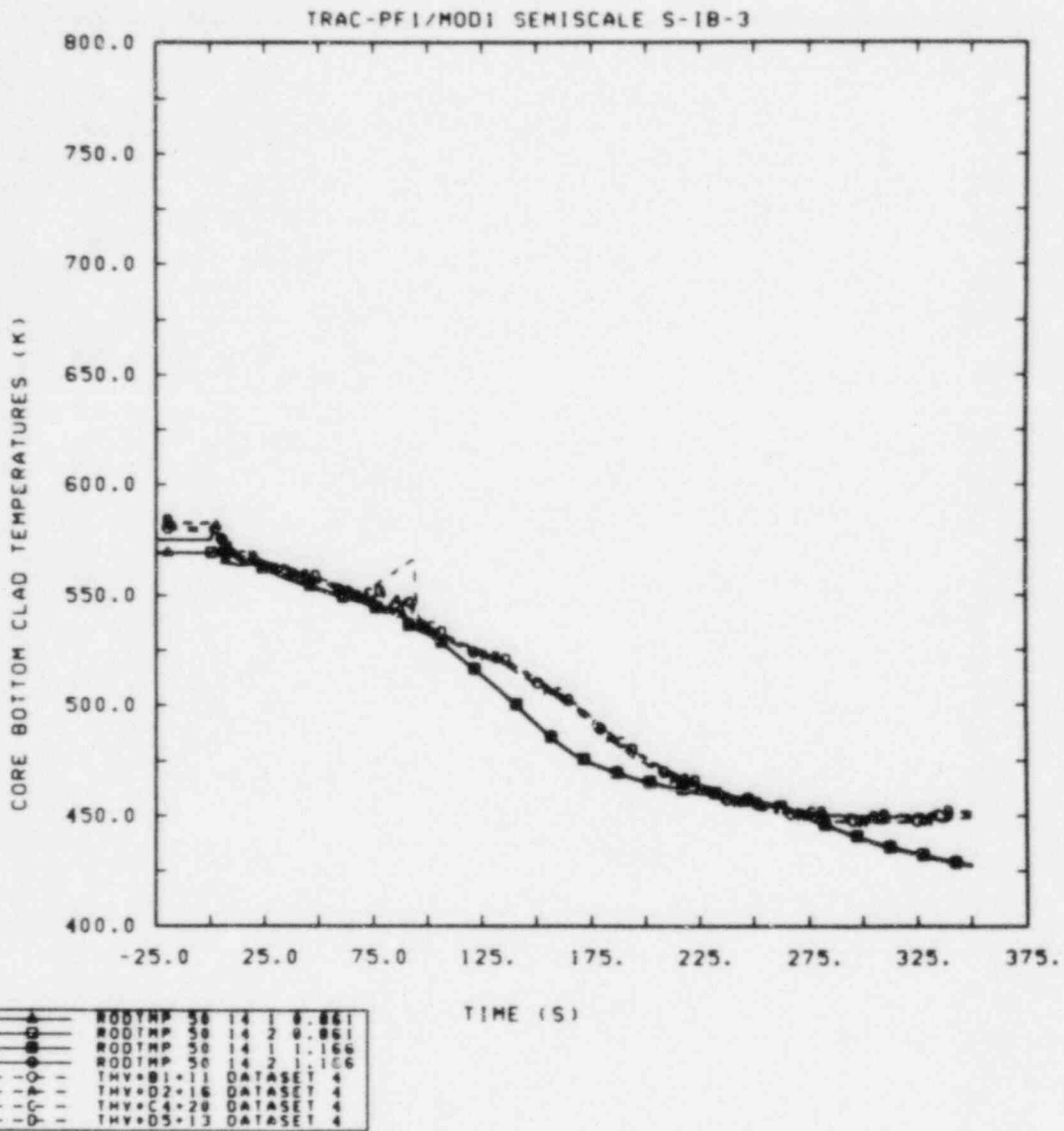


Figure 3.5.3 Lower Core Heater Rod Temperatures (0.15 m Core Elevation)

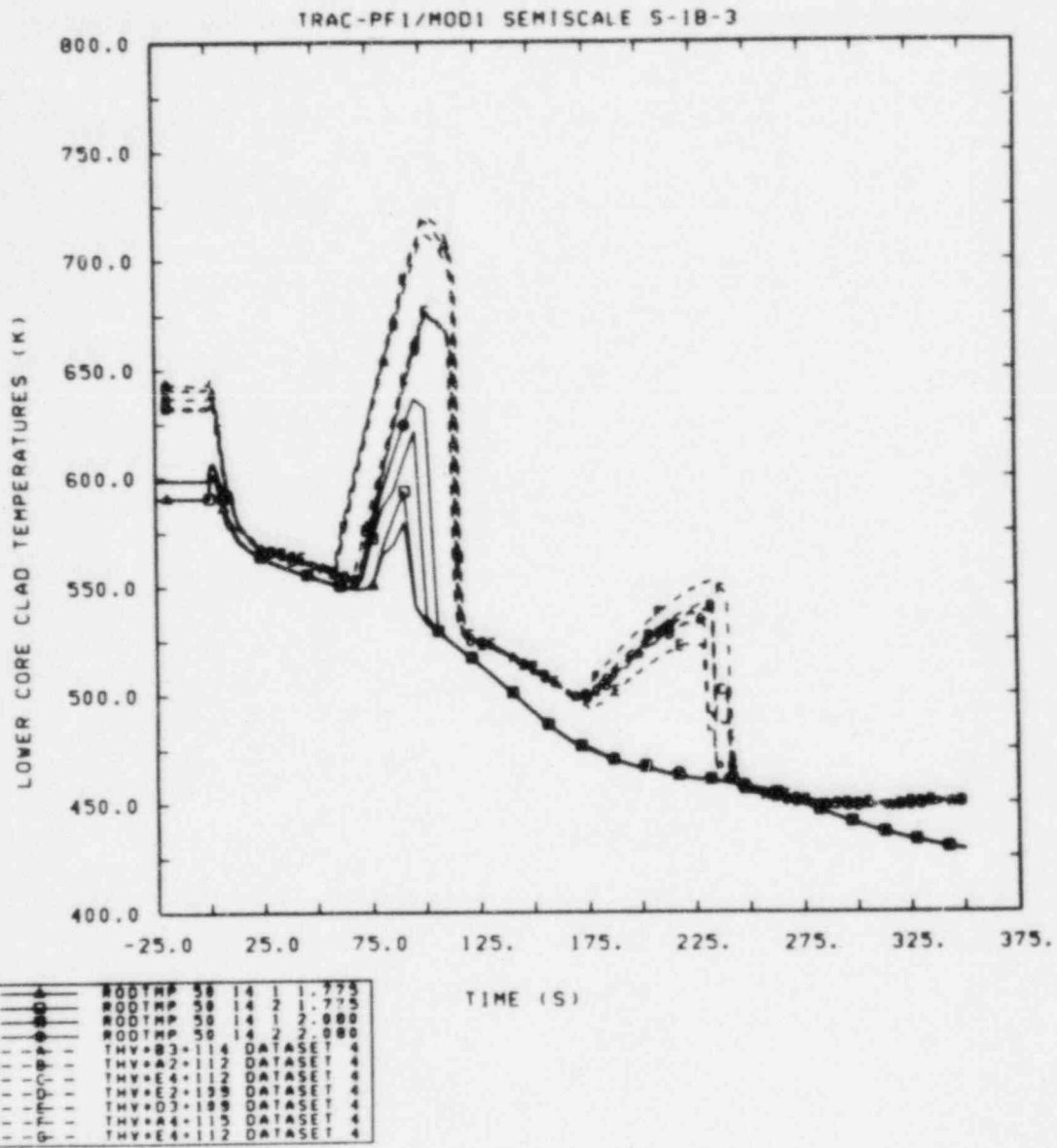


Figure 3.5.4 Lower Core Heater Rod Temperatures (1.12 m Core Elevation)

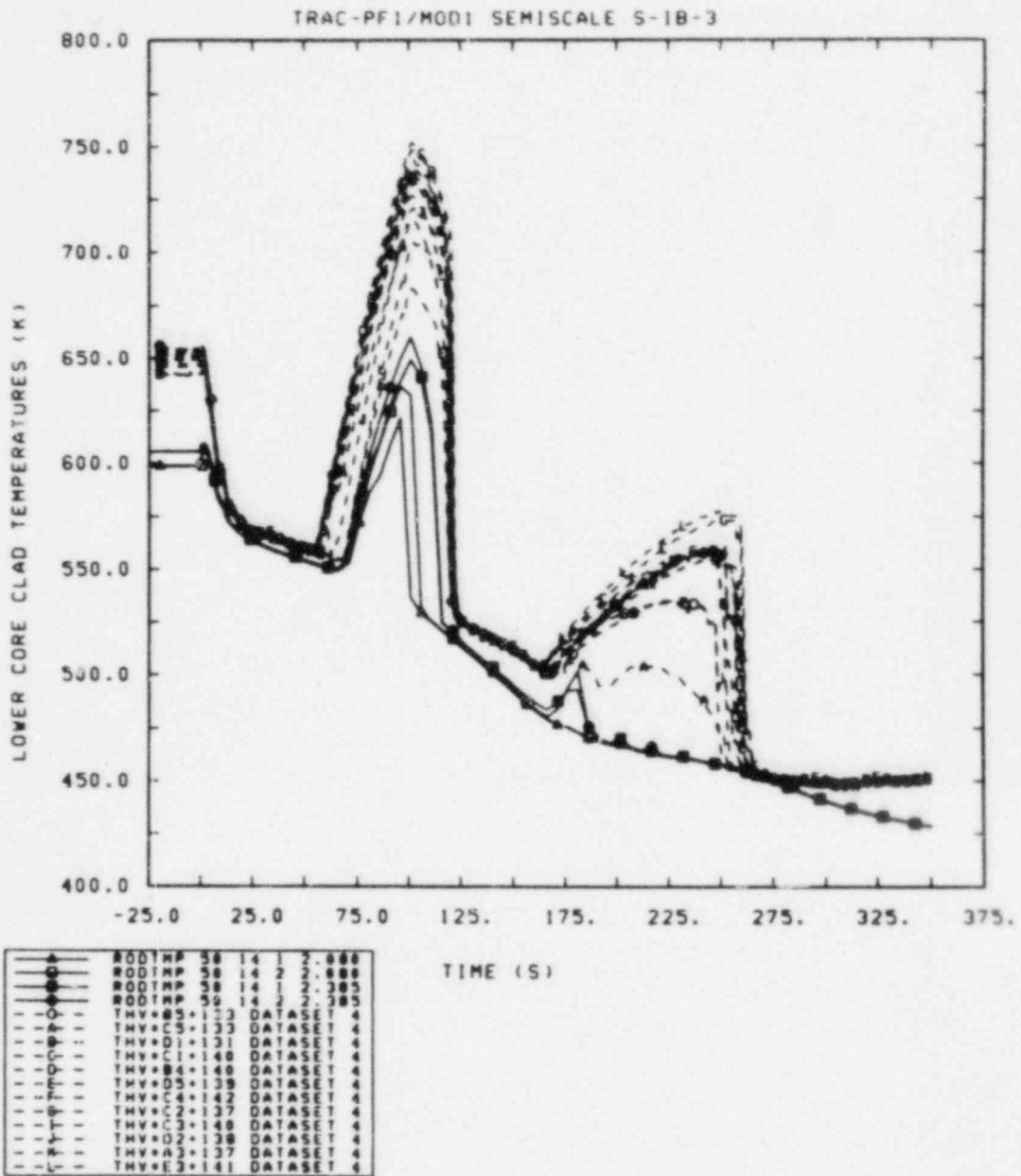


Figure 3.5.5 Lower Core Heater Rod Temperatures (1.36 m Core Elevation)

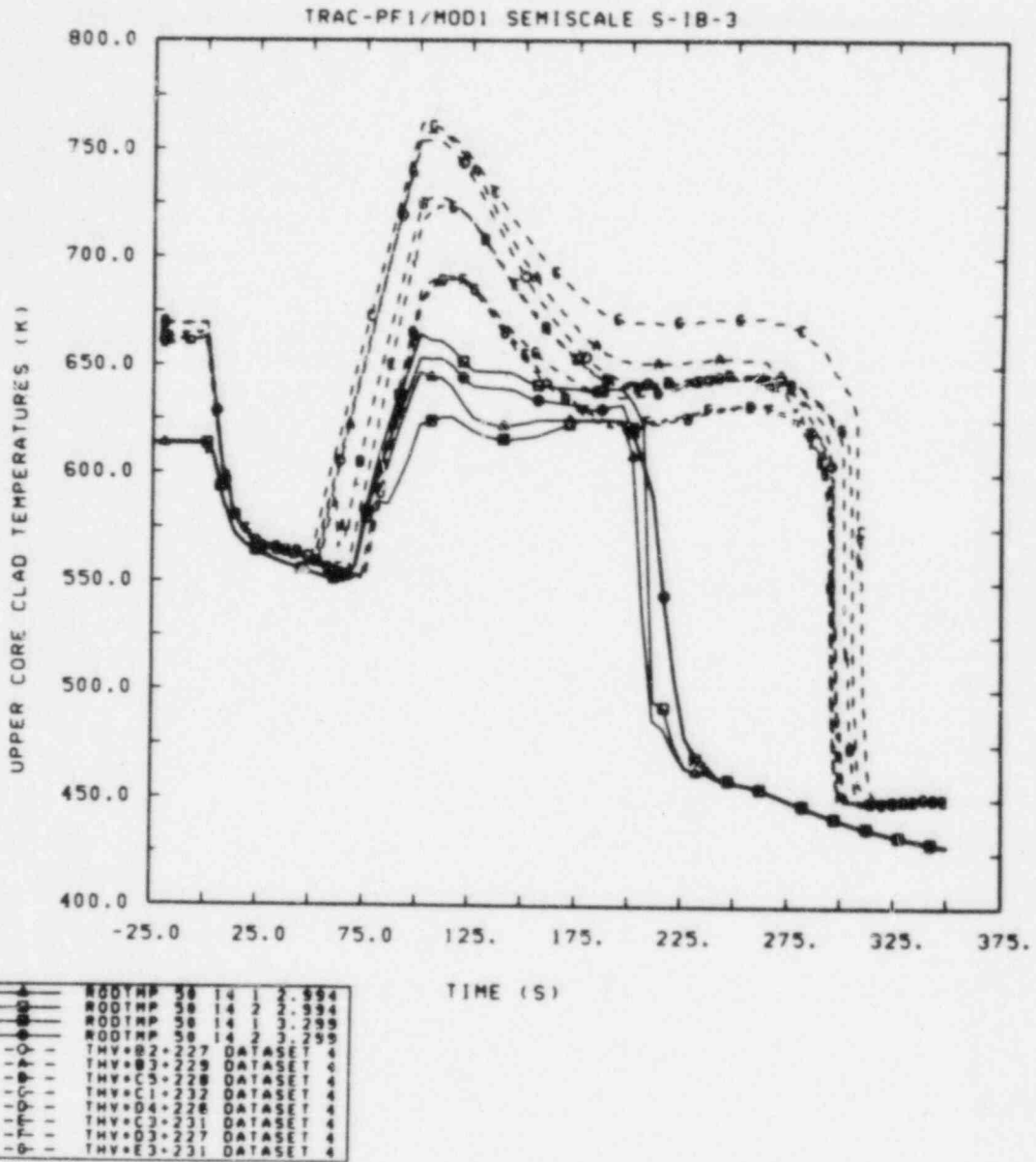


Figure 3.5.7 Upper Core Heater Rod Temperatures (2.30 m Core Elevation)

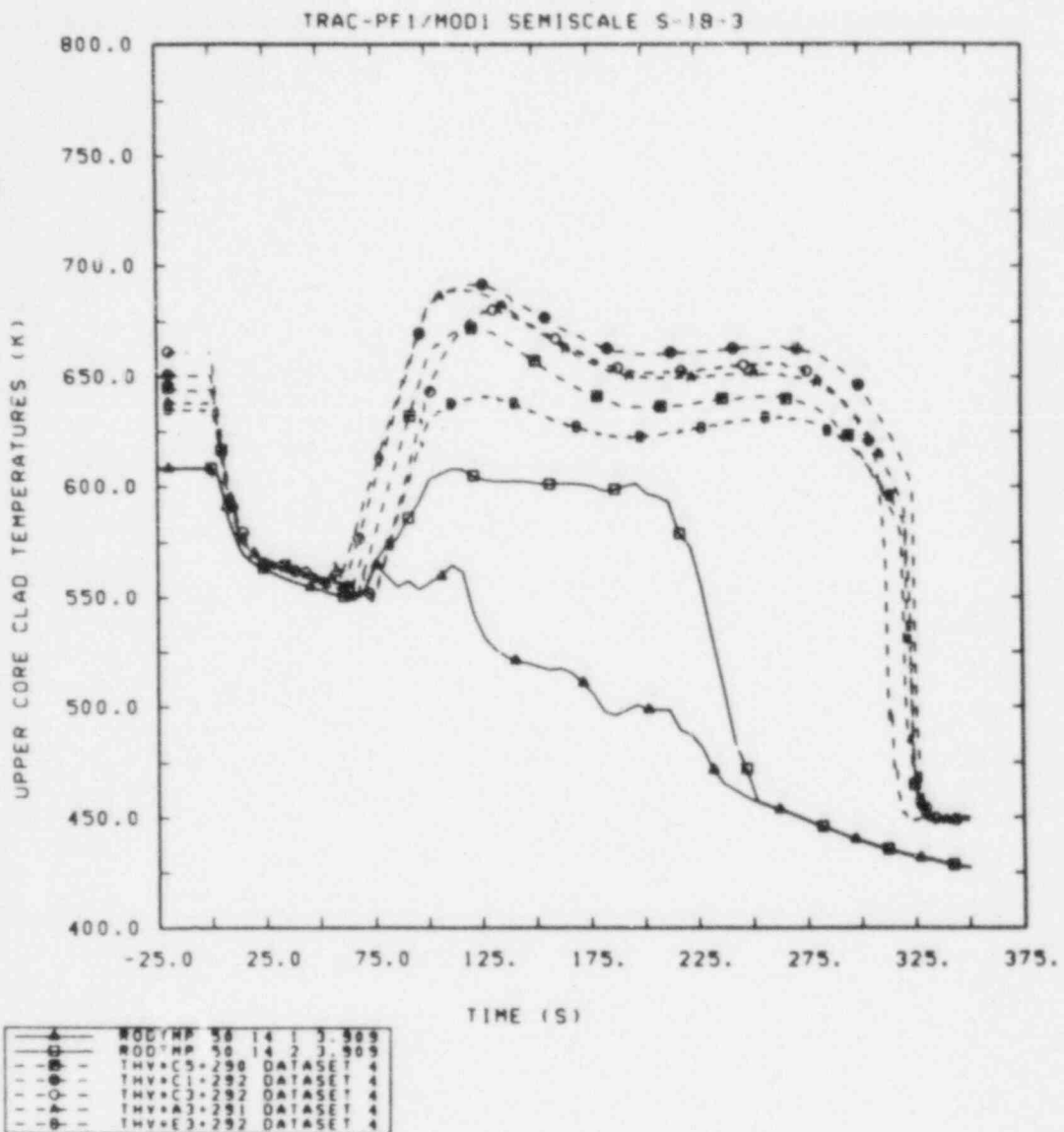


Figure 3.5.8 Upper Core Heater Rod Temperatures (2.91 m Core Elevation)

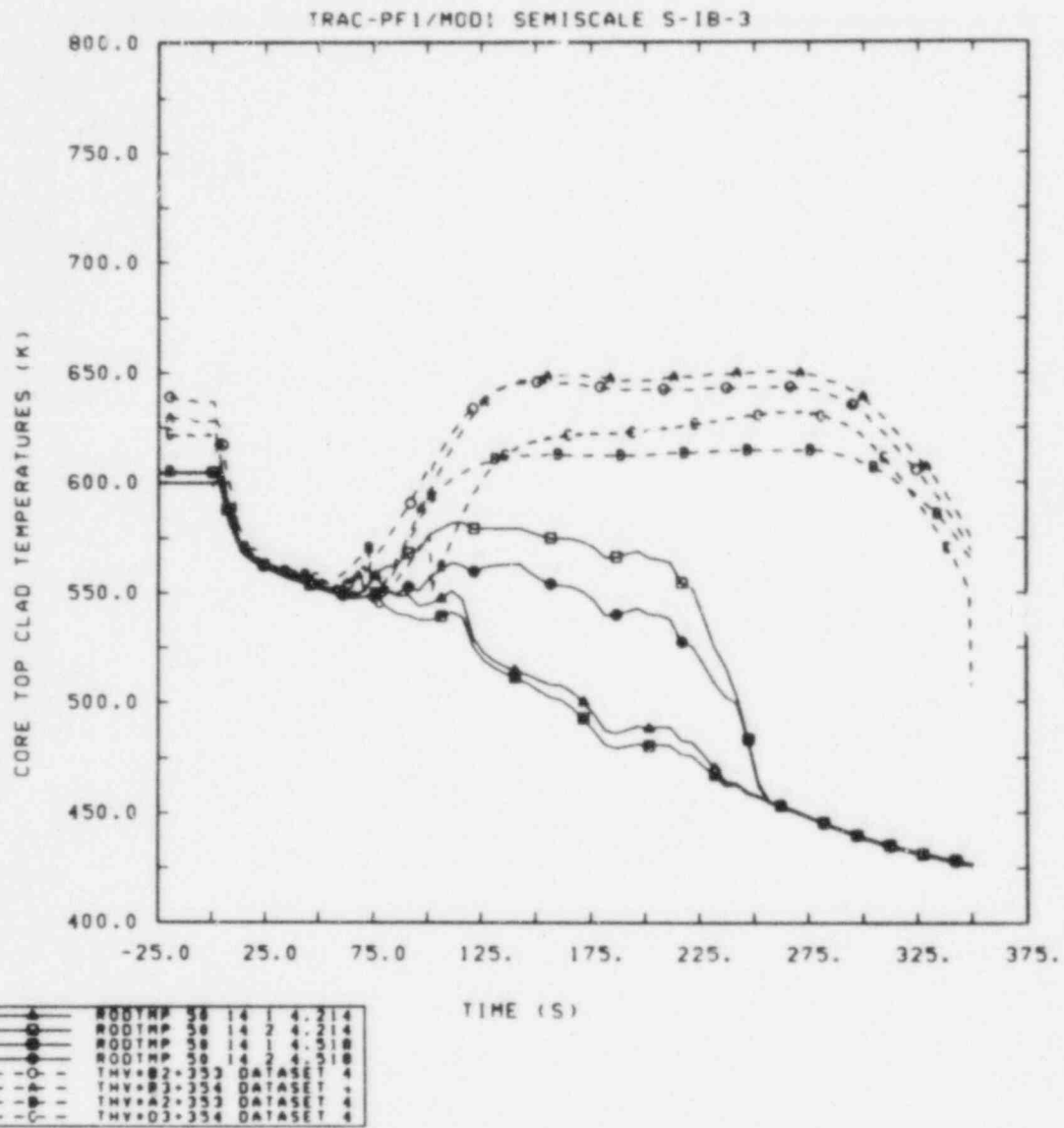


Figure 3.5.9 Upper Core Heater Rod Temperatures (3.53 m Core Elevation)

4.0 NODING STUDY

A purely 1-D model was developed for the Semiscale Mod-2A facility and the S-IB-3 test, using the 1-D CORE, TEEs, PIPEs and two PLENUM components to connect the hot and cold legs to the vessel and downcomer, respectively (as described in Section 2.2). This was intended to allow us to assess the new PLENUM component by comparing final results to those obtained with our corresponding 3-D VESSEL model, and to allow us to run sensitivity studies with a faster running model.

This section presents the results of both our "original" and "final" 1-D model results, and compares them to the results from our basecase 3-D model analysis (already described in Section 3). Here, "original" does not mean the first 1-D model calculation but rather the calculation done with the same code and the same input and default options as the 3-D model analysis; "final" refers to a later 1-D run with more code error corrections and some different input options implemented.

4.1 Basecase 3-D vs Original 1-D Model Results

Figure 4.1.1 shows the intact and broken loop cold leg pressures for our 3-D and original 1-D model calculations, together with the experimental data. The pressures from the 1-D are generally lower than those from the 3-D model calculation, visible after ~100 s. Because, as will be shown below, this 1-D model gave even lower core temperatures than the 3-D model had, this helps confirm the idea that the lower calculated pressures (relative to the observed pressures) are due to underpredicting the core heatup and associated steam generation and superheat.

There are very few differences in the break flows predicted using these two input models, as shown in Figure 4.1.2. The 3-D model calculation, with its slightly higher pressures, has slightly higher break flow rates except when the higher accumulator injection in the 1-D model calculation (Figure 4.1.3) causes higher ECC bypass to show up in the break flow; this higher accumulator flow for most of the injection period is due to the lower pressures predicted using the 1-D model.

The biggest difference in results calculated is for the vessel inventory. Figure 4.1.4 shows the vessel and downcomer liquid levels calculated using our 3-D and 1-D models, compared with data. There is a growing divergence between the levels in the two calculations, with the 3-D model results generally in better agreement with data (although the 1-D model results are in better quantitative agreement on the vessel level recovery after intact loop seal clearing at ~100 s). Throughout most of the transient, the 1-D model shows substantially more liquid in both the downcomer and the vessel than either the 3-D model or the test, especially at later times.

Figure 4.1.5 shows the individual lower plenum, core heated length and upper plenum liquid levels for the 3-D and 1-D model calculations. While there are some small differences in the upper plenum and while the lower plenum is more voided in the 3-D model, most of the discrepancy lies within the core heated length. The collapsed liquid level there both drops later initially and subsequently recovers more quickly after loop seal clearing. However, both models give almost identical minimum overall vessel and core heated length levels. These level minima are controlled by the amount of liquid in the loop seals and the steam generator U-tubes

before clearing, and the agreement on the minimum level values in the two calculations is a result of very similar loop hydraulic behavior being predicted using these two input models.

The differences in the core heated length liquid content are mirrored in the core temperatures predicted using the two models. Figure 4.1.6 shows the maximum rod clad temperatures (i.e., the maxima of all the thermocouple measurements throughout the core at any given time), and Figure 4.1.7 shows the individual heater rod temperatures at the core midplane, from the 3-D and 1-D model calculations. In both figures, the core heatup is slower in the 1-D CORE (due to the difference in collapsed liquid levels in the ~25-65 s time period), the recovery after PCT more rapid (due to the greater level recovery in the 1-D calculation after intact loop seal clearing), and the second heatup late in the transient almost fully suppressed in the 1-D model (due to the approximately-doubled core liquid inventory after ~100 s). After quench, the 1-D model rod temperatures are lower due to the lower system pressures and associated saturation temperatures predicted.

4.2 Density Gradient Inversion at Component Boundary

The qualitative behavior of the 1-D model vessel inventory distribution differs markedly from the corresponding local 3-D model behavior, in addition to the quantitative difference in magnitude already discussed.

Figure 4.2.1 gives the mid-downcomer densities for the 3-D and 1-D models. As discussed earlier in Section 3.4, the 3-D model results correctly show the downcomer partially voiding during the ~150-250 s period, although the calculated voiding does not extend as far down as was measured; in contrast, the 1-D model results show a density increase (rather than decrease) at about 150 s. The downcomer refilling at about 250 s is seen in the 1-D model calculation, as well as in the 3-D model calculation and in the test, but more rapidly in the calculations than in the data.

The lower plenum densities calculated with the 3-D and 1-D models are shown in Figure 4.2.2, with the corresponding measurement. In this location, although neither calculation shows the boiloff measured from 125 to 200 s, the 1-D model generally gives better agreement with data, particularly for the refill late in the transient (while the 3-D model tends to hold a more-or-less constant density after ~100 s).

In one sense, the original 1-D model densities in the core heated length also show better qualitative agreement with the test data than the 3-D model densities, albeit with more liquid present in the equivalent region. As shown in Figures 4.2.3 and 4.2.4 for the lower and middle core regions, respectively, the 1-D model calculation shows increasing densities during vessel refill late in the transient where the 3-D model densities stabilize once a void fraction of ~0.7 is reached. Besides the discrepancy in the amount of liquid present at any location after the first 100 s of transient, the 1-D model shows liquid appearing earlier than either the 3-D model or the data in the middle and upper core (shown in Figures 4.2.4 and 4.2.5, respectively).

Despite some local improvements in qualitative behavior, the 1-D model results for the vessel inventory have one major defect, which can be inferred from comparing Figures 4.2.2 and 4.2.3, but is better shown in Figure 4.2.6. This figure

gives the vessel void fraction profiles at 125 s in the transient from the 3-D and 1-D models, as a function of vessel elevation. (Similar behavior is seen at most times in the transient.) The vertical dashed lines correspond to the boundaries between the lower plenum, core heated length and upper plenum; upper head results are not included in this plot. The 3-D VESSEL component gives two void fractions at each axial level for the two azimuthal sectors; these have been volume-averaged before plotting. The resulting 3-D model void fractions show a graded two-phase region extending from the bottom of the lower plenum to near the middle of the core, with mostly steam above, at this time. The 1-D model, however, has a gradient inversion at the top of the lower plenum, so that cells in the 1-D CORE component (higher in the vessel) have substantially more liquid present than cells in the upper half of the lower plenum TEE component (lower in the vessel). Such a profile appears highly unphysical, and we have discovered that this behavior is a numerical artifact associated with the component boundary. (There is no difference in either volume or junction flow areas between the top cell in the lower plenum and the bottom cell in the core; there is no additional flow resistance or any other geometric reason for such behavior.)

Figure 4.2.7 shows details of the lower plenum/core region nodalizations used in this basecase 1-D model, and in a modified 1-D model where the component boundary between the lower plenum TEE and CORE was moved down one cell. That cell's geometry was unchanged; essentially, only the relative locations of the external and internal component junctions were switched. The results obtained using this modified 1-D model are shown in Figure 4.2.8, superimposed on the void fraction profiles from Figure 4.2.6. The gradient inversion has moved down one cell, just as the external component boundary was moved down one cell. The rest of the new results calculated with this modified 1-D model are very similar, although not identical, to those from the basecase 1-D model.

This result, together with the two 1-D model input decks, was given to the code developers at LANL. After some examination, they determined that the key difference in the two runs lay in the code assumption of inverted annular flow in the 1-D CORE component. This inverted annular flow regime is not documented in the TRAC manual. It is limited to 1-D components with generalized heat slabs, and is explicitly disallowed at the component boundaries (explaining the dependence of our results on the location of the component boundary). The use of this inverted annular flow regime can be affected by changing an undocumented NAMELIST variable, INVAN. The default value of zero causes the inverted annular flow regime to be considered whenever the wall temperature is greater than saturation; setting this flag to one causes this flow regime to be allowed only when the temperature is greater than the critical heat flux temperature, T-CHF (which to us seems more physically reasonable).

When LANL changed the value of INVAN and reran our input decks, they found the results shown in Figure 4.2.9; the void fractions in the lower part of the lower plenum TEES are virtually unchanged, but the void fractions at the top of the lower plenum and the two-phase region of the core are nearly constant (at ~ 0.7 , the 3-D model's "magic" void fraction) and, where before the 1-D and 3-D models' two-phase froth level were at the same elevation, LANL's results show a higher two-phase mixture level in the 1-D core. The new void fraction profiles are almost perfect step functions rather than resembling the more smoothly varying 3-D profile, but at least the unphysical density inversion has been eliminated.

4.3 Inverted Annular Flow Modelling Option

Before we could duplicate the LANL runs and compare the overall results to those of our previous 3-D and 1-D calculations, we had to obtain additional error corrections from LANL, as discussed in Section 5.1, correcting the T-CHF calculation so that the INVAN flag would have the proper effect. This correction set (either EC3 or EC12.3, as the nomenclature changed) was developed in June 1985 and obtained at Sandia in October 1985. After this was done, we reran our basecase 1-D model calculation for the transient period being analyzed, with the new code error corrections, setting INVAN=1; we did not rerun the modified 1-D model because our "final" 1-D results, and LANL's two calculations, strongly suggested no new and different results would be obtained.

Figure 4.3.1 shows the vessel void fraction profiles calculated with our basecase 1-D model using the different inverted annular flow logic paths, at the same transient time as the void fraction profiles given in Figure 4.2.6. As with the LANL results shown in Figure 4.2.9, the void fractions in the lower part of the lower plenum TEE are virtually unchanged in our "final" 1-D run, but the void fractions at the top of the lower plenum and the two-phase region of the core are nearly constant (at ~ 0.7 again), and the void fractions in the upper core show a higher two-phase mixture level in the 1-D core than either our 3-D or "original" 1-D calculations' two-phase froth level. The new void fraction profiles are more like step functions than the more smoothly varying 3-D profile, but there is no unphysical density inversion.

The lower plenum densities for our original and final basecase 1-D model calculations are given in Figure 4.3.2, together with experimental data. There are minor differences only in the calculated densities at this level, most notably in the vessel level depression during the 50-75 s period. The new 1-D calculation shows slightly lower densities from ~ 100 to ~ 200 s, and slightly higher densities from ~ 225 to ~ 325 s, than our original 1-D calculation, but neither result is obviously better.

A more substantial difference is seen in the predicted core densities, shown in Figures 4.3.3 through 4.3.5 for lower, middle and upper core elevations, respectively. The behavior prior to intact loop seal clearing at ~ 100 s is only marginally different (e.g., the more rapid level drop in the lower core with the new 1-D calculation). However, the behavior after that loop seal clearing and associated partial vessel level recovery is both qualitatively and quantitatively different for the two 1-D calculations (e.g., the quasi-steady densities corresponding to $\alpha \sim 0.7$ in the two-phase regions of the core in our final 1-D calculation). The timing of liquid reappearance in the middle and upper core is also different for the two 1-D calculations.

To summarize the differences in vessel inventory distribution, Figure 4.3.6 gives the lower plenum, core heated length and upper plenum collapsed liquid levels for these two calculations with our basecase 1-D model, using different inverted annular flow logic. The lower plenum response is only slightly affected, mostly late in the transient. The core heated length contains significantly less liquid throughout most of the transient with the new code logic than with the default logic. In contrast, the upper plenum contains substantially more liquid after ~ 150 s in our final calculation than in our original 1-D calculation for about 100 s, after which both runs show a similar amount of upper plenum liquid present.

Figure 4.3.7 shows the corresponding overall vessel and downcomer collapsed liquid levels. The final 1-D calculation predicts generally only slightly lower vessel and downcomer levels except at late times, where its results begin diverging substantially from those of the original 1-D model. Looking back at Figure 4.3.6, most of the divergence in vessel level is due to less liquid in the core heated length in our final calculation.

Although there is less overall liquid present within the core, the void fraction profiles and the local densities show that this liquid is much more spread out through the core heated length in the new calculation, resulting in somewhat less overall core heatup being predicted. Figure 4.3.8 gives the maximum rod clad temperatures for our two basecase 1-D calculations. The initial core heatup due to vessel level depression is very similar in the two calculations, but the final calculation then shows the temperature dropping more rapidly; neither 1-D calculation shows the substantial late-time core heatup due to level boiloff measured in the test. (The late-time difference in calculated temperatures in this and the next figure is due to different primary system pressures and associated saturation temperatures.) Figure 4.3.9 shows individual measured and calculated core heater rod clad temperatures at the core midplane (1.83 m core elevation), for calculations using our basecase 1-D model and the different inverted annular flow logic. As in the maximum rod clad temperatures in the previous figure, the clad temperatures in the final 1-D calculation are slightly lower than those in the original 1-D calculation, with the older results showing a slight core heatup due to late-time level boiloff where the new results show none at all; both calculations, however, substantially underpredict the core heatup observed in the test.

4.4 Basecase 3-D vs Final 1-D Model Results

The value of the INVAN flag should not affect the results of our 3-D model calculation, because the inverted annular flow regime is only considered in certain 1-D components. The error corrections added to the code may or may not affect the 3-D results calculated, but we did not have the resources for yet another rerun of the transient. Thus, this section does not compare results only for different input models using the identical code, but instead compares results for different input models using slightly different codes.

Figure 4.4.1 shows intact and broken loop cold leg pressures for our 3-D and final 1-D models, together with the measured data. Compared with Figure 4.1.1, the final 1-D model gives higher late-time system pressures, in better agreement with both our 3-D model results and the data. However, all our calculations show much lower system pressures during the 100-200 s period than observed in the test.

Figure 4.4.2 gives the accumulator injection flow rates calculated with our 3-D and final 1-D models (on the same scale as Figure 4.1.3 to facilitate comparison). The large injection spike in the original 1-D model calculation just after 150 s is no longer predicted, an unexpected difference for changing the use of the inverted annular flow regime in the CORE component; this may be due to slightly different time step histories in the two 1-D calculations, or the spike may still be present but between plot edits in the final 1-D calculation. Also, the accumulator injection in the original 1-D calculation was always higher than measured, resulting in a substantial overprediction of the total liquid injected by 350 s. The final 1-D

calculation (because of the different pressure calculated) has lower accumulator injection after ~200 s, resulting in better agreement with both data and the 3-D model result for overall liquid injection.

The final 1-D calculation still overpredicts the accumulator injection, particularly during the middle period of the transient (~150-225 s). The effect of this is seen in Figure 4.4.3, in the vessel and downcomer collapsed liquid levels in the 3-D and final 1-D models. The final 1-D model has both vessel and downcomer levels still substantially higher than either the 3-D model result or the measured data, although changing the use of the inverted annular flow regime from the default did result in improved agreement with data (as seen by comparing this figure with Figures 4.1.4 and 4.3.7).

Figure 4.4.4 gives the lower plenum, core heated length and upper plenum collapsed liquid levels calculated for our 3-D and final 1-D models. All three regions of the vessel generally have more liquid present in the 1-D model, particularly later in the transient, contributing to a higher vessel liquid level. The new 1-D core liquid level is in better agreement with the 3-D model result and the data than the original 1-D model result (although still high), but the upper plenum response is significantly worse.

The final 1-D model core liquid inventory is especially high relative to the data (or the 3-D model level) during the ~150-250 s period. This is reflected in the core heatup calculated in each calculation. Figure 4.4.5 shows the maximum rod clad temperatures, and Figure 4.4.6 shows individual rod clad temperatures at the core midplane, predicted with our 3-D and final 1-D models. Both calculations greatly underpredict the overall core heatup observed. However, the final 1-D calculation completely misses the secondary heatup later in the transient, both qualitatively and quantitatively, while the 3-D model only misses the magnitude and timing.

The mid-downcomer densities for the 3-D and final 1-D models in Figure 4.4.7 show the 1-D model calculating much more liquid in the downcomer than observed or predicted by the 3-D model (also seen in the downcomer collapsed liquid levels in Figure 4.4.3). The external downcomer nodalization in the two models is the same; the differences are all driven by the vessel modelling.

Figure 4.4.8 gives the lower plenum densities predicted using our 3-D and final 1-D models. At this location, the 1-D model results are in better qualitative and quantitative agreement with data than those of the 3-D model (unlike the majority of the results studied). Figure 4.4.9 shows the lower core densities (1.13 m core elevation) for the two calculations. At this location, there is very little difference between the results of the two models, with both maintaining a quasi-steady density (corresponding to $\alpha \sim 0.7$) after intact loop seal clearing rather than the inventory boiloff and subsequent refill measured. Figure 4.4.10 shows similar behavior in the core midplane densities, except for the timing (with the 3-D model result more like the data); the upper core densities in Figure 4.4.11 mirror the mid-core behavior. These density plots clearly show that there is something special in the code about void fractions near 0.7, with cell after cell in either the 3-D or 1-D vessel model reaching such values and then remaining nearly constant for long periods of time.

The vessel void fraction profiles at 125 s into the transient in our 3-D and final 1-D models are given in Figure 4.4.12. As with the collapsed liquid levels in Figure

4.4.4, the final 1-D model calculation has more liquid in the lower plenum and in the core, with a two-phase mixture level significantly higher than that calculated in the 3-D model. Both curves (but more so with the 1-D model, at this particular time) also suggest that there is something special about a void fraction around 0.7, maintaining nearly this value for a number of axial levels extending over substantial reaches of space. (Void fraction profiles at other, later, times show this "hang-up" extending over almost the entire vessel.)

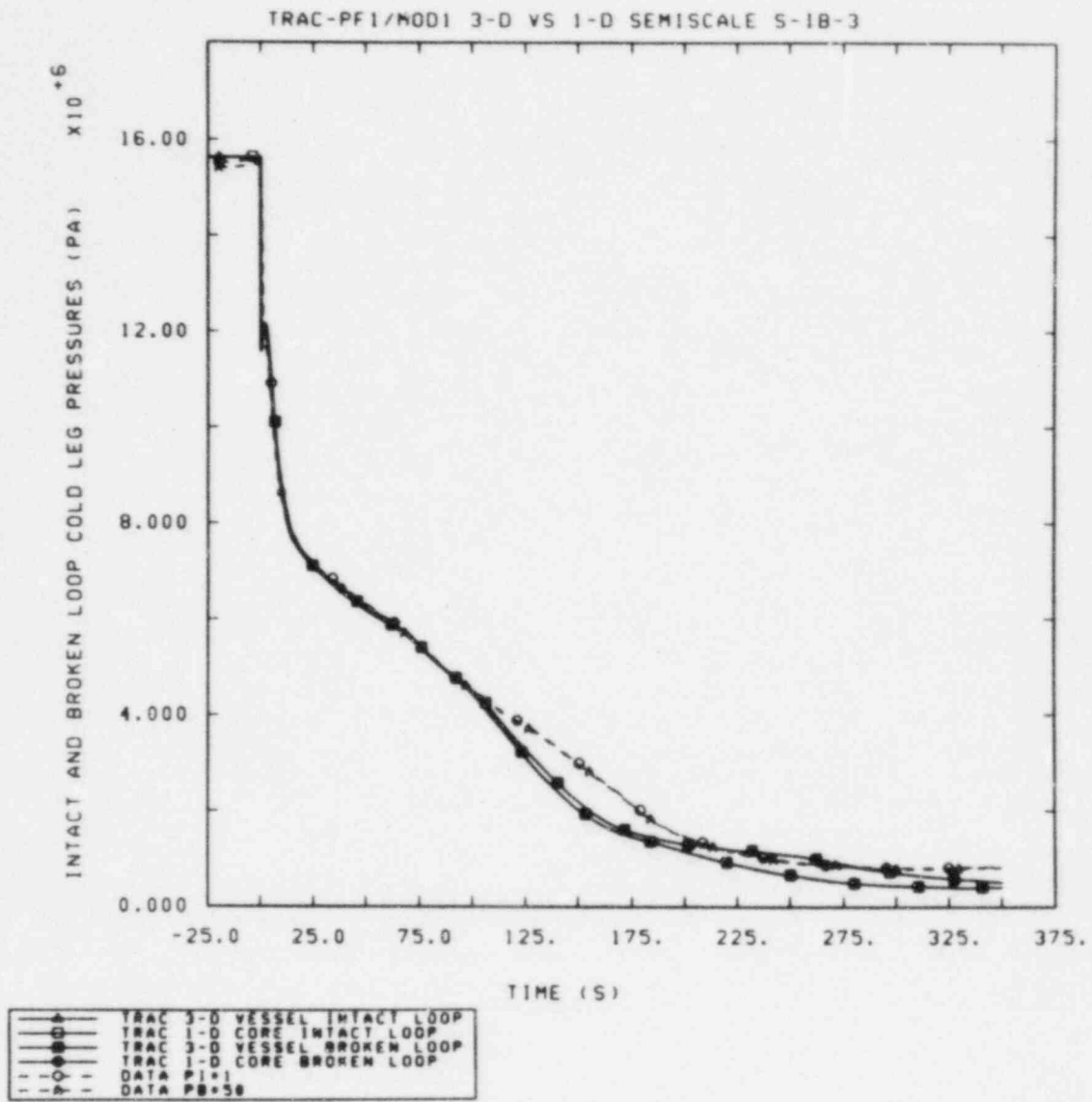


Figure 4.1.1 Intact and Broken Loop Cold Leg Pressures with 3-D and 1-D Models

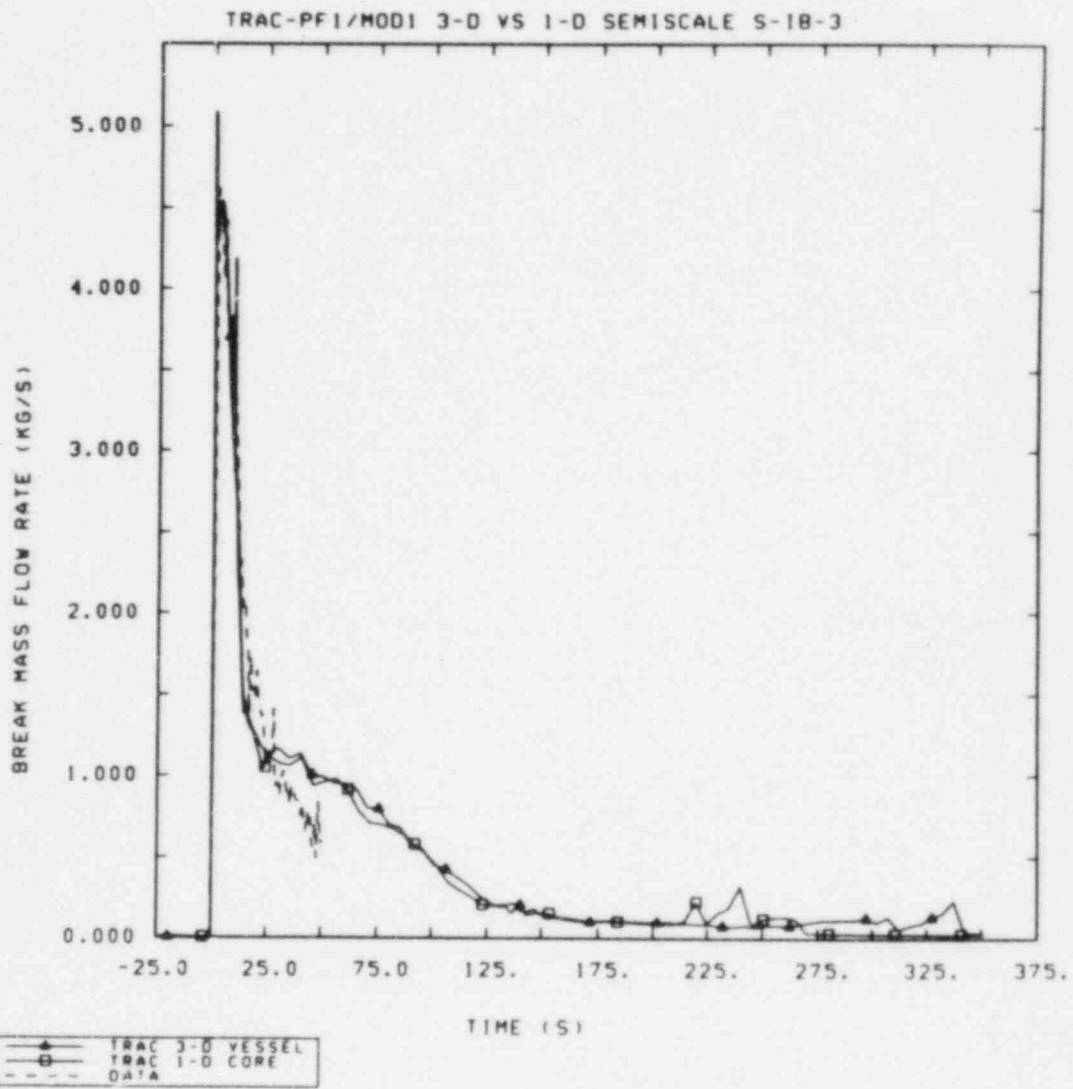


Figure 4.1.2 Break Flow Rates with 3-D and 1-D Models

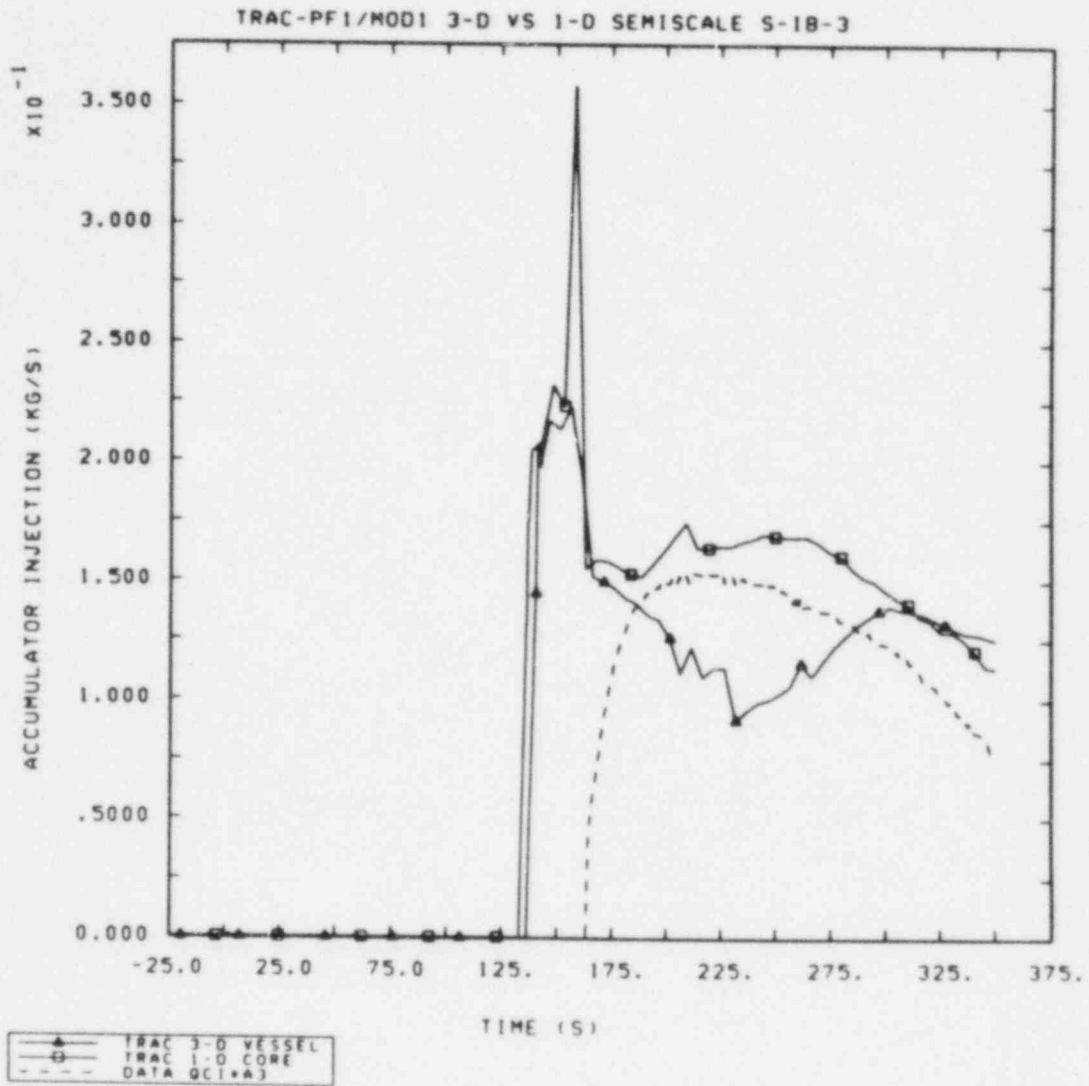


Figure 4.1.3 Accumulator Injection Flow Rate with 3-D and 1-D Models

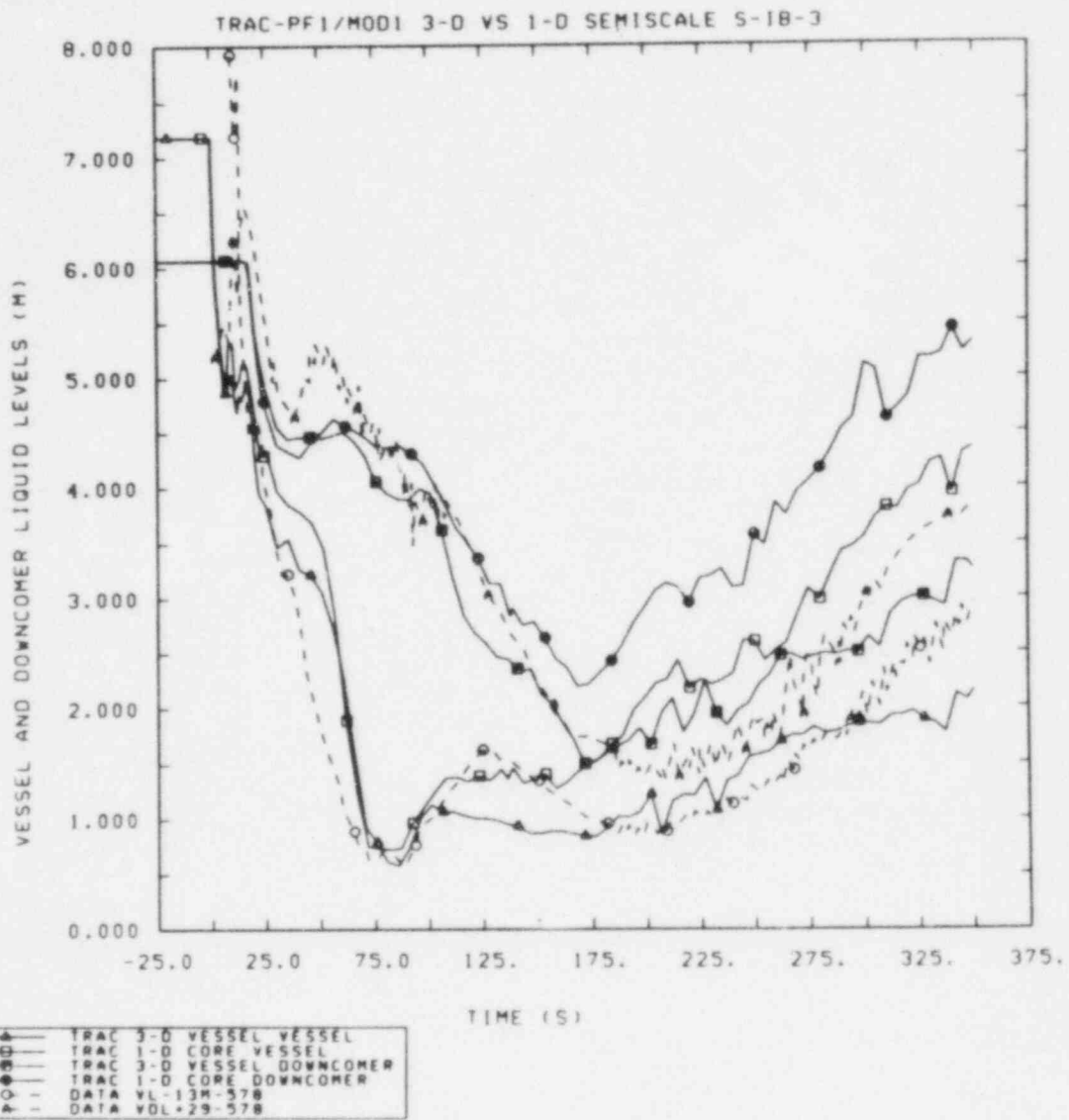


Figure 4.1.4 Vessel and Downcomer Liquid Levels with 3-D and 1-D Models

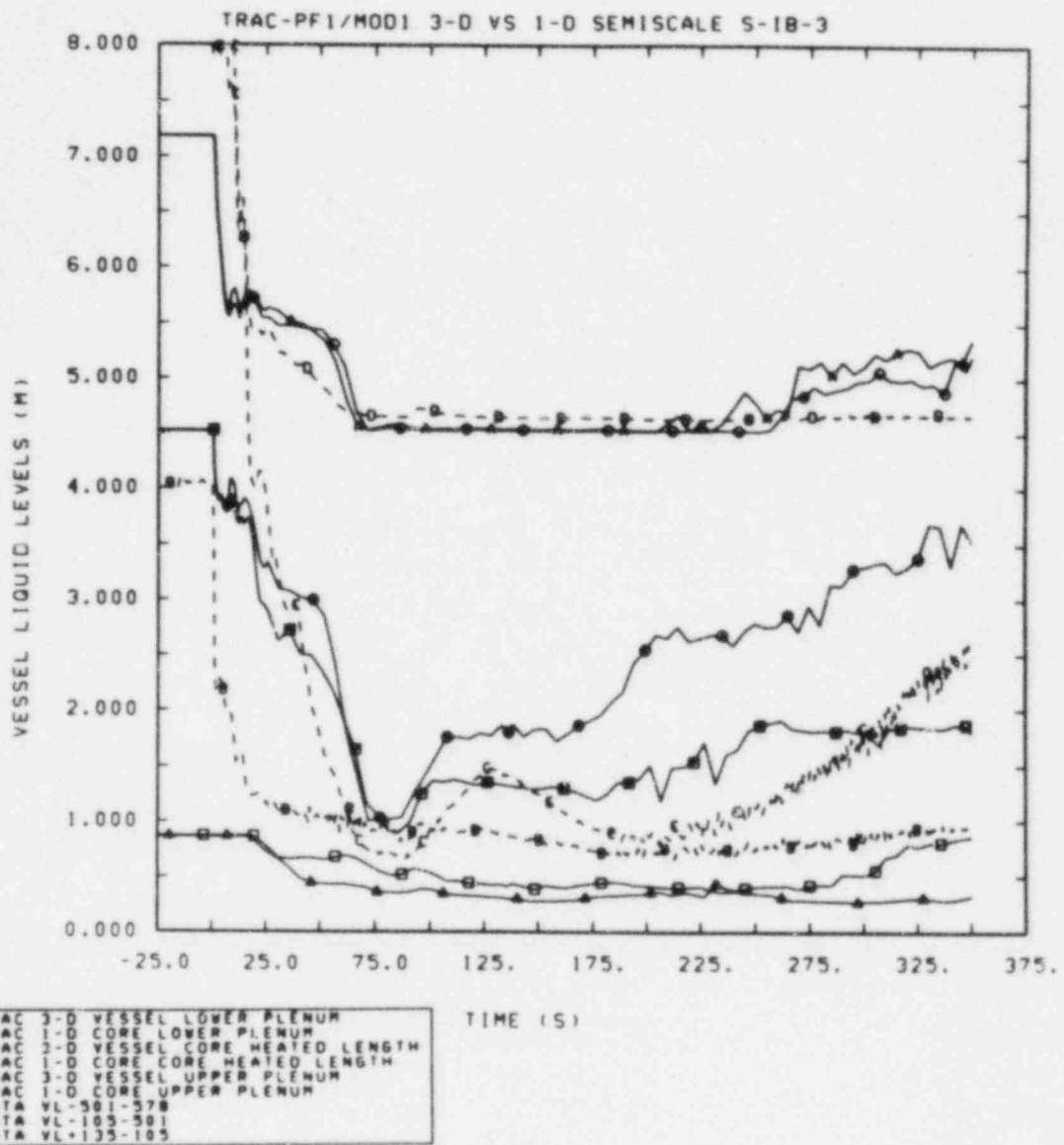


Figure 4.1.5 Lower Plenum, Heated Length and Upper Plenum Liquid Levels with 3-D and 1-D Models

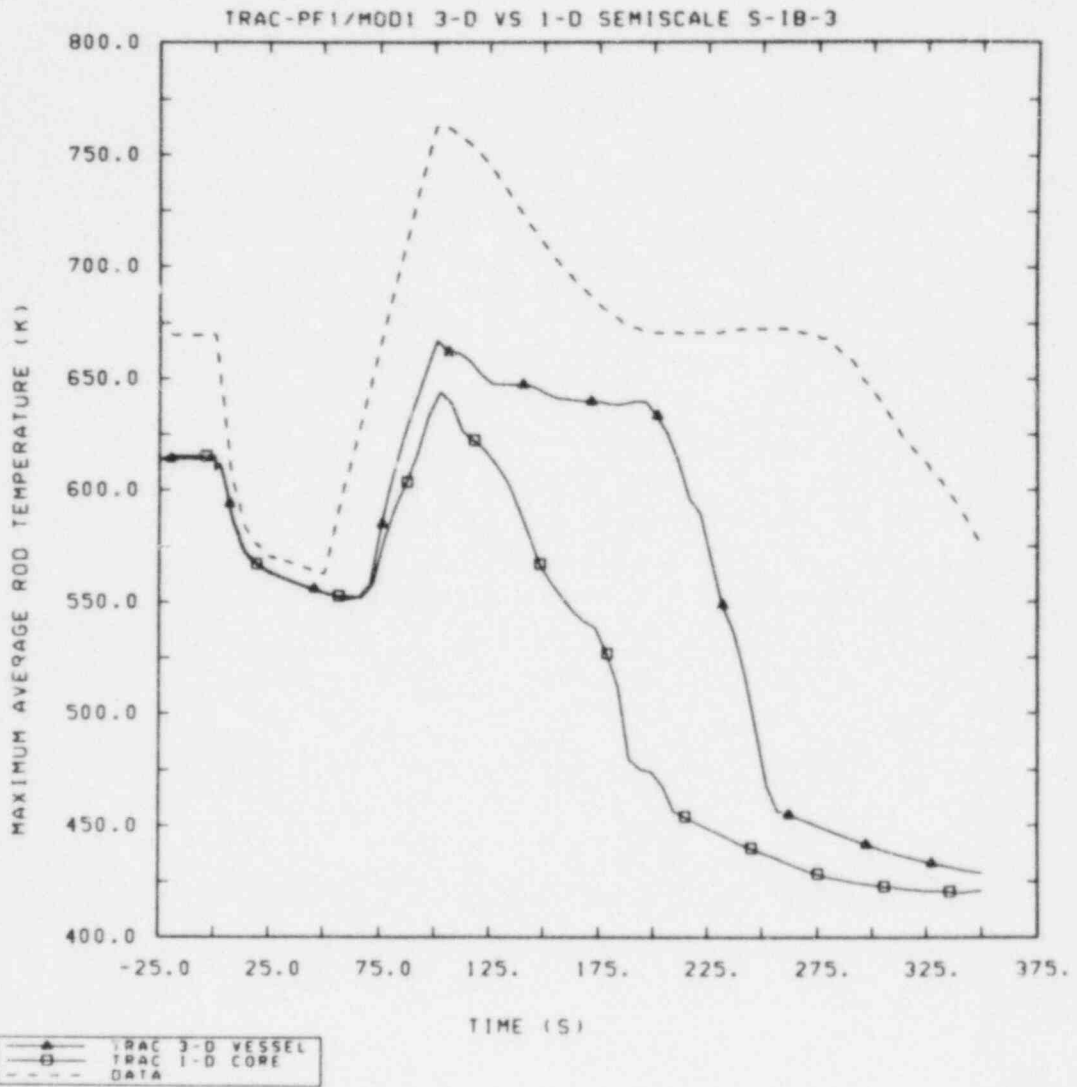


Figure 4.1.6 Maximum Rod Clad Temperatures with 3-D and 1-D Models

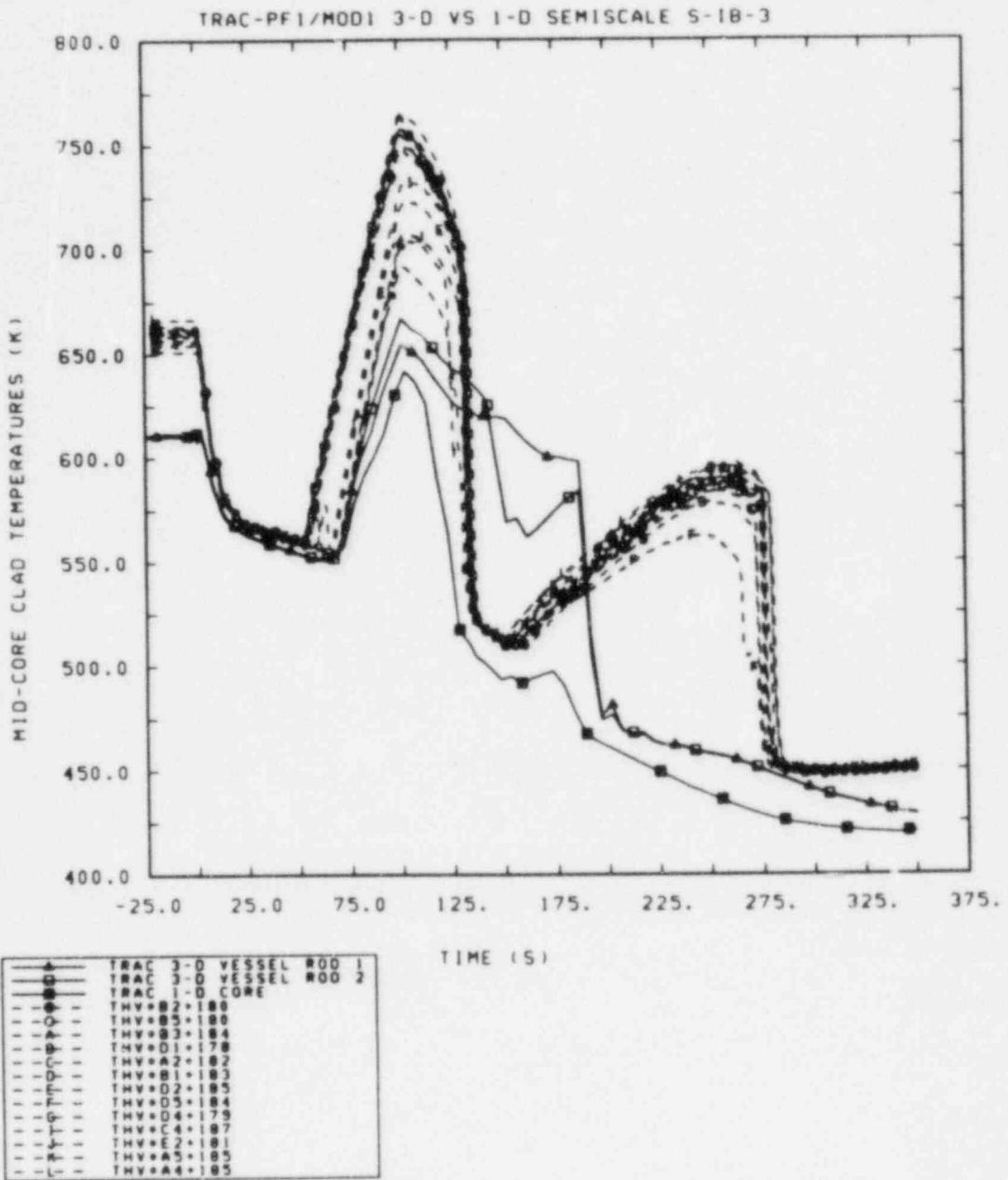


Figure 4.1.7 Middle Core Heater Rod Temperatures (1.83 m Core Elevation) with 3-D and 1-D Models

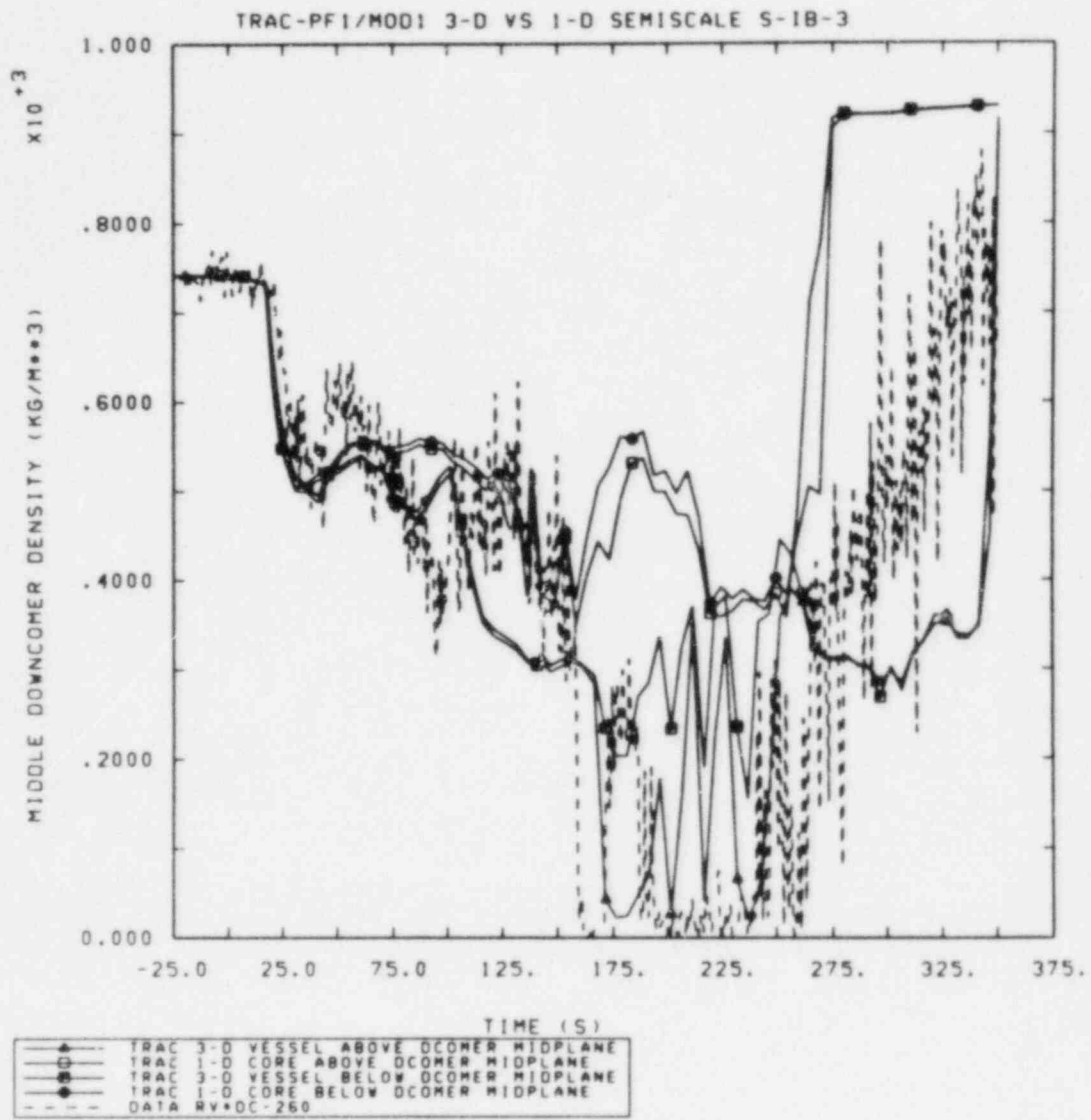


Figure 4.2.1 Mid-Downcomer Densities with 3-D and 1-D Models

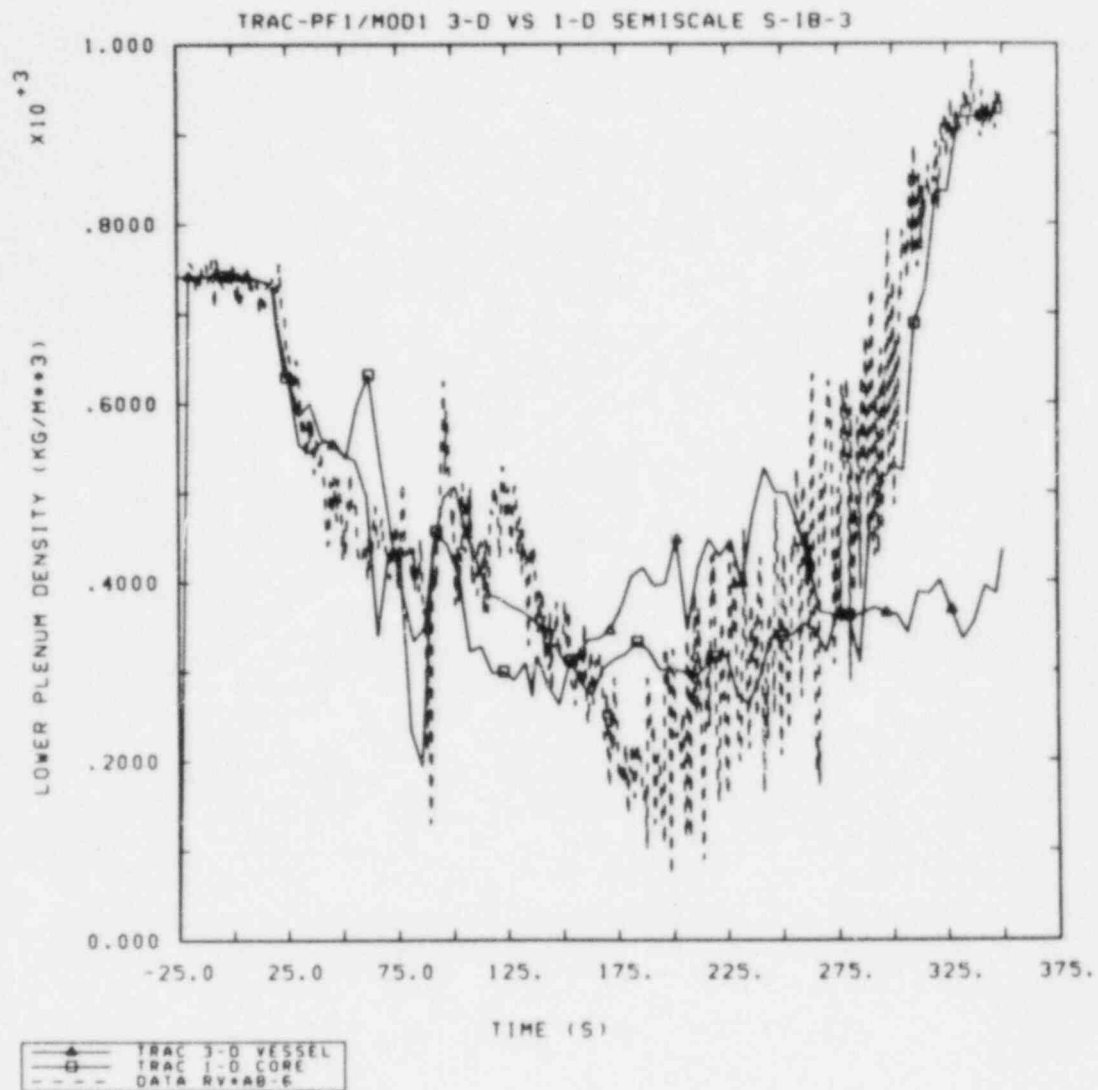


Figure 4.2.2 Lower Plenum Densities with 3-D and 1-D Models

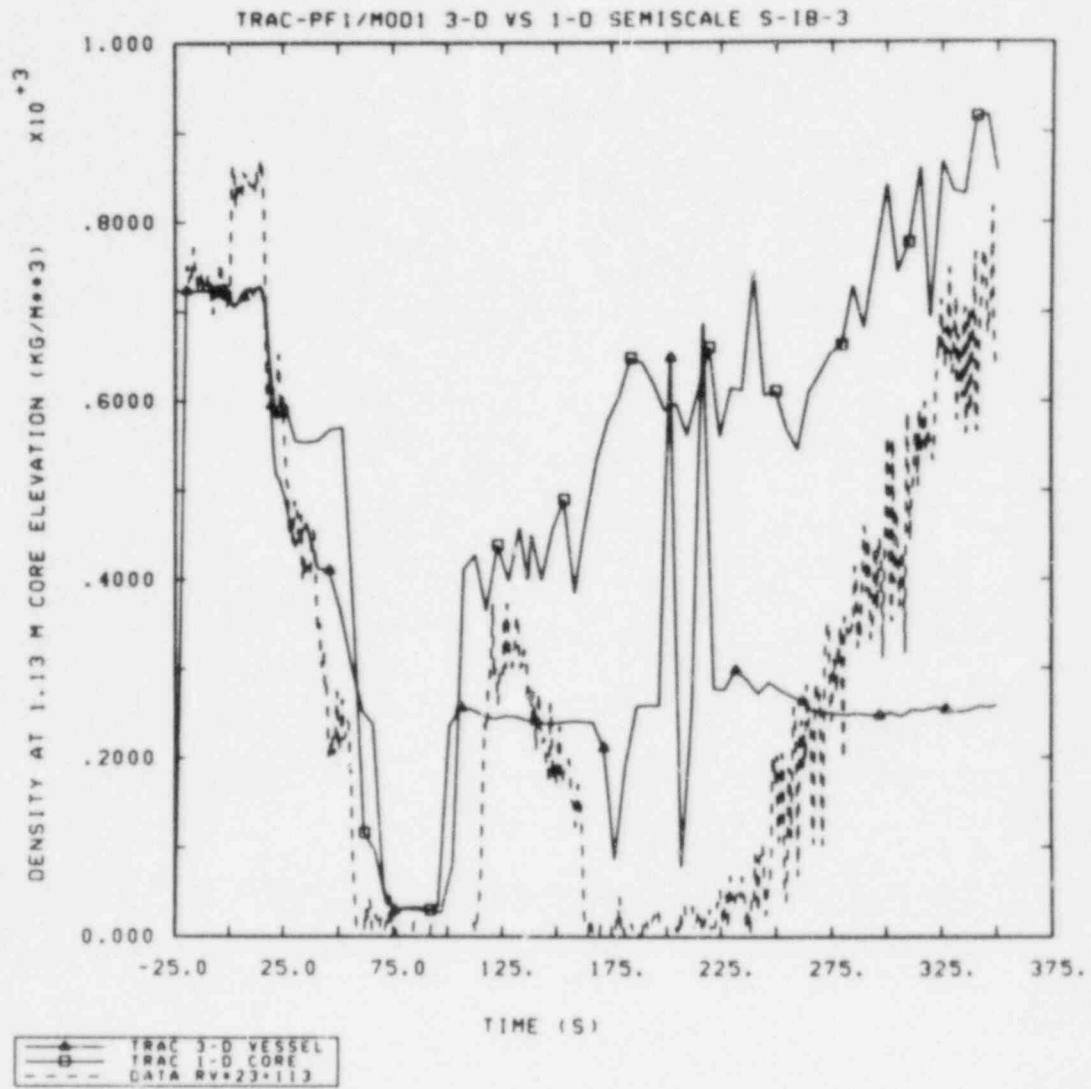


Figure 4.2.3 Lower Core Densities (1.13 m Core Elevation) with 3-D and 1-D Models

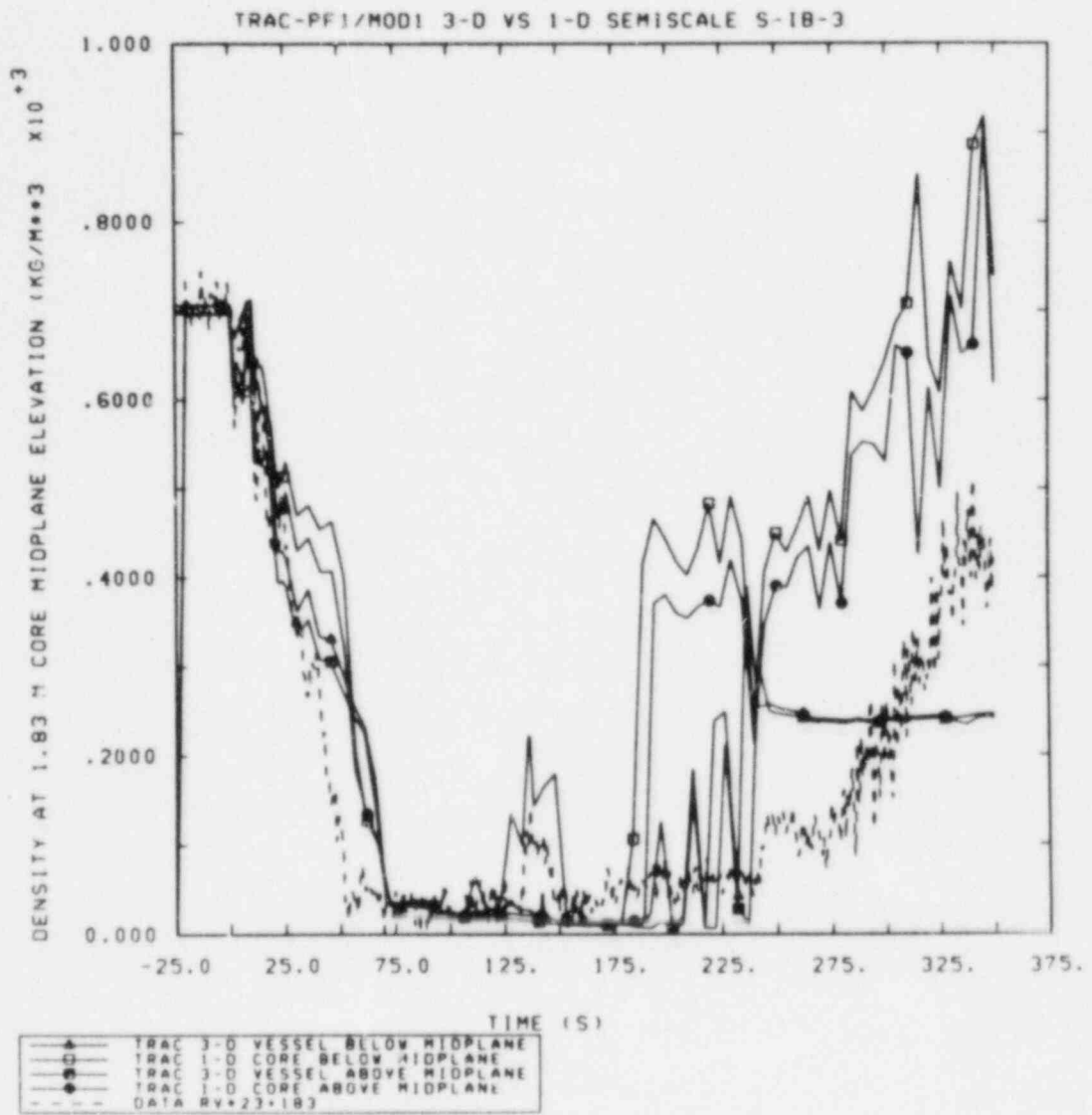


Figure 4.2.4 Middle Core Densities (1.83 m Core Elevation) with 3-D and 1-D Models

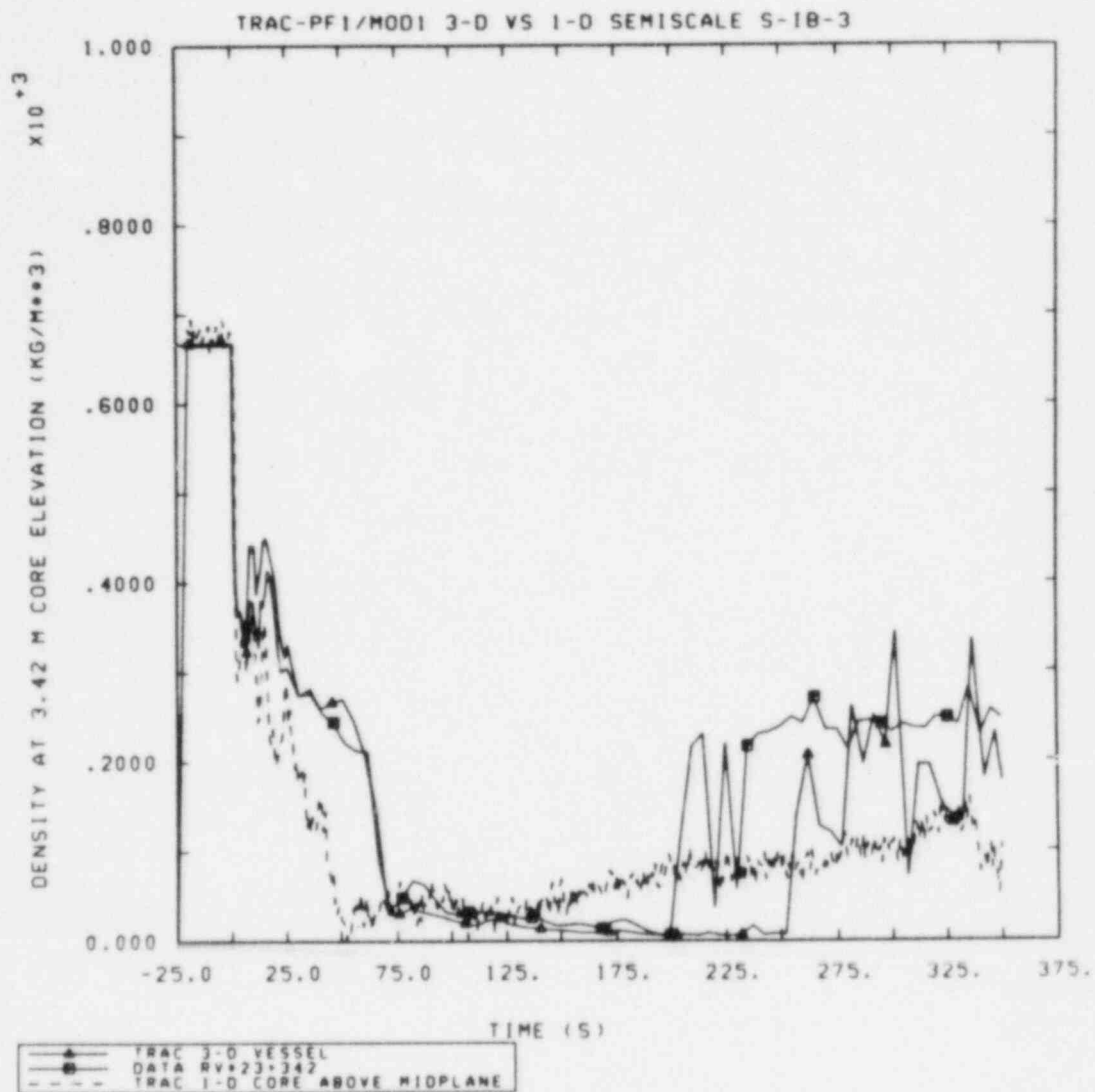


Figure 4.2.5 Upper Core Densities (3.42 m Core Elevation) with 3-D and 1-D Models

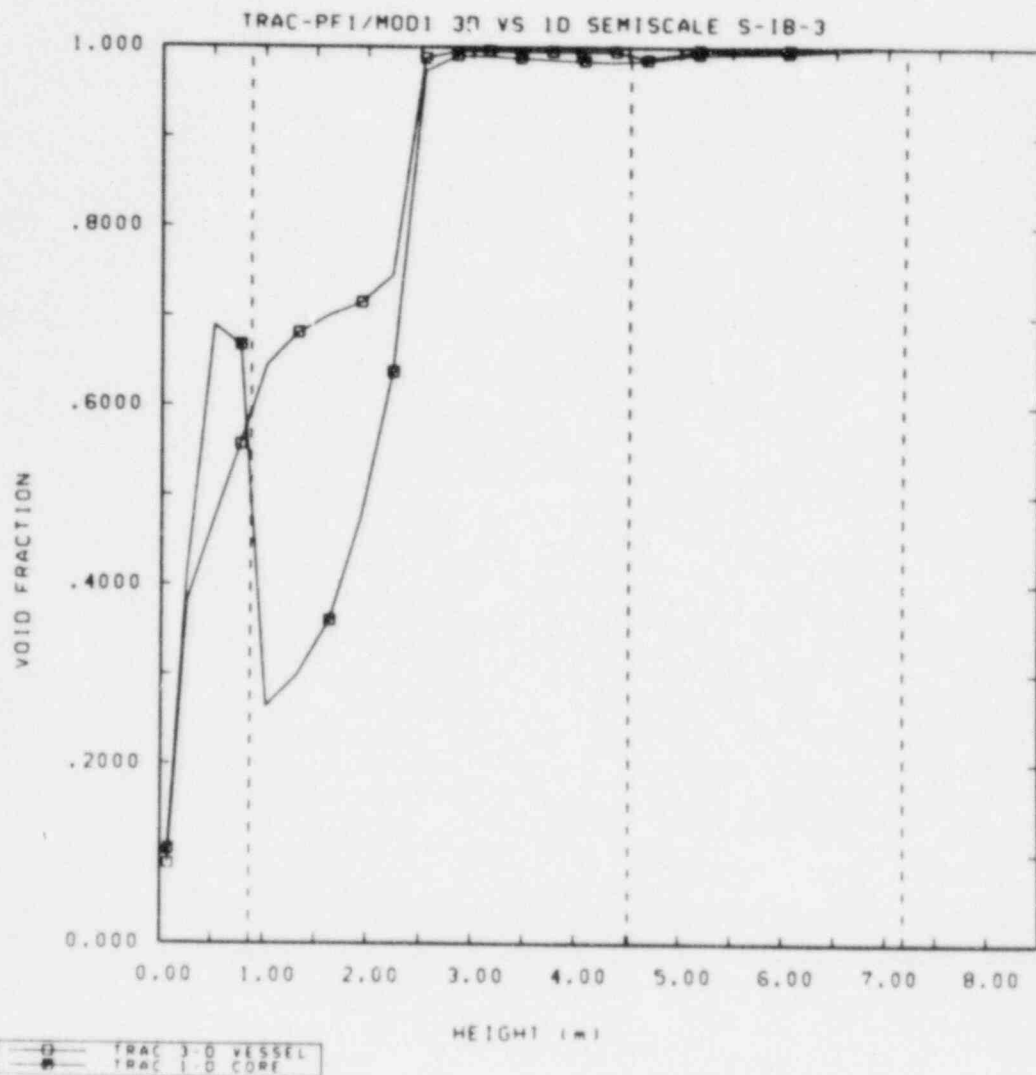


Figure 4.2.6 Vessel Void Fraction Profiles with 3-D and 1-D Models

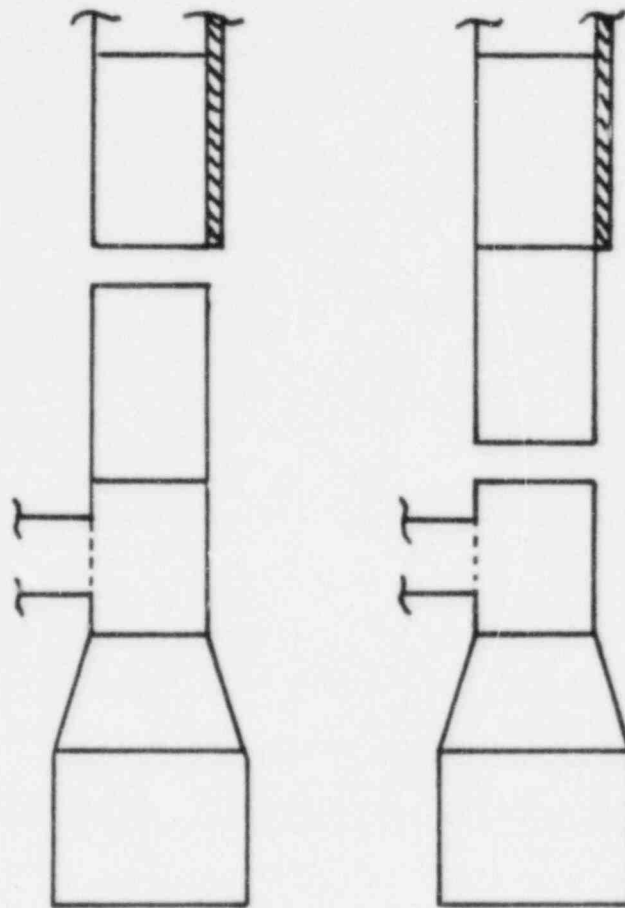


Figure 4.2.7 Lower Plenum/Core Nodalizations in (Basecase) 1-D and Modified 1-D Models

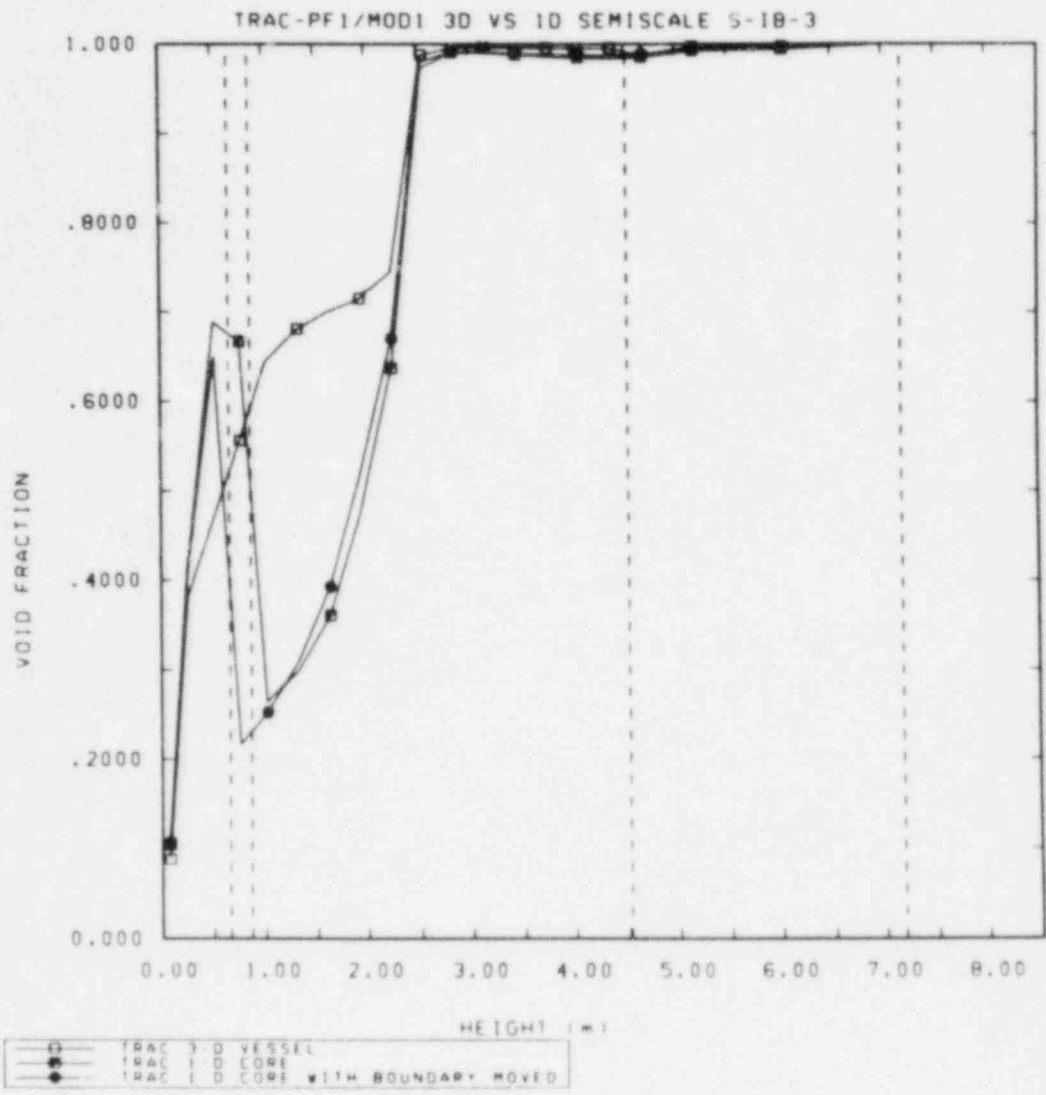


Figure 4.2.8 Vessel Void Fraction Profiles with 3-D, (Basecase) 1-D and Modified 1-D Models

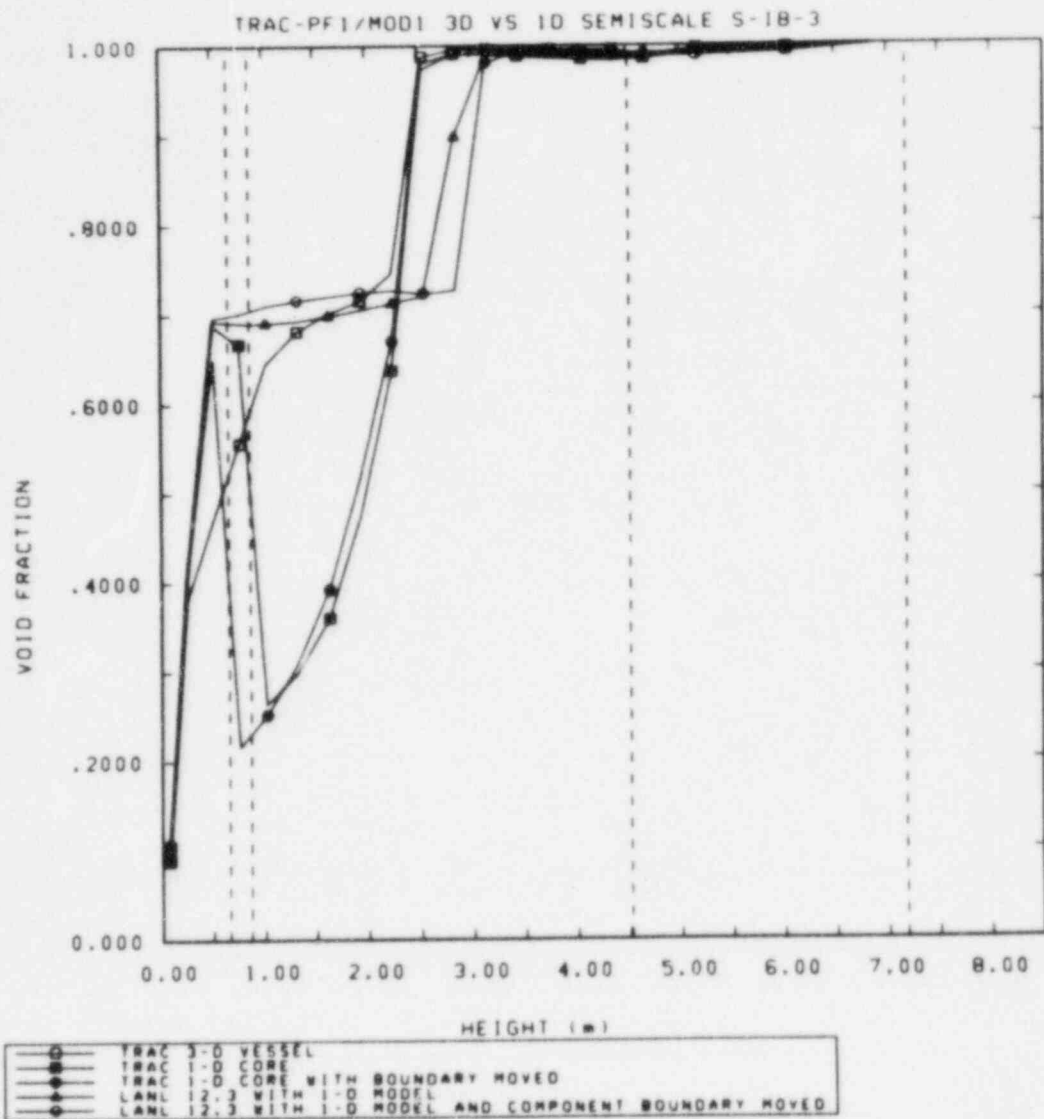


Figure 4.2.9 Vessel Void Fraction Profiles with our 3-D Model, and both our and LANL's (Basecase) 1-D and Modified 1-D Model Calculations

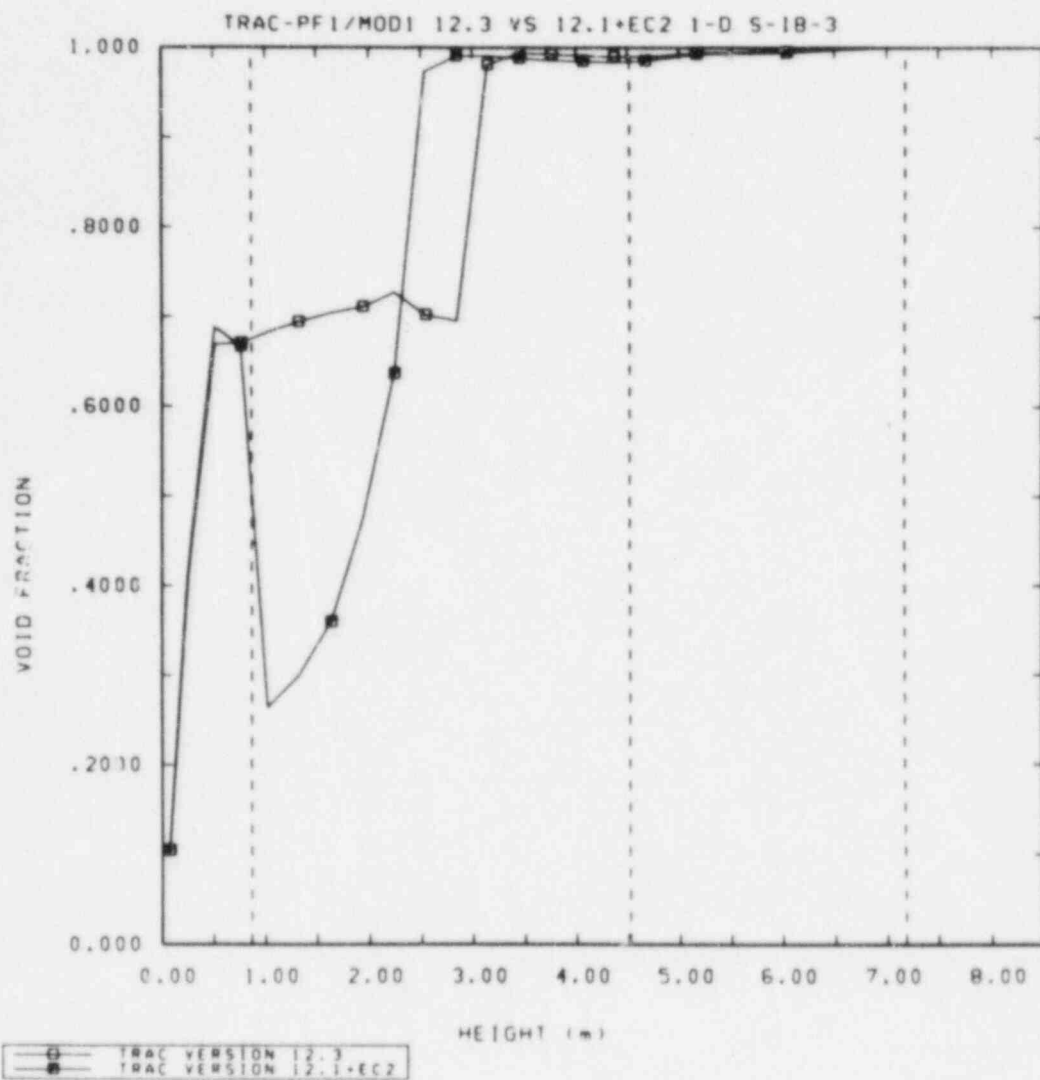


Figure 4.3.1 Vessel Void Fraction Profiles with (Basecase) 1-D Model using Different Inverted Annular Flow Logic

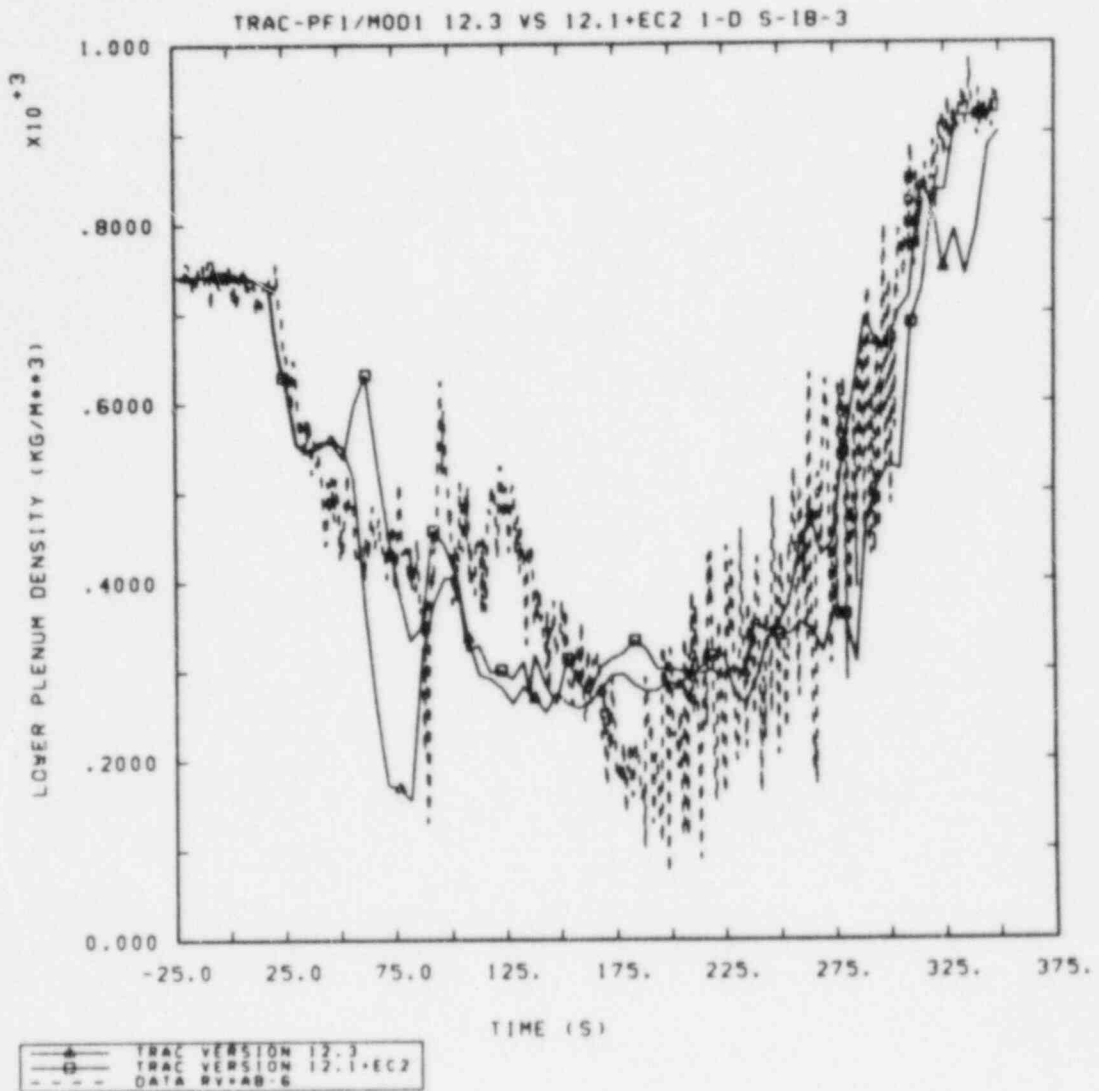


Figure 4.3.2 Lower Plenum Densities with (Basecase) I-D Model using Different Inverted Annular Flow Logic

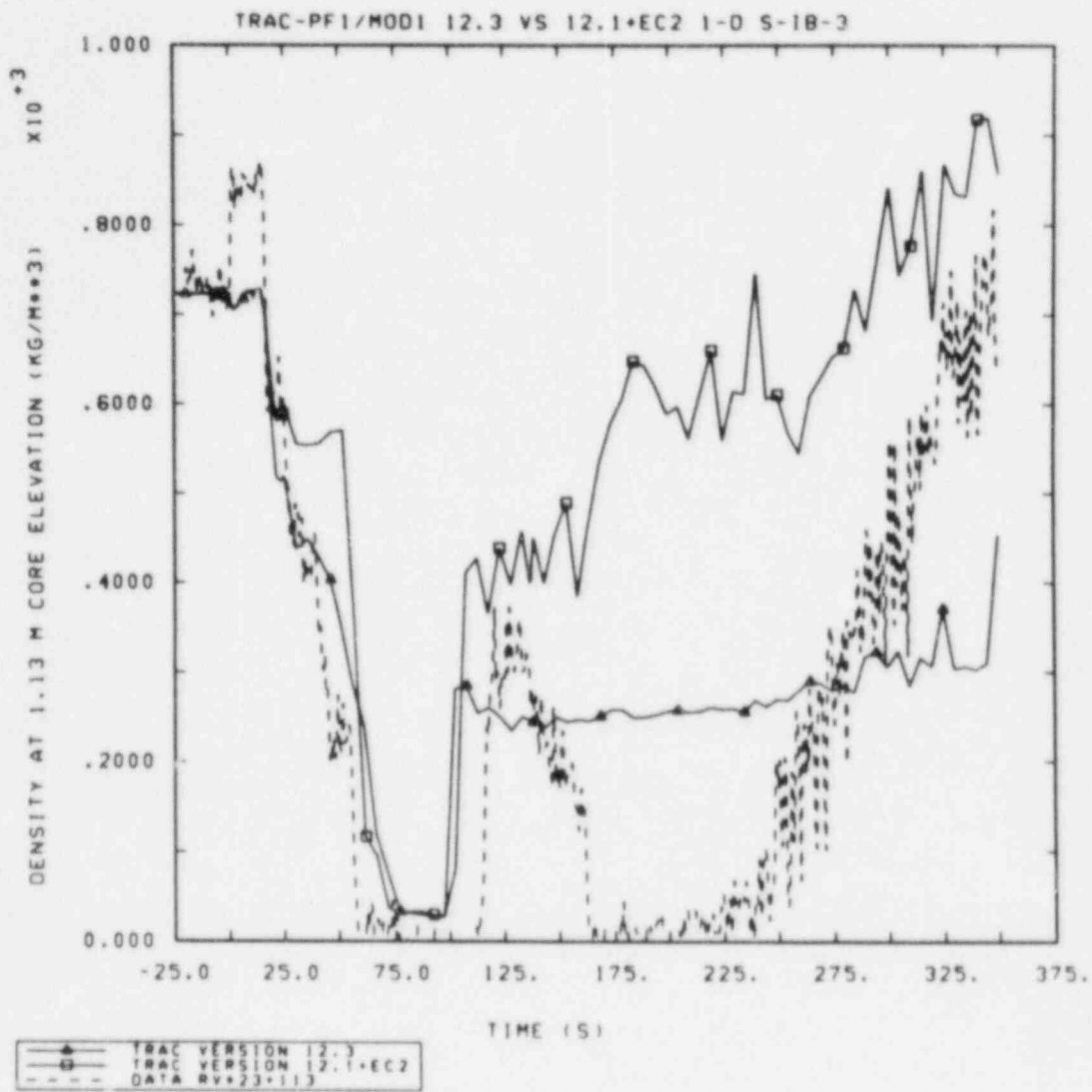


Figure 4.3.3 Lower Core Densities (1.13 m Core Elevation) with (Basecase) 1-D Model using Different Inverted Annular Flow Logic

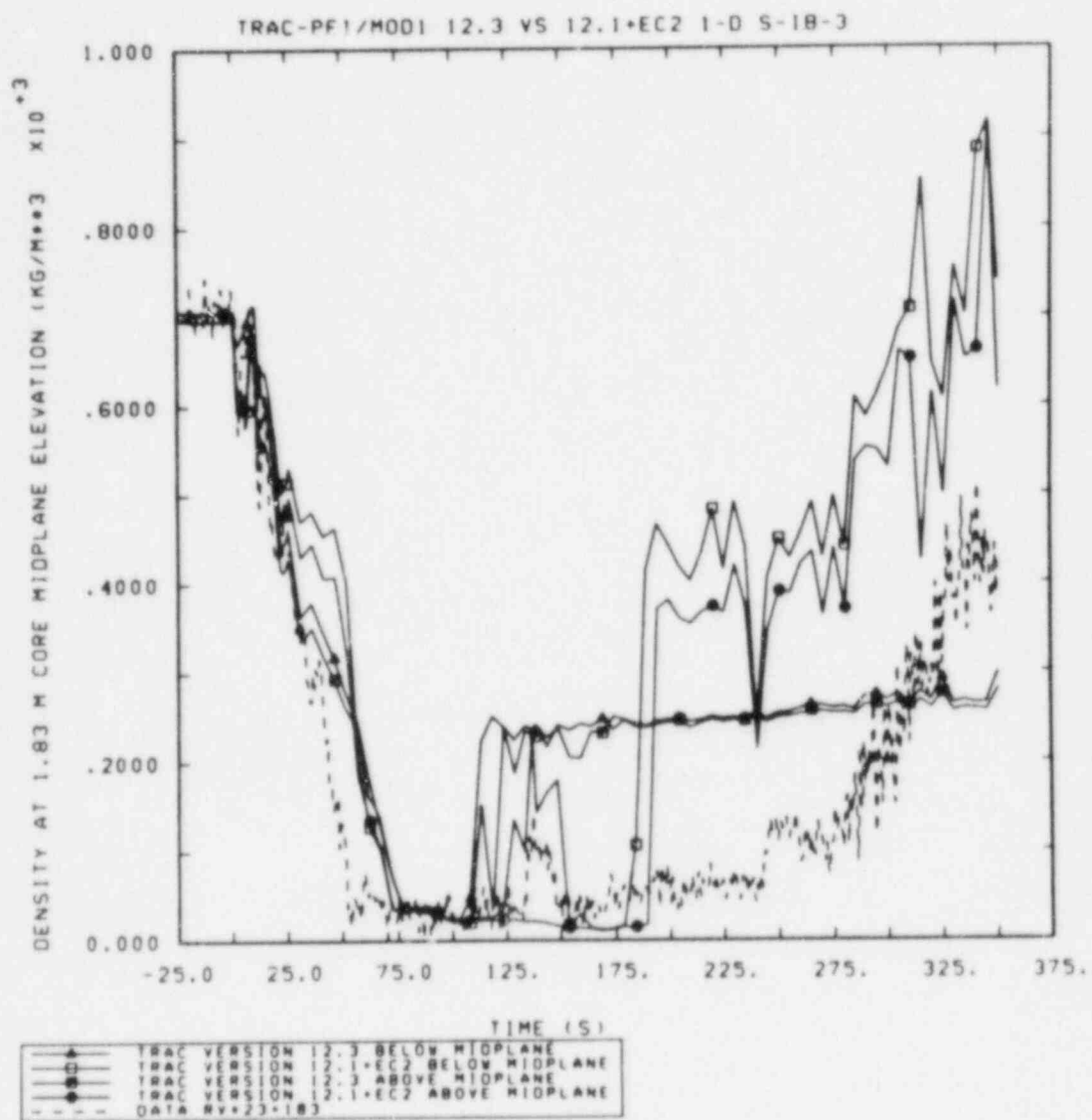


Figure 4.3.4 Middle Core Densities (1.83 m Core Elevation) with (Basecase) 1-D Model using Different Inverted Annular Flow Logic

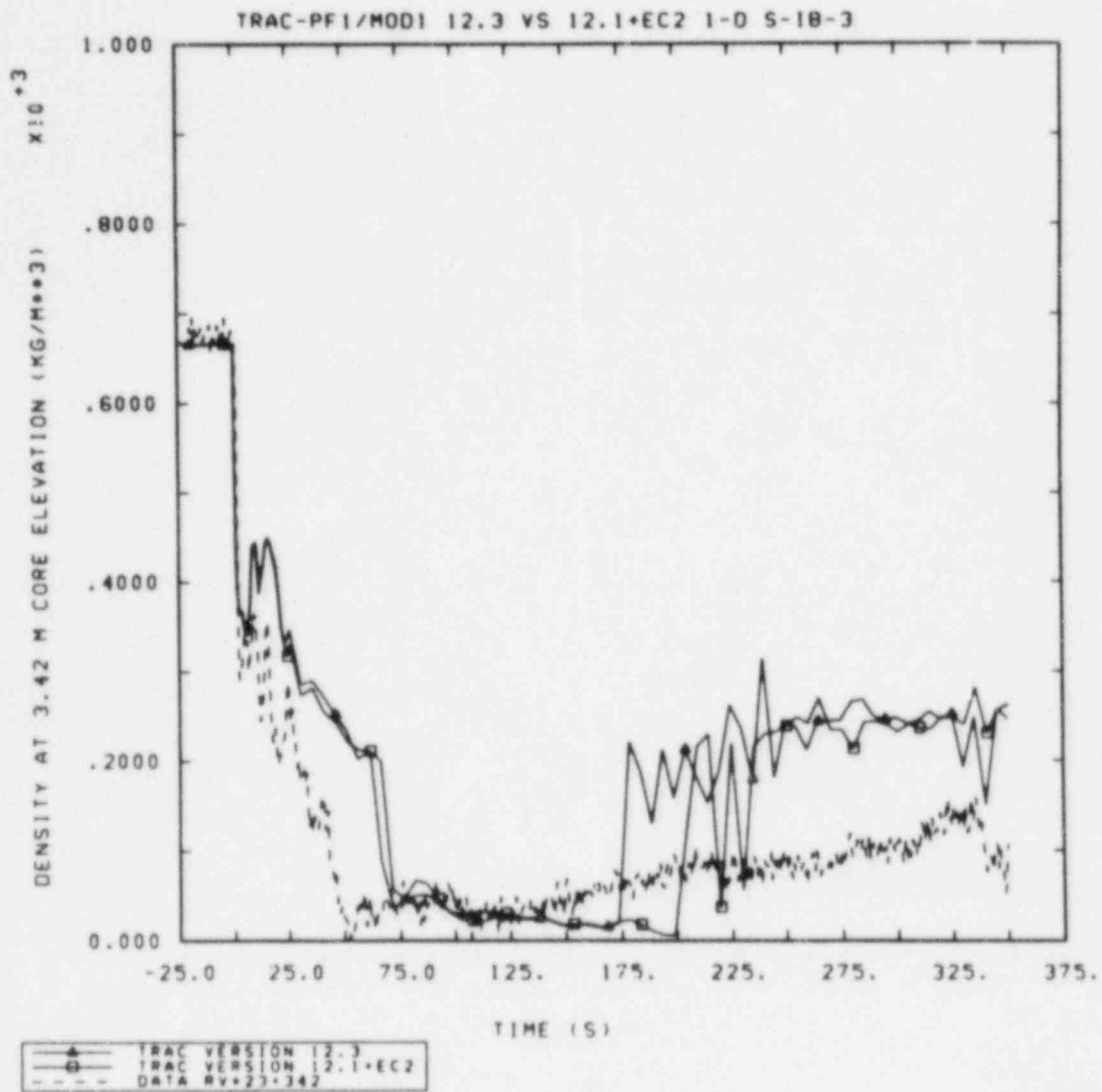


Figure 4.3.5 Upper Core Densities (3.42 m Core Elevation) with (Basecase) 1-D Model using Different Inverted Annular Flow Logic

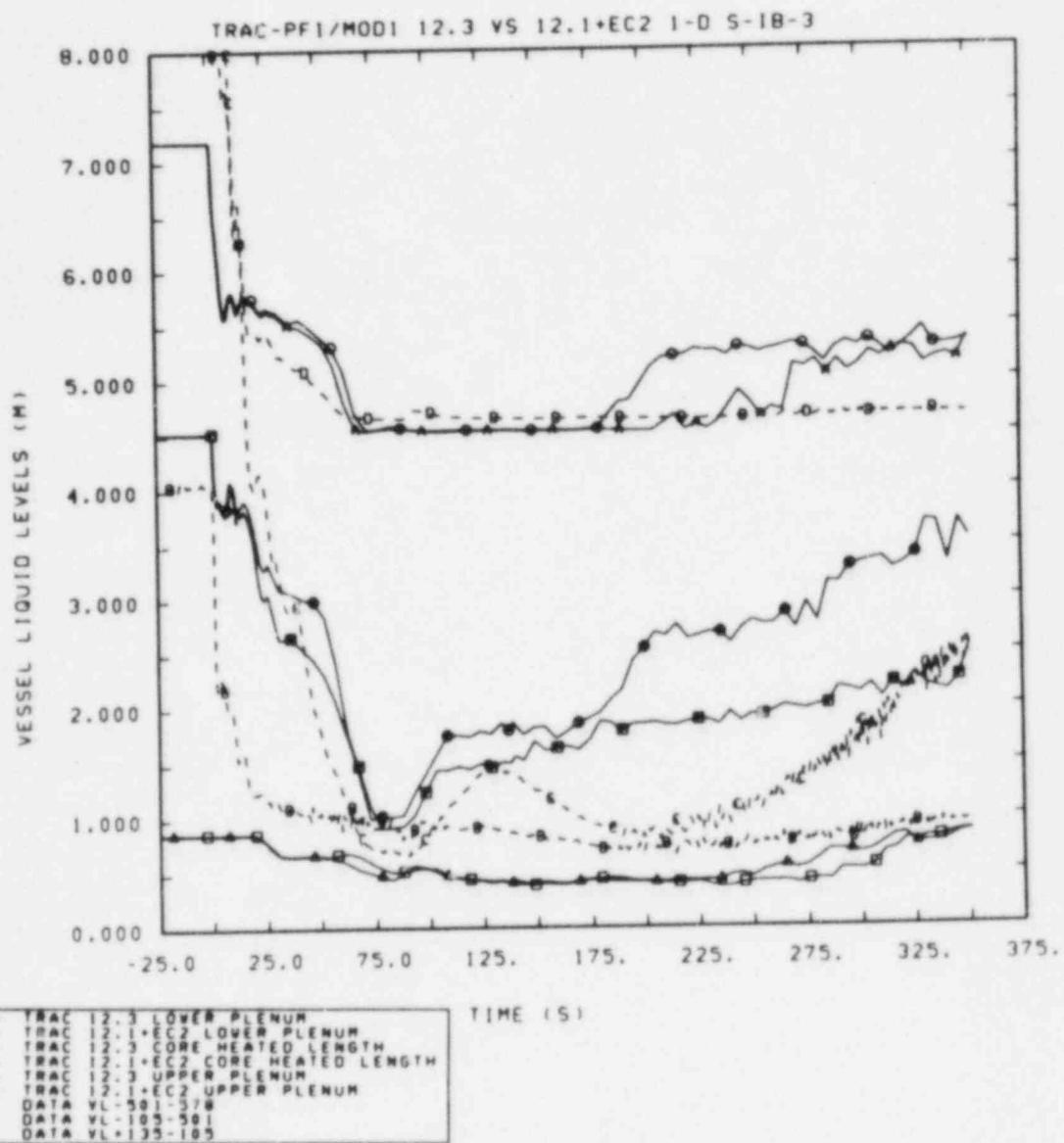


Figure 4.3.6 Lower Plenum, Heated Length and Upper Plenum Liquid Levels with (Basecase) 1-D Model using Different Inverted Annular Flow Logic

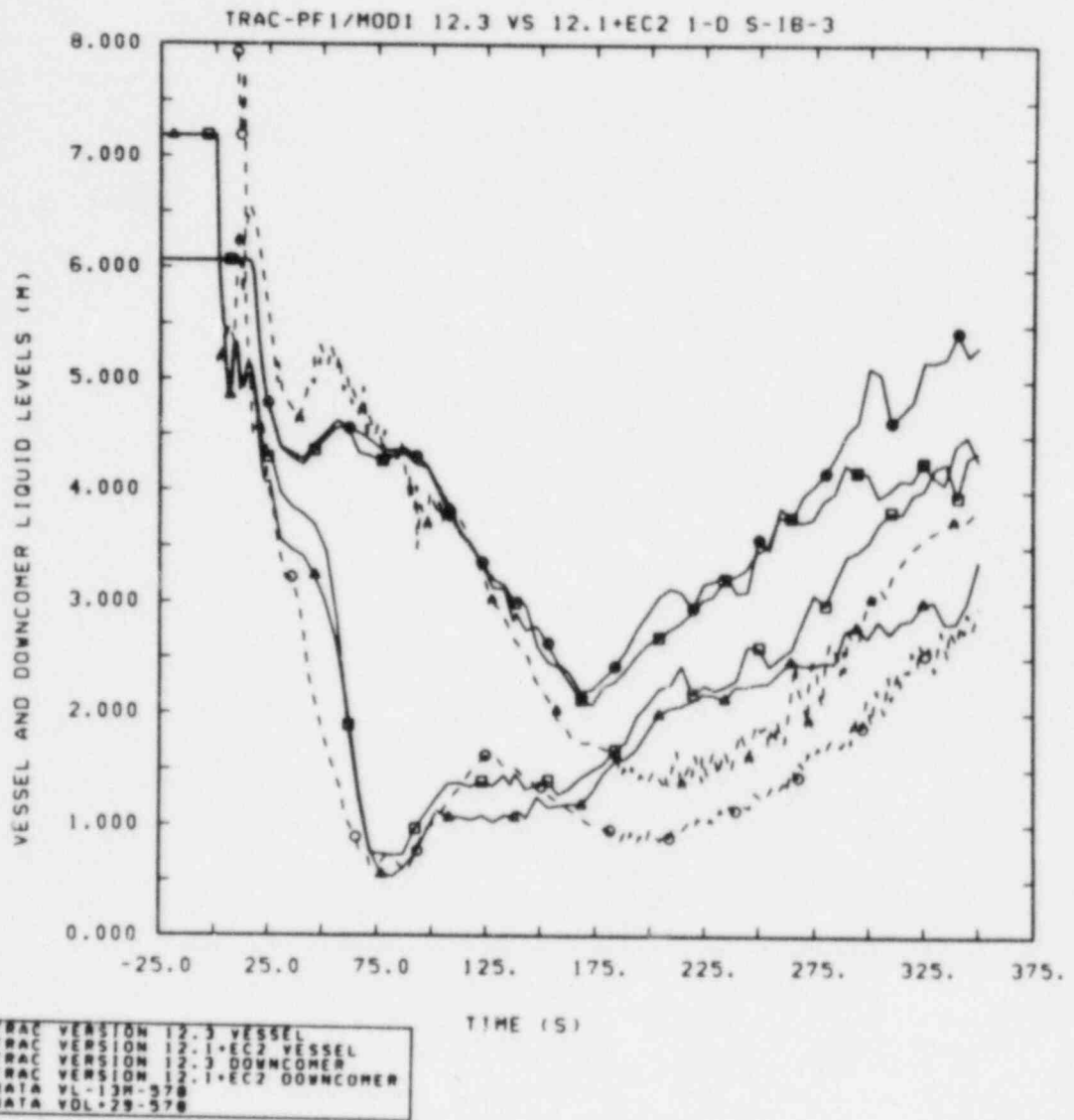


Figure 4.3.7 Vessel and Downcomer Liquid Levels with (Basecase) 1-D Model using Different Inverted Annular Flow Logic

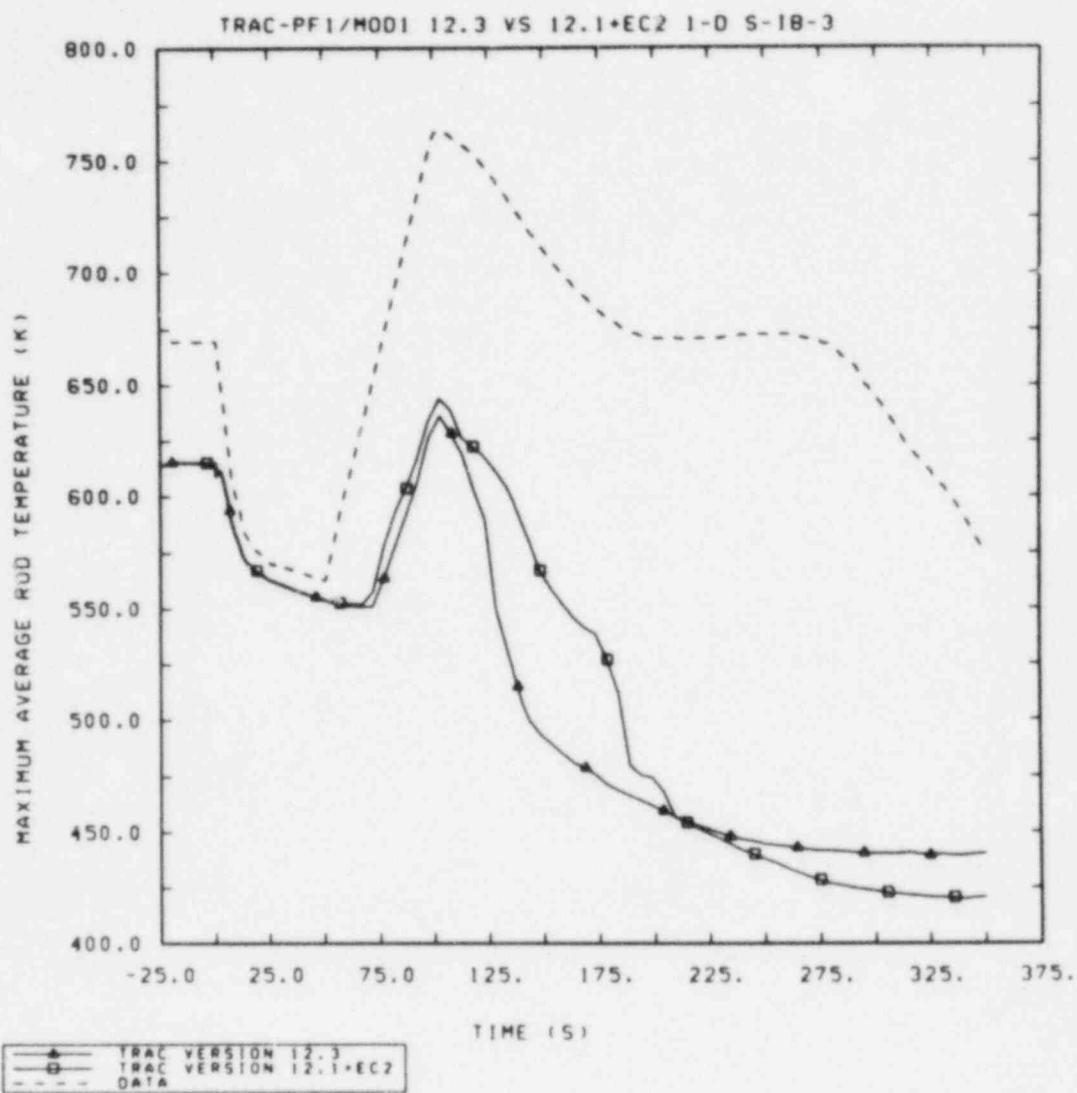


Figure 4.3.8 Maximum Rod Clad Temperatures with (Basecase) I-D Model using Different Inverted Annular Flow Logic

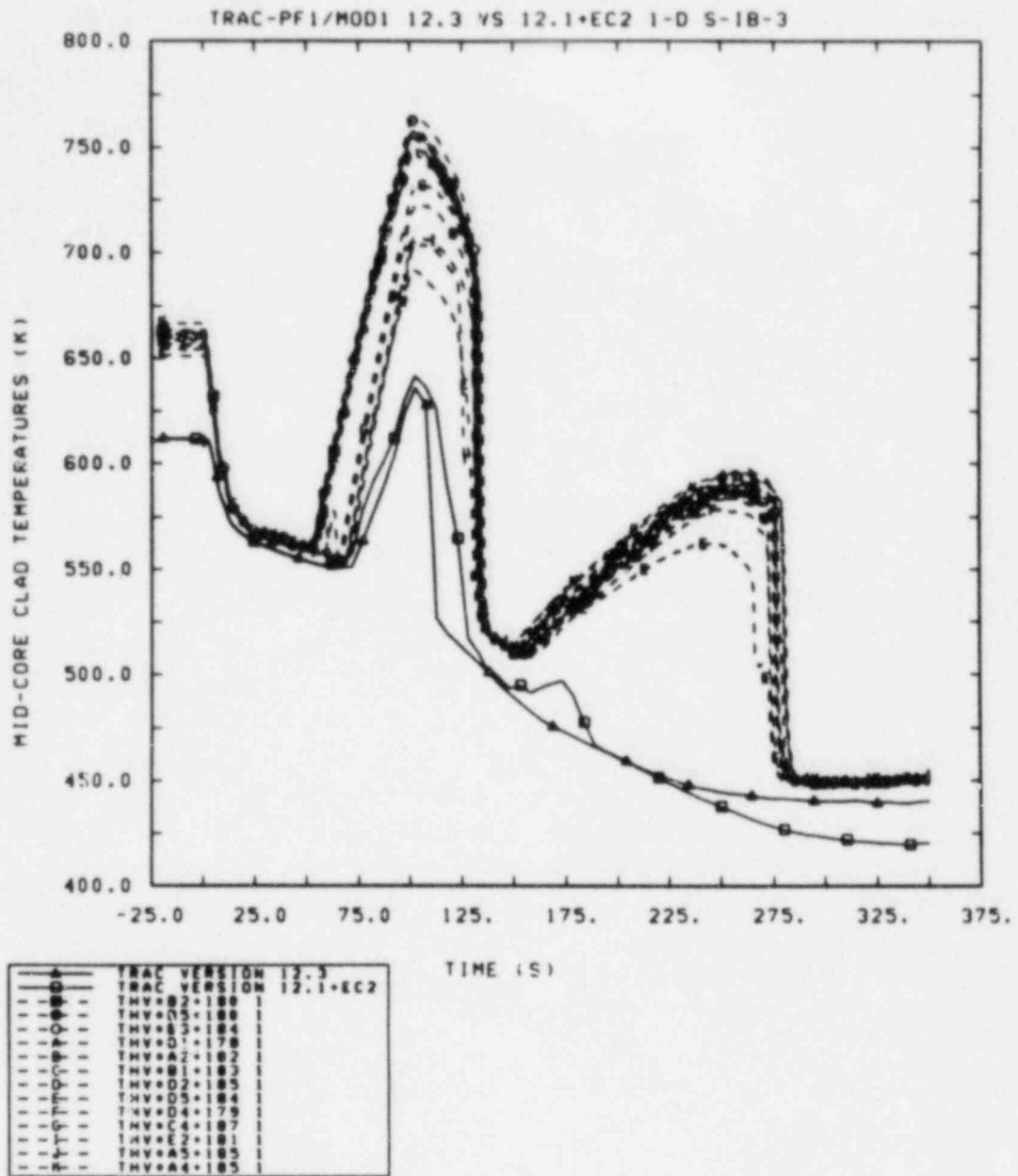


Figure 4.3.9 Middle Core Heater Rod Temperatures (1.83 m Core Elevation) with (Basecase) 1-D Model using Different Inverted Annular Flow Logic

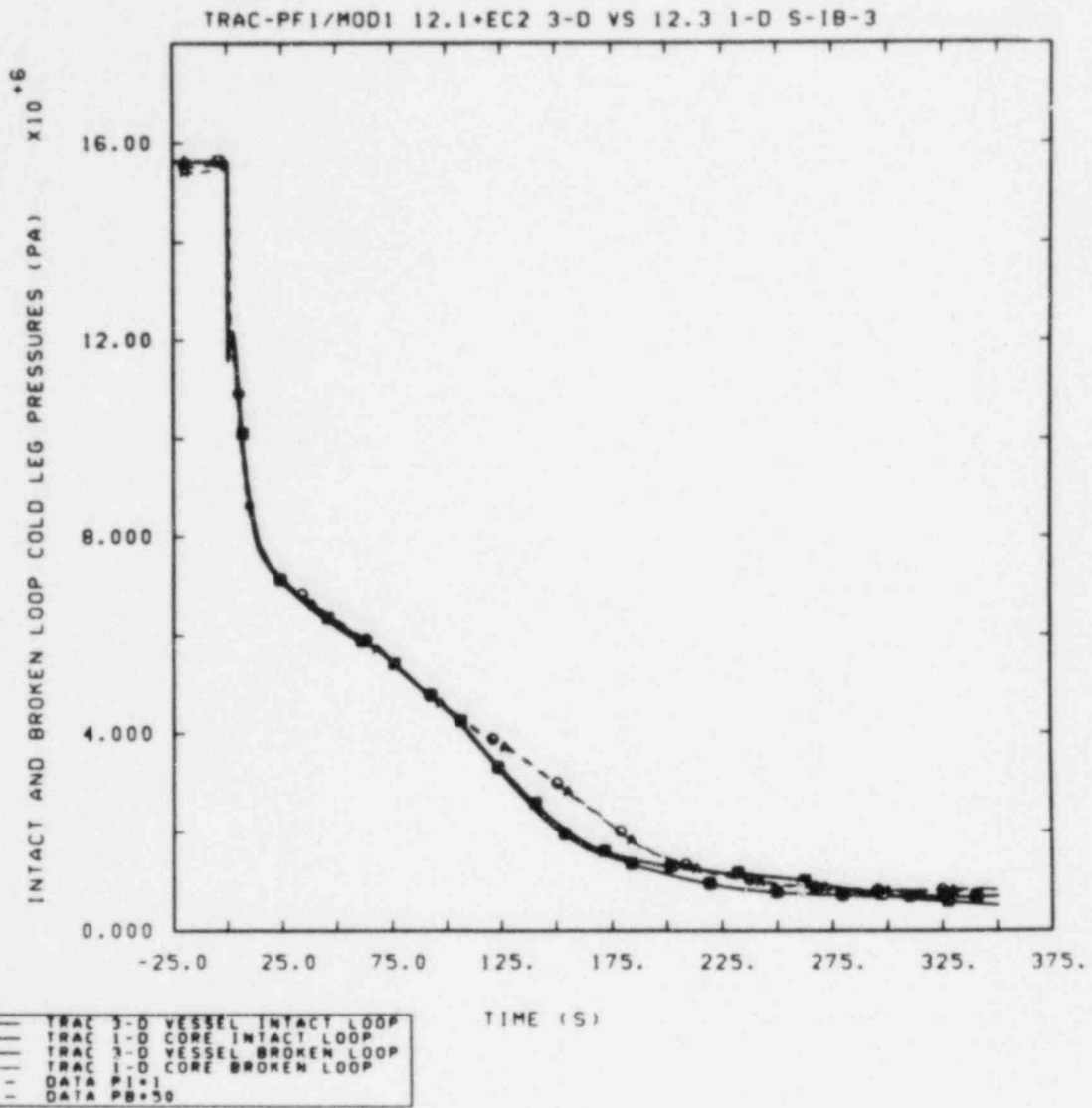


Figure 4.4.1 Intact and Broken Loop Cold Leg Pressures with 3-D and Final 1-D Models

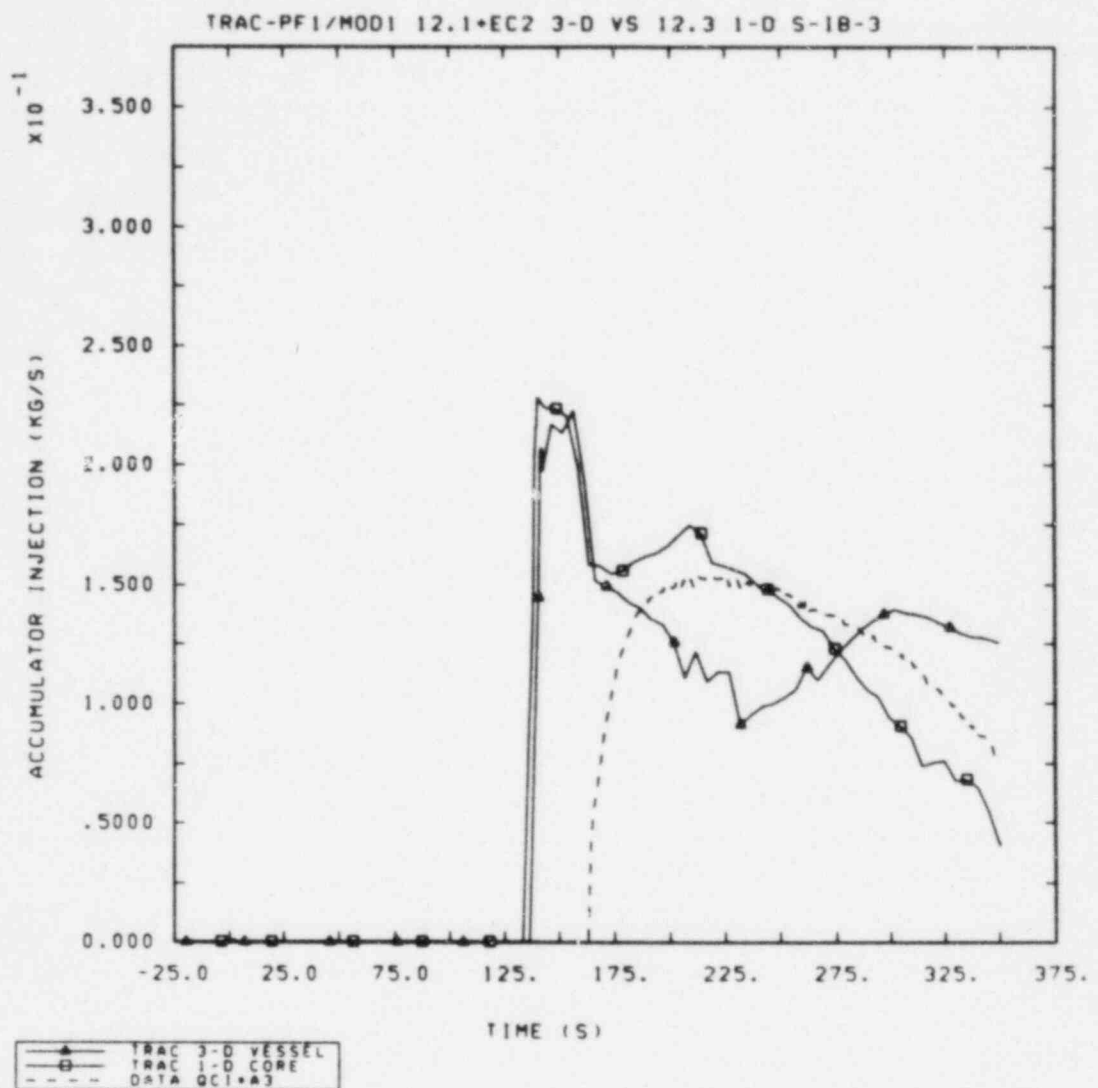


Figure 4.4.2 Accumulator Injection Flow Rate with 3-D and Final 1-D Models

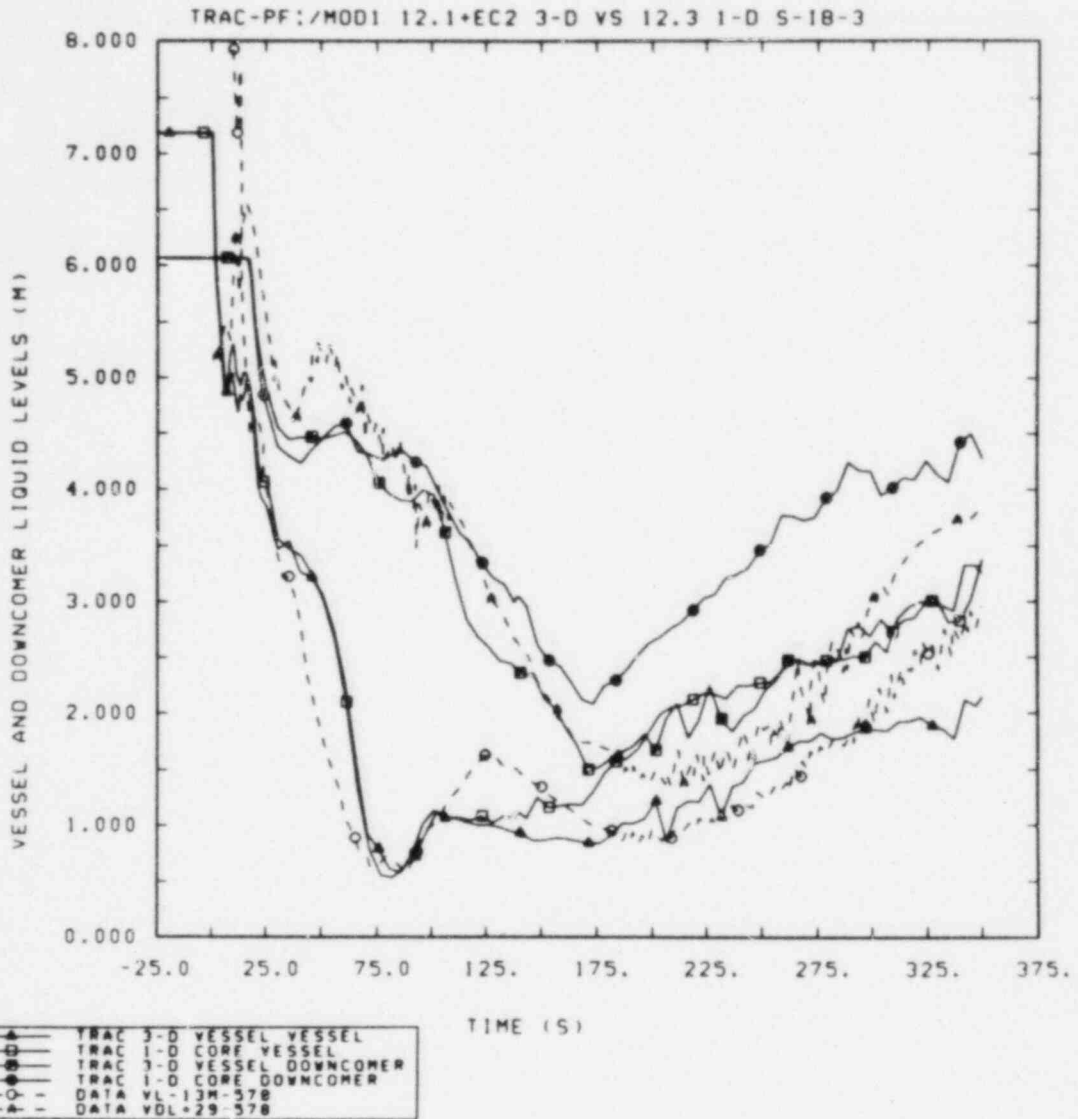


Figure 4.4.3 Vessel and Downcomer Liquid Levels with 3-D and Final 1-D Models

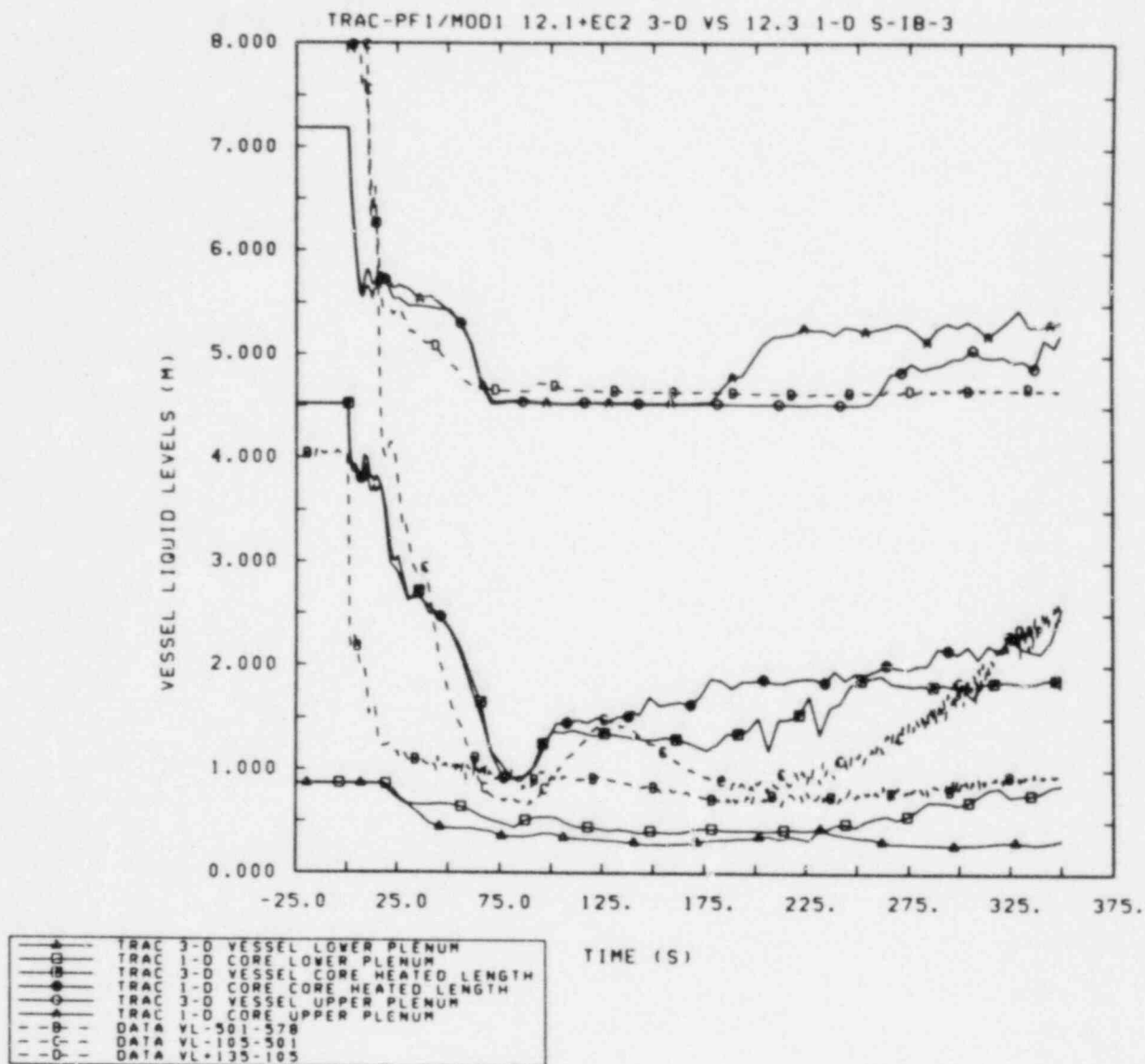


Figure 4.4.4 Lower Plenum, Heated Length and Upper Plenum Liquid Levels with 3-D and Final 1-D Models

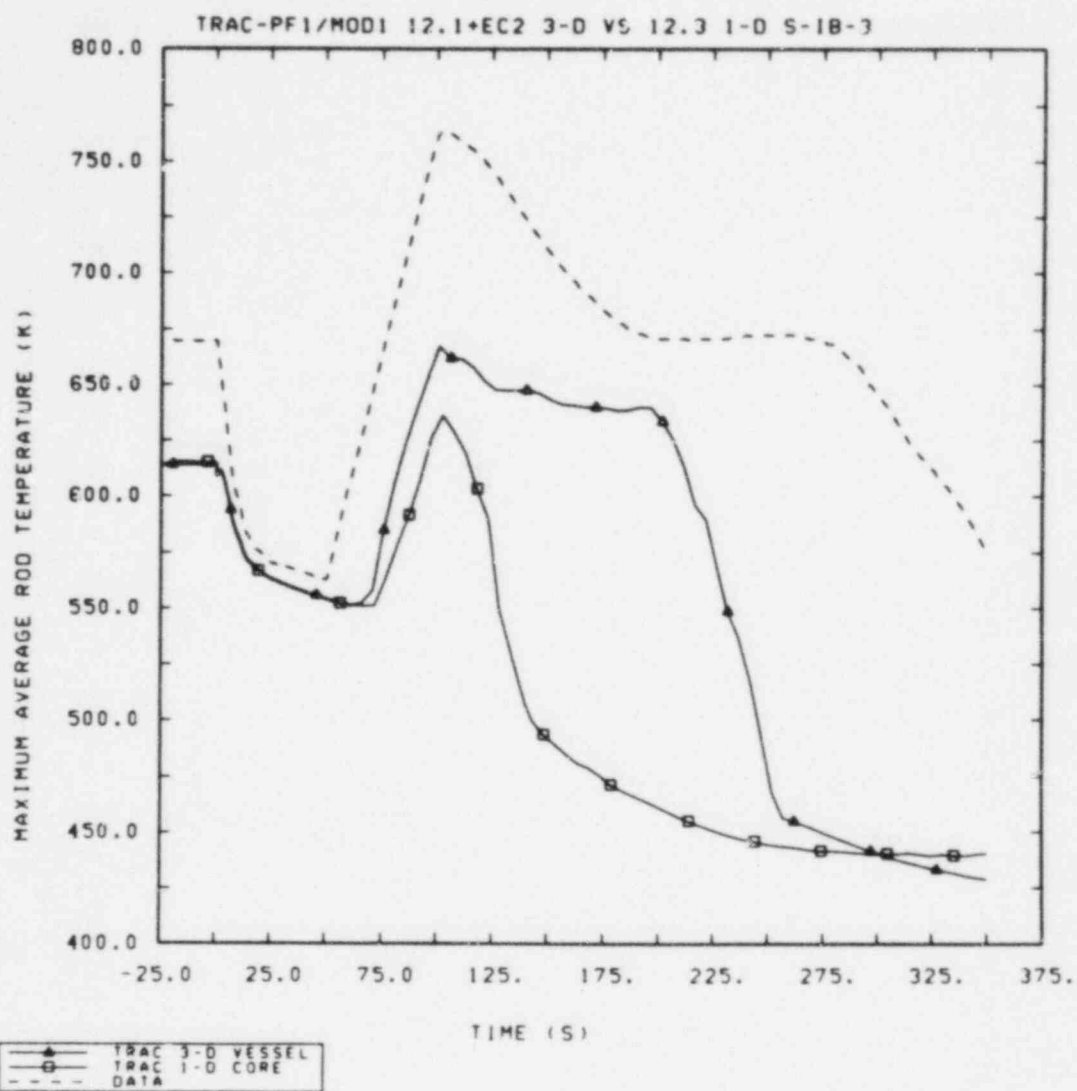


Figure 4.4.5 Maximum Rod Clad Temperatures with 3-D and Final 1-D Models

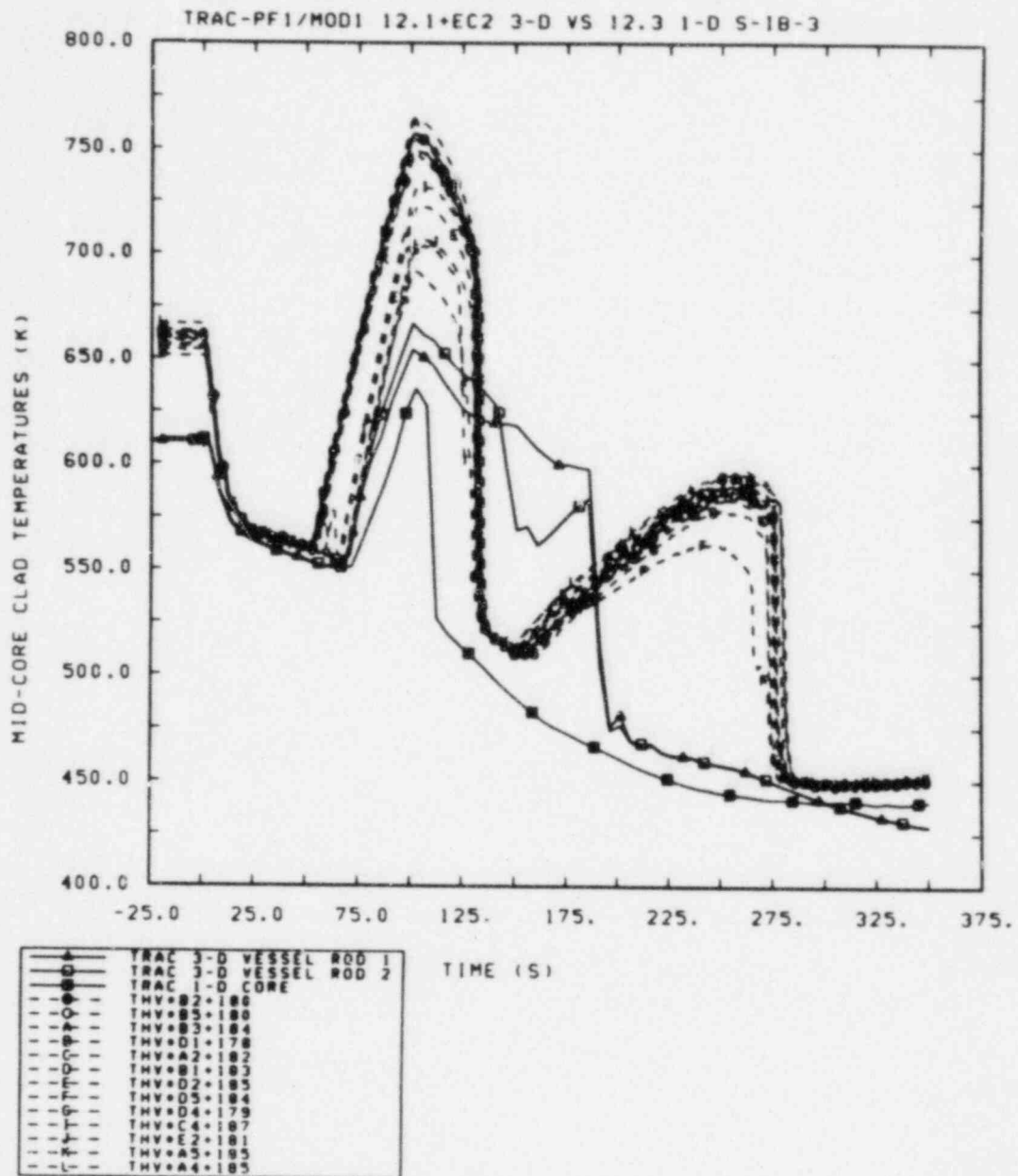


Figure 4.4.6 Middle Core Heater Rod Temperatures (1.83 m Core Elevation) with 3-D and Final 1-D Models

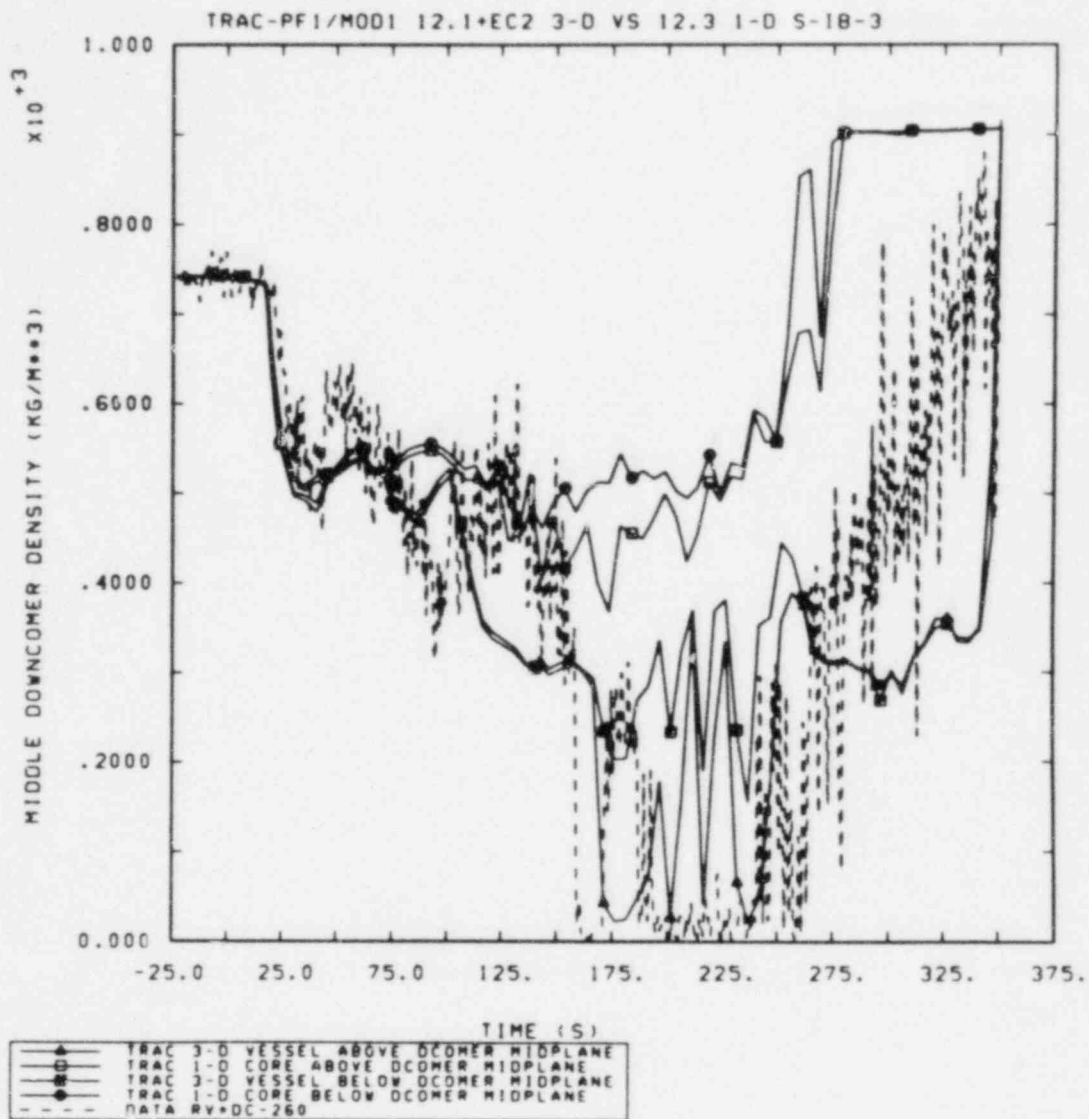


Figure 4.4.7 Mid-Downcomer Densities with 3-D and Final 1-D Models

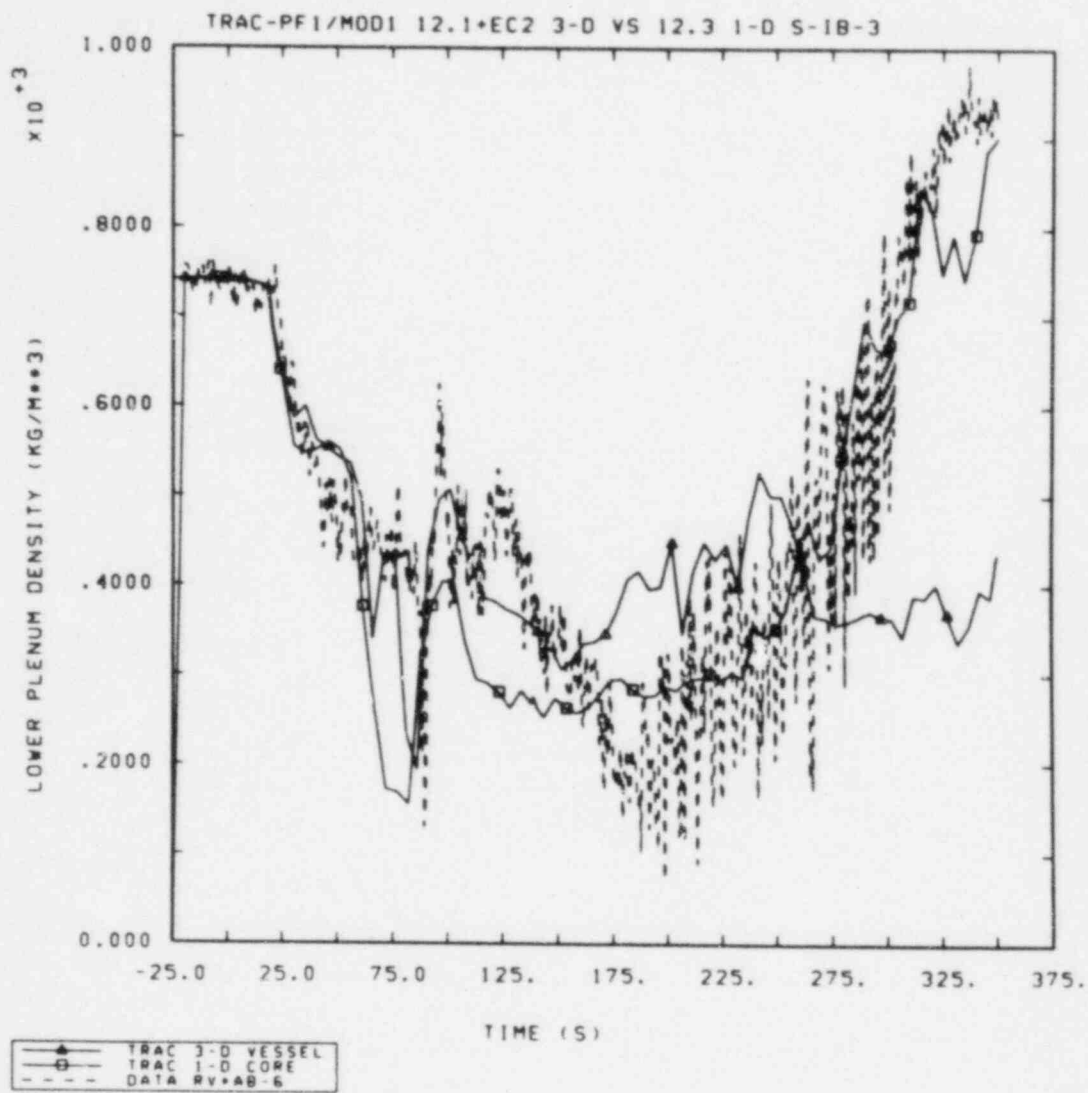


Figure 4.4.8 Lower Plenum Densities with 3-D and Final 1-D Models

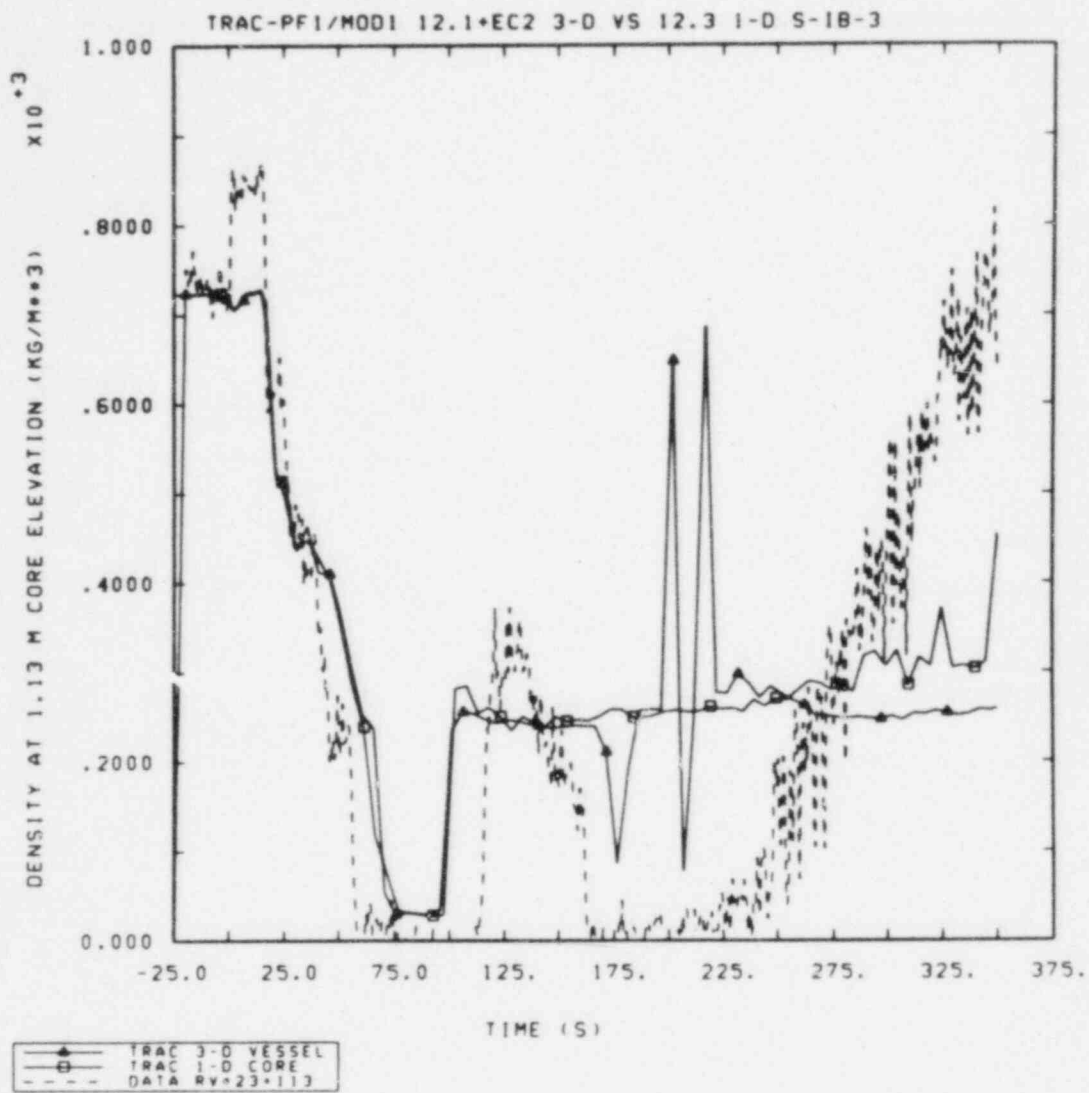


Figure 4.4.9 Lower Core Densities (1.13 m Core Elevation) with 3-D and Final 1-D Models

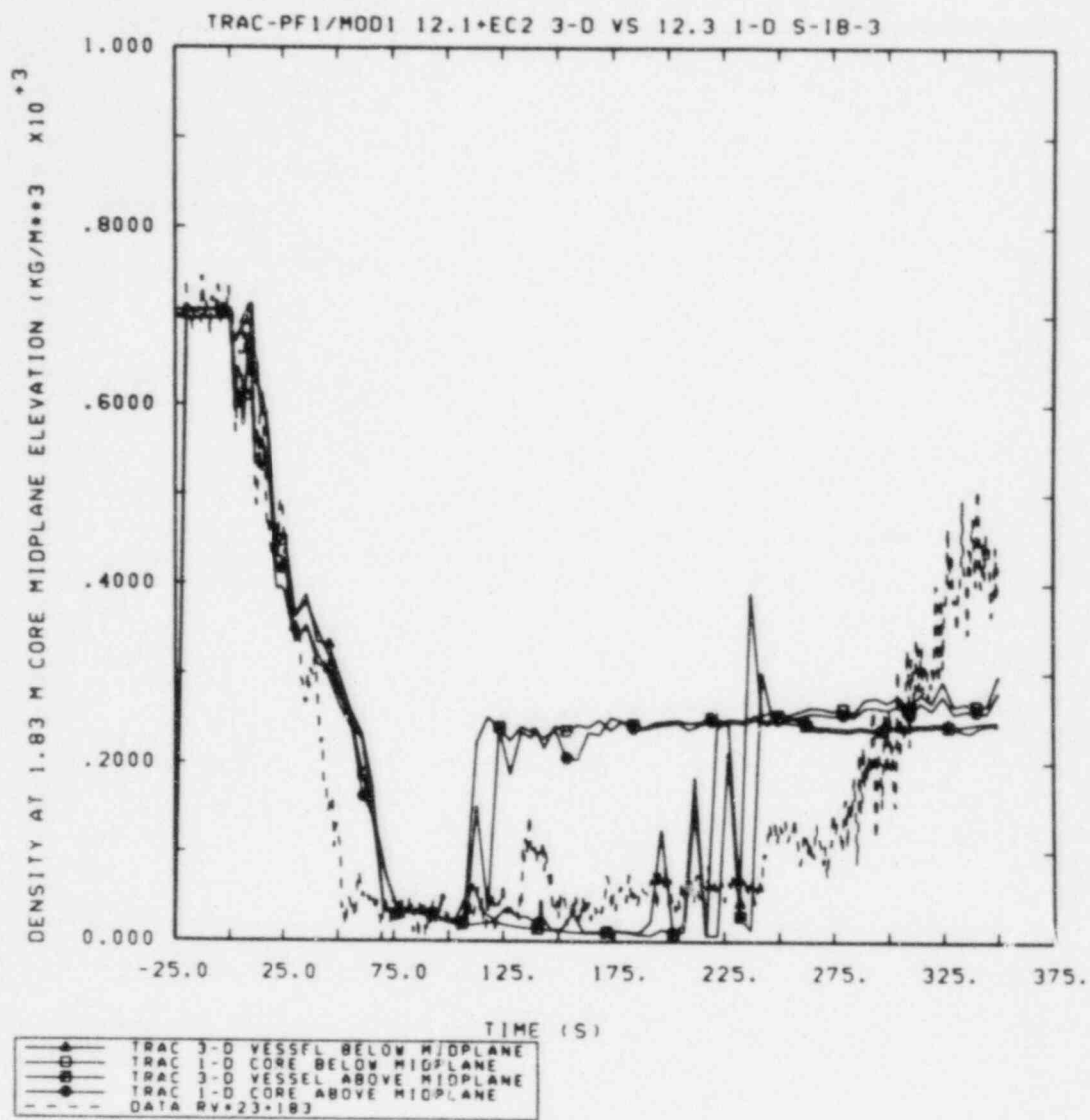


Figure 4.4.10 Middle Core Densities (1.83 m Core Elevation) with 3-D and Final 1-D Models

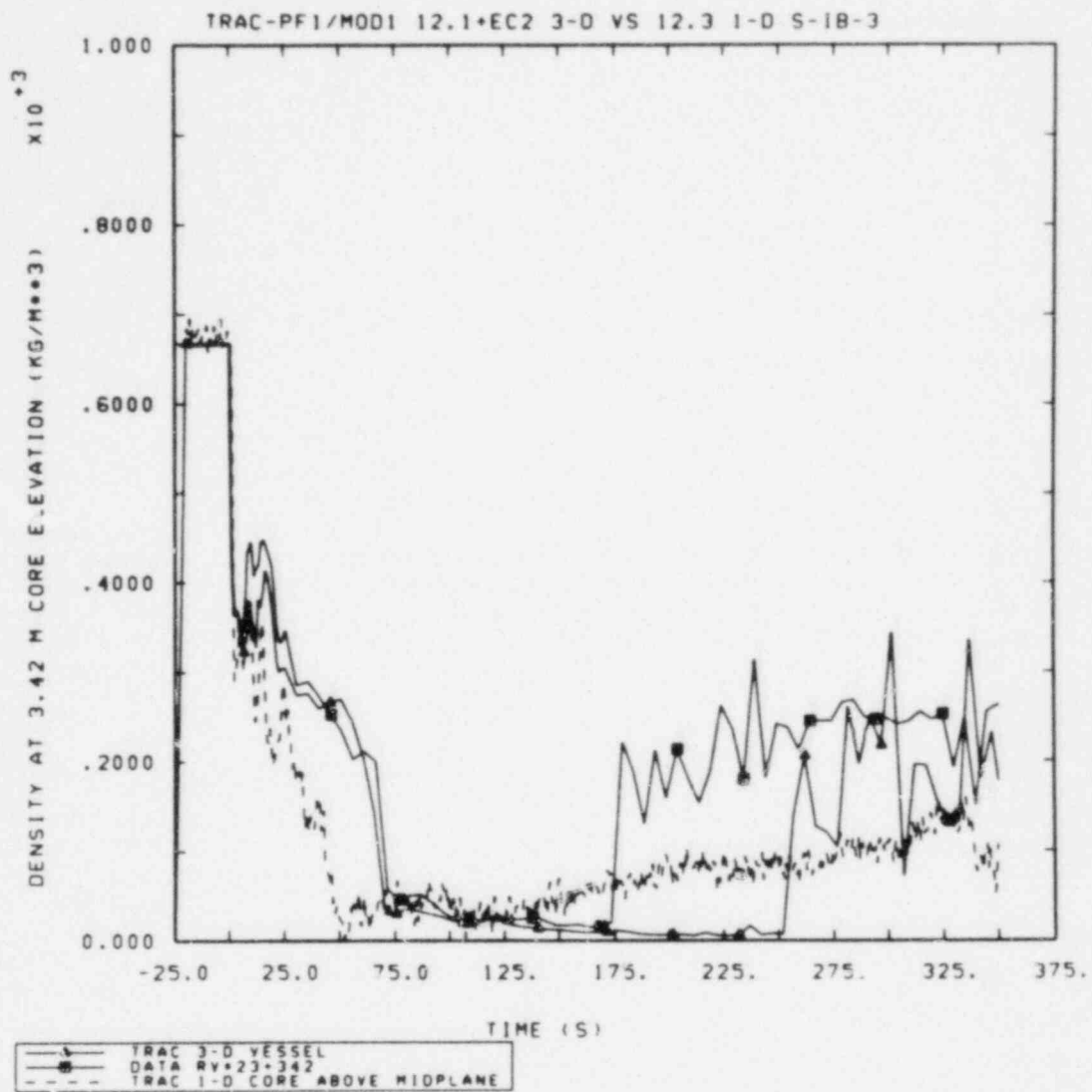


Figure 4.4.11 Upper Core Densities (3.42 m Core Elevation) with 3-D and Final 1-D Models

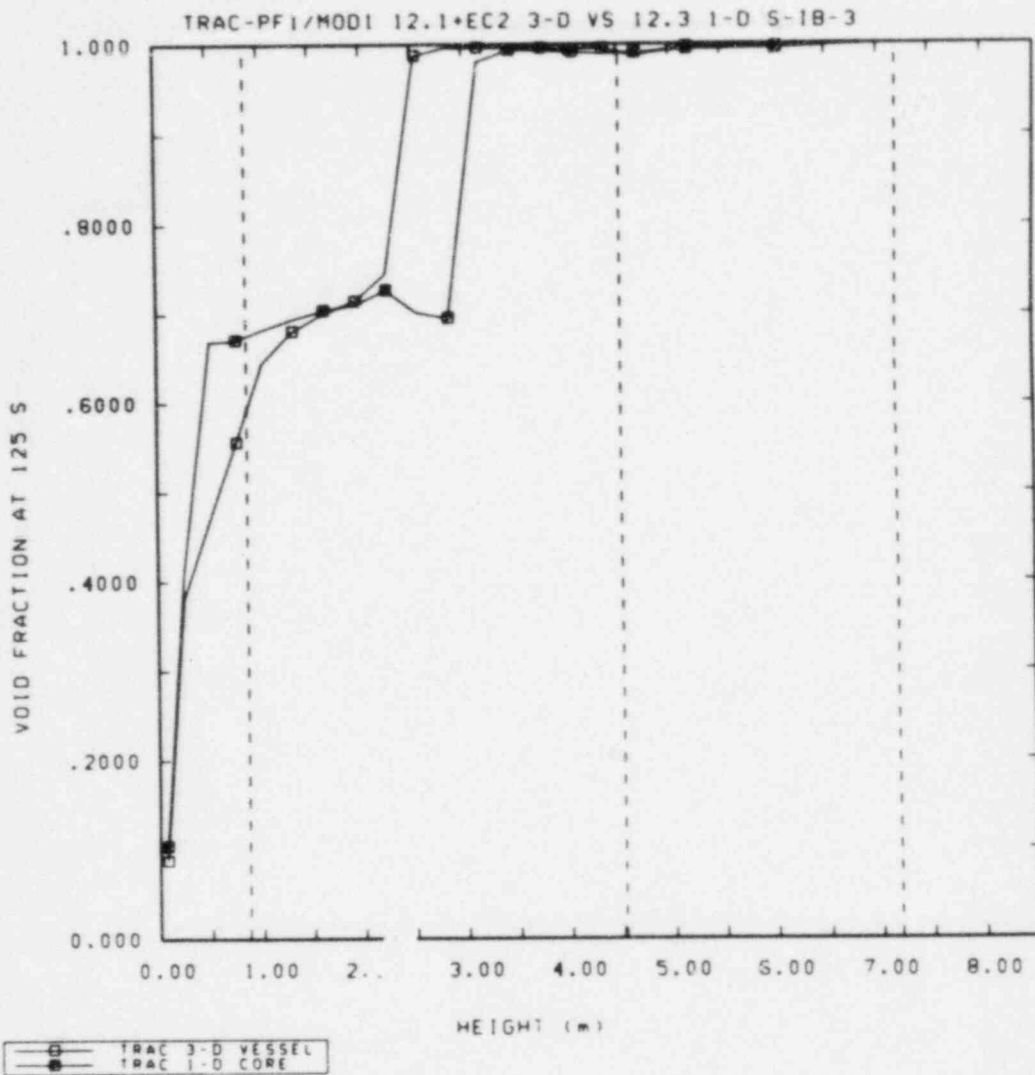


Figure 4.4.12 Vessel Void Fraction Profiles with 3-D and Final 1-D Models

5.0 DISCUSSION

This section presents our user experiences, the results of some sensitivity studies for our 3-D model Semiscale S-IB-3 analyses (whose final basecase calculation results were given in Section 3) and for our 1-D model (used in the 3-D vs 1-D noding study of S-IB-3 presented in Section 4), a description of a code error discovered in the course of our 1-D model analyses, and run time statistics.

5.1 User Experience

The TRAC steady state calculation for S-IB-3 was begun from the usual cold no-flow conditions, because no good estimate of the steady state was previously available. As described in Section 3.1, the resulting primary side conditions are in reasonably good agreement with data, except for the broken loop pump speed (which was expected) and the intact and broken loop cold leg temperatures (which were too high for the given secondary side conditions even with the minimum tube-to-tube spacing used as the heated equivalent diameter). Based primarily upon the results of our LOBI B-RIM analyses, we were especially careful to ensure a good secondary side steady state before beginning any transient analyses.

The first 40 seconds of the transient were then run, with Version 11.9. The early-time break flow was in good agreement with data; however, the calculated primary system pressure dropped too rapidly during subcooled blowdown and then continued decreasing too slowly during saturated blowdown, compared to the data. Besides being due to the higher steady state cold leg temperatures, this discrepancy was mainly due to the fact that the predicted secondary side pressures did not agree with the measured values.

This can partly be explained by the difficulties in modelling the experimental procedures. In the test, the feedwater flows were turned off during the first 2.5 s (broken loop) and 30 s (intact loop), but the steam valves remained open until late in the transient. These partially open steam valves had a high enough flow resistance to maintain the steady state secondary side pressure with atmospheric conditions downstream; no documentation was provided on their flow area or resistance. Several calculations were done with a constant downstream atmospheric pressure and with various valve positions and resistances assumed, and better qualitative behavior was seen. However, the expense involved in such "backfitting" to the data was deemed inappropriate and we ultimately decided to simply run with the measured steam generator pressures imposed as boundary conditions, to see what effect these secondary side discrepancies have on the primary side response.

The first ~150 seconds of the S-IB-3 transient (up to the time of accumulator injection start) were then run with Version 12.0, after some small input errors in the core bypass line, support columns and guide tube were fixed and the steady state was rerun. We then reran the calculation for the same ~150 seconds with the new PLENUM component used to connect the cold legs, downcomer and core bypass line rather than the TEE network used previously, to see what impact the different treatment of momentum effects in TEE and PLENUM components have on the results. No significant differences in results were seen.

A number of calculations were done in which the upper head drainage path flow resistances (i.e., of the bypass line, the support columns and the guide tube) were

varied. The draining of the upper head affects the vessel liquid level depression and core heatup during the transient, and the geometry of the relevant flow paths (particularly the accidental leakage path through the incorrectly-plugged support columns) is not well documented. Differences in the timing, duration and magnitude of the level depression and core heatup were seen, but the calculations were too long and expensive for truly adequate sensitivity studies.

A purely 1-D model was then developed for the Semiscale Mod-2A facility and the S-IB-3 test, using the 1-D CORE, TEEs, PIPEs and two PLENUM components to connect the hot and cold legs to the vessel and downcomer, respectively. This was intended to allow us to assess the new PLENUM component by comparing final results to those obtained with our corresponding 3-D VESSEL model, and to allow us to run more sensitivity studies with a faster running model.

The first ~150 seconds of the S-IB-3 transient (up to the time of accumulator injection start) were rerun a number of times with the new all 1-D model. The major problem then being analyzed was the significantly higher intact loop mass flows and hot leg densities being predicted after the pump head degrades. Sensitivity studies were done on break flow discharge coefficients, nodalization detail, pump curves, structural heat and upper head drain rate, some of which are described in more detail in Section 5.2. No significant differences in results have been seen.

Another uncertainty in the vessel geometry was the modelling of the vessel structural heat, which we found to have a significant effect on the calculated vessel level depression and core heatup (as presented in Section 5.3). Calculations were done with the 3-D VESSEL model in which: all the metal mass was approximated and assumed in contact with the liquid; all metal except heater rods was perfectly insulated; and only a few of the inner structures were represented as VESSEL heat slabs.

The entire S-IB-3 transient was then run with the basecase input model (using a 3-D VESSEL component), with the results given in Section 3. We then reran the basecase analysis using the purely 1-D model, with final results compared to those obtained with our equivalent 3-D VESSEL model in Section 4.

(This final 1-D calculation was somewhat delayed due to code errors found in signal variable definitions when multiple PLENUM components are present, as described in Section 5.4. These were reported to the code developers at LANL, but after they indicated that they did not expect to have the error corrections soon, we developed special updates to our plot program to obtain the needed information for plotting purposes.)

The calculation with the purely 1-D model ran about twice as fast as that with our equivalent 3-D model (as shown in Section 5.5), but the results of the two models diverged significantly for a number of major variables, with the 3-D vessel model results generally in better agreement with data. Further analysis showed the 1-D model predicting an unphysical void fraction profile, with a discontinuity at the component boundary between the lower plenum TEE and CORE. An additional 1-D transient calculation was then done, in which the top cell in the lower plenum TEE was redefined to be the lowest cell in the CORE (with no other change in actual geometry), confirming that the presence and location of the component boundary appears to be the source of the problem.

This problem was discussed with LANL (specifically, Thad Knight and Susan Woodruff), and the two 1-D input decks were subsequently transmitted to LANL at their request. At first, they could not run our decks because they did not have in their internal code version an update allowing STGEN heat slabs to communicate with the same cell on both heat transfer surfaces (an update we received from the code developers at the TRAC-PFI/MOD1 workshop in December 1983). With this corrected, they eventually identified the source of the discontinuous void fraction profile as being the (undocumented) inverted annular flow regime model, which is used only in 1-D components with generalized heat slabs and which is explicitly disallowed at component boundaries.

This regime by default is allowed whenever the wall temperature is greater than saturation; a(n also undocumented) NAMELIST flag INVAN specifies this regime to be used only when the temperature is greater than T-CHF. When LANL reset this NAMELIST input flag and reran the calculation, they found smooth well-behaved void fraction profiles. When we made the same change in our input and reran the 1-D model basecase calculation at Sandia, we saw no change in the results from those we had previously obtained; the discontinuous void fraction profiles were still being calculated.

At first Rick Jenks, the user liaison person at LANL was surprised because he believed we and they were running the identical code, but producing different results. Upon examination, we felt that the problem was not in the inverted annular flow logic but in the T-CHF logic, because our run printed zeros where the Los Alamos run printed non-zero T-CHF values in the CORE component major edit output. LANL later found that an error correction set (EC3, dated June 1985) was being used in their internal code, but had not yet (i.e., mid-October 1985) been put on the VAX node for external users to acquire. When we reran our 1-D basecase calculation after implementing this additional update set (which in the meantime had had its name changed to EC12.3), we got essentially the same results as LANL had.

5.2 Pump Degradation/Flow Stagnation Sensitivity Studies

Our purely 1-D Semiscale model was developed partially to allow us to run more sensitivity studies with a faster running model. (The 1-D components can use the Courant-limit-defying two-step numerics, but this has not been implemented for the 3-D VESSEL component.) The first ~150 seconds of the S-IB-3 transient, up to the time of accumulator injection start, were rerun a number of times with the 1-D model. The major problem being analyzed was the significantly higher intact loop mass flows and hot leg densities being predicted after the pump head degrades; which we felt were ultimately responsible for the underprediction of core heatup throughout the transient (as discussed in Section 3).

Sensitivity studies were done on the saturated break flow discharge coefficient, the nodalization detail and the intact loop pump flow resistance and two-phase multiplier curve. Some of these calculations succeeded in slowing the intact loop flow more rapidly, by increasing the pump resistance or by altering the two-phase multiplier curve to degrade the pump head fully as soon as small amounts of vapor ($\alpha < 0.1$) appear; all such calculations showed a more rapid vessel and core uncover and an earlier onset of core heatup. However, no great differences in results were seen, although some insights were obtained.

The intact loop (and associated downcomer and vessel) flows stagnate to near zero in the data at ~15 s; the calculated flows decay more gradually and reach zero at ~45 s. The only phenomenon occurring at ~15 s is the onset of major flashing of the cold leg fluid, which is correctly predicted. The data imply strongly that, as the intact loop cold leg flashes and vapor appears in the pump, the pump flow essentially stops as the head degrades. The calculation shows the head degrading to near zero by ~20 s, but this is apparently insufficient to immediately overcome the pre-existing flow momentum, with the result that the flow slowly decays after two-phase pump head degradation. To slow the flow as much as observed in the test would seem to require a negative degraded pump head.

This is certainly possible if the pump in the experiment was effectively operating on the fully degraded homologous head curve HTP2 (in the TRAC nomenclature [1]) rather than on the HTP1 curve after pump degradation, as the calculation is predicting (on the HVN curve rather than the HAN curve, in RELAP5 nomenclature). The HTP1 curve being used in our calculation shows a very small residual positive head, for forward or back flow; the HTP2 curve would give a significant negative head for most of its range. There is no obvious way to force the pump to use the other curve. However, there are certainly enough known errors and inapplicabilities in the (out-of-date) given Semiscale pump homologous curve descriptions that it is easily believable for such a difference between test and calculation to occur.

5.3 Vessel Heat Slab Sensitivity Studies

We found that the modelling of the vessel structural heat also had an effect on the calculated vessel level depression and core heatup. The two major difficulties we encountered were that TRAC allows only interior heat slabs in a 3-D VESSEL (one per cell) and that the Semiscale vessel has very complicated inner structure with some interior insulation and fillers in addition to an excess metal-to-liquid ratio. Calculations were done with all metal mass approximated and in contact with the liquid (i.e., no internal insulation), with all metal except heater rods perfectly insulated, and with only a few of the inner structures represented as VESSEL heat slabs in addition to the core heater rods.

These were not sensitivity studies done after the final basecase transient analysis had been completed; these were part of a series of preliminary calculations done testing various input and modelling options and assumptions. These particular preliminary calculations were run only to the onset of accumulator injection. However, the results are interesting and are included here for the reader's information.

Figure 5.3.1 shows the vessel and downcomer collapsed liquid levels for two otherwise-identical calculations with no vessel internal insulation and perfect vessel internal insulation, respectively. (The calculated downcomer collapsed liquid levels in these two calculations were low by a constant factor of ~0.65 m due to a user input error; the agreement with data is thus better than appears.) At first glance, the vessel collapsed level for the calculation with no internal insulation appears to be in better agreement with data than the alternative result, especially for the initial level drop, although the subsequent partial level recovery is not calculated. One might then expect the calculation with no internal insulation to predict more (or even overpredict) core heatup, in better agreement with data; however, this was not the case.

Figure 5.3.2 gives the lower plenum, core heated length and upper plenum collapsed liquid levels calculated with no vessel internal insulation and with perfect vessel internal insulation (with the measured vessel liquid level superimposed). The core heated length collapsed liquid level is very similar for both runs prior to ~60 s; the lower collapsed vessel level during this period in the calculation with no internal vessel insulation modelled comes from differences in the upper plenum clearing. As with the vessel liquid levels in Figure 5.3.1, the subsequent partial core heated length level recovery is not calculated in the absence of any internal vessel insulation.

The lower plenum and middle core densities predicted with no vessel internal insulation and with perfect vessel internal insulation are shown in Figures 5.3.3 and 5.3.4, respectively. These local density results generally parallel those for the collapsed liquid levels, just discussed. The calculation with no vessel internal insulation modelled predicts qualitatively different behavior than the data or the calculation assuming perfect internal vessel insulation, for the level depression and loop seal clearing phenomena; heat transfer from the lower vessel structure is maintaining an elevated two-phase level during the ~40-100 s time period and then causing an inventory boiloff after ~120 s.

Figure 5.3.5 gives the maximum rod clad temperatures calculated with no vessel internal insulation and with perfect vessel internal insulation modelled. While neither is in good quantitative agreement with data, the run with vessel internal insulation neglected qualitatively predicts a core heatup later in the transient due to level boiloff, while the run assuming perfect vessel internal insulation qualitatively predicts the earlier core heatup due to vessel level depression prior to loop seal clearing.

These results suggest that early in the transient the internal vessel insulation is effective at preventing the atypically large structural heat source/sink from affecting the transient, but that later in the transient the structural heat may nonetheless contribute significantly to the vessel fluid heating. Representing the details of the various vessel structures explicitly is essentially impossible with the limited heat slab modelling capabilities in TRAC; therefore, we did not pursue the issue further but simply assumed the vessel internal insulation provided perfect insulation, which allowed calculation of the vessel level depression due to loop seal formation.

5.4 "Multiple PLENUMs" Code Error

In both the 3-D and 1-D models, collapsed liquid levels have generally been calculated from combinations of signal variables (for any section of constant cross-sectional area) and control blocks (adding up such signal variables). The liquid level signal variable available in TRAC ("Number 20") does not produce collapsed liquid levels as would be obtained from Δp measurements in a multi-volume stack unless the cross-sectional area is constant in all the volumes in the stack; otherwise, it yields the effective liquid level that would be seen if all the liquid would separate out vertically and fill the stack from the bottom up. The difference in these two liquid level definitions can be seen in Figure 5.4.1 for a simple case of a "fat" cell above a "skinny" cell.

Such combinations of signal variables and control blocks worked very well for collapsed liquid levels in the U-tubes, loop seals, vessel and downcomer, until a 1-D calculation was done which used PLENUM components for both the vessel-hot leg and downcomer-cold leg connections. The collapsed liquid levels calculated in both the vessel and downcomer then were incorrect. In the presence of a PLENUM component, the liquid level signal variable cannot be used directly because the PLENUM does not have a single unique flow area and height associated with it; instead we attempted to calculate a collapsed liquid level using the geometrical height of the PLENUM region and the void fraction signal variable ("Number 21"). This had produced the expected results in our 3-D model. (The basecase 3-D model used a single PLENUM component, for the downcomer-cold leg connection.)

The incorrect vessel and downcomer collapsed liquid levels in the 1-D calculation were found to result from nonsense numbers (e.g., $-4 \times 10^{**5}$) being passed to the signal variable routines for the PLENUM void fractions. (The void fractions plotted and printed for the PLENUM components were believable values between 0 and 1.) We traced the source of this problem to code errors in the signal variable definitions and pointers when multiple PLENUM components are present, which we reported to the code developers at LANL. Although we encountered this problem while attempting to use the void fraction signal variable, the code error is such that any signal variable for a PLENUM component should be similarly affected. After some initial confusion, LANL indicated that they did not expect to have error corrections for this soon (and such an error correction has still not been released). In order to continue our analyses, special updates to our plot program were used to obtain the needed signal variable information indirectly from the graphics file.

5.5 Computational Run Times

Figure 5.5.1 shows the total CRAY-XMP CPU times for our TRAC calculations of Semiscale test S-IB-3 with the 3-D and 1-D input models. To run 350 seconds of the S-IB-3 transient calculation took ~2500 seconds of CPU time with the basecase 3-D model; the purely 1-D transient run was almost exactly twice as fast. The twenty-five seconds of steady state (included for plot purposes) were much faster running than the transient, as would be expected. The time step for these calculations also was reduced to 10^{**4} s through input at trouble spots, such as the opening of the break valve and the onset of accumulator injection, because code failures were common at these points when no such adjustment was made.

Figure 5.5.2 gives the time step histories for the S-IB-3 transients run with 3-D and with 1-D vessel models, and shows that the speed-up in the purely 1-D calculation is due to the larger average time steps being taken at early times. The base calculation time step is mostly Courant-limited in the 3-D VESSEL component, while the two-step numerics in the 1-D model often violates the Courant limit, although other time step checks prevent a greater speed-up for this transient calculation.

The various run time statistics for the B-RIM [15] and S-IB-3 calculations are summarized in Table 5.5.1. Besides the 3-D/1-D comparison on the CRAY-XMP for S-IB-3, data for an incomplete S-IB-3 transient calculation (with 3-D VESSEL) on

the CYBER-76 is included for comparison to the LOBI B-RIM CYBER-76 calculation (with 3-D VESSEL). Those results show that there is just over a factor of two speed-up going from the CYBER to the CRAY, as would be expected, due to the smaller grind time on the faster machine. There is no significant difference in the time steps being taken on the two machines.

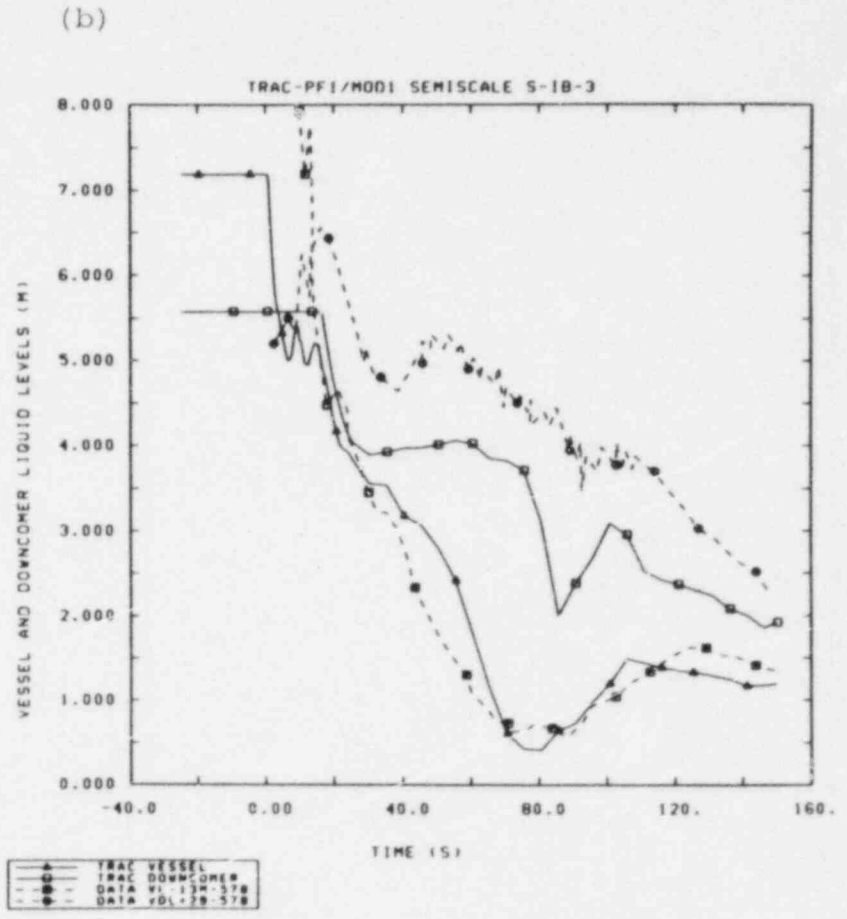
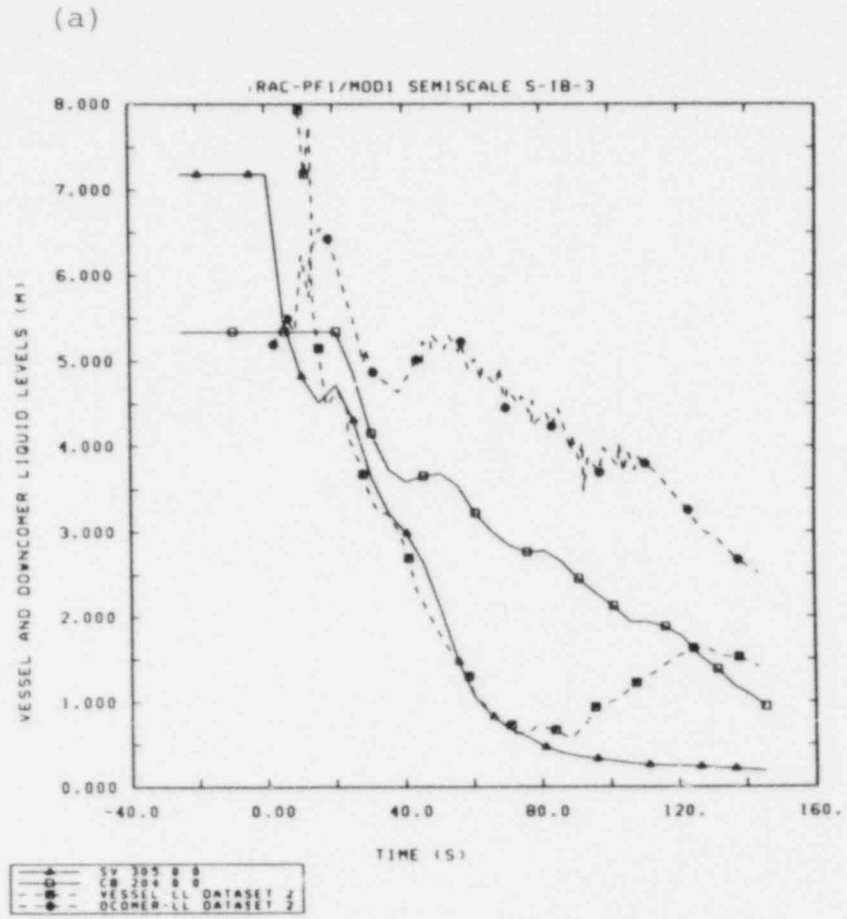


Figure 5.3.1 Vessel and Downcomer Liquid Levels with (a) no Vessel Internal Insulation and (b) Perfect Vessel Internal Insulation

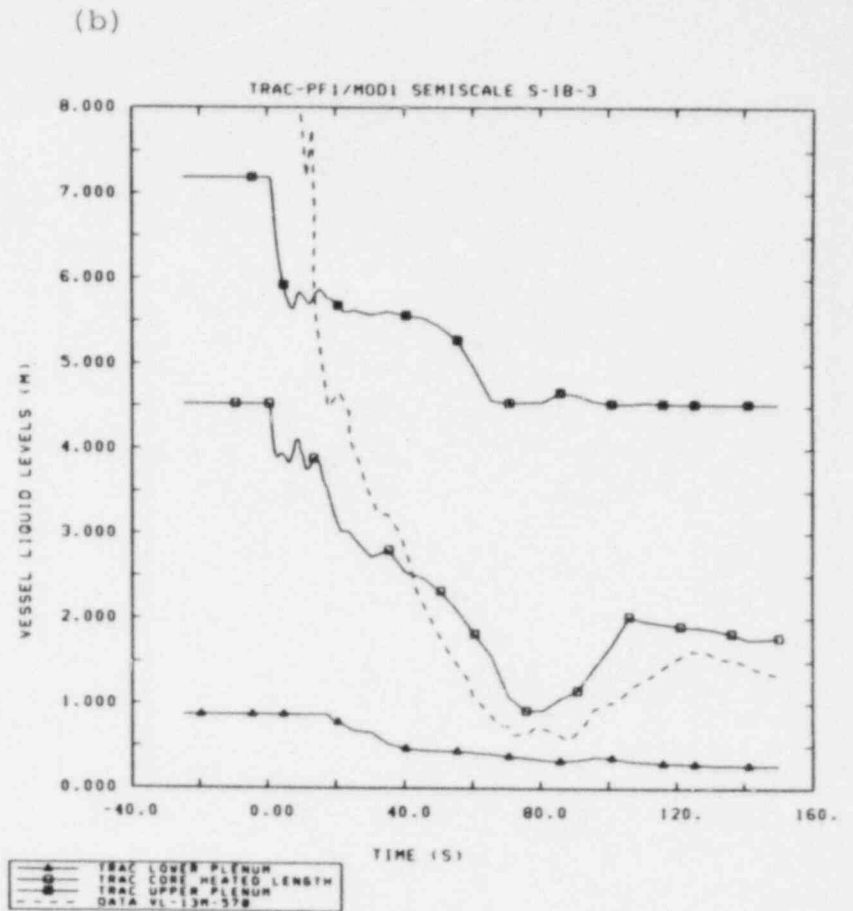
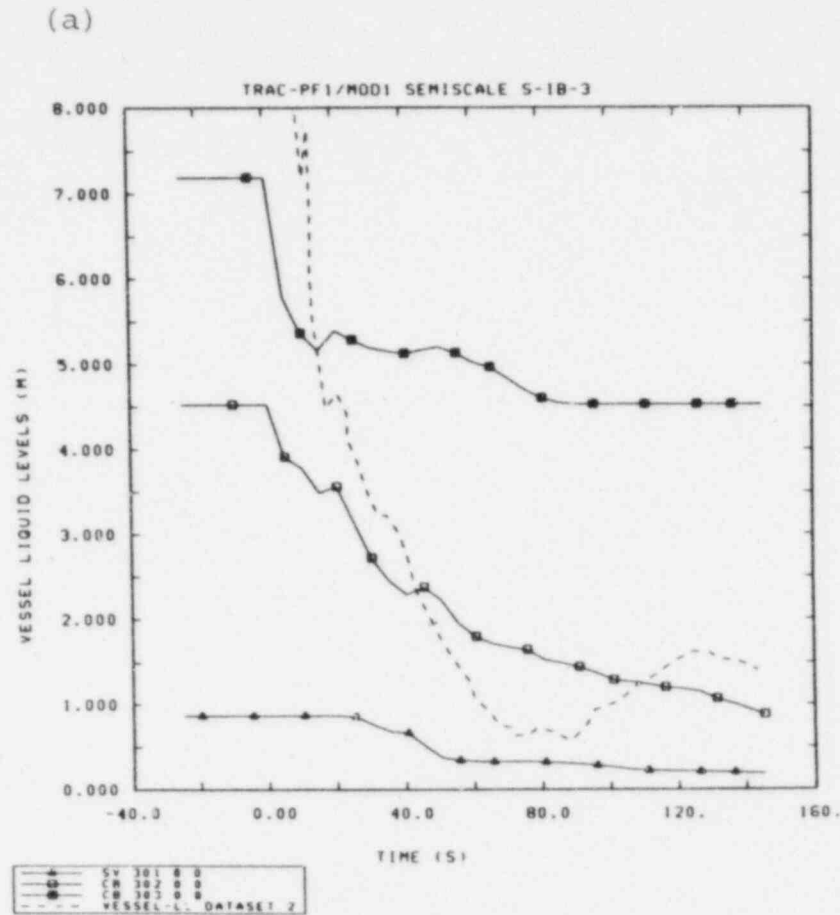


Figure 5.3.2 Lower Plenum, Heated Length and Upper Plenum Liquid Levels with (a) no Vessel Internal Insulation and (b) Perfect Vessel Internal Insulation

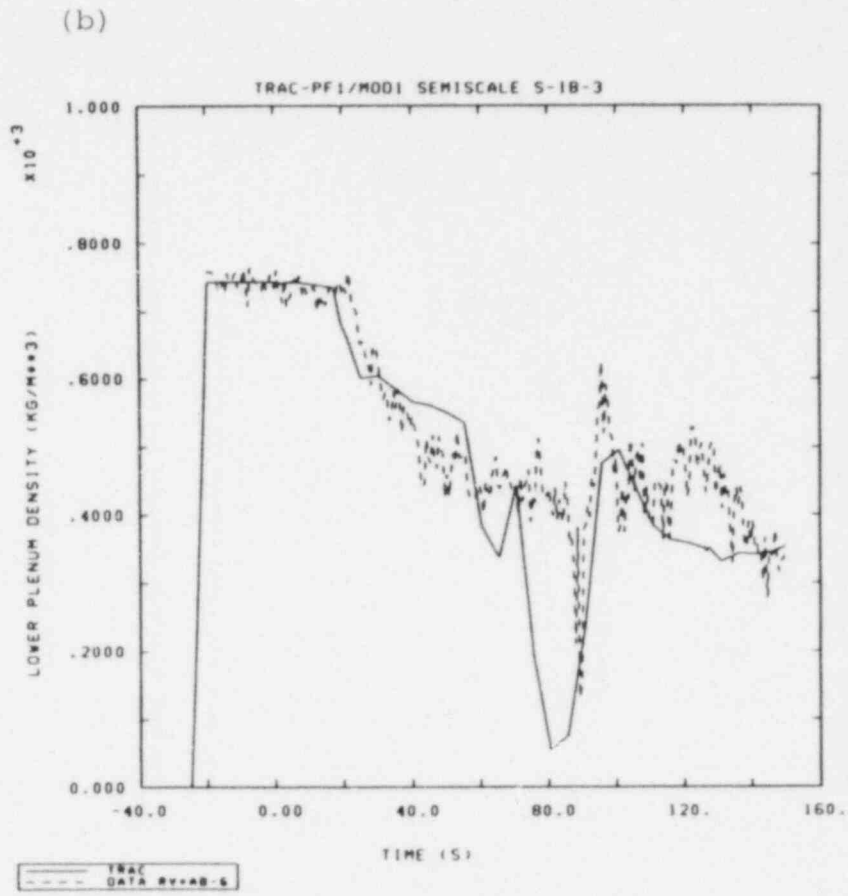
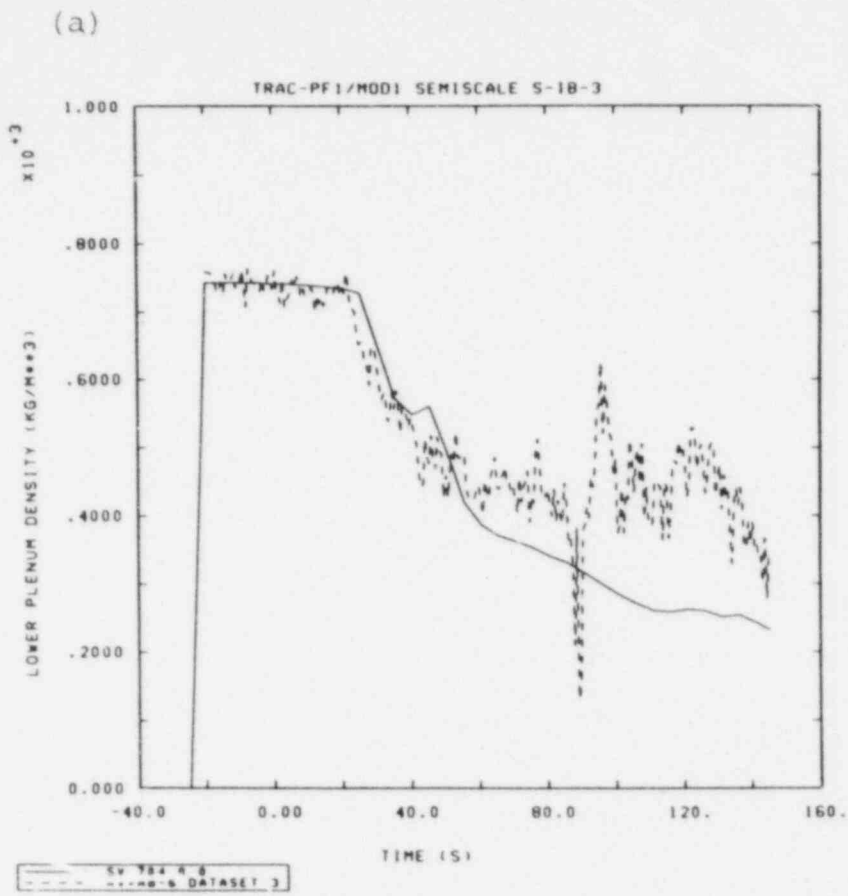


Figure 5.3.3 Lower Plenum Densities with (a) no Vessel Internal Insulation and (b) Perfect Vessel Internal Insulation

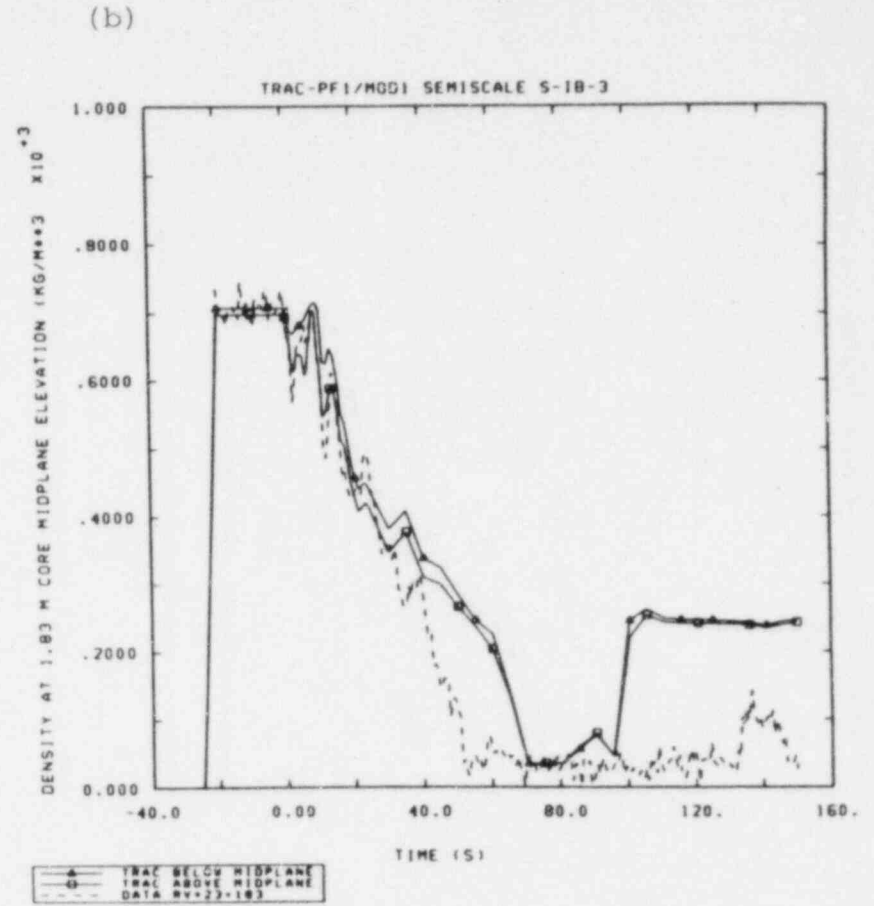
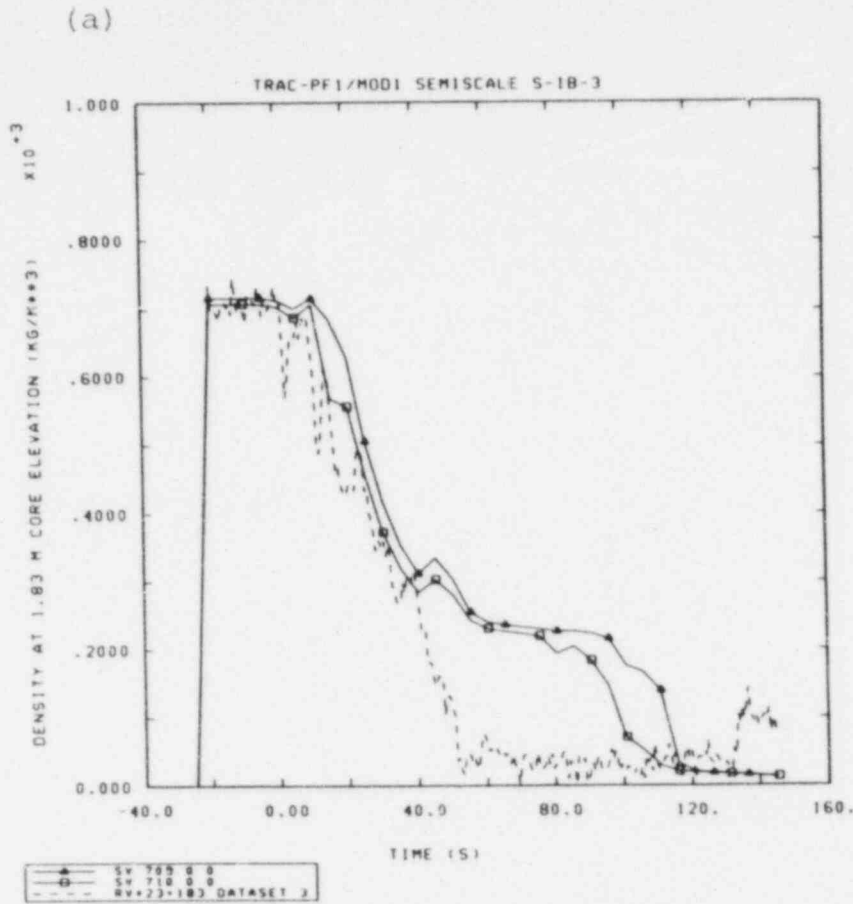


Figure 5.3.4 Middle Core Densities (1.83 m Core Elevation) with (a) no Vessel Internal Insulation and (b) Perfect Vessel Internal Insulation

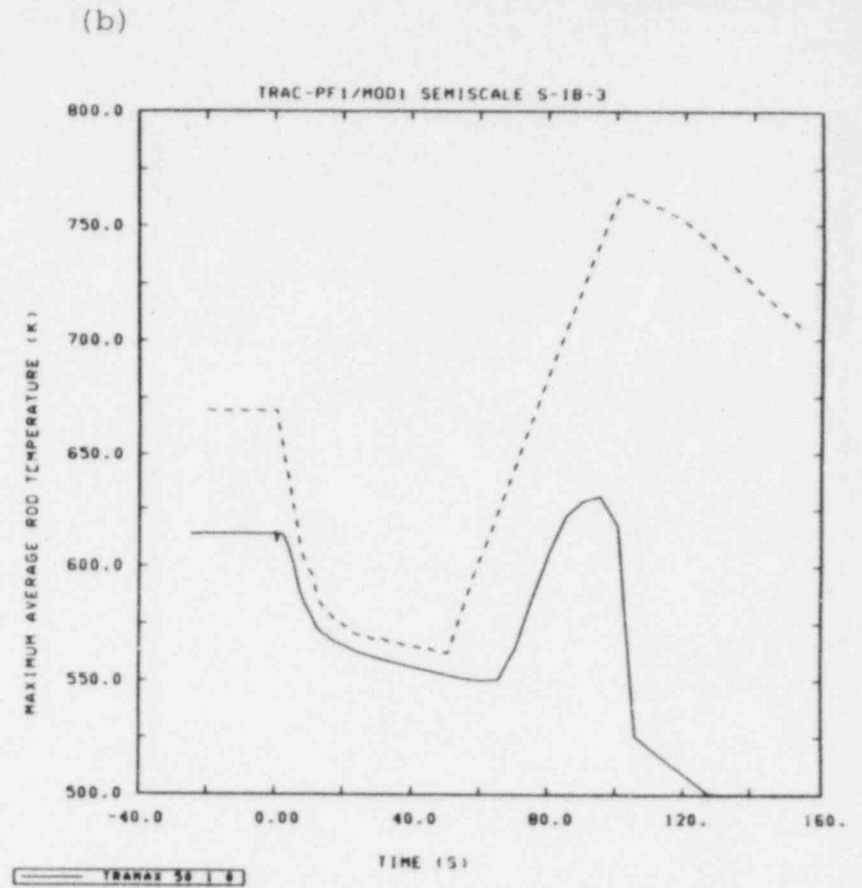
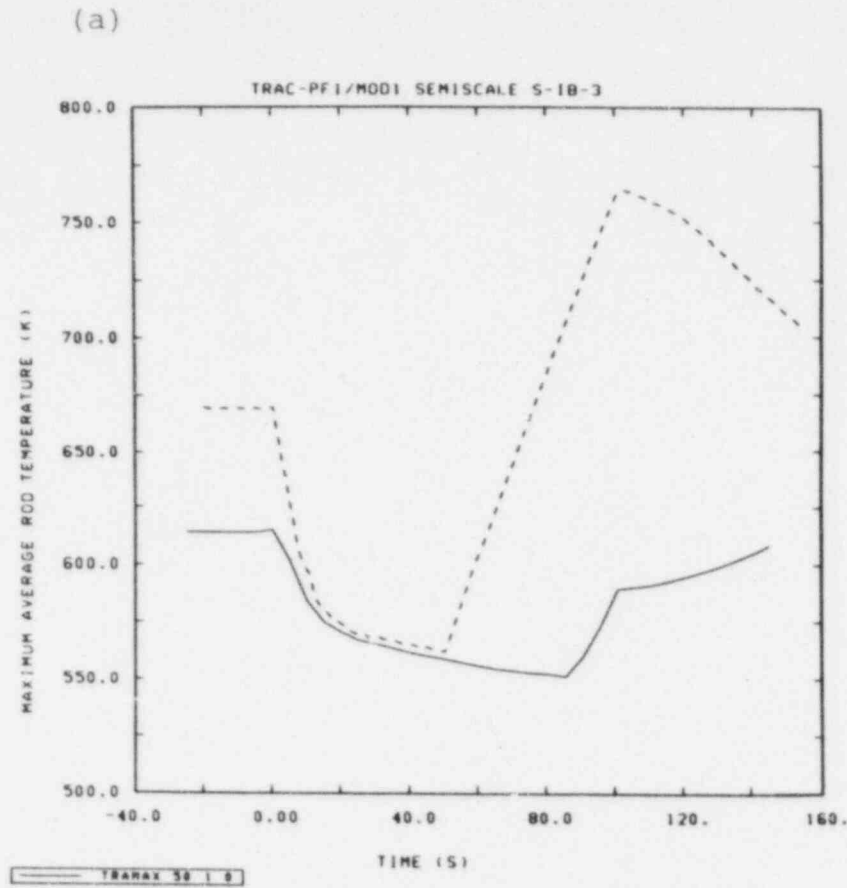


Figure 5.3.5 Maximum Rod Clad Temperatures with (a) no Vessel Internal Insulation and (b) Perfect Vessel Internal Insulation

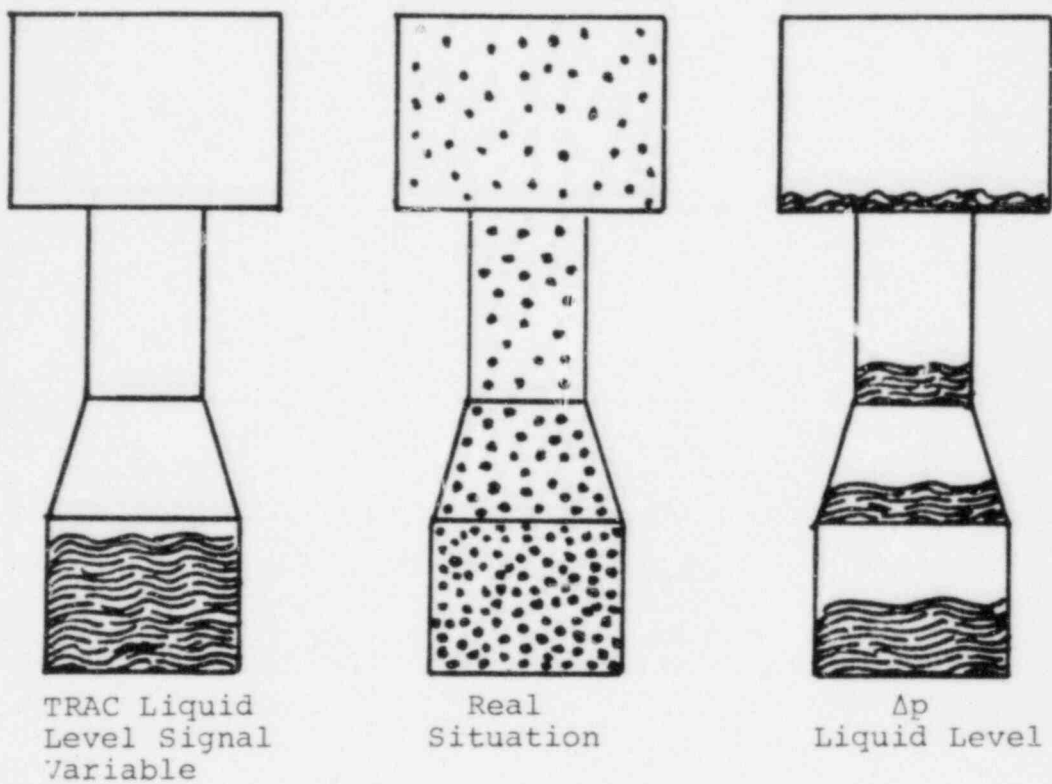


Figure 5.4.1 Different Interpretations of "Liquid Level"

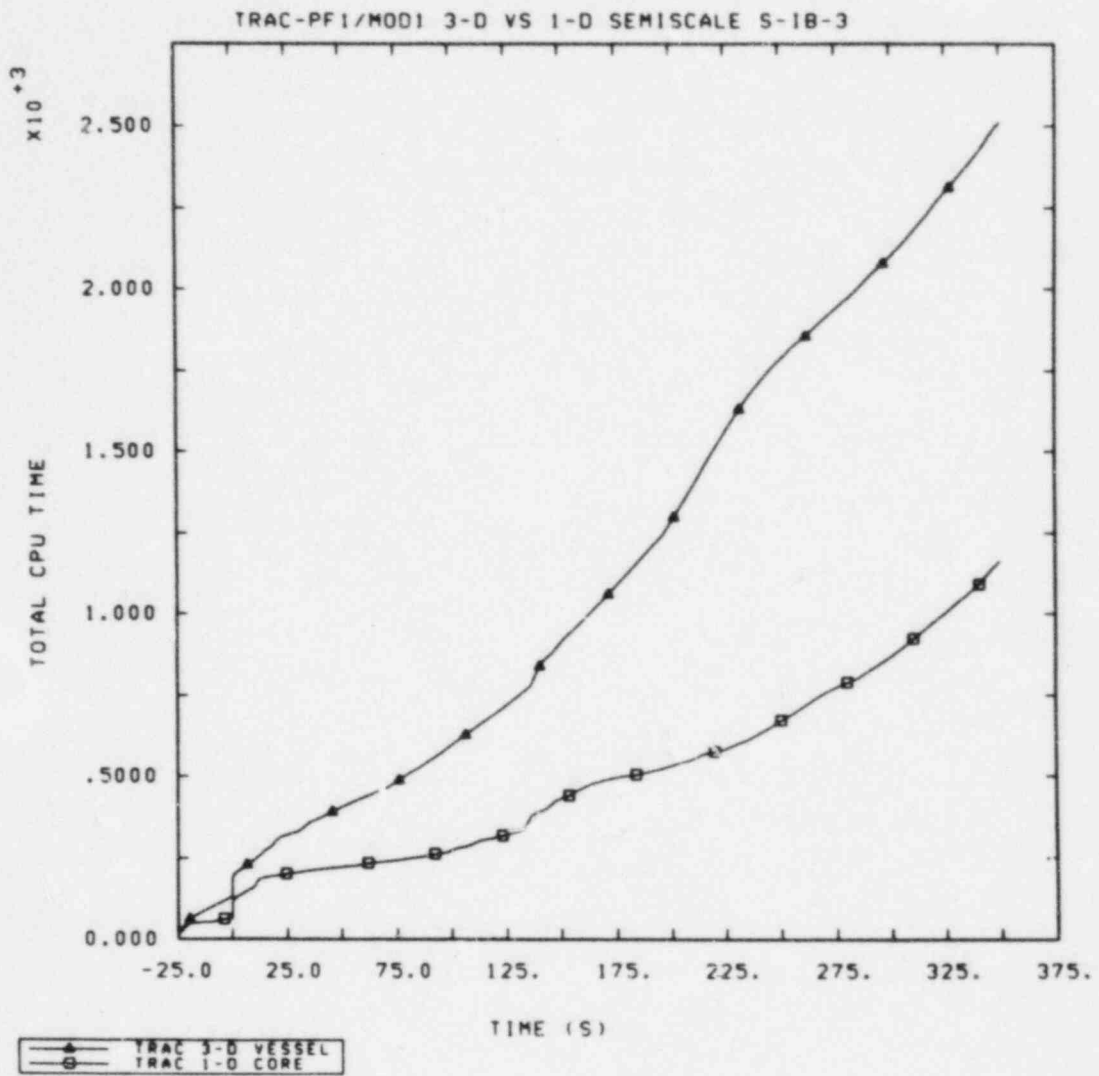


Figure 5.5.1 Total CRAY-XMP CPU Time with 3-D and 1-D Vessel Models

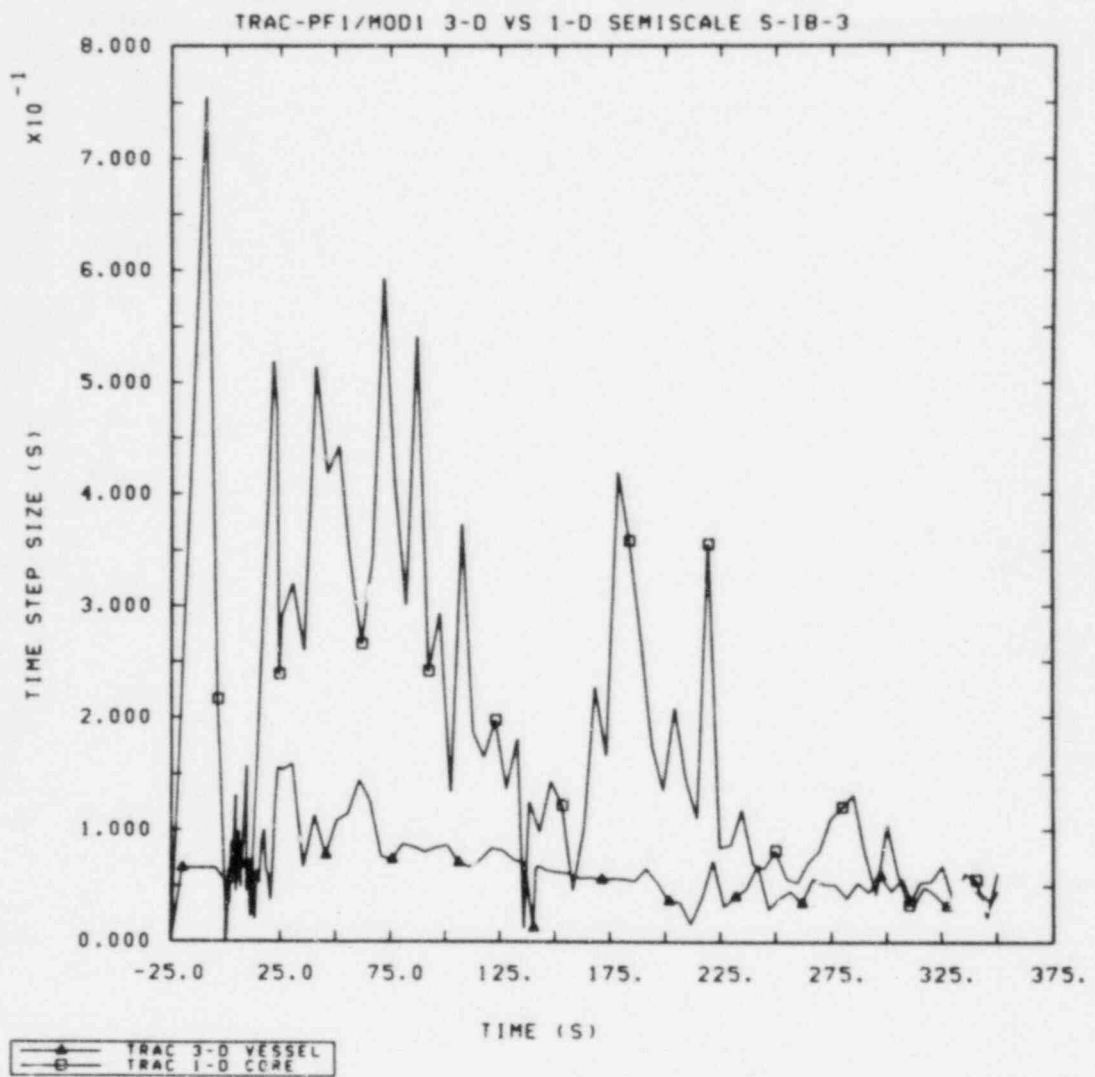


Figure 5.5.2 Time Step History with 3-D and 1-D Vessel Models

Table 5.5.1 Run Time Statistics

(Steady State)	LOBI B-RIM (CYBER-76)	3-D S-IB-3 (CYBER-76)	3-D S-IB-3 (CRAY-XMP)	1-D S-IB-3 (CRAY-XMP)
Problem Time (s)	25.	25.	25.	25.
CPU Time (s)	359.	427.	130.	64.
Number of Time Steps	414	494	494	230
Average Time Step Size (ms)	60.4	50.6	50.6	108.7
CPU-Time/Problem-Time	14.3	17.1	5.2	2.6
CPU-Time/Problem-Time/Cell	0.056	0.073	0.022	0.012
CPU-Time/Time-Step (s)	0.87	0.86	0.26	0.28
CPU-Time/Time-Step/Cell (ms)	3.39	3.69	1.12	1.31
(Transient)	LOBI B-RIM (CYBER-76)	3-D S-IB-3 (CYBER-76)	3-D S-IB-3 (CRAY-XMP)	1-D S-IB-3 (CRAY-XMP)
Problem Time (s)	237.	289.	350.	350.
CPU Time (s)	5793.	5809.	2378.	1099.
Number of Time Steps	6243	5393	6983	3692
Average Time Step Size (ms)	38.0	53.6	50.1	94.8
CPU-Time/Problem-Time	24.4	20.1	6.8	3.1
CPU-Time/Problem-Time/Cell	0.095	0.086	0.029	0.015
CPU-Time/Time-Step (s)	0.93	1.08	0.34	0.30
CPU-Time/Time-Step/Cell (ms)	3.62	4.60	1.46	1.40

6.0 SUMMARY AND CONCLUSIONS

There was very good agreement in primary system pressure between calculation and experiment for the first and last thirds of the transient. The calculated pressure fell significantly below the measured value around ~100-200 s; as discussed later, the calculation underpredicted the core heatup throughout the transient and the associated steam production and superheat (beginning at ~100 s), which maintained the higher pressures observed in the test. The intact loop seal also cleared at around 100 s in both test and analysis, which would be expected to increase the depressurization rate. The broken loop seal cleared at around 25-30 s in both experiment and calculation. Accumulator injection began when the primary system pressure fell below the accumulator pressure of 2.6 MPa, at 163 s in the test. Due to the lower pressures predicted during this period, this setpoint was reached at 138 s in the calculation and accumulator injection was predicted to begin early. In addition to beginning early, the calculated injection was not as smooth and well-behaved as the data, although the integrated flow rate of injected liquid was nearly that observed by the end of the period analyzed.

The partial break flow data available indicates good agreement for subcooled break flow early in the transient (using a discharge coefficient of 1.0) and suggests the subsequent saturated break flow (for a discharge coefficient of 0.9) may be high. Overpredicted saturated break flow would be consistent with the greater depressurization calculated starting at ~100 s; however, the data is not adequate for true quantitative judgement. As mentioned above, the more rapid depressurization during the middle of the transient could as easily be due to general underprediction of vapor generation and superheat; although some superheated steam was calculated at about the right times, particularly in the broken loop, it was much less than measured.

The delay in core uncover and heatup was due to higher calculated intact loop (and vessel) flows after ~25 s than measured. The measured intact loop mass flow rates stagnated at about 20-25 s, when the intact loop pump head had fully degraded due to cold leg fluid flashing. The calculation showed a flow decrease at that time followed by a more gradual flow stagnation. A number of sensitivity studies were done concentrating on this discrepancy, with the ultimate conclusion that this discrepant behavior was more likely due to errors in the Semiscale pump curves used (in their applicability rather than in their implementation) than to code errors, and that the inadequacy and uncertainty in the pump modification descriptions precluded any significant improvement in calculated results. The problem appears to be associated with the intact loop pump head degradation and flow stagnation only, as evident from the broken loop mass flow rates where there was good agreement between calculation and data.

The problems in matching the intact loop flow stagnation early in the transient were also visible as discrepancies in predicting the vessel and downcomer flow response correctly. The delayed intact loop and downcomer flow stagnation after ~25 s showed up as a delayed vessel level depression at the same time. The calculated vessel level was then correctly depressed to the observed minimum level after 75 s, but the subsequent predicted vessel level recovery upon intact loop seal clearing at ~100 s was only half that observed. After intact loop seal clearing, the calculation had more water in the downcomer and less in the vessel than measured.

This discrepancy was then exacerbated by the differences in observed and predicted accumulator injection flows. The data showed the lower plenum staying essentially full throughout the transient; the calculation showed substantial void in the lower plenum starting after about 20 s, with significant liquid in the core heated length above the lower plenum. Late in the transient, at ~250 s, the calculation showed liquid appearing in the upper plenum, above a substantially voided core heated length. These results both suggest that more phase separation and/or less entrainment is needed in the vessel, to ensure the liquid inventory is being distributed correctly.

Uncertainties in the upper head flow paths made modelling the upper head response a matter of trial and error. The upper head in the calculation initially drains too quickly, but at later times has more water remaining than was measured. A few studies with different support column, guide tube and bypass flow areas and resistances were done, but the discrepancies were not judged important enough to justify the resource spending required for resolution.

The calculated core thermal response reflects the discrepant vessel hydraulic response just discussed. The delayed flow stagnation and associated retarded vessel level depression and core uncover resulted in a delayed core rod heatup. This later predicted dryout and heatup, combined with intact loop seal clearing and vessel level recovery at the correct time, produced lower core temperatures. The underprediction of core heatup resulted in reduced steam generation and superheat helping to maintain the primary system pressure in mid-transient. The lower pressures predicted caused earlier and more accumulator injection than occurred, resulting in more water in the vessel and an earlier total quench by the end of the transient period analyzed.

The calculated rod temperatures are progressively more discrepant compared to data both in transient time and in core elevation. The deviations seen in the lowest core levels, after the initial heatup and rewet, are primarily due to differences in saturation temperature due to mispredicting the primary system pressure in the 100-200 s time period. At slightly higher core elevations, there is also a discrepancy at later times due to missing the magnitude of the inventory boiloff after loop seal clearing; the duration of this late-time inventory boiloff before accumulator-driven refill is also underpredicted. The lower rod temperatures throughout the core in the calculation generate less superheated steam and allow more of a two-phase mixture to exist in the core so that, at the higher core elevations, the calculated rod temperatures are lower due to less depleted heat removal capacity in the adjacent fluid flow.

After our basecase analysis was completed, a purely 1-D model was developed to allow us to assess the new PLENUM component by comparing final results to those obtained with our equivalent 3-D VESSEL model. The purely 1-D model ran about twice as fast as the equivalent 3-D vessel model, but the results of the two models diverged significantly for a number of major variables, with the 3-D vessel model generally in better agreement with data. Further analysis showed the 1-D model predicting an unphysical void fraction profile, with a "discontinuity" (i.e., a density gradient inversion) at the component boundary between the lower plenum TEE and CORE.

This result was given to the code developers at LANL. After some examination, they determined that the key lay in the code assumption of inverted annular flow in the 1-D CORE component. This inverted annular flow regime is not documented in the TRAC manual, is limited to 1-D components with generalized heat slabs only, and is explicitly disallowed at the component boundaries (explaining the dependence of our results on the location of the component boundary). The use of this inverted annular flow regime can be affected by changing an undocumented NAMELIST variable, INVAN. The default value of zero causes the inverted annular flow regime to be considered whenever the temperature is greater than saturation; setting this flag to one causes this flow regime to be allowed only when the temperature is greater than the critical heat flux temperature, T-CHF (which seems more physically reasonable).

Before evaluating the impact of changing the inverted annular flow option, we had to obtain additional error corrections from LANL, correcting the T-CHF calculation so that the INVAN flag would have the proper effect. After this was done, we reran our (basecase) 1-D model calculation for the transient period being analyzed, with the new code error corrections, setting INVAN=1. The new void fraction profiles from this "final" 1-D calculation were more like step functions than the more smoothly varying 3-D profile, but the unphysical density inversion had been eliminated. However, the 3-D model results were still generally in better overall agreement with data than the final 1-D model results. This was a surprising final result, as the design and scaling of the facility is such as to preclude any significant 3-D effects in Semiscale experiments.

As is unfortunately usual in analyses of Semiscale tests, facility configuration uncertainties preclude definitive conclusions on code abilities (i.e., whether TRAC per se or the pump curve input was ultimately responsible for the substantial underprediction of core heatup in this test). However, our analyses identified significant nodalization sensitivities in the code results, affected by a previously undocumented input option and flow regime. Given the expected tendency for users to construct purely 1-D models in order to take full advantage of the fast-running two-step numerics, we feel that the results of our 3-D/1-D noding study indicate the need for more assessment and publicity of such noding sensitivities.

7.0 REFERENCES

1. TRAC-PF1/MOD1: An Advanced Best-Estimate Computer Program for Pressurized Water Reactor Thermal/Hydraulic Analysis (DRAFT), Safety Code Development Group, Energy Division, Los Alamos National Laboratory, 1983.
2. W. Riebold, et.al., Specifications: LOBI Pre-Prediction Exercise, Influence of PWR Primary Loops on Blowdown (LOBI), Technical Note No. I.06.01.79.25, Commission of the European Communities, J.R.C.-Ispra, February, 1979.
3. L. Piplies and J. Bachler, Single-Phase Performance Characteristics of the LOBI Pump, Technical Note No. I.06.01.79.80, Commission of the European Communities, J.R.C.-Ispra, August 1979.
4. L. Piplies and W. Kolar, Preliminary Two-Phase Performance Characteristics of the LOBI Pump (Curves for Fully Degraded Head), Technical Note No. I.06.01.81.13, Commission of the European Communities, J.R.C.-Ispra, February 1981.
5. E. Ohlmer, et.al., Pressure Drop Behavior of the LOBI Installation, EUR 6971 EN, Commission of the European Communities, J.R.C.-Ispra, September 1980.
6. M. L. Patton, Semiscale Mod-3 Test Program and System Description, NUREG/CR-0239, TREE-NUREG-1212, Idaho National Engineering Laboratory, July 1978, Revision B, January 1981.
7. G. W. Johnsen, Semiscale System Description, Handout at Joint LOFT/Semiscale Modelling Workshop, August 18-19, 1981, at Idaho Falls, ID.
8. M. T. Leonard, RELAP5 Standard Model Description for the Semiscale Mod-2A System, EGG-SEMI-5692, Idaho National Engineering Laboratory, December 1981.
9. T. J. Boucher, Experiment Operating Specification for Semiscale Mod-2A Experiment S-IB-3, EGG-SEMI-5787, Idaho National Engineering Laboratory, February 1982.
10. T. J. Boucher and M. T. Leonard, Quick Look Report for Semiscale Intermediate Break Test S-IB-3, EGG-SEMI-6013, Idaho National Engineering Laboratory, August 1982.
11. K. E. Sackett and L. B. Clegg, Experiment Data Report for Semiscale Mod-2A Intermediate Break Test Series (S-IB-3), NUREG/CR-2738, EGG-2198, Idaho National Engineering Laboratory, June 1982.
12. C. Addabbo, G. De Santi and L. Piplies, Quick Look Report on LOBI Test B-RIM, Communication LQC 82-08, Commission of the European Communities, J.R.C.-Ispra, March 1982.
13. T. Fortescue, LOBI Test B-RIM: Preliminary Data Report, Techn. Note No. I.06.01.81.153, Commission of the European Communities, J.R.C.-Ispra, December 1981.

14. E. Ohlmer and J. Sanders, Experimental Data Report on LOBI Test B-RIM, LEC 82-08, Commission of the European Communities, J.R.C-Ispra, April 1982.
15. L. N. Kmetyk, TRAC-PF1/MOD1 Independent Assessment: LOBI Intermediate Break Test B-RIM, NUREG/CR-3970P, SAND85-2264, Sandia National Laboratories, February 1986.
16. J. M. McGlaun and L. N. Kmetyk, RELAP5 Assessment: Semiscale Natural Circulation Tests S-NC-2 and S-NC-7, NUREG/CR-3258, SAND83-0833, Sandia National Laboratories, May 1983.
17. A. C. Peterson, RELAP5 Assessment: Semiscale Small Break Tests S-UT-1, S-UT-2, S-UT-6, S-UT-7 and S-UT-8, NUREG/CR-3772, SAND84-0884, Sandia National Laboratories, November 1984.
18. L. D. Buxton and L. N. Kmetyk, TRAC-PF1/MOD1 Independent Assessment: PKL Natural Circulation Tests, NUREG/CR-4423, SAND85-2181, Sandia National Laboratories, to be published.
19. D. Dobranich, TRAC-PF1/MOD1 Independent Assessment: B&W 19-Tube Once-Through Steam Generator Tests, NUREG/CR-3877P, SAND84-1229, Sandia National Laboratories, July 1984.
20. D. Dobranich, TRAC-PF1/MOD1 Independent Assessment: Semiscale Mod-2A Feedwater-Line Break (S-SF-3) and Steam-Line Break (S-SF-5) Tests, NUREG/CR-4189, SAND85-0576, Sandia National Laboratories, November 1985.
21. T. J. Boucher and R. A. Dimenna, Semiscale Mod-2A Intermediate Break Test Series - Test Results Comparison, NUREG/CR-3126, EGG-2238, Idaho National Engineering Laboratory, January 1983.
22. G. G. Loomis, Experiment Operating Specification for Semiscale Mod-2C 5% Small Break Loss-of-Coolant Experiment S-LH-1, EGG-SEMI-6813, Idaho National Engineering Laboratory, February 1985.

APPENDIX I

SEMISCALE MOD-2A FACILITY

The standard Semiscale Mod-2A system [6-8], shown in Figure AI.1, consists of a vessel with its associated internals and an external downcomer, an intact loop and a broken loop both with active steam generators and pumps, a break effluent measuring system and a steam generator secondary system. Other subsystems include the emergency core cooling system, external heat loss makeup system, leakage makeup system and a noncondensable gas injection system. The Semiscale system was scaled from a reference PWR system based on the core power ratio, 2/3411; component elevations, dynamic pressure heads and liquid distribution were maintained as similar as practical, most notably in the design of a full-length core, full-length upper plenum and upper head, and full-height steam generators. The major primary coolant system elevations are given in Table AI.1.

The intact loop consists of a steam generator, primary coolant pump, and pressurizer connected by piping; the intact loop piping itself is composed of individual pipe sections called spool pieces. These spool pieces and their relative locations in the intact loop are identified by spool numbers in Figure AI.2; the upper drawing unfolds the intact loop for easier viewing by preserving the orientation of the components in the vertical plane without regard to the actual horizontal orientation, which is shown in the lower drawing. The spool piece lengths and blueprint numbers are given in Table AI.2. The intact loop piping, other than the vertical spool pieces leading to the steam generator inlet and outlet (spools 4 through 12) and spool 3, are constructed of 3-in. Sch 160 Type 316 stainless steel pipe; spool pieces 3 through 12 are constructed of 2-1/2-in. Sch 160 pipe. The intact loop pump is a volute-type, heavy duty, horizontal centrifugal pump; a venturi is located in the pump discharge to increase the flow resistance.

The broken loop is designed to simulate a single loop of a four-loop PWR; in addition to a break assembly (not present during the natural circulation tests), it also contains an active steam generator and pump. The spool pieces in the broken loop are constructed of 1-1/2-in. Sch 160 Type 316 stainless steel piping; these spool pieces and their relative locations in the broken loop are identified by spool numbers in Figure AI.3, and the corresponding spool piece lengths and blueprint numbers are given in Table AI.3. The broken loop pump is a high-speed vertical centrifugal pump with a bottom suction and side discharge, similar to PWR pumps. The break simulator for S-IB-3 is designed to simulate a centerline communicative break. As shown in Figure AI.4, the break simulator includes a converging diverging nozzle, which provides the proper break area, and an instrumented spool piece located downstream of the break assembly. The transient is initiated by overpressurizing a rupture disk downstream of the instrumented spool piece.

The intact and broken loop steam generators, shown in Figure AI.5 and summarized in Table AI.4, consist of a two-pass tube and shell design with primary fluid flowing through vertical inverted U-shaped tubes and secondary coolant passing through the shell side. With the secondary side operating at saturation conditions, a centrifugal separator at the top of the riser or boiler section increases the exit quality of the steam rising through the steam dome and out a discharge line,

while liquid separated from the steam falls down a downcomer outside the boiler shroud creating a recirculation flow path. The intact loop steam generator has two short, two medium and two long tubes representative of the range of bend elevations in a PWR steam generator, while the broken loop steam generator contains just one short tube and one long tube. The same tube stock (2.22 cm, 0.124 cm wall) and tube spacing (3.175 cm triangular pitch) used for PWR U-tubes are used in this "Type II" steam generator. Since the heat transfer area is specified based on the ratio of PWR to Semiscale primary system volume, the number of tubes is thereby fixed by the specified tube diameter and lengths.

Fillers are installed on the shell side in both the boiler and downcomer regions to provide a more properly scaled secondary fluid volume. The addition of these filler pieces not only reduces the total secondary coolant volume, but also changes the flow geometry of the boiler and downcomer, as shown in the cross-sectional view in Figure AI.5. The boiler section filler pieces create a parallelogram-shaped flow channel along the length of the U-tubes, while the downcomer filler pieces reduce the downcomer annulus to a set of slotted flow channels. Baffle plates are located at several axial positions in the boiler section of the steam generator, creating a substantial flow restriction to the rising coolant. Feedwater enters the downcomer above the filler pieces at approximately the elevation of the top of the U-tubes; auxiliary feedwater is also added at this point. The elevations of the steam generator nozzles, plena and tubes are similar to those in a PWR; however, the steam dome is shorter than a PWR steam dome and the steam drying equipment is of a simpler and less efficient design. (As a result of these dissimilarities, the secondary fluid operating level at full power conditions is about 75% of the operating level in a PWR, with the lower level required to ensure stable steam generator operation.)

The pressurizer, which is connected to the intact loop hot leg, is shown in Figure AI.6. The pressurizer vessel is made of 10-in. Sch 160 Type 347 stainless steel pipe, is approximately 1.14 m high and has a total volume of 0.034 m³. Heat is supplied by 24 0.05-kW vertically-oriented electric heater rods, which are inserted in 2.2 cm stainless steel tubes sealed at the bottom. A pressurizer spray system is not included in the Mod-2A system. The pressurizer operates in a manner similar to its counterpart in a large PWR in that the vessel is partially filled with water and maintained at a saturation temperature corresponding to the desired system pressure. The pressurizer surge line and tubing (1.27 cm OD, 0.165 cm wall, ~2.7 m length and ~1.53 m total elevation drop from bottom of pressurizer vessel to hot leg centerline) is sized for a flow restriction that provides representative flow rates.

The Mod-2A vessel, shown in Figure AI.7, consists of a multi-section pressure vessel containing a lower plenum, heated core, upper plenum and upper head, and an external inlet annulus and downcomer. The pressure vessel is constructed primarily of 6-in. Sch XXS stainless steel pipe, with stainless steel Grayloc clamps used to connect the various vessel sections; the complete pressure vessel is approximately 10 m long.

The upper head region, shown in more detail in Figure AI.8, is contained within the top ~25% of the pressure vessel, and contains ports for upper head ECC injection, a filler to provide the proper upper head internal volume, an insulator designed to provide a steam gap between the filler ID and the insulator OD, and a simulated control rod guide tube. An upper core support plate simulator forms the

boundary between the upper head and upper plenum regions; this upper core support plate provides support for the simulated guide tube and for the upper ends of the two simulated core support columns which extend down through the upper plenum region. Approximately 4% of the total primary coolant flow into the vessel bypasses the downcomer and core through an external upper head bypass line from the top of the downcomer inlet annulus to the upper head. The bypass coolant rejoins the heated coolant in the vessel upper plenum via the simulated control rod guide tube and core support columns. The exit of the upper head bypass line standpipe and the inlets of the control rod guide tube and core support columns are at different elevations within the upper head.

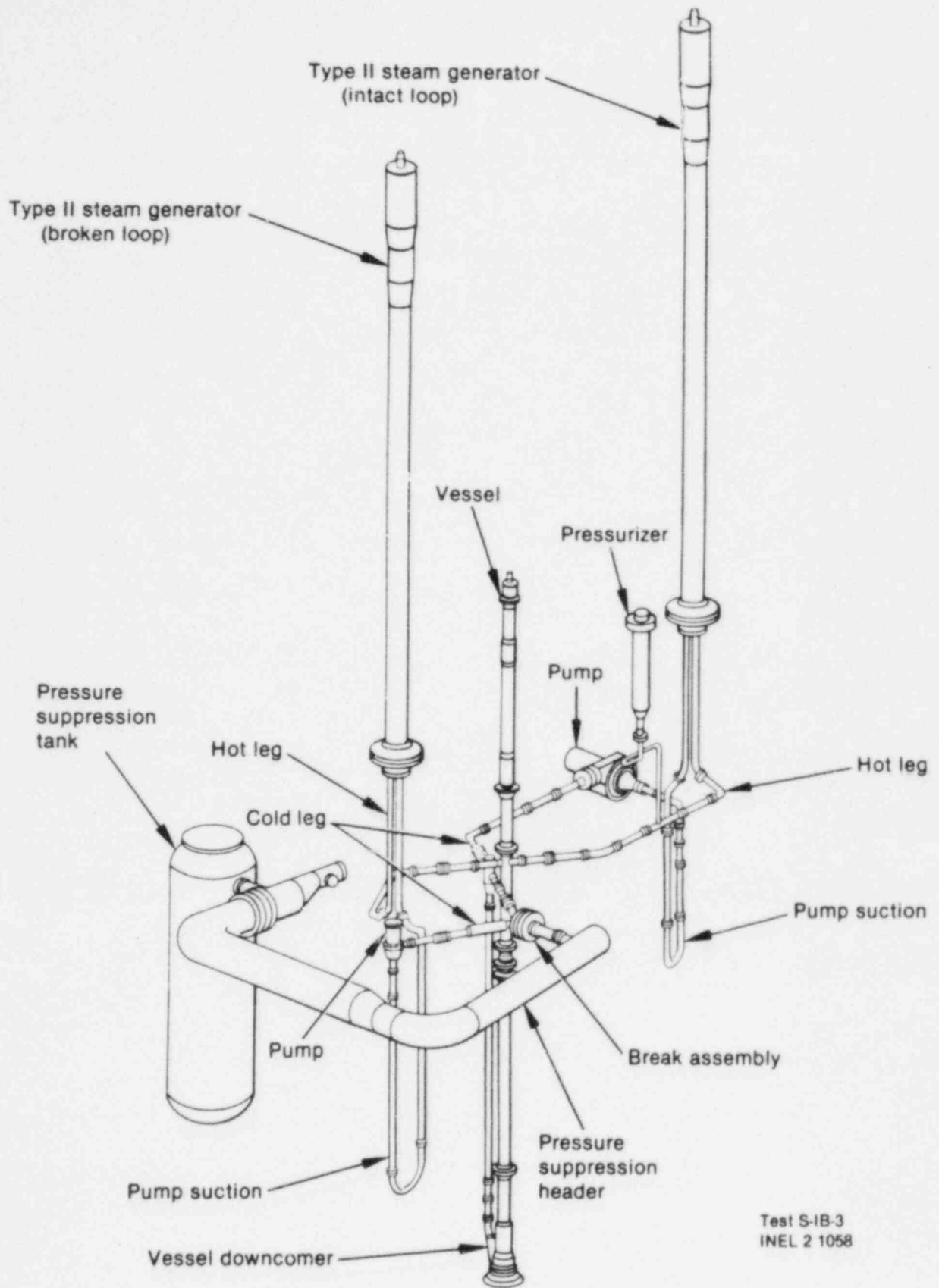
The upper plenum region, shown in more detail in Figure AI.9, extends from the upper core support plate to the top of the heated core region, and is approximately 2.5 m long. The upper and lower sections of the upper plenum contain fillers and insulators similar to those in the upper head. Two hot leg nozzles extend from the vessel upper plenum approximately 21.6 cm above the cold leg centerline to provide connections for the intact and broken loop hot leg piping. The flow path above the core to the hot leg nozzles is quite tortuous; in addition to a core flow measurement assembly, a simulated control rod guide tube and two simulated core support columns obstruct the flow path, and a short set of vertical tubes creates a horizontal flow restriction across the vessel at the hot leg elevation. This flow restrictor assembly simulates the flow restriction in a PWR caused by control rod guide tubes and core support columns. Above the hot legs, the upper plenum contains a significant amount of fluid which is not involved in the main flow path. The simulated control rod guide tube and core support columns extend from the upper head through the upper plenum and terminate open-ended in the upper core plate located in the heater ground hub which forms the boundary between the upper plenum and the top of the active heated core region. The guide tube is slotted in the upper plenum region.

The 3.66 m heated length of the core, shown in Figure AI.10, extends downward from the heater rod ground hub to the top of the mixer box (approximately 4.96 m below the cold leg centerline), which separates the core and the lower plenum regions. This figure includes a cross-sectional view of the Mod-2A vessel over the core region. The 25-rod electrically heated core is enclosed in a square housing with no coolant bypass. The heater rods, 1.07 cm in diameter, are positioned and held in the core with 10 grid spacers (at elevations shown in Figure AI.11) which maintain the heater rods on a typical PWR pitch of 1.43 cm. The 16 peripheral rods are powered separately from the 9 central rods, permitting a radial profile (although normally no radial peaking is simulated); two of the 16 peripheral rods, however, are not powered. The Semiscale Mod-2A heater rod design consists of a helically-wound constantan filament, electrically insulated from the dual-sheath stainless steel clad by compacted boron nitride powder. Chromel-alumel thermocouples are swaged between cladding sheaths in six symmetrical polar locations and ten axial elevations distributed along the rod. The heater rods have a symmetric chopped-cosine axial power distribution (shown in Figure AI.11); the peak-to-average power ratio is 1.55.

The lower plenum, shown in Figure AI.12, consists of an annular region between the flow mixer box and the pressure vessel, which serves to distribute flow from the downcomer pipe around the vessel periphery, and a lower head chamber region below

the mixer box which approximates the scaled volume of a PWR lower plenum. (The lower plenum is the only part of the vessel which is not height-scaled.) Coolant flow from the downcomer distribution annulus changes direction within the lower head, turning up into the core housing. A simulated lower core plate at the entrance of the core housing provides a significant reduction in coolant flow area. The outer walls of the downcomer distribution annulus and the lower head are lined with honeycomb insulation to reduce heat transfer between the outer vessel wall and the fluid in the lower plenum. The heater rods pass through the length of the lower plenum and penetrate the vessel through the bottom head. There is a drain line in the lower plenum (not shown in the figure) that allows controlled draining of the vessel so that the system mass inventory can be varied.

Coolant enters the vessel through an external downcomer inlet annulus (shown in Figure AI.9). This annular entrance section reduces to an instrumented pipe over the major length of the lower vessel, until the bottom of the downcomer rejoins the vessel at the lower plenum through an annular distribution annulus, as shown in Figure AI.12. The downcomer pipe is fabricated from 3-in. Sch 160 pipe, and the inner wall of the downcomer pipe is lined with a honeycomb insulator to limit heat transfer between the pipe wall and the fluid. An instrumented spool piece provides the connection between the lower end of the downcomer pipe and the downcomer nozzle connecting to the downcomer distribution annulus. The inlet annulus assembly contains the cold leg nozzles and is designed to provide an annular inlet geometry similar to that in a PWR. Both surfaces of the inlet annulus are covered with insulators that maintain a steam gap to isolate the fluid from the hot walls of the assembly. The lower end of the inlet annulus contains a transition section that funnels the flow into the downcomer pipe. The downcomer inlet annulus is connected to the vessel upper head with 1/2-in. tubing which simulates the bypass flow paths in a PWR; as already mentioned, about 4% of the total combined loop flows is routed through the bypass line into the upper head.



Test S-IB-3
INEL 2 1058

Figure AI.1 Isometric View of the Semiscale Mod-2A System

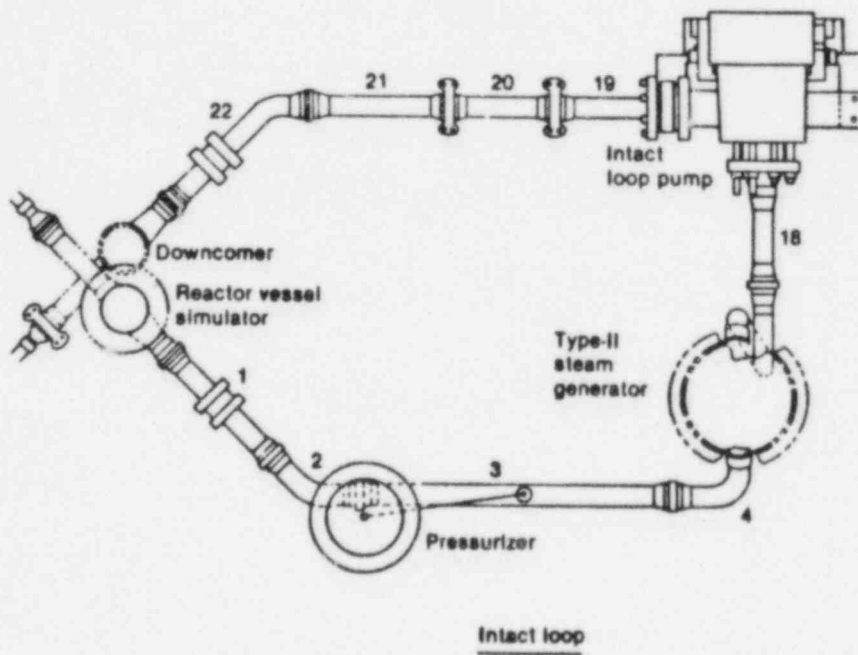
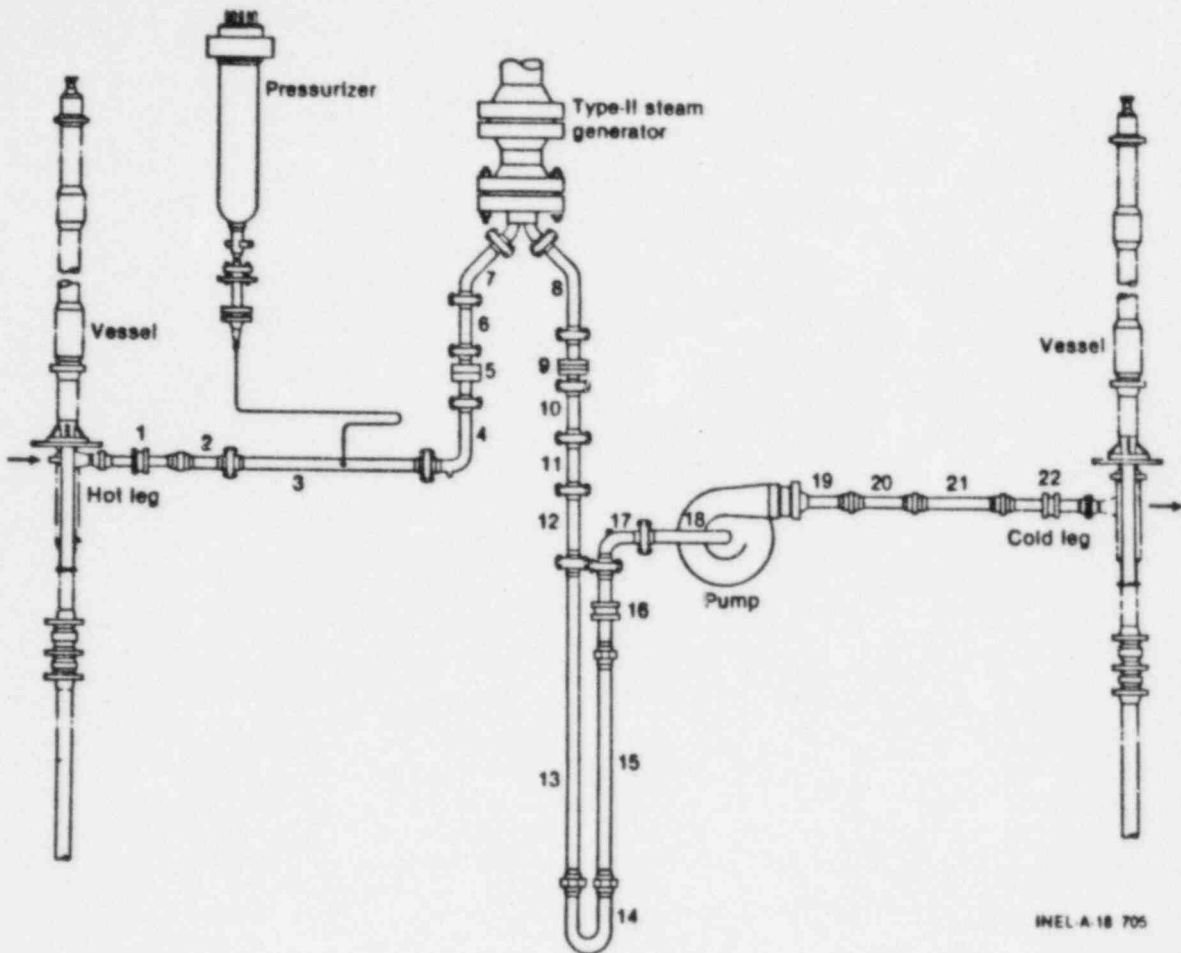


Figure A1.2 Semiscale Mod-2A Intact Loop Spool Pieces

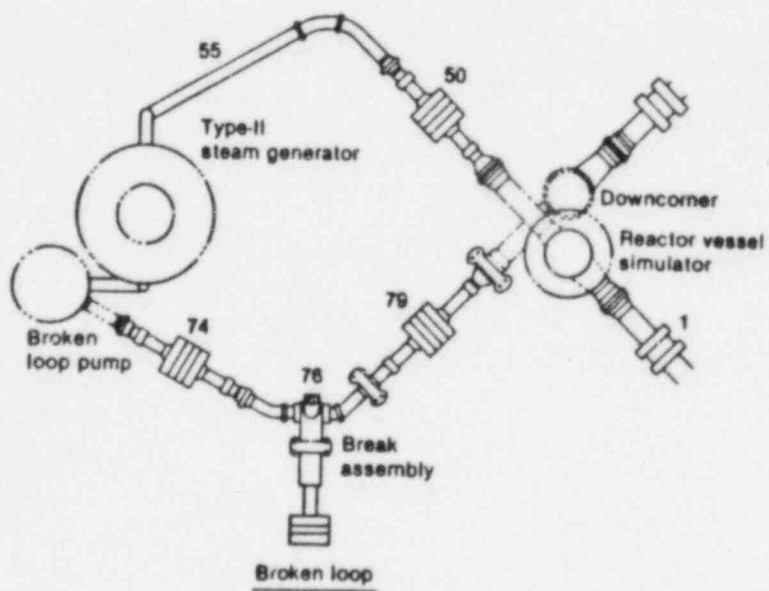
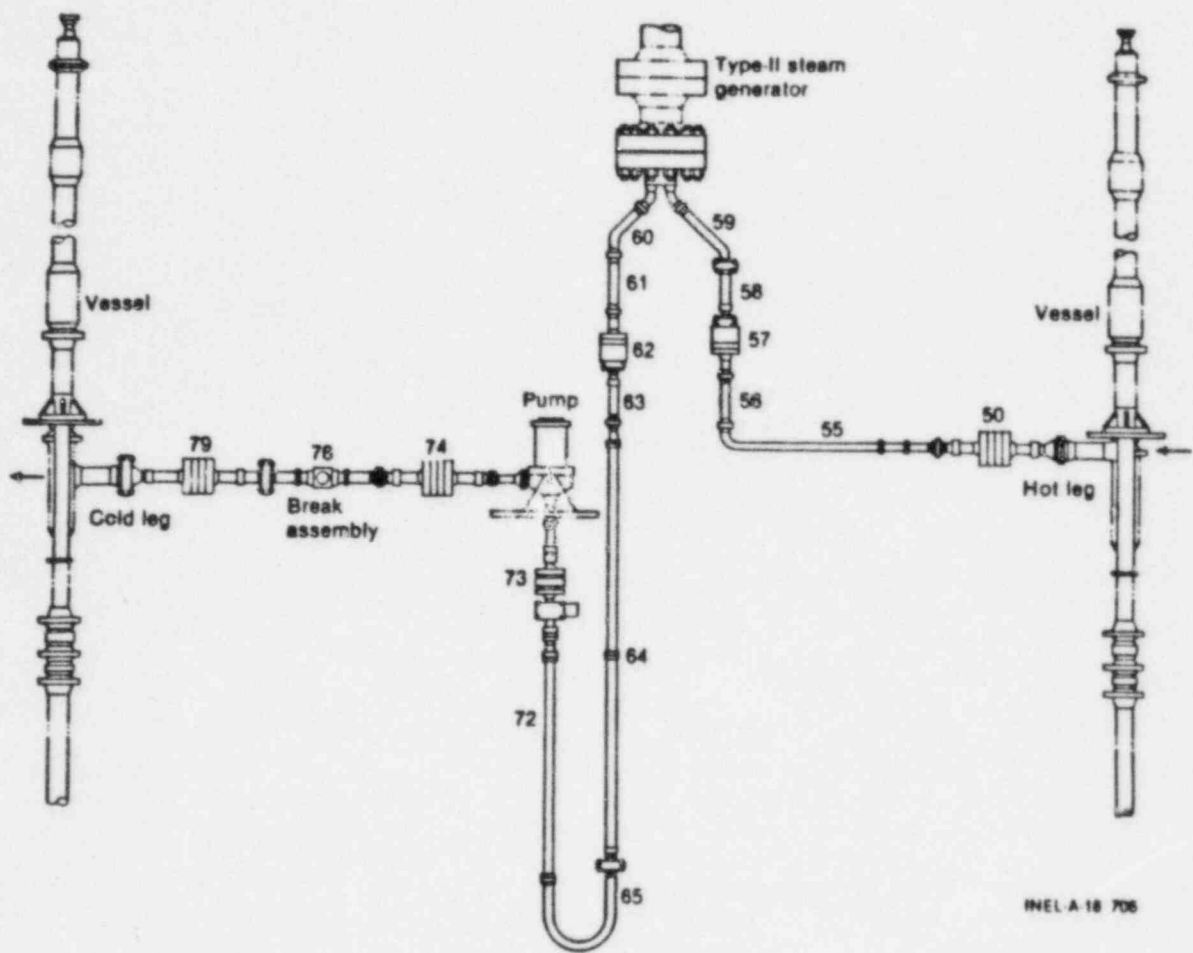
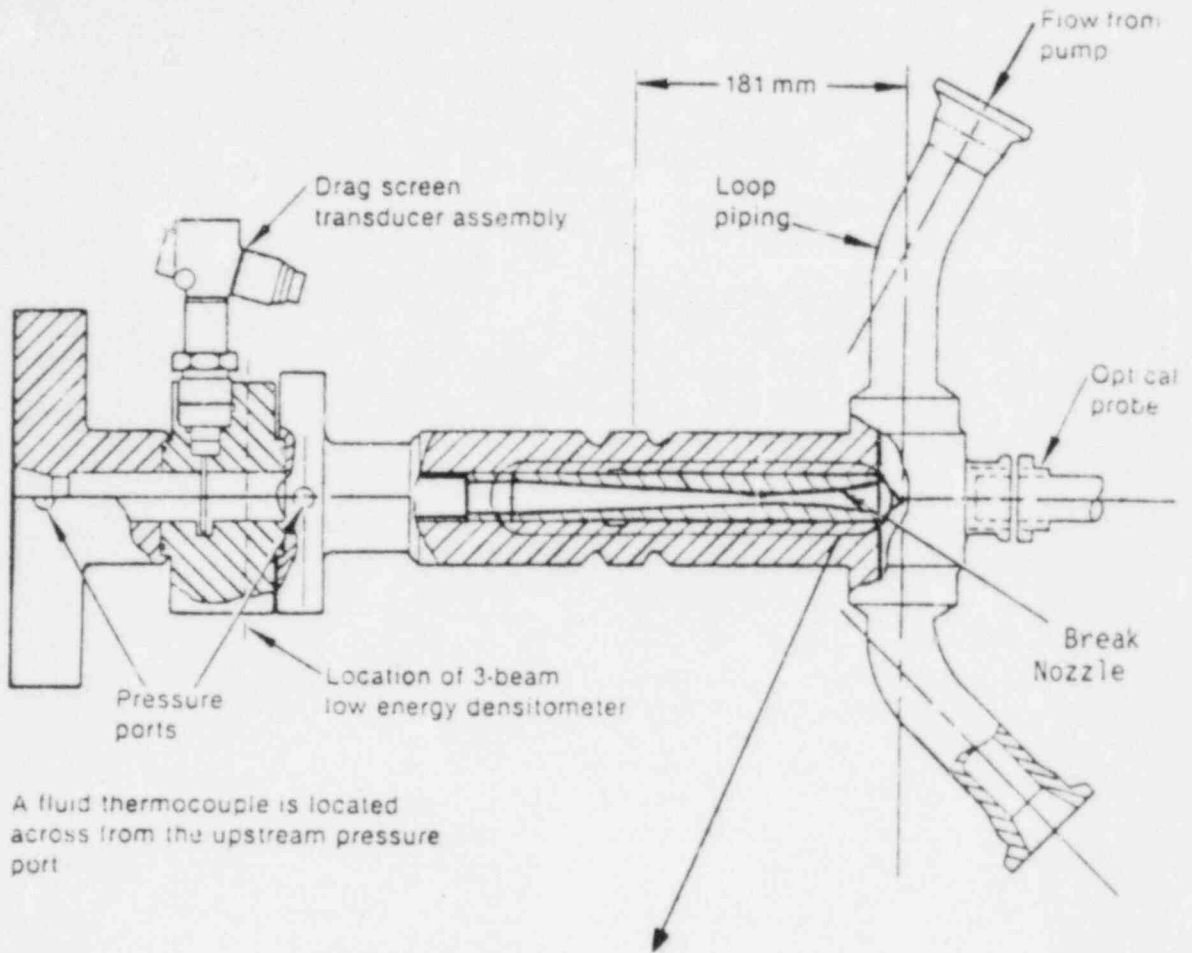


Figure AI.3 Semiscale Mod-2A Broken Loop Pool Pieces



21.7% Break Nozzle
(All dimensions in mm)

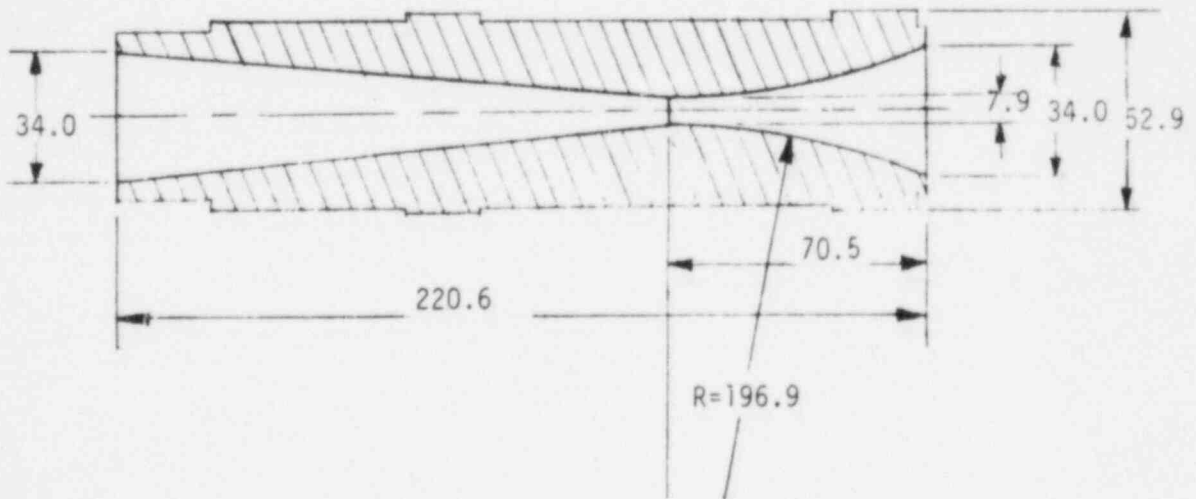


Figure AI.4 Break Simulator for Semiscale Test S-IB-3

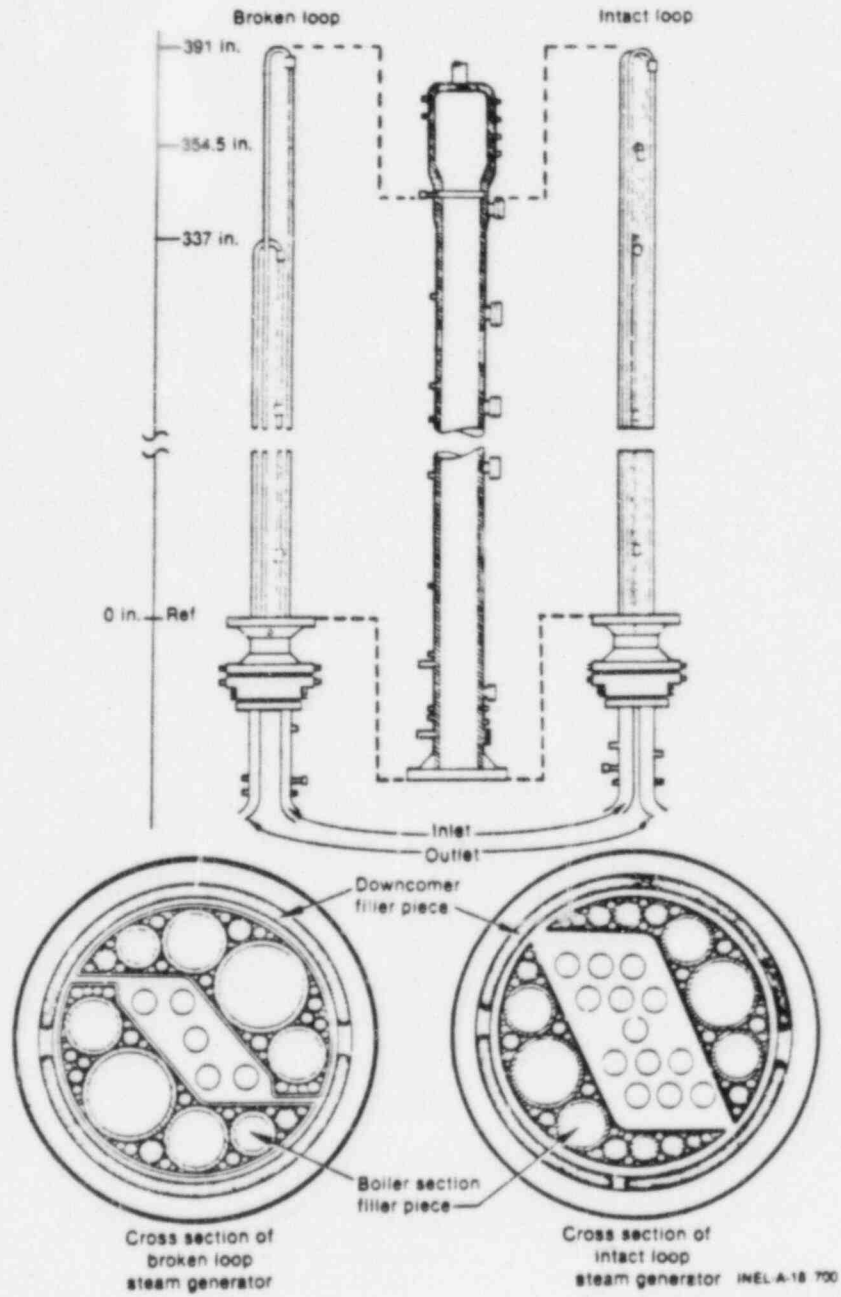


Figure AI.5 Semiscale Mod-2A Steam Generator Assembly

PRESSURIZER

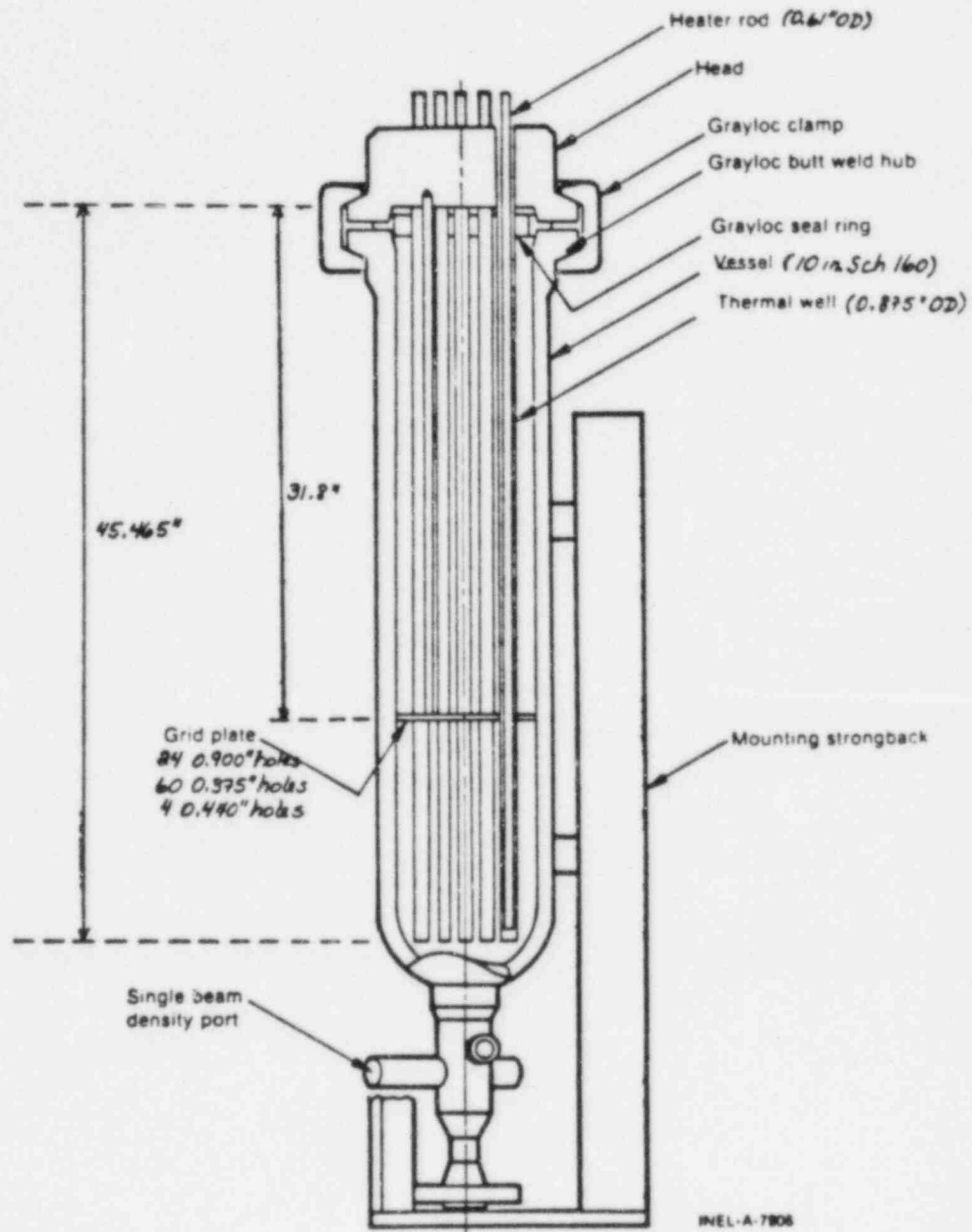


Figure A1.6 Semiscale Mod-2A Pressurizer Vessel

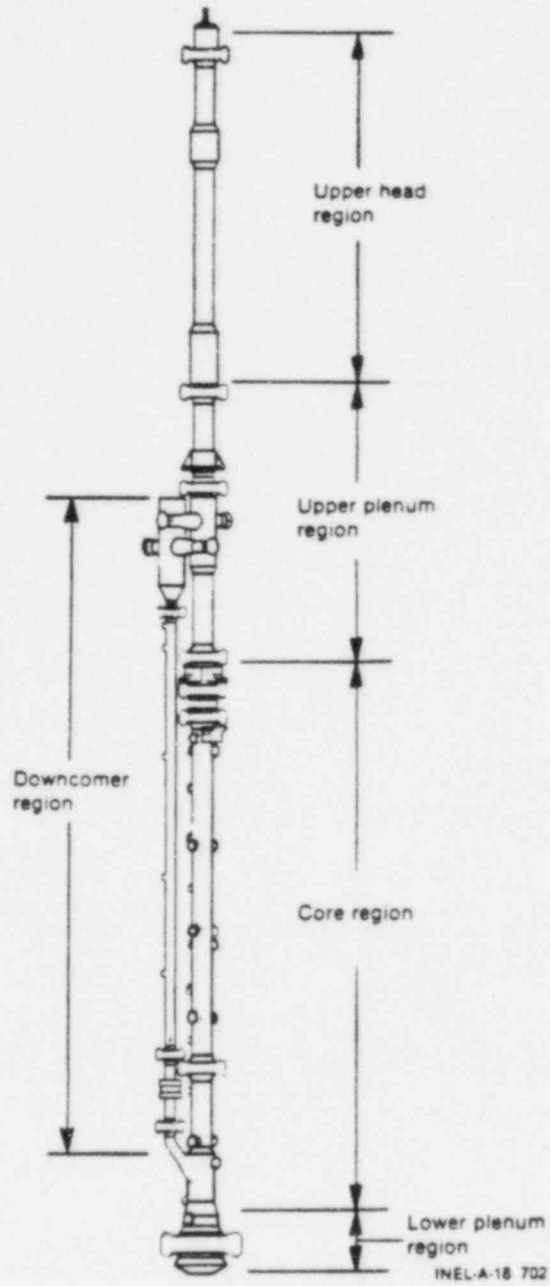


Figure AI.7 Semiscale Mod-2A Vessel Assembly

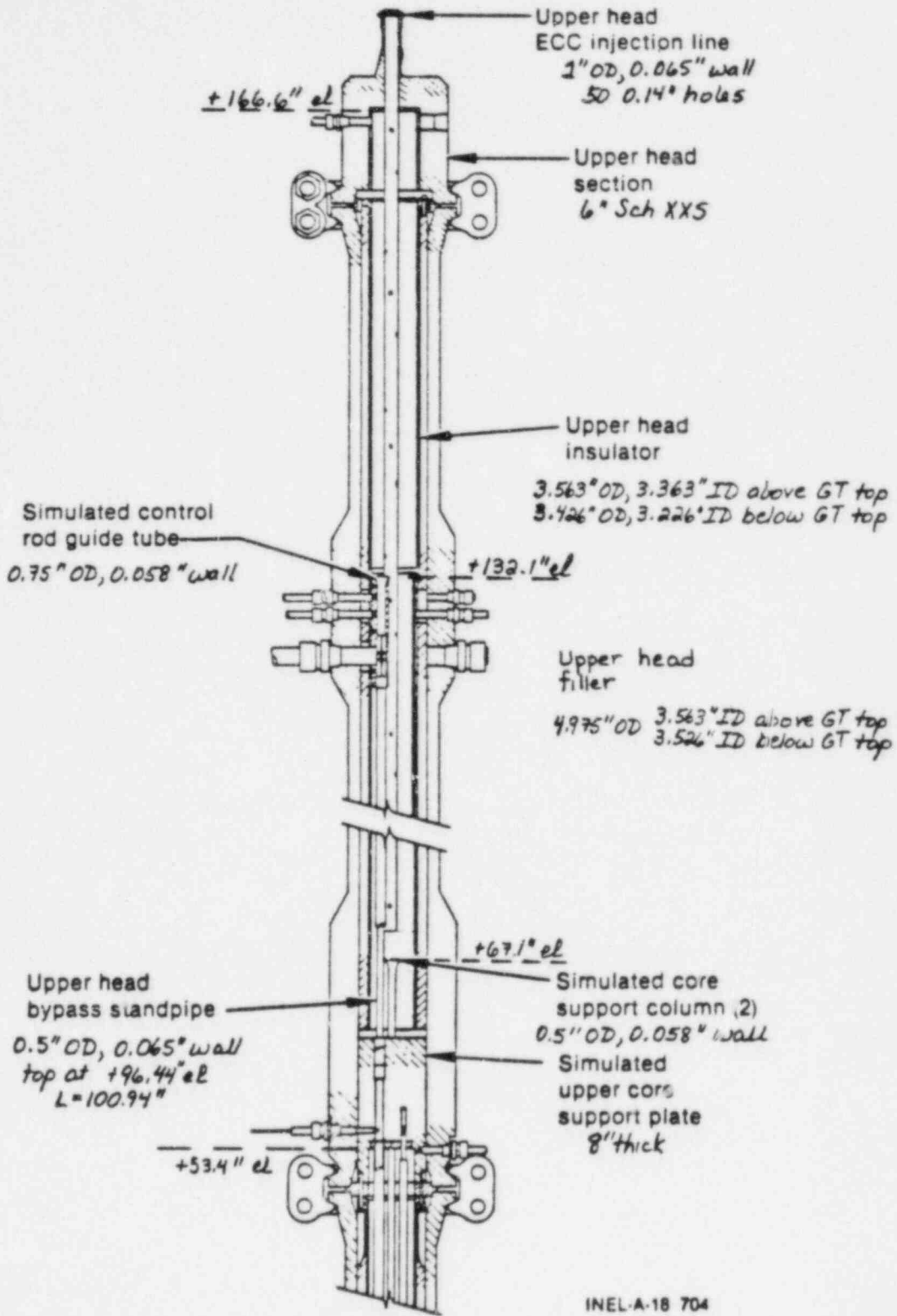


Figure AI.8 Semiscale Mod-2A Vessel Upper Head Region

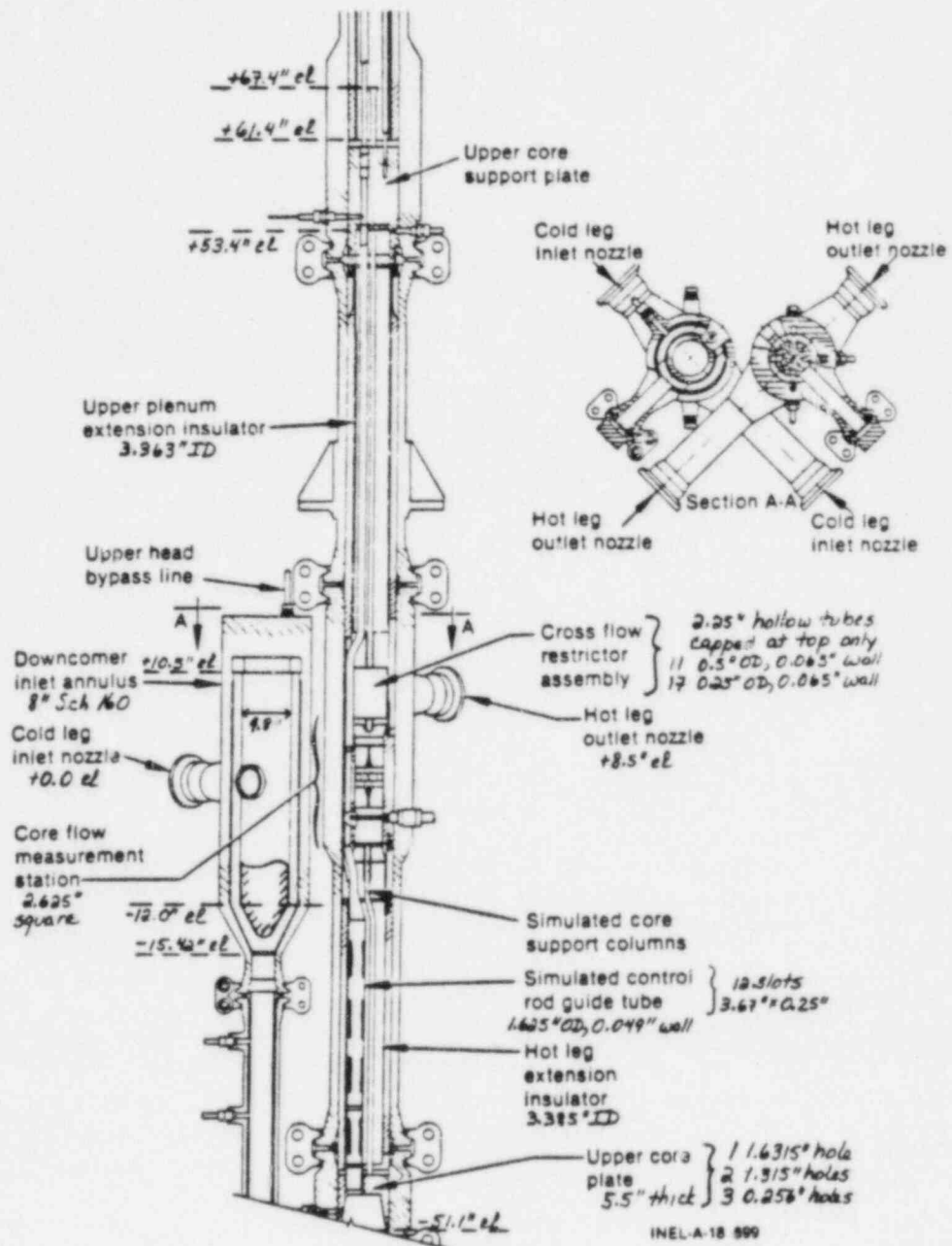


Figure AI.9 Semiscale Mod-2A Vessel Downcomer Inlet and Upper Plenum Region

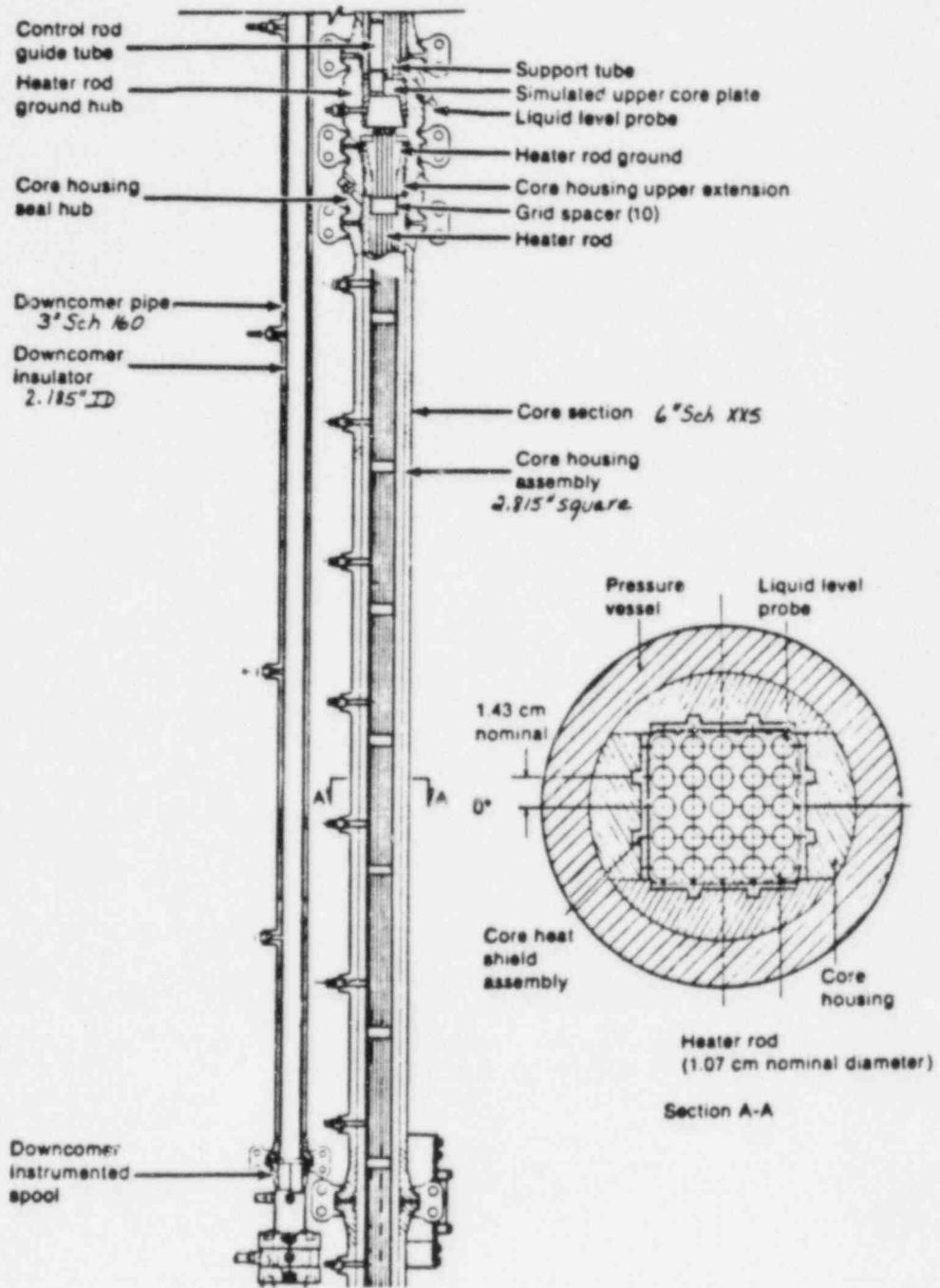


Figure A1.10 Semiscale Mod-2A Vessel Core Region

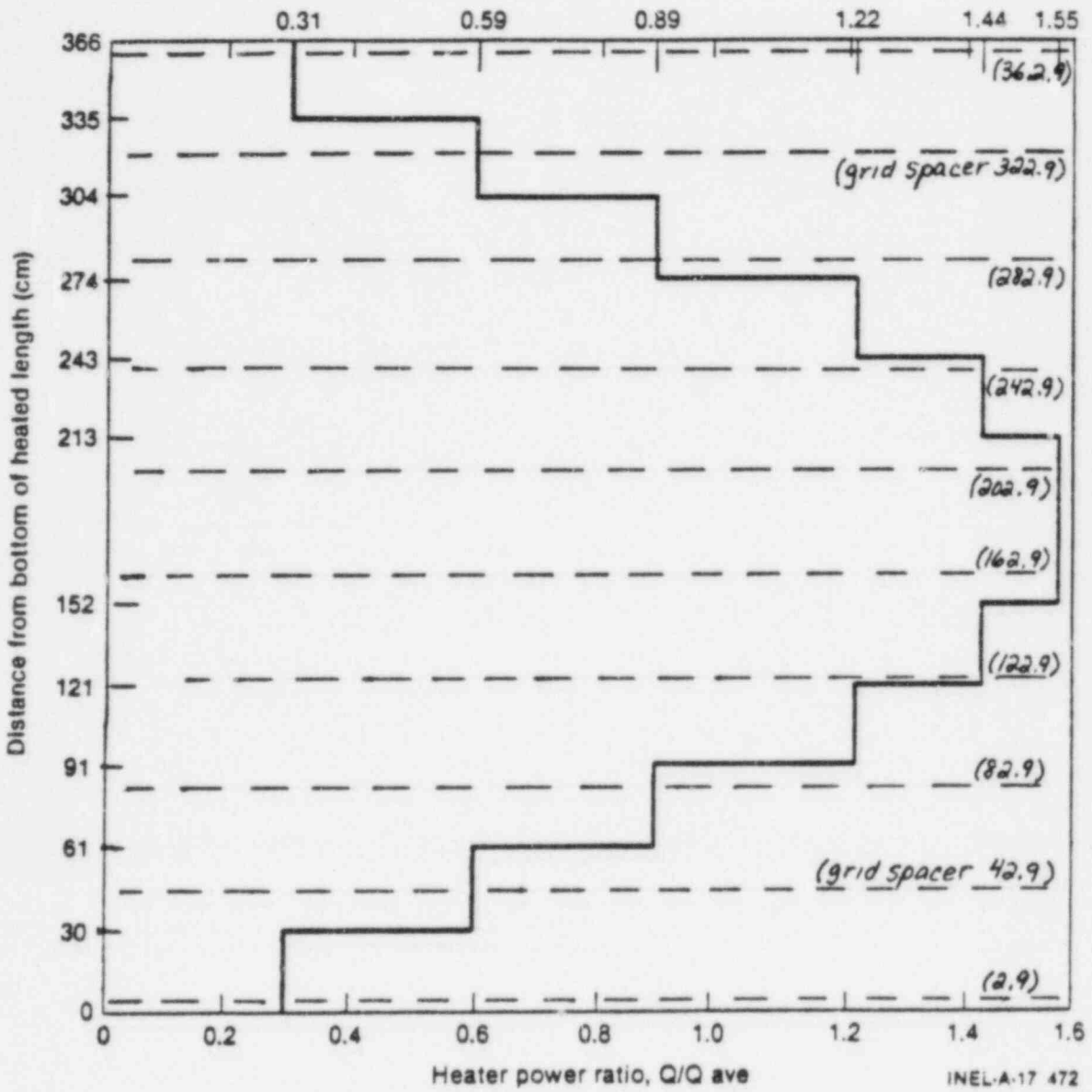


Figure AI.11 Semiscale Mod-2A Core Axial Power Profile

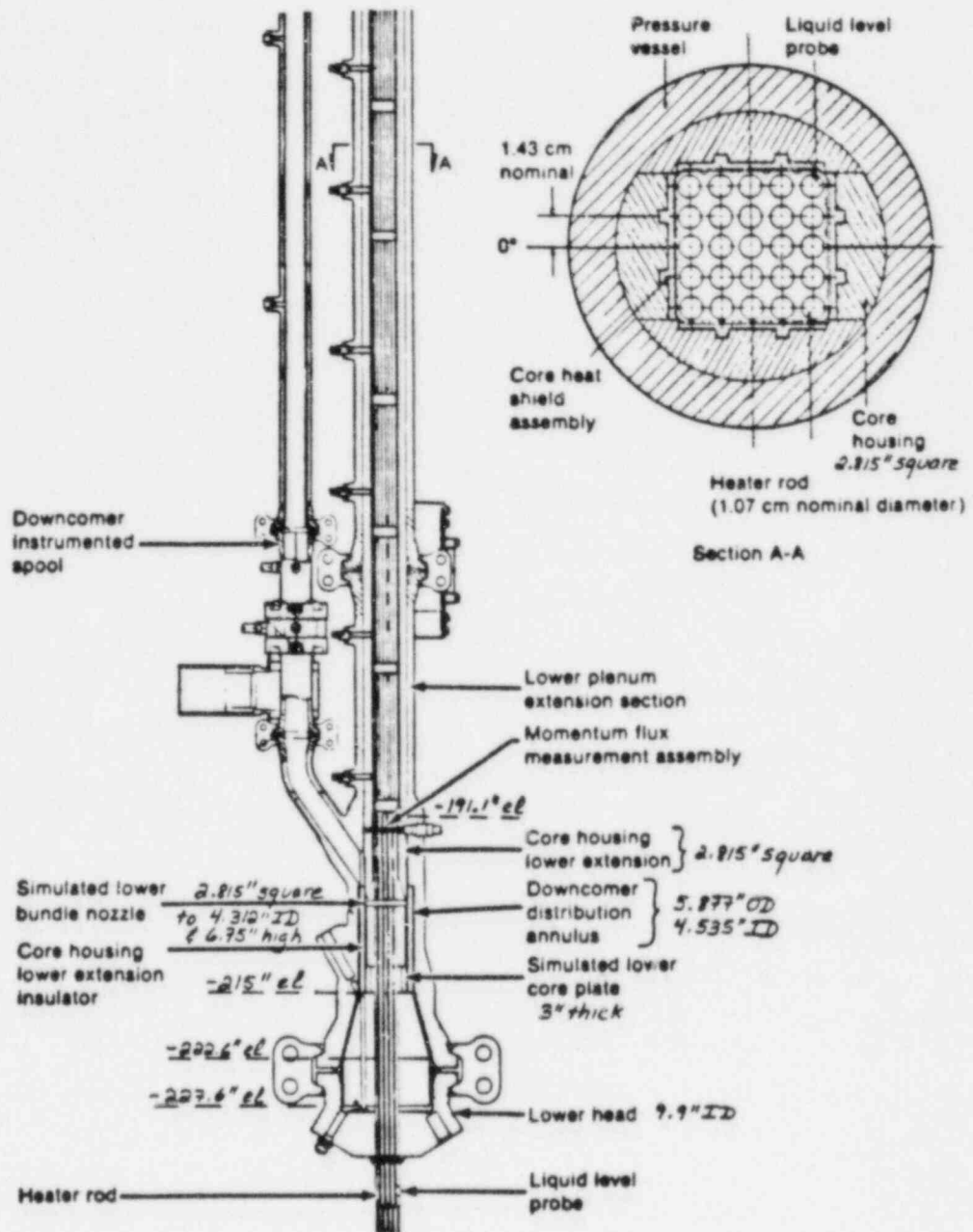


Figure AI.12 Semiscale Mod-2A Vessel Lower Plenum and Lower Downcomer Region

Table A1.1 Semiscale Primary Coolant System Elevations

<u>LOCATION</u>	<u>ELEVATION (IN.)</u>
VESSEL	
TOP OF UPPER HEAD	+166.6
TOP OF GUIDE TUBE	+132.1
BOTTOM OF UHI INJECTION TUBE	+127.1
TOP OF CORE SUPPORT TUBES	+67.1
TOP OF UPPER SUPPORT PLATE	+61.4
BOTTOM OF UPPER SUPPORT PLATE	+53.4
HOT LEG NOZZLE CENTERLINE	+8.5
COLD LEG NOZZLE CENTERLINE	0.0
TOP OF HEATED CORE	-51.1
BOTTOM OF HEATED CORE	-191.1
TOP OF LOWER PLENUM	-215.0
BOTTOM OF LOWER PLENUM	-227.6
INTACT LOOP	
BOTTOM OF STEAM GENERATOR TUBE SHEET	+81.6
SHORT TUBE TOP, SPILLOVER	+436.9
MIDDLE TUBE TOP, SPILLOVER	+465.4
LONG TUBE TOP, SPILLOVER	+491.9
PUMP SUCTION CENTERLINE	-111.0
BOTTOM OF PRESSURIZER INTERNAL VOLUME	+68.8
TOP OF PRESSURIZER INTERNAL VOLUME	+117.3
BROKEN LOOP	
BOTTOM OF STEAM GENERATOR TUBE SHEET	+81.6
SHORT TUBE TOP, SPILLOVER	+436.9
LONG TUBE TOP, SPILLOVER	+491.9
PUMP SUCTION CENTERLINE	-110.3

* ELEVATIONS ARE RELATIVE TO COLD LEG CENTERLINE

Table AI.2 Semiscale Intact Loop Spool Pieces

Spool Piece Number	Spool Piece Indent	Total Length (in)	Blueprint Number
H. L. Nozzle		8.65	407968
1	3-PC-1B	23.06	414684
2	3-PC-18	15.61	407346
3	2½-PC-2	52.51	415155
4	2½-PC-6	26.31	414431
5	2½-PC-7	13.995	414425
6	2½-PC-8	14.00	414426
7	2½-PC-9	19.195	414427
SG Inlet		6.32	414271
SG Outlet		6.32	414271
8	2½-PC-10	27.195	414428
9	2½-PC-11	13.995	414425
10	2½-PC-12	14.00	414426
11	2½-PC-13	14.00	414429
12	2½-PC-14A	19.41	414430
13	3-PC-20	85.25	409027
14	3-PC-20	20.638	409027
15	3-PC-20	62.00	409027
16	3-PC-20	23.06	414684
17*	3-PC-9A	19.319	404749
18*	3-PC-10A	20.53	408613
IL Pump*			
19*	3-PC-11A	17.00	412858
20*	3-PC-12	17.25	404759
21	3-PC-13	23.06	404794
22	3-PC-19A	37.90	414684
C. L. Nozzle		7.15	407986

* Replaced by pump replacement spool piece in all natural circulation tests (drawings 415276 through 415281).

Table A1.3 Semiscale Broken Loop Spool Pieces

Spool Piece Number	Spool Piece Indent	Total Length (in)	Blueprint Number
H. L. Nozzle	(3 in. Sch. 160)	16.07	407975
50	1½-ABL-1	24.01	407670
55	1½-ABL-14A	59.517	414670
56	1½-ABL-30	11.83	414671
57	1½-ABL-31	13.872	414672
58	1½-ABL-32	13.75	414673
59	1½-ABL-33	19.826	414674
SG Inlet		4.142	414272
SG Outlet		4.142	414272
60	1½-ABL-34	15.316	414675
61	1½-ABL-35	13.75	414676
62	1½-ABL-36	13.872	414672
63	1½-ABL-37	13.75	414673
64	1½-ABL-6A	109.17	414677
65	1½-ABL-7	33.834	407384
72	1½-ABL-9	61.82	407380
73	1½-ABL-11	27.56	407673
BL Pump			
74*	1½-ABL-12	23.64	407674
76*	1½-ABL-17	19.77	407875
79	1½-ABL-15	28.01	407675
CL Nozzle	(3 in. Sch 160)	15.314	407986

* Replaced by cold leg piping used in hot leg breaks for NC-7 since cold leg break assembly not needed (1½-ABL-13 from 407386 and 1½-ABL-2 from 407381).

Table AI.4 Semiscale Type II Steam Generator Data

	<u>INTACT LOOP</u>	<u>BROKEN LOOP</u>
Number Tubes	6	2
Tube Dimensions	(0.875 in. OD x 0.049 In.	Wall x 1.25 in. Pitch)
Tube Height ⁽¹⁾	2 @ 391 in. 2 @ 364.5 in. 2 @ 336 in.	1 @ 391 in. 1 @ 336 in.
Primary Volume, Bundle	1.27 ft ³	0.40 ft ³
Primary Plenum Volume	0.058 ft ³ each	0.042 ft ³ each
Secondary Volume ⁽²⁾	4.03 ft ³	1.85 ft ³
Downcomer Volume	0.91 ft ³	0.58 ft ³
Total Secondary Volume ⁽³⁾	11.2 ft ³	8.69 ft ³
Secondary Heat Transfer Area	83.3 ft ²	27.76 ft ²

- (1) Above top of tube sheet
 (2) Tube sheet to top of tubes
 (3) Tube sheet to top of steam dome

APPENDIX II

INPUT LISTINGS

Input listings for the final basecase Semiscale S-IB-3 (with 3-D and 1-D models) transients are given on attached microfiche.

DISTRIBUTION:

U. S. Government Printing Office
Receiving Branch (Attn: NRC Stock)
8610 Cherry Lane
Laurel, MD 20707
300 copies for R4

U. S. Nuclear Regulatory Commission (5)
Reactor Systems Research Branch
Division of Accident Evaluation
Office of Nuclear Regulatory Research
7915 Eastern Avenue
Silver Spring, MD 20910
Attn: F. Odar
L. M. Shotkin
D. Solberg
H. S. Tovmassian
N. Zuber

EG&G Idaho (5)
Idaho National Engineering Laboratory
P. O. Box 1625
Idaho Falls, ID 83415
Attn: T. R. Charlton
G. W. Johnsen
V. H. Ransom
S. Z. Rouhani
R. J. Wagner
G. E. Wilson

Brent Boyack
T. D. Knight
Rick Jenks
Los Alamos National Laboratory (3)
K553 Q-9
Los Alamos, NM 87545

U. S. Rohatgi, 130
Department of Nuclear Energy
Brookhaven National Laboratory
Associated Universities, Inc.
Upton, New York 11973

N. H. Shah
Babcock & Wilcox Co. (NPGD)
P. O. Box 1260
Lynchburg, VA 24505

Oddbjörn Sanderväg
Studsvik Energiteknik AB
S-611 82 Nyköping
SWEDEN

Jesse Fell (5)
Deputy Director, Water Reactor Programs
Atomic Energy Establishment
Winfrith
Dorchester, Dorset DT28DH
ENGLAND

6400 A. W. Snyder
6410 J. W. Hickman
6417 D. C. Carlson
6420 J. V. Walker
6421 T. R. Schmidt
6422 D. A. Powers
6423 P. S. Pickard
6425 W. J. Camp
6427 M. Berman
6440 D. A. Dahlgren
6442 W. A. von Riesemann
6444 L. D. Buxton (2i)
6444 R. K. Byers
6444 R. K. Cole, Jr.
6444 D. Dobranich
6444 M. G. Elrick
6444 L. N. Kmetyk
6444 J. M. McGlaun
6444 J. L. Orman
6444 W. H. Schmidt
6444 R. M. Summers
6444 S. W. Webb
6449 K. D. Bergeron
3141 S. A. Landenberger (5)
3151 W. L. Garner
8024 P. W. Dean

NRC FORM 335 (2 84) NRCM 1102 3201, 3202		U.S. NUCLEAR REGULATORY COMMISSION		1. REPORT NUMBER (Assigned by TIDC add Vol. No. if any) NUREG/CR-4465 SAND85-2563	
BIBLIOGRAPHIC DATA SHEET				3. LEAVE BLANK	
2. TITLE AND SUBTITLE TRAC-PF1/MOD1 Independent Assessment: Semiscale MOD-2A Intermediate Break Test S-IB-3				4. DATE REPORT COMPLETED MONTH: January YEAR: 1986	
5. AUTHOR(S) Lubomyra N. Kmetyk				5. DATE REPORT ISSUED MONTH: February YEAR: 1986	
7. PERFORMING ORGANIZATION NAME AND MAILING ADDRESS (Include Zip Code) Sandia National Laboratories Thermal/Hydraulic Analysis Division 6444 P. O. Box 5800 Albuquerque, NM 87185				8. PROJECT TASK WORK UNIT NUMBER A-1374	
10. SPONSORING ORGANIZATION NAME AND MAILING ADDRESS (Include Zip Code) Reactor Systems Research Branch Division of Accident Evaluation Office of Nuclear Regulatory Research U. S. Nuclear Regulatory Commission Washington, DC 20555				11. TYPE OF REPORT Technical	
12. SUPPLEMENTARY NOTES				6. PERIOD COVERED (Inclusive dates) ---	
13. ABSTRACT (200 words or less) The TRAC-PF1/MOD1 independent assessment project at Sandia National Laboratories is part of an overall effort funded by the NRC to determine the ability of various system codes to predict the detailed thermal/hydraulic response of light water reactors during accident and off-normal conditions. The TRAC code is being assessed at SNLA against test data from various integral and separate effects test facilities. As part of this assessment matrix, an intermediate break test (S-IB-3), performed at the Semiscale Mod-2A facility, has been analyzed. Using an input model with a 3-D VESSEL component, the vessel and downcomer inventories during S-IB-3 were generally well predicted, but the core heatup was underpredicted compared to data. An equivalent calculation with an all 1-D input model ran about twice as fast as our basecase analysis using a 3-D VESSEL in the input model, but the results of the two calculations diverged significantly for many parameters of interest, with the 3-D VESSEL model results in better agreement with data.					
14. DOCUMENT ANALYSIS - KEYWORDS DESCRIPTORS				15. AVAILABILITY STATEMENT Unlimited	
6. IDENTIFIERS (OPEN ENDED TERMS)				16. SECURITY CLASSIFICATION This paper: Uncl This report: Uncl	
				17. NUMBER OF PAGES 156	
				18. PRICE	

120555078877

1 1A1R4

US NRC
ADM-DIV OF TIDC
POLICY & PUB MGT
W-501
WASHINGTON

BR-PDR NUREG
DC 20555

